Investigation of the Enhancement of Convective Heat Transfer for Wall-Bounded Flows Utilizing Nanofluids

SALEH ETAIG

PhD

2017

Investigation of the Enhancement of Convective Heat Transfer for Wall-Bounded Flows Utilizing Nanofluids

SALEH ETAIG

A thesis submitted in partial fulfilment

Of the requirements of The University of

Northumbria at Newcastle

For the degree of

Doctor of Philosophy

Research undertaken in the

School of Engineering and Environment

April 2017

ABSTRACT

Heat transfer is one of the main phenomena in many industrial processes and applications such as heat exchangers and power generation. For many years, liquids such as water, oil and ethylene glycol had been used as the heat transfer fluids. These fluids have a poor inherent thermal conductivity. Thus, innovation in developing another generation of heat transfer fluids is required for better efficiency. Nanofluids represent a class of pioneering engineering heat transfer fluids. These fluids are made by dispersing metallic or non-metallic particles with nanometer size in various base fluids. With their predominant thermophysical properties, nanofluids are promising medium for heat transfer enhancement of next generation heat dissipation in many industrial applications.

This research is focused on studying the enhancement of heat transfer in wall-bounded flows using nanofluids. The enhancement was investigated numerically by modelling nanofluids using CFD technique. Several configurations were tested with different flow types namely, natural convection in a square cavity, forced convection in a backward facing step and flow in micro-channels. The effect of Brownian motion on the heat transfer performance and fluid flow characteristic was investigated for natural convection flow using various nanofluids with different volume fractions for a range of Raleigh numbers. The results showed that the increase in the volume fraction deteriorates the heat transfer. On the other hand, the increase in Ra number promotes the heat transfer rate.

For backward facing step, the effect of the inclination angle of the face step using nanofluid was investigated thoroughly. The increase in the facing step angle was found not preferable from a heat transfer perspective, the results showed that the Nu number decreased by up to 3% when 90^{o} inclination angle is tested compared to 125^{o} inclination angle and this information may be valuable for designing industrial equipment. An empirical effective viscosity model is proposed as part of the study. The model is based on available experimental, numerical and theoretical data. The sensitivity of the model has been rigorously

scrutinized for different volume fractions and wide range of temperatures. The results showed that the proposed model is reliable and can be employed for various flow configurations.
The proposed model has also been used to predict flow through microchannels of various cross-sectional shapes and area. The effect on friction factor for such channels as well as the heat transfer performance has been thoroughly investigated. It was found from this investigation that most of the heat transfer occurred in the U-bend microchannel took place at the downstream flow and it was higher by up to 40.5% compared to the upstream when 6% volume fraction was tested.

Finally, a general purpose test rig was designed and built in the lab to conduct some experimental investigation for a double pipe heat exchanger with nanofluids as a coolant. Four different nanoparticles were purchased and are ready for synthesising the nanofluid using ultrasound bath and magnetic stirrer. The rig is ready for the run and several test runs were conducted using water as the base fluid. Unfortunately, due to certain technical extenuating circumstances, experiments using nanofluids could not be conducted within the time span of the project.

List of Contents

List of Figures

List of Tables

Acknowledgment

First, I must thank the Almighty Allah for his providential care on me and for giving me the courage, determination and guidance in conducting this research.

Special and foremost, I would like to thank my supervisors Dr Reaz Hasan and Dr Noel Perera, for their invaluable guidance, patience, encouragement and support over the duration of this research. Without their ideas, advice, suggestions, and support, this project would never have been completed.

I would like to express my appreciation to my beloved parents for their continuous support and wisdom over the course of my academic journey. Furthermore, I would like to thank my brothers and sisters for their care and assistance throughout my years of education. Special thanks, of course, are due to my wife for her love, support, care and patience since the beginning of this work and thanks to my four children.

Moreover, I am indebted to my colleagues and friends in the UK for providing an enjoyable and fun environment. Many thanks are due to the academic and technical staff at Northumbria University for their support and encouragement. I am very grateful to Prof. Chris Underwood for his support during the experimental work of this research.

I would like to thank the laboratory technicians who have given me their valuable time and assistance for the experimental work.

I would also like to take this opportunity to express my gratitude to the Ministry of Education and the Culture Affairs Department of the Libyan Embassy in London for providing the managerial and financial support during my PhD study at Northumbria University.

Declaration

I declare that the work contained in this thesis has not been submitted for any other award and that it is all my own work. I also confirm that this work fully acknowledges opinions, ideas and contributions from the work of others.

Name: SALEH ETAIG

Signature:

Date: April 2017

Nomenclature

A	Area	m^2
C_f	Skin friction factor	
C_p	Specific Heat at Constant Pressure	$kJ.kg^{-1}.K^{-1}$
D	Diameter, Hydraulic diameter	m
E	Energy	J
F	Force	N
g	Gravitational acceleration	$m.s^{-2}$
H	Height	m
h	Heat transfer coefficient	W/m^2K
h	Enthalpy	kJ
K	Thermal conductivity	$W.m^{-1}.K^{-1}$
L	Length	m
m	Mass	kg
N_s	Entropy generation number $N_s = \frac{S_{gen}^{'''} H^2}{K}$	
P	Pressure	Pa
Q	Heat flux	W/m^2
R	Radius	m
S	Entropy generation	$W/K.m^3$
T	Temperature	K
t	Time	s
V	Volume	m^3
V	Velocity (u, v ,w)	m/s
W	Width	m
x,y,z	Coordinates	m
Subscripts		
f	Fluid	
s	Solid	
np	Nanoparticle	
eff	Effective	
H	Hot	

C	Cold	
i	Initial	
in	Inlet	
out	Outlet	
Greek symbols		
α	Thermal diffusivity	m^2/s
A	Inclination angle	
τ	Shear stress	Pa
ϕ	Volume fraction	
Φ	Dissipation function	
μ	Viscosity	Kg/m.s
β	Thermal expansion coefficient	
P	Density	Kg/m^3
δ_{ij}	Kronecker delta function	
Dimensionless		
Groups		
Grashof Number	$Gr=\beta g L3\Delta T/\nu^2$	
Prandtl Number	$Pr=C_p.\ \mu/K$	
Rayleigh number	Ra=Gr.Pr	
Reynolds number	$Re\frac{v.\mu L}{\mu}$	

1 Introduction

1.1 Background

Heat transfer engineering is one of the fundamental steps in numerous industrial processes such as heating, cooling, and transportation of power generation. Accordingly, convective heat transfer plays a key role in the thermal applications and can be classified according to the flow nature as forced or natural convection as shown in Figure 1.1. The design and analysis of engineering systems require an accurate prediction of thermophysical properties of fluid. The thermophysical properties are referred to both thermodynamic properties and transport properties.

The thermodynamic properties describe equilibrium states of the system such as temperature, pressure, density, internal energy, heat capacity, speed of sound, enthalpy, and entropy. The transport properties which are related to the transfer of momentum or energy within the system such as thermal conductivity, viscosity, and thermal diffusivity. In practical applications, the study, analysis and design of heat transfer systems require an understanding of both transport and thermodynamic properties. However, the experimental approaches for measuring the transport properties showed lower accuracy compared to the thermodynamic properties, which are well established in measurement for most common fluids[1].

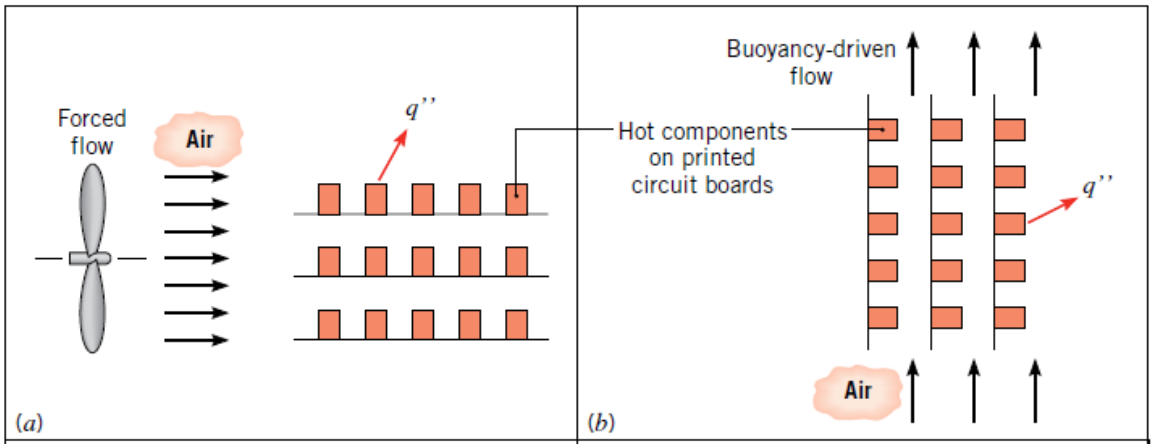

Figure 1-1 Convection heat transfer processes. (a) Forced convection. (b) Natural convection. [2]

Recently, conventional fluids such as water and oil have been used as heat transfer fluids. These fluids have a major drawback due to their low thermal conductivity. Therefore, improvement in developing a new generation of heat transfer fluids is required in many industrial applications so efficient thermal systems can be achieved.

This new innovative class of fluids containing ultrafine nanoparticles was first introduced by Choi [3] used in cooling processes has shown superb performance during tests including increased thermal conductivity and augmented heat transfer coefficient compared to conventional liquids. Numerous studies have shown that nanofluids have superior thermophysical properties, among of which is thermal conductivity, which has been studied most extensively but remains controversial. As a novel strategy to improve heat transfer performance of coolants by adding nano-sized particles. Nanofluids show superior heat transfer properties and are being considered as promising cooling fluids and has demonstrated feasible applicability in many fields to be used for cooling hot systems such as solar collectors, electronic cooling systems, heat pipes, and nuclear reactors.

The Nanofluids are suspensions with less than 100-nanometre diameter. Nanofluids have been found to retain improved thermophysical properties of the fluid; these properties are thermal conductivity, viscosity, density and heat capacity. Furthermore, the convective heat transfer was found increased compared to that of base fluids like ethylene glycol, oil or water.

In the last two decades, the number of researches on nanofluids has risen significantly as shown in Figure 1.1 (Google Scholar search). However, despite the massive number of works whether experimental or numerical, there is still a big gap in these studies. For example, several discrepancies have been reported between experimental and numerical works. Furthermore, the experimental results consistency is yet to be to be ascertained.

Exploring the literature has demonstrated several gaps in utilizing the nanofluids for improving the heat transfer rate. These gaps can be found in various flow scenarios, for instance, natural convection with Brownian motion needs to be investigated thoroughly in order to understand the effect of the Brownian motion on the heat transfer and flow characteristics, in particular, the Ra number and the volume fraction and its influence on the velocity gradient.

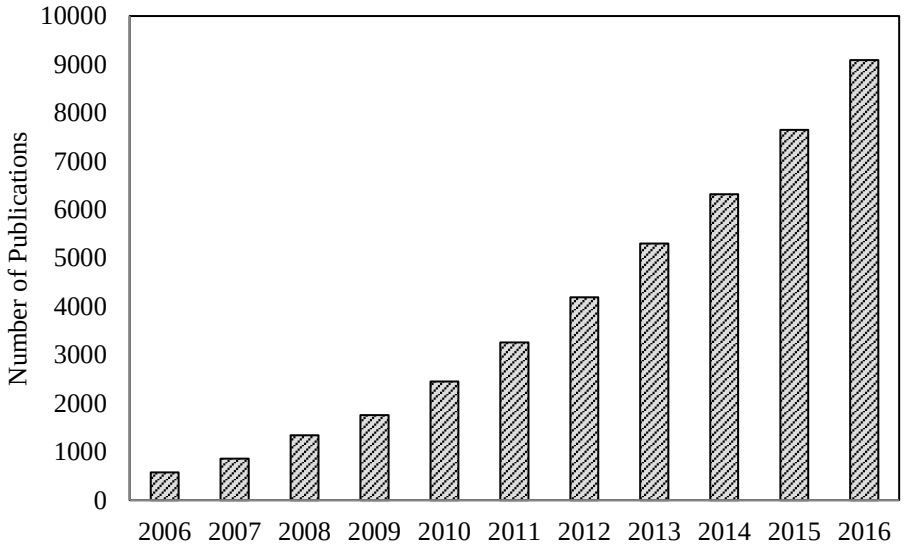

Figure 1-2 Increasing publications per recent years related to Nanofluid (Google Scholar)

Backward-facing step flows using nanofluids have been investigated by many researchers and several parameters have been tested. However, the influence of the inclination of the face step on the heat transfer rate needs further investigation in accordance with the aspect ratio effect on the heat performance and fluid flow.

Despite the various models proposed to predict the effective viscosity of nanofluids, there is no unified model to accurately predict the viscosity. The effective viscosity modelling through regression analysis can be a useful alternative approach. The deviation in the estimated values from the equations with the experimental values is due to the divergent experimental values reported in the literature. In the present situation, the correlation was validated with experimental data and achieved with an acceptable range of deviation.

Cooling devices in micro-scales, such as microchannels, are in increasing demand in current and future heat deduction applications, these applications can be found in computer chips, laptops, mobile phones, notepads, biomedicine and many other applications.

The applications of nanofluids in the microchannel is promising due to their high heat transfer rate compared to their compact size. Since microchannels are just channels with diameters less than 1000 μm and the governing equations are the continuity, momentum and energy equation. However, the viscous dissipation effect becomes significant in microchannel as reported by Koo and Kleinstreuer [4] and should be added to the energy equation even at low Re numbers.

Microchannel can take several configurations according to the specific application design and the flow conditions. Several cross-sectional shapes for microchannels have been reported in the literature. However, only a few studies focused on the entry region of the circular cross section microchannel. Furthermore, investigations of rectangular cross section microchannel with various aspect ratio showed gaps in the effect of nanoparticle volume fraction in line with the aspect ratio on the heat transfer rate and flow characteristics.

The flows in U-bend can be found in many applications, in microchannel, only a few were reported with nanofluid as the working fluid. The main feature in the U-bend flows is the change of the pressure in the bend as well as the shear stress which ultimately affects the flow and the heat transfer in the domain.

The understanding of the flow in the U-bend microchannel geometry is essential to provide optimisation and design when employing nanofluid at design working conditions in terms of volume fraction, nanoparticle type and the base fluid. The triangular cross section U-bend microchannel as a special case and its influence on the heat performance and the fluid flow features are investigated in the literature on very limited occasions. The extensive investigation in such a configuration can help in optimisation of heat transfer enhancement in the microchannel.

The applications of nanofluid in heat exchangers was investigated by numerous researchers as nanofluids have proved their superior performance in improving the heat transfer rate. However, despite the number of experimental works in measuring the heat transfer using various nanoparticle types and ranges of volume fractions, the researches on testing several nanoparticle types in double pipe heat exchanger at the same rig to give a comparison and optimisation of the nanoparticle type and the volume fraction type in order for optimum design is still needed. One of the main key factors in enhancing the heat performance in heat exchangers is the stability of the nanofluid, where many studies contradict in homogeneity and stability of the nanofluid.

In order to study the heat transfer enhancement employing nanofluids, an efficient and powerful tool should be implemented, as experimental investigations and theoretical solutions may not be applicable in different flow configurations. Computational fluid dynamics (CFD) is a robust approach developed to study and analyse flows from simple to

very complex flow configurations beyond the standard performance operating conditions. Furthermore, this can be achieved at very low cost and minimum required time.
The CFD method provides an additional approach to study a physical problem in addition to the pure theory and experimental measurements.

1.2 Aims and Objectives

The main focus of this work is to investigate the enhancement of the convective heat transfer rate utilising nanofluid in several wall-bounded flows. A number of flow scenarios were carefully selected of such that they represent typical geometric configuration and at the same time allow significant challenge in terms of flow physics. In addition to establishing a numerical methodology for predicting natural and forced convective flows, efforts were made to propose a new viscosity model which can be usable for a wider range of volume fraction and temperature.
To achieve the overall aims, the objectives of the present study can be summarised as:

- To carry out a comprehensive literature review associated with the thermophysical properties of nanofluids particularly the thermal conductivity and effective viscosity and their expressed models.
- Establish the methodology to numerically simulate the thermophysical properties for a wide range of volume fraction and temperature range by writing a user defined function using the commercial CFD package available within ANSYS.
- To study the influence of Brownian motion in natural convection and its impact on heat transfer rate for various nanoparticle types and concentrations at different Ra numbers.
- To investigate the effect of the inclination angle of the face step in backward facing step and the aspect ratio on the heat transfer rate at a range of nanoparticle volume fraction.
- To propose a new viscosity model in order to predict the effective viscosity of nanofluids with reliable implementation under a wider range of temperature and volume fraction.

- To examine the flow and heat transfer in rectangular cross section microchannel with various aspect ratios
- To study the flow characteristics and heat transfer improvement in circular U-bend microchannel flow.
- To scrutinise the fluid flow and thermal performance in triangular U-bend microchannel.
- To design, fabricate and commission a test rig to conduct an experiment involving nanofluid for a double pipe heat exchanger.

1.3 Research Novelty and Originality

The main contributions from the research can be summarised as follows:

- A robust numerical methodology capable of incorporating the thermo-physical properties of nanofluids has been developed and scrutinised. The methodology can be applied for any type of nanofluid for both natural and forced convection flows.
- It was found from a thorough literature review that a gap exists in terms of 'effective viscosity' expressions for nanofluids. As a result of this study, a new effective viscosity model was proposed and tested for a variety of flow configurations. This model is believed to be applicable to a wider range of volume fraction and temperature range.
- The implementation of Brownian motion approach for natural convection flows shows insignificant improvement in terms of flow field and heat transfer. The findings from the present study questions the validity of such approach that may be rooted to the fundamental formulation of nanofluid dispersion mechanism in fluids.
- Systematic investigations of micro-channels for various rectangular ducts, U-bends of circular and triangular cross-sections were carried out. The findings from these studies are deemed to be useful to the designers of electronic devices. Similarly, the results on the effect of inclination angle for backward facing step geometry using nanofluids will also be valuable for practitioners.

1.4 Thesis Construction

This thesis comprises nine chapters supported by three appendices. One of these chapters is the present introductory chapter, which summarises the background, aims, objectives, and publications while other chapters are prescribed as follows:

- **Chapter 2 Literature review.** This chapter explores the literature on the nanofluid concepts from preparation methods to thermophysical properties. Previous studies on numerical simulation and experimental work on enhancing the heat transfer employing nanofluids in various applications were critically discussed.
- **Chapter 3 Mathematical Model and Numerical simulations.** This chapter presents the mathematical formulations of the governing equations of the flow and modelling of the thermophysical properties through the user defined functions.
- **Chapter 4 Natural Convection with Brownian motion.** In this chapter, the enhancement of the heat transfer rate in natural convection was investigated for a range of Ra numbers. Brownian motion approach is incorporated to study the flow characteristics.
- **Chapter 5 Investigations of Backward-facing step flow**. This chapter studies the effect of the inclination angle of the face step on the heat transfer rate as well as the aspect ratio for various inclination angles.
- **Chapter 6 Investigation of a new effective viscosity model**. This chapter proposes a new viscosity model to predict the nanofluid effective viscosity with acceptable level of accuracy for a wider range of applications
- **Chapter 7 Investigation of microchannel flows**. This chapter reports the flow in various microchannel configurations utilising nanofluid as a cooling fluid. The enhancement of heat transfer in different geometries and a range of volume fraction is reported.
- **Chapter 8 Experimental Work**. Chapter 8 describes the experimental procedure in building the rig test and details the different nanoparticles types which planned to conduct in the lab.
- **Chapter 9 Conclusions and Future work Recommendations**. This chapter details the main findings from this research, and the recommendations for future researches.

1.5 Publications

- Investigation of Enhancement of Heat Transfer in Natural Convection utilising Nanofluid. Saleh Etaig, Reaz Hasan and Noel Perera. 17th International Conference on Heat Transfer and Applications in London, UK, January, 19-20, 2015
- Numerical Study on the Effect of Inclination Angle on Heat Transfer Performance in Back-Ward Facing Step Utilizing Nanofluid. Saleh Etaig, Reaz Hasan and Noel Perera. UK Heat Transfer Conference 2015 Edinburgh September 2015
- Investigation of a New Effective Viscosity Model for Nanofluids," *Procedia Engineering*, vol. 157, pp. 404-413, 2016. Saleh Etaig, Reaz Hasan and Noel Perera.
- Investigation of the flow characteristics of Titanium –Oxide -Water Nanofluid in Microchannel with Circular Cross Section. Saleh Etaig, Reaz Hasan and Noel Perera Proceedings of the ASME 2017 Power and Energy Conference PowerEnergy2017 June 25-30, 2017, Charlotte, North Carolina, USA.
- Investigation of The Effect of Brownian Motion on the Flow Characteristic in Natural Convection using Different Nanofluids. Saleh Etaig, Reaz Hasan, Noel Perera and Ahmad Ramadan. 7th International Symposium on Advances in Computational Heat Transfer. Napoli, Italy. 28 May-02 June 2017.
- A New Effective Viscosity Model for Nanofluids. Saleh Etaig, Reaz Hasan and Noel Perera. International Journal of Numerical Methods for Heat and Fluid Flow. Accepted manuscript.
- Investigation of flow in triangular U-bend microchannel utilising nanofluid. Saleh Etaig, Reaz Hasan and Noel Perera. Submitted to International Communications of Heat and Mass Transfer.
- Investigation of the effect of the inclination angle in Backward facing step on the heat transfer enhancement using Titanium oxide-water nanofluid. Saleh Etaig, Reaz Hasan and Noel Perera. Submitted to Applied Thermal Engineering

2 Literature review

2.1 Introduction

This chapter presents a comprehensive review of convective heat transfer utilising nanofluids in wall-bounded flows. This review will focus on the concepts behind nanofluids and their thermophysical properties, along with appropriate ways to perform mathematical and computational modelling of such nanofluids. Approaches of the synthesis of nanofluids will also be surveyed. The numerical and experimental investigations used to investigate nanofluids in convective heat transfer are the focus of this chapter; the findings of these investigations will also be given.

2.2 Heat Transfer in Nanofluids

Convective heat transfer can be found in many industrial applications such as heat exchangers, nuclear reactors, and cooling systems; enhancing heat transfer has been one of the main targets of researchers for several decades. Convective heat transfer can be enhanced by changing flow geometry or boundary conditions or promoting turbulence, or by enhancing the thermal conductivity of the fluid used.

Numerous techniques have been proposed to enhance the heat transfer performance of fluids. Researchers have also tried to augment the thermal conductivity of base fluids by dispersing micro- or larger-sized solid particles in those fluids where the thermal conductivity of the particle is higher than that of the liquids. A great deal of experimental and theoretical works on such solid suspensions has been done by multiple researchers since the initial theoretical study by Maxwell[5]. However, due to the large density and size of many of these particles, it was difficult to avoid the sedimentation, while the issue of clogging tended to arise when using micro-sized particles.

One of the most recent techniques for enhancing the thermal conductivity is by dispersing nanoparticles in a base fluid to form a so-called Nanofluid. The nanofluids concept creates a novel form of heat transfer in fluids by suspending nano-scale metallic or non-metallic particles in base fluids. Examples of base fluids used in this way include water, glycol, and oils. Nanofluids are fluids that contain metallic nanoparticles such as alumina, titanium

dioxide and copper, while common base fluids such as water, ethylene glycol, and engine oil are generally used as base fluids.

The pioneering work in introducing this new class of these fluids was first done by Choi [3] and it was when he coined the term nanofluid. Nanofluids are dilute suspensions of nanoparticles with diameters of less than 100 nm, and they have been recognised as a new type of solid-liquid mixture. This new generation of fluids offers high stability with higher thermal conductivity and hence higher convective heat transfer performance compared to conventional liquids. Due to the nanoscale size of the particles used, nanofluids suffer from less particle sedimentation and pipe clogging than micro-fluids or fluids with larger scaled suspensions, with no penalty in pressure drop.

2.2.1 Effective parameters

In terms of investigating the thermophysical properties of nanofluids, several parameters play vital roles and are of interest to researchers. These parameters include nanoparticle volume and concentration, the base liquid, the type of nanoparticle, nanoparticle size and shape, and particle migration patterns are the most influential parameters.

2.2.1.1 Type of nanoparticle and base fluid

Several researchers have attempted to study the effects of nanoparticle type on heat transfer performance. Oztop et al [6] investigated the influence of different nanoparticle (TiO2 and Al_2O_3) on the fluid flow in an enclosure. They found that adding nanoparticles to water affects heat transfer performance, particularly at high Rayleigh numbers. However, an enhancement in heat transfer was observed for all Rayleigh numbers, though only low volume fractions were tested in this study.

Ghasemi and Aminossadi [7] carried out a numerical study investigating the effect of several nanoparticles on the cooling performance. Three nanoparticles (Cu, Al_2O_3 and TiO2) were examined in their study. At higher volume concentrations, TiO2 was found to have the best heat transfer rate. However, the volume fraction tested in this study did not exceed 2%.

Vajjha and Das[8] conducted an experimental investigation for three nanofluids utilising aluminium oxide, copper oxide and zinc oxide nanoparticles in which maximum thermal conductivity enhancement was found when using Al_2O_3 nanoparticles. However, the

results for thermal conductivity in this investigation did not agree with many existing models.

2.2.1.2 Nanoparticle volume concentration

The volume fraction of the nanofluid (also known as volume concentration) is defined as the ratio of the volume of nanoparticles to the volume of the base fluid. The volume concentration is one of the most significant parameters for nanofluids because the solid particles have higher thermal conductivity than the base fluid; thus as the percentage of nanoparticles increases, the thermal conductivity of the nanofluid also increases.

Lee et al [9] measured thermal conductivity for four different nanofluids (CuO-water, CuO-ethylene glycol, Al_2O_3-water and Al_2O_3-ethylene glycol). They highlighted that the thermal conductivity could be increased by up to 20% at a 4% volume fraction of the best-performing mix, Cuo-ethylene glycol. The thermal conductivity ratios increased almost linearly with increase in volume fraction. The experimental data suggested that the thermal conductivity of nanofluids was dependent on the thermal conductivity of both the nanoparticles and the host fluids. However, the investigators did not give an explanation for this enhancement in thermal conductivity.

Khanfer et al [10] numerically investigated the heat transfer rate in 2-D enclosure. They investigated heat transfer enhancement for a range of Grashof numbers and volume concentrations. They noted that the heat transfer rate of the nanofluid was enhanced as the nanoparticles volume concentration increased. Variation in the density and viscosity used in various models were also reported in this study.

The effect of volume fraction on the thermal conductivity for copper and aluminium oxide nanoparticles was also reported by Li and Peterson [11] in their experimental investigation. They tested a wider range of volume fractions but only for a limited range of temperature between 27.5 and 34.7 ^{o}C. Thermal conductivity was found to increase as the volume concentration, and the temperature increased. For higher volume concentrations, however, their experimental data revealed an insignificant increase in the thermal conductivity ratio.

2.2.1.3 Nanoparticle diameter

Other important parameters that play a vital role in the hydraulic and thermal behaviours of nanofluids are the particle size and shape. Many researchers report contradictory effects of nanoparticle diameter on heat performance [12, 13]. Mirmasoumi and Behzadmehr [14] numerically studied the effect of the nanoparticle diameter on an Al_2O_3-water mix in terms of heat transfer in a horizontal tube. They employed a two-phase mixture model in the laminar mixed convection. They reported a substantial increase in the heat transfer coefficient as the nanoparticles mean diameter decreased. However, particle size did not change the skin friction coefficient significantly. Prasher et al [15] measured the nanofluid viscosity of alumina-based nanofluids for three different particle diameters (27, 40 and 50 nm). Viscosity was found to increase as the nanoparticle diameter increased. The researchers also noticed that the viscosity of nanofluids is much greater than predicted by theoretical models. Pak and Cho [16] studied the heat transfer performance of suspensions consisting of water and metallic oxide particles such as ɣ-alumina (Al_2O_3) with a nanoparticle diameter of 13 nm and titanium dioxide (TiO2) with a nanoparticle diameter of 27 nm. They found that the size of the nanoparticles plays a vital role in determining the viscosity. They also reported that the heat transfer coefficient of the suspensions at a volume concentration of 3 percent was 12 percent smaller than that of pure water when compared under the condition of constant average velocity. This finding contradicts a great deal of previous researches[17]. Another effect of the nanoparticle was investigated by Aminfar and Motallebzadeh [18] when they numerically studied the effect of nanoparticle diameter on the velocity field and nanoparticle distribution. They highlighted that as the nanoparticle diameter increased, the velocity of the fluid and nanoparticle was reduced. They attributed this reduction in velocity to the loss in Brownian forces caused by the increase of nanoparticle diameter. It is worth noting that these researchers built their simulation on the assumption that the nanofluid was a two-phase mixture, while many other numerical simulations have assumed that the nanofluid can behave as a single-phase fluid.

Chon et al [19] measured the thermal conductivity of Al_2O_3 for different diameters of nanoparticle (12.92 nm, 49.47 nm, and 182.4 nm). They reported that the thermal conductivity increased with a decrease in nanoparticle diameter. In their experiment, they introduced an experimental correlation for thermal conductivity as a function of the

nanoparticle diameter. However, they found that at higher temperatures, the thermal conductivity increased mainly due to nanoparticle Brownian motion; no reason was given for this increase.

2.2.1.4 Brownian diffusion and thermophoresis effects

When an infinitesimal particle is mixed with a fluid, it is subjected to the molecules of the fluid. For nanoparticles (colloids), the momentum imparted to the particle by this interaction changes randomly, which causes the particle to move forward in an arbitrary direction; this is known as Brownian motion.

Many researchers have studied the Brownian motion effect in order to understand the mechanism of change in the thermophysical properties of nanofluids. One of the earliest publications on the Brownian motion effect on nanofluids was by Keblinsky et al [20]. They explored several possible reasons for the anomalous increase in thermal conductivity, and four different factors were investigated: Brownian motion of the particles, molecular-level layering of the fluid at the particle-fluid interface, the transported heat to the nanoparticles, and the effects of clustering of particles. They described the role of Brownian motion as not important in the enhancement of thermal conductivity. However, they did not exclude the possibility that other mechanisms may be important. Furthermore, their findings required further experimental and numerical studies to help understand the mechanisms of augmentation of thermal conductivity of the nanofluid.

A similar finding was also reported by Evans et al [21]. These researchers used a kinetic theory-based analysis of heat flow of solid nanoparticles. They concluded that thermal conductivity does not show any significant increase due to effects related to Brownian motion-induced hydrodynamic effects. However, they limited their study to stationary fluids and neglected the direct contribution of Brownian motion of the particle to thermal transport.

Jang and Choi [22] performed a theoretical study to investigate the role of Brownian motion in thermal behaviour. They found that Brownian motion is a key mechanism influencing the thermal performance of both nanoscale and molecular scale particles. Their investigation was in agreement with other available experimental data for thermal conductivity ratios for Al_2O_3 and Cu nanofluids for the range of temperatures tested.

Although they only tested for one volume fraction (1%), the model predicted thermal conductivity enhancement better than Maxwell's theoretical model. However, these were inconsistent results.

The role of Brownian motion on the thermal conductivity enhancement was also investigated by Gupta and Kumar [23]. They showed in their Brownian dynamic simulations that Brownian motion increased the thermal conductivity of nanofluids by 6%, mainly as a result of arbitrary motion rather than diffusion. However, this result was limited by the maximum volume fraction of each nanoparticle diameter. The Brownian velocity was also investigated by Chon et al[19]. They reported an experimental formula for nanofluids' thermal conductivity as a function of nanoparticle diameter. They highlighted that the Brownian motion of nanoparticles can be considered the main mechanism in the enhancement of thermal conductivity as the temperature increases and nanoparticle diameter decreases.

2.3 Thermophysical properties of nanofluids

Understanding the thermophysical properties of nanofluids is fundamental when employing them in practical applications. There are a number of essential formulas for predicting the thermophysical properties of nanofluids, and these are frequently investigated by researchers. This work has investigated the heat transfer behaviour of nanofluids both theoretically and experimentally. Heat transfer performance using nanofluids is expressed by the convective heat transfer coefficient, which is a function of a number of thermophysical properties such as thermal conductivity, viscosity, specific heat, density, and the thermal expansion coefficient. Recently, the development of a model to predict the thermophysical properties of nanofluids has attracted the attention of many researchers. However, although several models have been proposed in the literature, only a few correlations have been favourably received. In order to determine the convective heat transfer coefficients, the most appropriate thermophysical properties of nanofluids models must be discovered and utilised. Of all the experimental investigations found in the literature, very few are concerned with the comparison of the thermophysical properties of nanofluid. Duangthongsuk and Wongwises [24] reported a comparison between the differences of the computed and the measured thermophysical properties of a TiO2 water nanofluid, which highlighted that all of the available models underestimate the viscosity

and the thermal conductivity of nanofluids in comparison to the measured data. Duangthongsuk and Wongwises [25] also conducted experimental work to report the effect of the thermophysical properties model on the predicted values of the convective heat transfer coefficient of a TiO2–water nanofluid passing in a horizontal double-pipe heat exchanger with counter flow under turbulent flow conditions. TiO2 nanoparticles in a water-based fluid with volume fraction 2% dissolved in water were tested, and discrepancies in the results for the different models of the thermophysical properties of the nanofluid were found. However, when using a very low volume fraction, the different thermophysical models had no substantial influence on the measured values of the heat transfer coefficient. Although the subject of thermal properties of nanofluids is covered by a broad body of literature, the findings are inconsistent in terms of thermal conductivity enhancement due to the poor modelling of nanofluids and a lack of accuracy in various measurement techniques. It is worth noting that the nature of the measurement of temperature gradients in the prepared nanofluid can cause considerable errors when measuring thermal conductivity due to the difficulty of retaining accuracy at nano-scale. Furthermore, nanofluids are likely to settle, and agglomerate, and the effects of these tendencies have not been deeply investigated by researchers. Thus, caution must be taken to provide a steady sample temperature when taking readings in order to avoid any changes in the sample's microstructural behaviours during the experiment. The next section will explore the thermal properties of the nanofluids and their effect on heat transfer performance.

2.3.1 Thermal conductivity

Thermal conductivity of nanofluids has attracted the attention of many researchers; in fact, thermal conductivity has received the most significant attention from researchers among the thermophysical properties of such fluids. This means that this property has been investigated by many authors theoretically, numerically, and experimentally. One of the pioneering works on the thermal conductivity was conducted more than one hundred years ago by Maxwell [5], who proposed a new static model for predicting the thermal conductivity of fluids with multiphase in his theoretical work. The aim of his model was to determine the effective electrical or thermal conductivity of solid-liquid mixtures for low volume concentration suspensions with uniform spherical particle size as shown in Table

2.1. However Maxwell assumed spherical particles in a very dilute mixture; moreover, he neglected the effects of interactions among these particles.

Based on his work, a vast number of studies have made use of, and further developed, Maxwell's equation. Fricke [26] developed Maxwell's equation to predict the thermal conductivity of particles with ellipsoidal shapes in a homogenous dispersion. In general, he considered similar assumptions as used by Maxwell. Bruggeman [27] proposed a classical model based on continuum formulations, which are a function of the particle size/shape and volume concentration. The model assumes diffusive heat transfer in both solid and fluid phases. This theory was tested in terms of thermal conductivity of the dispersion, but the results were not consistent with previous studies.

Davis [28] introduced a theoretical model for calculating the thermal conductivity of a mixture with spherical particles. This model is a function of the volume fraction of the solid particle and the continuous phase. The result was found to be similar to that produced by previous techniques. Lu and Lin [29] used two microstructural models in their study, the well-stirred model and the hard spheroid mode. These models were able to predict the thermal conductivity for volume fractions of up to 3 %.

Bhattacharya et al [30] developed a model for calculating the thermal conductivity of a nanofluid based on Brownian dynamic simulation, a technique that is considered easier than molecular dynamics. This model was only tested at 300 K and hence the application at higher temperatures is not known.

Koo and Kleinstreuer [31] developed a new model to predict a nanofluid's thermal conductivity. This model takes into account the effects of nanoparticle volume concentration, particle size, and temperature dependence, as well as including the properties of the base liquid and particle phase. The advantage of this model is that it considers the base fluid's liquid motion as influenced by arbitrarily moving nanoparticles. These researchers highlighted the fact that the influence of Brownian motion is more pronounced at high temperatures, and that it can be measured with higher accuracy experimentally. Their model demonstrated that the temperature gradient changes significantly at some specific heat fluxes as a result of variable thermal conductivity; this is mainly affected by nanoparticle volume concentration, the material of the nanoparticle, nanoparticle size, and temperature. However, additional experimental work is still required to improve the accuracy of the model. Prasher [32] introduced a semi-empirical Brownian

model for calculating the thermal conductivity of nanofluids. He suggested that, as a result of the convective nature of the heat transports, any useful model must adopt a semi-empirical structure, because of the complicated interaction in the convective currents due to multiple colloids. His proposed model also needed further numerical and experimental investigations for full validation.

Although the classical models can predict the behaviour of micro or larger-size level multiphase mixtures with good accuracy, they generally underestimate the improvement of nanofluids' thermal conductivity as the volume concentration increases. This enhancement of thermal conductivity has been reported in many experimental studies. One of the earliest works on the measurement of the thermal conductivity of dispersion was done by Masuda et al [33]. They measured thermal conductivity for ɣ- Al_2O_3, SiO2, and TiO2 water-based fluids. They showed in their experiment that ɣ- Al_2O_3 nanoparticles at a volume concentration of 4.3% could enhance the effective thermal conductivity of water by 30%. Different volume concentrations were also tested in the investigation, and for Al_2O_3-water and TiO2-water nanofluids, effective thermal conductivities were observed to rise much more as nanoparticle volume concentration increased. However, in the case of SiO2-water, no increase in thermal conductivity was observed.

Eastman et al [34] measured the thermal conductivity of Cu-oil, CuO-water, Al_2O_3-water, and CuO-water nanofluids using transient hot wire apparatus. They noted that thermal conductivity increases linearly with an increase in the volume concentration. They also observed an increase in thermal conductivity by 60% when using a volume concentration of 5% in a CuO-water nanofluid. This improvement in thermal conductivity in the case of Cu-water was greater at very low volume fractions. However further work is needed to investigate the effects of larger volume concentrations of Cu nanoparticles in oil based fluids. Venerus et al [35] conducted an experimental investigation of thermal conductivity using the optical technique known as force Rayleigh scattering. They observed that the thermal conductivity of both Au and Al_2O_3 nanofluids is not affected by temperature. In comparison to previous experimental works for thermal conductivity measured by transient hot wire, their findings are in more agreement with the effective medium theory calculation. It is evident that their observations contradict data produced by both theoretical and experimental methods to investigate thermal behaviour in nanofluids, however. Putnam et al [36] used an optical beam deflection approach to measure the

thermal conductivity of Au-ethanol-water nanofluid up to a volume fraction of 0.6%. They did not observe any enhancement in thermal conductivity. These experimental results do, however, contradict many existing theoretical models and experimental data reports.

Zhang et al [37] reported on the effective thermal conductivity measurements for different nanofluids. Thermal conductivity was found to increase as the volume fraction increased, but this increase was not found to be significant. Moreover, the results were not in agreement with other published data. The researchers attributed this conflict to electrical insulation of the transient hot-wire probe.

Zhu et al [38] experimentally investigated the thermal conductivity of Fe3O4 nanofluid at volume concentrations of up to 5%. They observed higher thermal conductivity than that calculated by means of the classical models. Fe3O4 nanoparticles were also found to have higher thermal conductivity compared to other oxide nanofluids. However, this increase in thermal conductivity was seen to be nonlinear; the reason for this may be nanofluid preparation methods and stability. Yoo et al [39] conducted an experimental investigation to measure the thermal conductivity of TiO_2, Al_2O_3, F3 and WO3 with water and ethylene glycol base fluids. Various volume fractions ranging from 0.1% to 1% were tested. The researchers reported that the thermal conductivity increased as the volume fraction increased. However, no explanation for this enhancement was reported.

Hwang et al [40] measured thermal conductivity for four nanofluids at volume fractions of up to 1% using transient hot wire methods. The thermal conductivity enhancement of MWCNT-water nanofluid was enhanced by up to 11.3% when using a volume concentration of 1%. The results show that the nanofluids' effective thermal conductivity depends on the thermal conductivity of both the suspended particles and base fluids. The lowest thermal conductivity ratio enhancement was in the case of a SiO2-water nanofluid, which did not exceed 3% at the same volume fraction.

Shalkevich et al [41] measured the thermal conductivity of different nanofluids with different ranges of volume fractions. They observed that the thermal conductivity increases linearly with the volume fraction. The highest thermal conductivity enhancement was reported when using alumina nanoparticles; this was an 18% enhancement for SiO2 at a volume concentration of 31%, and a 10% enhancement for Al_2O_3 at 4.8% volume concentration. All measurements were taken at a temperature of 25^{o}C, and hence no effect of temperature on the enhancement was investigated. Duangthongsuk and Wongwises [42]

measured the thermal conductivity of a TiO2-water nanofluid for volume fractions ranging from 0.2 to 2% and temperatures ranging from 15 to 35^{o}C. They observed that the thermal conductivity ratio of nanofluids increased with the increase in nanoparticle volume fraction and marginally decreased with the increase in temperature. However, these results are not consistent with other available theoretical models. Chandrasekar et al [43] have also reported an experimental investigation to measure the thermal conductivity of an Al_2O_3-water nanofluid at volume fractions between 0.33% and 5%. They measured the thermal conductivities of Al_2O_3/water nanofluids and found that they increased linearly with volume fraction. Although their observations were in agreement with other published data, they concluded that nanofluids are non-Newtonian, which contradicts many other researchers.

Beck et al [44] conducted an experiment to measure the thermal conductivity of seven nanofluids with different diameter alumina nanoparticles (8 to 282 nm in diameter) dissolved in ethylene glycol or water. They observed that the effects of thermal conductivity enhancement decrease as the nanoparticle diameter decreases below 50 nm. Their findings also apply to the decrease in thermal conductivity shown by alumina nanoparticles as the diameter of the nanoparticle decreases. However, the level of uncertainty in their experiments was not reported.

The effect of temperature on thermal conductivity enhancement was also investigated experimentally by Murshed et al [45]. They tested TiO2 and Al_2O_3 in water and ethylene glycol, respectively, within a temperature range from 20 to 60^{o}C and volume concentrations from 1% to 5%. They observed that the effective thermal conductivity of nanofluids substantially increased as the nanoparticle volume concentration increased. A linear increase in the effective thermal conductivity of nanofluids as temperature altered was also observed. Comparing their results to other available data, they found that their results showed greater enhancement of this effect. They attributed this difference to the surfactant added to the nanofluid for stability purpose.

Wang et al [46] conducted an experimental investigation to measure the effective thermal conductivities of fluids with Al_2O_3 and CuO nanoparticles in water, engine oil, and ethylene glycol. Their measurements highlighted that the thermal conductivity of the nanofluids increased relative to those of the base fluids. They also observed an increase in thermal conductivity with a decrease in nanoparticle diameter. Murshed et al [47] used a

transient hot wire to measure the thermal conductivity of TiO2 10nm rod shape nanoparticles and 15 nm spherical shapes in water. Their experimental data showed that thermal conductivity increased with an increase in the nanoparticle volume concentration. They also highlighted that the diameter of the nanoparticle and its shape also affect the level of thermal conductivity enhancement. However, they highlighted the gap between the theoretical and experimental prediction of thermal conductivity.

The thermal conductivity of Al_2O_3-water suspension was measured by Xie et al [48]. Their observations showed that the addition of nanoparticles to fluids increased the thermal conductivity of the fluids. The agglomeration in thermal conductivity ratios increases as the nanoparticles volume fraction increase. In contrast, using the same nanoparticles, the thermal conductivity ratio decreases as the thermal conductivity of the base fluid increases. However, these measurements varied appreciably from the values predicted by theoretical models.

Gallego et al [49] investigated the thermal conductivity of a nanofluid comprised of Al_2O_3- with a diameter of 43 nm in ethylene glycol. Here, the thermal conductivity increased as the volume concentration increased; in addition, when the temperature increased, the thermal conductivity also increased. Enhancements of up to 19% increased thermal conductivity over that of the base fluid were found. However, Maxwell's method over-predicts these experimental measurements.

The studies on thermal conductivity models can be summarised in Table 2.1.

Table 2-1 Summary of studies on thermal conductivity models

Reference	Year	Model	Notes	Range of validity
Maxwell[5]	1881	$\frac{K_{eff}}{K_f} = \frac{k_s + 2k_f + 2\emptyset(k_s - k_f)}{k_s + 2k_f - \emptyset(k_s - k_f)}$	Solid and liquid suspension	<2%
Bruggeman[50]	1935	$\frac{K_{eff}}{K_f} = \frac{1}{4}\left[(3\emptyset - 1)\frac{k_s}{k_f} + (2 - 3\emptyset)\right] + \frac{K_f}{4}\sqrt{\Delta}$	Spherical particles	0-4%

Hamilton & Crosser[51]	1962	$\frac{K_{eff}}{K_f} = 4.97\emptyset^2 + 2.72\emptyset + 1$	$\frac{K_s}{K_f} > 100$	0-4%
Davis[28]	1986	$\frac{K_{eff}}{K_f} = 1 + \frac{3(k-1)}{(k-2) - \emptyset(k-1)}[\emptyset + f(k)\emptyset^2 + O\emptyset^3]$	$f(k)$ = 2.5 for k=10 $f(k)$=0.5 for k=∞	0-2%
Lu & Lin[29]	1996	$\frac{K_{eff}}{K_f} = 1 + a\emptyset + b\emptyset^2$		0-3%
Koo and Klenstreuer[52]	2004	$\frac{K_{eff}}{K_f} = \frac{k_s + 2k_f + 2\emptyset(k_s - k_f)}{k_s + 2k_f - \emptyset(k_s - k_f)} + 5 \times 10^4 \beta \rho_S C_p$	CuO/ethylene glycol CuO/oil	0-2%
Xue[53]	2005	$\frac{K_{eff}}{K_f} = \frac{1 - \emptyset + 2\emptyset \frac{k_s}{k_s - k_f} \ln \frac{k_s + k_f}{2k_f}}{1 - \emptyset + 2\emptyset \frac{k_f}{k_s - k_f} \ln \frac{k_s + k_f}{2k_f}}$	Nano-spherical with interfacial shell	0-6%
Li & Peterson[54]	2006	$\frac{K_{eff-K_f}}{K_f} = 0.764\emptyset + 0.0187(T - 273.15) - 0.462$	Al_2O_3-water	0-4%
Buongiorno[55]	2006	$\frac{K_{eff}}{K_f} = 1 + 2.92\emptyset - 11.99\emptyset$	TiO2-water	0-10%
Timofeeva[56]	2007	$\frac{K_{eff}}{K_f} = (1 + 3\emptyset)$	Al_2O_3-water	0-5%
Avsec & Oblack[57]	2007	$\frac{K_{eff}}{K_f} = \left[\frac{k_s + (n-1)k_f + (n-1)(1+\beta)^3}{k_s + (n-1)k_f - (1-\beta)^3\emptyset(k$	$n = (3/\varphi)$	0-4%

Chandrsekar[58]	2009	$\frac{K_{eff}}{K_f} = \left[\frac{k_s + (n-1)k_f + (n-1)(1+\beta)^3}{k_s + (n-1)k_f - (1-\beta)^3\emptyset(}\right.$ $+ \frac{C\emptyset(T - T_O)}{\mu k a^4}$	Al_2O_3-water Al_2O_3-ethylene glycol	0-8%
Vajjha[59]	2010	$\frac{K_{eff}}{K_f} = \frac{k_s + 2k_f + 2\emptyset(k_s - k_f)}{k_s + 2k_f - \emptyset(k_s - k_f)} + 5$ $\times 10^4 \beta \rho_s C_{ps} \sqrt{\frac{k_s T}{\rho_s D}} f(T, \emptyset)$	Al_2O_3-(60:40) EG-water	0-6%
Godson[60]	2010	$\frac{K_{eff}}{K_f} = 0.9692\emptyset + 0.9508$	Ag-water	0-3%
Corcione[61]	2011	$\frac{K_{eff}}{K_f} = 1$ $+ 4.4Re^{0.4}Pr^{0.66}\left(\frac{T}{T_{fr}}\right)^{10}\left(\frac{k_s}{k_f}\right)^{0.03}\emptyset^{0.}$	Al_2O_3-water	0-5%

2.3.2 Nanofluid viscosity

2.3.2.1 Introduction

Viscosity is a key property of fluids. It directly affects pumping power, pressure drops in laminar flows, and convective heat transfer. An understanding of viscosity analysis is therefore needed in order to ascertain the thermal heat transfer performance of fluids. In order to evaluate the applicability of nanofluids to a range of industrial applications, any increase in the viscosity of nanofluids as compared to the pure fluids should be comprehensively explored. A more efficient nanofluid should not only retain higher thermal conductivity but should also offer lower viscosity. Unlike the question of effective

thermal conductivity, research on viscosity is rather limited; more work on this subject is needed in the field.

2.3.2.2 Theoretical models

The pioneering work on viscosity was done by Einstein[62]. He derived a theoretical model to predict the viscosity of a suspension; this linear model was a function of the base fluid and the volume fraction, and it was valid for concentrations up of to 2%. Various models were later developed to extend Einstein's model. Taylor [63] proposed a mathematical model that assumed the drops are spherical and liquid. His model is therefore an approximation and only valid under these assumptions.

Brinkman [64] extended this model by introducing an equation for solutions and suspension viscosity. This theoretical model has been found to apply up to 4% volume fraction.

In 1948 Vand [65] presented a formula for viscosity for rigid spherical particles. He assumed, for simplicity, that particles are homogeneously distributed throughout the liquid and that most of them are therefore far from the walls. Another assumption is that there is no interaction between solid particles. These rigid and somewhat unrealistic assumptions make the applicability of this model is very limited.

Roscoe [66] presented a formula for relative viscosity that enables the modeller to ignore the effect of non-similarity of particle shape; however, the overall formula is still based on spherical particles and high concentration. Another modified Einstein's viscosity equation presented by Batchelor [67] to incorporate the effect of Brownian motion. He considered the isotropic suspension of spherical and rigid nanoparticles in his model, and the model is still widely used, though it is only valid at low volume fractions. Lundgren [68] developed a model based on statistical formulation that extends Einstein's equation by using Taylors' series. The model considers a very slow flow in a porous medium comprised of rigidly suspended solid particles.

Graham [69] developed a generalised form model by taking into consideration the radius of the particles and the inter-particle spacing; this model is equivalent to Einstein's formula for low volume fractions. Frankel and Acrivos [70] derived a dependence model of effective viscosity based on the volume fraction of solid particles, assuming uniform suspension. They theoretically developed the model assuming a cubic order of uniform

solid particles; however, it can be used for curve fitting of other highly concentrated suspensions.

Bicerano et al [71] developed a mathematical model for the viscosity of suspensions. Their model is based on the theories of universality and scaling, and its implementation relies on a combination of mathematical arguments. Cheng et al [72] derived an exponential formula for effective viscosity. The theoretical assumptions restrict it to the dilute condition, and it ignores the effects of dynamic particle interactions and fluid motion. Their investigation showed a power series expression to be a function of particle volume fraction.

Avsec and Oblak [73] also introduced a mathematical model for viscosity based on Einstein's model. They performed a statistical analysis in order to calculate the interactions between solid particles in a single system.

2.3.2.3 Experimental work

In order to analyse and validate the theoretical models proposed by many researchers, experimental studies are required. These experimental observations of the effects of nanofluids' viscosity help to develop an understanding of the rheological behaviour that has equal significance in experimental work and practical heat transfer applications. Several experimental investigations exploring various parameters such as temperature, volume concentration, nanoparticle size and shape, surfactants, and pH indicate that these factors have direct influences on nanofluid viscosity.

Nguyen et al. [74] investigated the effect of nanoparticle diameter on the viscosity of Al_2O_3–water nanofluids. They observed in their experiments that at 4% particle volume concentration, 47 nm and 36 nm diameter alumina/water nanofluids displayed the same viscosity. As the volume concentration increased, fluids with larger nanoparticle diameters exhibited higher viscosity than those with smaller diameter nanoparticles. In other experimental work by the same authors, they cited previous findings for higher particle volume fraction of 7 and 9 % [75].

Yang et al. [76] experimentally studied the effects of temperature on viscosity for a range of temperatures (35^o, 43^o, 50^o, and 70^o C) for various nanofluid suspensions where the nanoparticles were made from graphite. They observed that viscosity decreased with an

increase in temperature for all samples tested. This highlighted the need for a new heat transfer correlation for nanoparticle dispersions with non-spherical shapes.

Anoop et al [77] measured the viscosity of CuO–ethylene glycol, Al_2O_3–water and Al_2O_3–ethylene glycol for a temperature range of 20^o to 50^o C, with a range of volume fractions from 0.5% to 6% vol. They observed a reduction in viscosity with an increase in temperature. They also highlighted the significance of the electroviscous effect on viscosity increase.

An exponential decrease in the viscosity when temperature was increased was observed by Namburu et al.[78] for a range of temperature of 35^o C to 50^o C. They reported that, at low temperatures, nanofluids containing SiO2 nanoparticles with two different base fluids exhibited non-Newtonian behaviour, whereas, at high temperature, they exhibited the properties of Newtonian fluids. In a different study, the same authors observed Newtonian behaviour for CuO nanoparticles in ethylene glycol and water with a wide range of temperatures (-35^o to 50^o C) using a volume concentrations from 0 to 6.12%. [79] they observed a Newtonian behaviour for CuO nanoparticles in ethylene glycol and water with the range of temperature (-35^o to 50^o C) study with a volume concentration from 0–6.12%.

In a similar manner, Kulkarni et al. [80] observed an exponential decrease in viscosity as temperature increased. With an increase in the volume fraction, the nanofluid viscosity also increases. From their measurements, a CuO nanofluid showed the highest viscosity, followed by the Al_2O_3-mixture. The SiO2 nanofluid showed the lowest viscosity.

Chevalier et al. [81] measured the viscosity of SiO_2 -ethanol for three different sizes of nanoparticle diameter, 35, 94, and 190 nm, for volume fractions between 1.4 and 7%. They found that viscosity values for these were in agreement with classical models, contradicting many other experimental studies.

Pastoriza-Gallego et al.[82] conducted an experimental study to measure the viscosity of CuO-water nanofluids for various nanoparticle diameters and volume fractions. Two different samples of CuO of 23–37 nm were tested at various volume fractions (0 to 10%) for a temperature range of 10 to 50^{o}C. The researchers observed that the viscosity increases as particle diameter decrease. The increase of relative viscosity with the volume fraction does not obey the classical dependency on volume fraction rules, however.

Chen et al [83] measured the viscosity of nanofluids containing carbon nanotubes. For lower volume concentrations (less than 0.4%), nanofluids showed lower viscosity than

their base fluids. The researchers attributed this to the lubricative effect of nanoparticles. With the increases in the volume fraction (higher than 0.4 %), viscosity increases.

Turgut et al [84] measured the viscosity of TiO2-water nanofluids for temperature ranges of between 13 to 55^{o}C and volume fractions between 0.2 and 3%. They highlighted that the increase in viscosity observed with the increase of particle volume concentration was much higher than that calculated using the Einsteinian model.

Naik et al [85] measured the viscosity of CuO nanofluids with different volume concentrations (0.025, 0.1, 0.4, 0.8 and 1.2%). Their results revealed that temperature and volume fraction affected the viscosity of nanofluids significantly. Zhu et al [86] presented experimental work that measured the viscosity of CaCO3-water nanofluids at room temperature. They reported observing a linear relationship which showed Newtonian behaviour in the tested samples for volume concentrations of 0.12% to 4.11%. Their findings highlighted the fact that as the volume concentration increases, the relative viscosity of the nanofluids increases nonlinearly, with rapid increases at high volume fractions.

Yang et al [87] reported viscosity measurements for copper nanofluids. Cu nanofluids showed non-Newtonian behaviour, and the viscosity increased with increases in the volume fraction and decreases in the temperature. In a recent study, Toghraie et al [88] conducted an experimental determination of the effective viscosity of Fe3O4-water nanofluids. The viscosity was measured within a temperature range of 20 to 55°C for various samples with solid volume concentrations of 0.1 to 3%. They observed that the viscosity substantially decreased with an increase in temperature. Furthermore, the viscosity was enhanced as the volume concentration increased. Observation also revealed that at higher volume concentration (2% and 3%), the viscosity ratio is higher than at lower volume fractions (0.1 to 1%). The predicted viscosity ratios showed that the highest viscosity enhancement was 129.7%. This was observed at a volume fraction of 3.0% and temperature of 55°C.

The effect of temperature and volume fraction on the viscosity was also investigated experimentally by Esfe et al [89]. They measured the effective viscosity of Al_2O_3-engine oil nanofluids at temperature ranges from 5 to 65°C for various samples with volume concentrations from 0.25% to 2%. All samples tested in this way behaved as Newtonian fluids. Measurement also showed that nanofluid viscosity increases along with volume

concentration. Additionally, the researchers reported that the viscosity of nanofluids decreases as temperature increase, particularly at the lower temperatures. Their results were not in agreement with the theoretical models, as these models fail to predict the correct values of the nanofluids' effective viscosities at all volume concentrations. They also reported that the maximum viscosity enhancement of nanofluid was 132% over that of its base fluid.

Abdolbaqi et al[90] prepared a nanofluid with TiO2 nanoparticles to measure its viscosity. The experiment was conducted in a temperature range between 30° and 80 ° C and for volume fractions between 0.5 and 2.0%. The results revealed that the viscosity of the nanofluid increases as the volume concentrations increase, but decreases with an increase in temperature. Among all the nanofluids, the highest viscosity enhancement was observed for nanofluids at a volume fraction of 2.0% at a temperature of 70 °C, with a 1.53 times improvement. The main finding of these results is that the classical models and semi-empirical equations fail to predict the viscosity of nanofluids once the effects of volume concentration and temperatures are added. A similar finding was also reported by Abdobaqi et al [91] when they experimentally investigated the viscosity of SiO2 nanofluids. They measured the effective viscosity in a temperature range between 30°C and 80°C and for volume fractions between 0.5 and 2.0%. The results showed that the viscosity increased as the volume concentrations increased, but decreased with an increase in temperature. The maximum enhancement in effective viscosity observed was 1.38 times; this occurred at a volume concentration of 2.0% at a temperature of 70°C. The classical models and semi-empirical correlations failed to predict the effective viscosity of nanofluids in these conditions.

Soltani and Akbari [92] examined temperature effects and particle fraction influences on the effective viscosity of MgO-ethylene glycol. The samples tested were in the volume concentration range of 0 to 1.0% under temperatures ranging from 30 to 60°C. The results showed that the hybrid nanofluid exhibited Newtonian behaviour for all volume concentrations and temperatures measured. They highlighted that that the effective viscosity increases when the volume concentration increases and decreases when the temperature increases. The relative viscosity was enhanced significantly when the solid volume concentration increases from 0.1 to 1%, and the effective viscosity increased by up to 168%.

Ilhan et al [93] conducted an experimental investigation to measure the effective viscosity for a Hexagonal boron nitride (hBN) nanofluid with various base fluids containing nanoparticles of diameter 70 nm with particle volume fractions in the range 0.03 to 3%. Their results revealed that the increase in viscosity was up to 22% for water nanofluids, while the viscosity of EG and EG/water based nanofluids increased by 33% and 62%, respectively. The researchers reported that the viscosity of the base fluids had an important effect on the resulting nanofluids' viscosity, but no explanation was given for such an increase.

Zyla and Fal [94] presented an experimental investigation on the viscosity of alumina nitride nanoparticles in an ethylene glycol base fluid. The effective viscosity was measured at a constant temperature of 298.15 K for a range of volume fractions of 0.05 to 0.079%. All samples tested showed non-Newtonian behaviour.

Aladag et al. [95] explored the experimental effects of temperature and shearing time on the effective viscosity of Al_2O_3-water nanofluids at low volume fractions and low temperatures. They observed that the nanofluid mixture exhibited either Newtonian or non-Newtonian behaviour depending on the shear rate. They investigated Al_2O_3-water based nanofluids which showed non-Newtonian properties within the range of low temperatures. They also studied a carbon nano-tube/water based nanofluid that behaved as a Newtonian fluid when the shear rate increased.

Sundar et al. [96] initiated viscosity experiments with nanofluids comprised of Al_2O_3 in various base fluids in the temperature range 0 to 60°C for volume fractions between 0.3 and 1.5%. The viscosity enhancements for fractions of 1.5% were between 1.37 to 2.58 times those of the base fluid at a temperature of 0°C. Nanofluids dispersed in higher viscosity base fluids showed further enhancement compared to those dispersed in low viscosity base fluids. The classical models failed to predict the nanofluids' effective viscosity under the influence of varying temperatures. John and Krishnakumar [97] investigated the variation within nanofluid effective viscosity by looking at ethylene glycol copper oxide and alumina nanofluids, taking into account particle volume concentration and temperature. The effective viscosity of nanofluids was observed to be higher than the values predicted by theoretical models. However, the researchers did not mention the dependency on temperature of the relative effective viscosity of the nanofluids.

Jarahnejad et al.[98] explored the effects of temperature, volume concentration, and size of nanoparticles on nanofluid effective viscosity in Al_2O_3-water solutions. They measured viscosity in the temperature range 20^o to 50°C with volume fractions of 3 to 14.3%. The results revealed that the viscosity decreased along with an increase in the temperature. These results were not in agreement with the classical models, particularly for volume fractions higher than 1.5%.

Nikkam et al.[99] conducted an experiment to investigate the viscosity of nanofluids consisting of copper nanoparticles in diethylene glycol The samples tested utilised volume fractions between 0.4 and1.6% in the temperature range 20^o to 50°C. The viscosity results were compared to classical models, and the maximum enhancement in viscosity was 5.2% at volume fraction 1.6%.

2.3.2.4 Empirical works

Graf [100] recommended that the results obtained from experiments should be expressed in the form of Taylor series in order to compare them with the classical models. He further noted that intrinsic viscosity should be determined experimentally. Rashin and Hemalatha [101] proposed an empirical correlation for the effective viscosity of CuO-coconut oil nanofluids for a range of volume fractions (0 to 2.5%) and temperatures (308 to 328^{o}K).

Abaresh et al [102] presented an empirical model for the effective viscosity of α-Fe2O3-glycol, and this model was expressed in exponential form. However, their work was based on a very limited range of volume fractions (0.2 to 0.8%).

Kole and Dey [103] suggested a formula to calculate the viscosity of CuO-gear oil nanofluids based on experimental work. This formula also followed the exponential form. Chen et al [104] introduced a new formula based on regression analysis to predict the effective viscosity of TiO2-ethylene glycol nanofluids in the range of volume concentrations 0 to 1.75%. Tseng and Chen [105], meanwhile, proposed an empirical correlation to predict the effective viscosity for nanofluids with nickel nanoparticles. The model was based on experimental work where the volume fractions ranged between 2 and 10%. However, the model has been criticised for over-prediction of the viscosity values; furthermore, no temperature change effect was investigated. The same authors in a different study [106] modified the empirical viscosity model for TiO2-water in the volume

fraction range 4 to 12%. Again, the influence of temperature on viscosity was not tested in this work.

Horri et al [107] presented an empirical model to predict the ceramic suspension viscosity. The model was based on experimental work with a volume fraction range of 0 to 0.4%. However all measurements were taken at a constant temperature, so no temperature effects were observed or modelled.

Sahoo et al [108] suggested a new correlation for predicting the effective viscosity of Al_2O_3-water nanofluids. The volume fraction range tested in the experiment was 1 to 10%. Deviation in the results between the experimental data and the proposed model was up to 10%, however, calling the accuracy of the model into question. Battez et al [109] introduced two empirical viscosity models for ZnO and ZrO2 in polyalphaolefin nanofluids in the temperature range 40 to 100C^o for a volume fraction range of 0.5 to2%. The maximum error between the models and the measured data was 2.28%, a relatively low deviation.

Another model was proposed by Nezhaad and Dorany [110] for walled carbon nanotube and lube oil nanofluids in the volume fraction range 0.01 to 0.2 % and the temperature range 25 to 100C^o, while Suganthi and Rajan [111] introduced an empirical correlation based on their numerical work for ZnO-water in the range 35 to 55 C^o for a volume fraction range of 0.25 to 2%. They reported that this model was independent of temperature.

Suganthi et al [112] presented a correlation for predicting the viscosity of ZnO-propylene glycol at a wide range of temperatures; however, the volume fraction range tested in this work was limited (0 to 2%). Timofeeva et al [113] suggested an equation for predicting the effective viscosity for Al_2O_3-ethylene glycol nanofluids in a volume fraction range of 0 to 7% in the temperature range 15 to 85C^o. The deviation between the measured data and the proposed model was not reported, however, which is a major oversight. Zyla and Cholewa [114] proposed a viscosity correlation for Y2O3-diethylene glycol nanofluids in the volume fraction range 0.5 to 2.5 %. The error between the results produced by the proposed model and the experimental data was up to 20%, however, which implies that this model is less than reliable.

Table 2-2 Effective viscosity models summary

Reference	Year	Model	Notes	Range of volume fraction
Einstein	1906	$\frac{\mu_{eff}}{\mu_f} = 1 + 2.5\emptyset$	Infinitely suspension	<2%
Saito	1950	$\frac{\mu_{eff}}{\mu_f} = 1 + \frac{2.5\emptyset}{(1-\emptyset)}$	Spherical rigid particles	<2%
Brinkman	1952	$\frac{\mu_{eff}}{\mu_f} = \frac{1}{(1-\emptyset)^{2.5}}$	Very small particles	<2%
Lundgren	1972	$\frac{\mu_{eff}}{\mu_f} = \frac{1}{(1-2.5\emptyset)}$	Dilute concentration	0-3%
Batchelor	1977	$\frac{\mu_{eff}}{\mu_f} = 1 + 2.5\emptyset + 6.2\emptyset^2$	Brownian motion	0-2%
Drew and Passman	1999	$\frac{\mu_{eff}}{\mu_f} = 1 + 2.5\emptyset$	$\emptyset < 5\%$	<5%
Wang	1999	$\frac{\mu_{eff}}{\mu_f} = 1 + 7.3\emptyset + 123\emptyset^2$	Cu-water Al_2O_3-water	<10%
Tseng	2003	$\frac{\mu_{eff}}{\mu_f} = 13.47\exp(35.98\emptyset)$	TiO2-water	0-10%
Maiga	2005	$\frac{\mu_{eff}}{\mu_f} = 1 - 0.19\emptyset + 306\emptyset^2$	Al_2O_3-EG	0-8%
Song	2005	$\frac{\mu_{eff}}{\mu_f} = (1 + 56.5\emptyset)$	SiO2-water	
Buongiorno	2006	$\frac{\mu_{eff}}{\mu_f} = 1 + 5.45\emptyset + 108.2\emptyset^2$	TiO2-water	1-3%
Chen	2007	$\frac{\mu_{eff}}{\mu_f} = 1 + 10.6\emptyset + 112.36\emptyset^2$	TiO2-EG	0-8%
Nguyen	2007	$\frac{\mu_{eff}}{\mu_f} = 1 + 0.025\emptyset + 0.015\emptyset^2$	Al_2O_3-water d=36 nm	0-14%
Namburu	2007	$\log(\mu_{eff}) = Ae^{-BT}$	CuO-(60:40)	0-4%

		$A = 1.8375\emptyset^2 - 29.643\emptyset + 165.56$ $B = 4 \times 10^{-6}\emptyset^2 - 0.001\emptyset + 0.0186$		
Grag	2008	$\frac{\mu_{eff}}{\mu_f} = 1 + 11\emptyset$	Cu-EG	0-10%
Chandrasekar	2010	$\frac{\mu_{eff}}{\mu_f} = 1 + b\left(\frac{\emptyset}{1-\emptyset)}\right)^n$	Al_2O_3-water B=1631 n=2.8	0-8%
Vajjha	2010	$\frac{\mu_{eff}}{\mu_f} = Ae^{C\emptyset}$ A=0.9197, C=22.8539	CuO-(60:40)	0-5%
Corcione	2011	$\frac{\mu_{eff}}{\mu_f} = \frac{1}{\left(1 - 34.87\left(\frac{d_s}{d_f}\right)^{-0.3}\emptyset^{-1.03}\right)}$ $d_f = 0.1 + \left(\frac{6M}{N\pi\rho_{fo}}\right)^{1/3}$	SiO2/ethanol EG-water	<6%

2.3.3 Density of Nanofluid

Thermal conductivity and the viscosity of nanofluids have attracted the attention of many researchers, and, nevertheless, further investigation into these subjects is still needed due to the wide range of possible nanofluid combinations and states. The effects of the density of nanofluids have also been investigated by several researchers, and a unified expression for nanofluid density has been devised that is generally applicable for most volume fractions and for most nanoparticles, even those with different sizes of the particle.

The density correlation reported by Pak and Cho [16] is widely used by many researchers. However, they did not give sufficient density results for all additional investigations, so the formula has been expanded upon in many cases.

Vajjha et al [115] presented a comprehensive study of density measurements for different nanofluids. They measured the density of nanofluids over a temperature range of 0^o to 50^o C for a variety of volume fractions. Their results were compared with the widely used theoretical equation, and good agreement between the theoretical equation and their measurements was achieved for Al_2O_3 and Sb2O5 and SnO2 nanofluids.

Vajjha and Das [116] measured the density of Al_2O_3 nanofluids for a range of temperatures and volume fractions (0-10%). They presented their results in the temperature range 273 to 323 K. These experimental results were found to be in excellent agreement with Pak and Cho's correlation for all temperatures and volume fractions.

Satti et al [117] performed an experimental investigation to measure the density of several nanofluids containing particles of Al_2O_3, ZnO, CuO, TiO2, and SiO2. The samples were tested in the temperature range of 0 to 90°C for volume fractions ranging from 0 to 6% and with nanoparticle diameters from 10 to 76 nm. The experimental results showed very good agreement with the theoretical equation proposed by Park and Cho. Said et al [118] conducted an experimental study to measure density for various nanofluids, and their results were also consistent with the commonly used formula overall. However, at low-temperature range and low concentrations (less than 1%), some deviation was observed.

Kumar et al [119] presented experimental measurements for nanofluid density using the standard volumetric flask method at room temperature (30 to 32°C). Two standard volumetric flasks of 25 ml and 50 ml were used to determine the density of the fluids. The experimenters observed that nanofluid density increased in proportion to the concentration of the nanoparticles within the base fluid. Their data were in good agreement with the formula created by Cho and Pak at lower volume fractions.

2.3.4 Heat Capacity of Nanofluid

One of the key thermal properties in energy systems is specific heat, and this is directly linked with heat storage and transfer. Recently, researchers have shown that the specific heat of fluids can be improved by the addition of nanoparticles. Although the addition of nanoparticles to a base fluid enhances thermal conductivity, it sometimes decreases the overall heat capacity of the nanofluid. The fundamental governing mechanisms for these changes have not yet been agreed upon.

Vajjha et al [120] presented measurements for the specific heat of various nanofluids containing Al_2O_3, ZnO, and SiO2 nanoparticles dispersed in ethylene glycol and water. The experiments were conducted for a temperature range of 315 to 363 K. The volume fractions investigated ranged up to 10%. The model results for these factors were not in agreement with the experimental data. The researchers proposed a correlation for specific heat as a function of volumetric particle concentration, temperature, and specific heat.

Shin et al. [121] reported an experimental investigation to measure the specific heat of silica nanofluids. They observed that the specific heat of the nanofluids was enhanced 19-24% compared to the base fluid. Their data was not in agreement with other results reported in the literature.

Sommers and Yerkes [122] measured the specific heat of aluminium oxide nanofluids with size 10 nm particles over a volume fraction range of 0.5 to 3%. Their results for specific heat were found to be higher than modelled, but more consistent with available experimental data. Zhou [123] presented an experimental study to measure the specific heat of Al_2O_3-water nanofluids. The results revealed that the specific heat of the nanofluids decreases gradually with an increase in the nanoparticle volume fraction up to 21.7%. The results showed good agreement with the available correlation models of specific heat.

Barbes et al [124] presented specific heat capacity measurements of Al_2O_3-water and EG nanofluids as a function of particle volume concentration at a temperature range of 298 to 338 K. Their data were in agreement with the Cho and Pak formula when volume fraction effects were taken into account.

Satti [125] performed an experimental investigation to measure the specific heat of five different nanofluids in the temperature range 243 to363 K for volumetric fractions 0.5 to 6% and particle sizes 15 to 76 nm. They highlighted that particle size has no significant influence on the nanofluids' specific heat. Their results showed specific heat decreased as concentration increased and an increase in specific heat as temperature increased, in agreement with previously published data. However, the specific heat correlations were not identical with the measured values. An additional correlation was derived from a large quantity of recorded data with a deviation of −0.094%.

The specific heat capacity measurements of water were analysed by O'Hanley et al [126]. The nanofluids contained silica, alumina, and copper oxide in volume fractions ranging from 5 to 50%. The specific heat was found to decrease with an increase in volume

fraction. These test results were found to be in excellent agreement with the correlation proposed by Buongiorno [55], although there were some discrepancies with figures generated using Cho and Pak's formula. Sonawane et al [127] evaluated specific heat for Al_2O_3-water nanofluids. The volume fraction range varied between 0 and 1%. The measured specific heats of the nanofluids did not exhibit considerable variation within the range of volume fractions investigated. However, these investigators did not check their results with either of the available formulas for predicting specific heat.

Shin et al [128] reported an enhancement in the specific heat capacity of a suspension containing alumina in salt water with a nanoparticle diameter of 10 nm. The specific heat capacity was enhanced by up to 32% over that of the base fluid. Cabaleiro et al [129] tested the specific heat capacities for MgO, ZnO, and ZrO2 nanoparticles with various base fluids. MgO nanoparticles showed values up to twice those of ZnO or ZrO2 nanoparticles. Overall, specific heat capacity decreased as nanoparticle concentration increased; this contradicts the finding that the calculated specific heat capacity using the conventional formula and the experimental density data remained constant or even increased with an increase in nanoparticle concentration.

2.4 Syntheses of Nanofluids

There are numerous techniques used to form nanofluids. These methods include the single step method, the two-step process, and the direct mixing method. This section will focus on the first two methods, which are the most common approaches for nanofluid preparation.

2.4.1 Single Step Method

The one-step process involves making and dissolving the nanoparticles directly in the base fluid. The advantage of this method is that the processes of drying, storing, transporting, and dispersing the nanoparticles can be avoided, which helps to reduce the agglomeration of the nanoparticles and increase the stability of the resultant fluids [130]. The one-step method is preferred where uniformity in the nanoparticles dispersed in the mixture is required. Moreover, particles produced this way are more likely to be stable when suspended in the base fluid.

The single-step method was first introduced by Akoh et al [131], They prepared Fe, Co and Ni in the oil based fluid by vacuum who prepared Fe, Co, and Ni in oil-based fluids by means of vacuum evaporation. However, these researchers did not detail the stability of their new mixtures.

Eastman et al. [132] employed the single-step method to prepare nanofluids in their experiments with Cu-ethylene glycol, which was directly condensed into nanoparticles. They observed a small amount of agglomeration. Choi et al. [133] used the Direct Evaporation Condensation approach, which delivered excellent control of the nanoparticle diameter and formed a stable nanofluid with no additive required.

Munkhbayar et al. [134] used the same method to prepare Ag/MWCNT nanofluids. For their work, they purified the MWCNT by means of chemical processing: the exterior activity of the MWCNT was improved by using Nitric acid and sulphuric acid. Zhu et al [135] utilised the single step method to prepare a copper-ethylene glycol nanofluid using the chemical method. They reported no agglomeration in the resultant stable mixture, but the technique used in their work is expensive to reproduce. Tran Xp et al [136] prepared alumina nanofluids using laser ablation. This method produced a stable suspension containing homogeneously dispersed nanoparticles. However, the researchers did notice that the shape of the solid particles changed over time. Lee at [137] conducted an experiment to produce nickel ferrite powder by using pulsed wire discharge. The resultant powder was pure, but the method still has some drawbacks, namely that the use of low vapour pressure fluids are necessary and only small amounts of powder can be manufactured. The cost of such manufacture is also still quite high.

2.4.2 Two Step Method

This method is the most widely used method for synthesising nanofluids. The nanoparticles used in this method are first formed as dry powders using chemical or physical methods. Then, the powder, with its nano-sized particles, is dispersed into a base fluid in the second stage using measures such as concentrated magnetic force and ultrasonic or high-shear mixing. The two-step method is cheap compared to the single-step method, making it more suitable for preparing nanofluids in large quantities. The reason for this is that the nanoparticle powders are extremely high quality as they are prepared by industry manufacturers.

Nanoparticles added to fluids have a tendency to agglomerate as a result of their large surface area and high levels of surface activity. Using surfactants is a useful way to promote nanoparticle stability in fluids, but the applicability of particular surfactants is a big challenge, particularly in applications at high temperatures.

The two-step method has been used by many researchers, including Jena et al [138] who prepared copper/alumina-water nanofluids using surfactants. The alumina was found to be more stable than the copper under similar conditions.

Beck et al [139] composed Al_2O_3-ethylene glycol nanofluids using ultrasonic mixing for several minutes to obtain a homogeneous dispersion. They reported that the dispersed mixture stayed uniform over the duration of their experiments. Suresh et al [140] prepared Al_2O_3-Cu water nanofluids using ultrasonic mixing for six hours to achieve a stable suspension. They used pH measurements to ensure that the suspension was stable throughout testing.

Paul et al [141] synthesised Al95Zn05-ethylene glycol using a two-step method. They used ultrasound mixing followed by a magnetic stirrer in order to obtain a stable suspension. However, these researchers did not give any detail in their work about the time required for the ultrasound and the magnetic stirrer to achieve this result.

Another technique based on the two-step method was developed by Yu et al [142]. They prepared graphene-ethylene glycol by means of chemicals and electrically insulated the graphene. The mixture was then mixed by a magnetic stirrer and vibrated using ultrasound.

Baby and Ramaprabhu [143] prepared a silver graphene nanofluid without using any surfactants, and they reported an enhancement in thermal conductivity. However, they did not give an explanation of the mechanism for this enhancement. Xuan and [144] prepared several samples of nanofluids by directly mixing the nanoparticles and the base fluids. They observed that Cu-oil demonstrated better performance than Cu-water.

Patel et al [145] synthesised several kinds of solid particle-water nanofluids. They observed that the samples were stable for several months; furthermore, they did not observe any degradation during storage or in the course of the experiments. Hu et al [146] formed ethanol ethylene glycol nanofluid using a two-step approach. The mixture was stirred by means of magnetic resonance and then vibrated using ultrasound. The researchers also added castor oil to improve the stability of the mixture.

2.5 Experimental works on heat transfer characteristics of Nanofluids

Since Choi first developed nanofluids, a huge amount of effort has been invested into investigating heat transfer performance using nanofluids for a large number of different configurations of nanoparticle types and applications.

2.5.1 Laminar flow in a tube

Rea et al [147] investigated the convective heat transfer performance and pressure drop for alumina and zirconia-water nanofluids in laminar flow in a vertical tube. In their experiments, they measured the heat transfer coefficient and the pressure drop for volume fractions up to 6%. They reported an enhancement in the heat transfer coefficient of up to 27% compared to water; however, this was accompanied by a higher pressure loss than that seen with just water.

The pressure loss and the thermal characteristics of copper oil nanofluid in laminar flow in flattened tube were investigated experimentally by Razi et al [148]. They observed an enhancement in the heat transfers up to 26.4%. The researchers also developed a formula to predict the heat transfer coefficient in the tube. Kim et al [149] studied the effects of thermal conductivity due to the presence of nanoparticles on the heat transfer characteristics of fluids in a horizontal pipe in laminar flow. They reported an enhancement of only 15% in terms of the heat transfer coefficient for alumina nanoparticles, and amorphous carbonic nanofluids saw an enhancement of only 8%.

Meyhat et al [150] reported experimental observations of laminar pressure drop and convective heat transfer of Al_2O_3 nanofluids in a horizontal tube. Their results revealed that the nanofluid heat transfer coefficient was higher than that of water; it also increased as the Reynolds number and volume fractions increased. The increase in the heat transfer coefficient was found to be up to 32%. The pressure loss measurements for the nanofluids were, however, much higher than for conventional water-based fluids. The results did highlight that the nanofluids' properties in single-phase correlation meant that the researchers could not predict the heat transfer coefficient of nanofluids correctly.

The friction factor and heat transfer enhancement were investigated by Chandrasekar et al [151] in circular pipes in a laminar flow. The enhancement in the Nu number was found to

be 12.24%, 21.53% when using a wire coil insert. The pressure loss was also studied, and a pressure drop penalty was found compared to water. An empirical correlation was developed based on these results to predict the friction factor and Nu number. Suresh et al [152] conducted an experiment to study the friction factor, and the heat transfer performance for Al_2O_3-water nanofluids with spiral rod inserts in laminar flow. The results of testing the Nusselt number for a 0.5% volume fraction with spiralled rod inserts showed an enhancement of 24% over results obtained from a plain tube. Gherasim et al [153] studied the heat transfer enhancement of Al_2O_3-water nanofluids in confined radial flow in a range of Re numbers from 300 to 900. Their results revealed that heat transfer was enhanced in radial flow cooling systems by employing nanofluids. They reported that the Nusselt number rises alongside the Reynolds number and volume concentration.

Chen et al [154] tested the heat transfer coefficient for titanate nanotube-water nanofluids in laminar flow. The enhancement of heat transfer was found to be much higher than the enhancement of thermal conductivity. The researchers also suggested further experimental investigations to analyse possible mechanisms behind this heat transfer coefficient.

Suresh et al [155] studied the effect of Al_2O_3-Cu water nanofluids on heat transfer in a circular tube. Their results showed that convective heat transfer showed a maximum enhancement of up to 13.56% in terms of its Nusselt number as compared to water. Furthermore, the results revealed that 0.1% Al_2O_3-Cu-water nanofluids have a considerably higher friction factor than 0.1% Al_2O_3-water nanofluids. The researchers also proposed correlations for calculating Nusselt numbers and friction factors which differed from previous proposed correlations.

2.5.2 Turbulent flow in a tube

Many experimental investigations have been undertaken to study turbulent flows in pipes using nanofluids. Xuan and Li [156] reported experimental investigations into convective heat transfer and flow features of nanofluids in a tube. They measured both the friction factor and convective heat transfer coefficient of the nanofluid in the turbulent flow, and examined and discussed the effects of the volume fraction of the nanoparticles and the Reynolds number on the heat transfer and flow characteristics. They then proposed a correlation for the Nu number to predict convective heat transfer in nanofluids. The same authors [157] conducted an experiment to measure the heat transfer performance of

copper-water nanofluids in laminar and turbulent regions in a pipe. They highlighted that the heat transfer rate was enhanced when the volume concentration increased. Furthermore, they proposed a new correlation for calculating Nu number which differed from their previous work.

Duangthongsuk and Wongwises [158] studied the enhancement of heat transfer and pressure loss in TiO2-water nanofluids in turbulent flow. They observed that the heat transfer coefficient was higher than that of water and increased as the Reynolds number and volume fraction increased. The heat transfer coefficient of the nanofluids was 26% greater than that of pure water, and the results also revealed that the heat transfer coefficient of the nanofluids was approximately 14% lower than that of base fluids for given conditions. The results showed that the pressure loss of nanofluids was slightly higher than that of the base fluid, and that this increased with increases in the volume fraction. Furthermore, the researchers proposed correlations for predicting the Nusselt number and friction factor of the nanofluids.

Fotukian and Esfahany [159] examined the convective heat transfer performance of γ-Al_2O_3-water nanofluids under turbulent flow in a circular tube. Their results revealed that an increase in the volume fraction promoted heat transfer in this nanofluid as compared to water. However, they also observed a penalty in terms of pressure drop in comparison to water when using the nanofluid. Sundar et al [160] performed an experimental investigation to study the turbulent heat transfer characteristics, and friction factor for alumina oxide-water nanofluids in a pipe with a twisted tape insert. Their results showed that the heat transfer coefficient and friction factor increased by up to 33.5% and 1.096, respectively, compared to water. They developed correlations for the friction factor and Nusselt number for Al_2O_3-water nanofluids in a pipe with inserts.

Zamamian et al [161] investigated the forced convection heat transfer enhancement of Al_2O_3 and Cu in ethylene glycol nanofluids under turbulent flow in a double pipe heat exchanger. They highlighted that the heat transfer of the nanofluids was enhanced considerably compared to the water in most cases; this enhancement varied from 2% to 50%. Furthermore, the results revealed that as the volume fraction and nanofluid temperature increased, the heat transfer coefficient also increased. However, when

temperatures went higher with increased volume fractions, the results became contradictory.

Suresh et al [162] studied the friction factor and heat transfer enhancement of CuO-water in a helical tube under turbulent flow. They observed that heat transfer performance in the pipe was improved compared to that of water by adding the nanoparticles. The increase in the volume fraction and Reynolds number led to an increase in the heat transfer coefficient. The researchers observed an insignificant rise in the pressure drop of the nanofluids in comparison with that of water, which contradicts many other findings from the literature.

Heat transfer characteristics in the double pipe with twisted tape using Al_2O_3-water nanofluid under turbulent flow were investigated by Maddah et al [163]. They reported that the heat transfer rate and friction factor in the pipe with twisted tape, were 1.03 to 4 and 1.4 to 2.8 times of those in a plain pipe respectively. The convective heat transfer correlations can be summarised in Table 2.3

Table 2-3 Convective heat transfer correlations

Reference	year	correlation	information
Park and Cho [16]	1998	$Nu = 0.021Re^{0.8}Pr^{0.5}$	Turbulent flow
Li and Xuan [157]	2002	$Nu = 0.4328(1 + 11.285\emptyset^{0.754}Pe^{0.218})Re^{0.333}Pr^{0.4}$	Laminar flow
Xuan and Li [164]	2003	$Nu = 0.0059(1 + 7.6286\emptyset^{0.6886}Pe^{0.001})Re^{0.9238}Pr^{0.4}$	Turbulent flow
Yang et al [76]	2005	$Nu = aRe^{b}Pr^{1/3}\left(\frac{D}{L}\right)^{1/3}\left(\frac{\mu_w}{\mu_b}\right)^{-0.14}$	Laminar flow
Jung et al [165]	2006	$Nu = 0.0095\emptyset^{0.01}Re^{0.42}Pr^{0.55}$	Laminar flow in microchannel
Maiga [166]	2006	$Nu = 0.085Re^{0.71}Pr^{0.35}$	Turbulent flow
Buongiorno [55]	2006	$Nu = \frac{(f/8)(Re-1000)Pr}{1+\delta_{\emptyset}^{+}(f/8)^{1/2}\left(Pr_{\emptyset}^{2/3}-1\right)}$	Turbulent flow

Naphon [167]	2006	$Nu = 44.26\left(\frac{e}{d}\right)^{0.89}\left(\frac{P}{d}\right)^{-0.96}(Re - 1500)^{0.27}Pr^{-.26}$	Turbulent Flow
Polidori [168]	2007	$Nu = \frac{4\sqrt{5}}{3\Delta_{nf}}\left[\frac{\beta_{rK_r^4}}{378v_r^2(9\Delta_{nf}-5)\Delta_{nf}{}^4}Gr_b\right]_{1/4}$	Turbulent
Rea et al [169]	2009	$Nu = 1.619(x^+)^{-1/3}$	Laminar flow
Duangthongsuk and Wongwises [170]	2010	$Nu = 0.074Re^{0.707}Pr^{0.385}\emptyset^{0.074}$	Turbulent Flow
Vajjha et al [171]	2010	$Nu = 0.0065(Re^{0.65} - 60.22)(1 + 0.0169\emptyset^{0.15})Pr^{0.542}$	Turbulent flow
Asirvatham et al [172]	2011	$Nu = 0.0023Re^{0.8}Pr^{0.3} + (0.617\emptyset - 0.135)Re^{(0.445\emptyset-0.37)}Pr^{(1.081\emptyset-1.035}$	Turbulent flow
Sajdi and Kazemi [173]	2011	$Nu = 0.067Re^{0.71}Pr^{0.35} + 0.000Re$	Turbulent flow
Mansour et al [174]	2011	$Nu = Nu_o(1 - \emptyset^{0.625})(1 + 5.25 \times 10^{-5} \times Ra^{1.06})^{0.135}$	Laminar flow
Suresh et al [155]	2012	$Nu = 0.031(RePr)^{0.68}(1 + \emptyset)^{95.73}$	Laminar flow
Sundar et al [175]	2012	$Nu = 0.0217Re^{0.8}Pr^{0.5}(1 + \emptyset)^{0.5181}$	Turbulent flow

2.6 Numerical analysis of convective heat transfer of nanofluid

Despite a large number of experimental works on different types of applications working with nanofluid, the numerical analysis remains one of the most efficient tools for studying nanofluid properties and heat transfer performance, as it presents a saving in both time and costs as compared to studying a real problem. Various CFD methods can be used to model nanofluids, and several major numerical investigations will be discussed in this section.

2.6.1 Single-phase approach

This method is the most common approach, and it has been taken by many studies of convective heat transfer using nanofluids. However, the numerical predictions resulting from this technique may lead to minor deviations when compared with experimental data.

The main reason for these deviations is the assumption that there is no slip between solid particles and the base fluid.

2.6.1.1 Conventional single-phase approach

Despite the fact that the nanoparticle and base fluid mixture is a two-phase fluid because of the addition of the nanoparticles, it is generally assumed that the nanoparticles can be easily fluidised and, as a result, the nanofluid can frequently be considered to be a conventional single-phase fluid (homogenous) with the corresponding thermophysical properties. This type of model assumes that both the solid particle and liquid phase are in thermal equilibrium and that there is no slip between them, as reported by Vavaki et al [176].

Akhtari et al [177] reported a numerical and experimental investigation in double pipe heat exchangers and shell and tube heat exchangers for Al_2O_3-water nanofluids under laminar flow. They used the commercial code, Ansys–FLUENT 12.1, for their mathematical modelling, adopting a 2D computational domain for the double pipe heat exchanger and a 3D configuration for shell and tube heat exchanger. The deviation in results between the numerical predictions and the experimental results in the shell and tube and double pipe heat exchangers was 15.6% and 11.2%, respectively. The researchers highlighted that the heat transfer coefficient of both types of heat exchanger was enhanced by increases in the volume fraction, the hot and cold volume flow rates, and the inlet temperature of the nanofluid.

Bianco et al. [178] presented a comprehensive study comparing single-phase and two-phase model simulations for Al_2O_3-water nanofluids under laminar flow. They found that considering temperature-dependent thermophysical properties in the modelling led to better enhancement predictions. The difference in results between the single-phase and two-phase models was minor. The single phase showed better results when incorporating the temperature-dependent thermophysical fluid properties compared to the two-phase model.

Izadi et al. [179] numerically investigated the forced convection problem for Al_2O_3-water nanofluids under laminar flow in a 2D annulus. The finite volume method was used to perform discretization of the governing equations in the single-phase model. The researchers included the effects of a fine mesh near the wall in order to overcome the

velocity and temperature gradients. A good agreement between numerical predictions and experimental data for friction factor was reported. Furthermore, the results showed that the effect of volume concentration on the temperature profiles was significant.

Moraveji et al. [180] performed a CFD simulation to study convective heat transfer influence on Al_2O_3-water nanofluids in the developing region of a pipe. The single-phase model was adopted, and a range of Reynolds numbers (500 to 2500) was tested for volume fractions ranging from 0 to 6%. The researchers compared their numerical predictions with experimental data produced by Anoop et al [181] for a similar problem. The maximum error in the comparative heat transfer coefficients was 10%. The heat transfer coefficient improved the Reynolds number and volume fraction increased.

Hussein et al. [182] studied the friction factor of SiO_2-water nanofluids under laminar flow using a single-phase model. Their results highlighted the fact that the friction factor and Nusselt number were greatly dependent on the volume fraction and Reynolds number. They compared their simulations to data from their experimental work and found good agreement overall.

Mohammed et al.[183] used the single-phase model to investigate the effects of using different nanoparticles in water nanofluids on heat transfer and fluid flow in a triangular microchannel heat sink under laminar flow. Their results for temperature difference and pressure drop showed good agreement with experimental results. In these experiments, diamond and silver nanoparticles showed the higher heat transfer rates and lowest pressure losses.

2.6.1.2 Thermal dispersion single-phase approach

This modified approach assumes that the nanoparticles' relative velocity with respect to the base fluid introduces a perturbation to the velocity and temperature of the nanofluid; this allows for a correction to be added to the components of temperature and velocity in the governing equations.

This method was first introduced by Xuan and Roetzel [184]. According to their assumptions, thermal dispersion will increase and hence increase the heat transfer rate. However, further experimental work is needed to check the validity of this approach.

Heris et al. [185] adopted the dispersion model to investigate the problem of convective heat transfer of nanofluids under laminar flow in a circular pipe. The effect of the random motion of nanoparticles in the liquid modifies the behaviour of the flow field and subsequently promotes heat transfer. These researchers made a comparison between their model and experimental results to obtain a heat transfer coefficient; their model showed good agreement with experimental measures during this process.

The single phase dispersion model was also investigated by Kumar et al [186]. Simulations for natural convection using copper-water nanofluids were investigated, and the role of the random motion of nanoparticles in the base fluid was taken into consideration. The researchers reported that the dispersed thermal conductivity was profound near the wall region; also in this region, the velocity magnitude was higher than in the centre.

Mokmeli and Saffar-avval [187] studied the laminar convective heat transfer problem in a tube. They rearranged Xuan and Roetzel's model and included a radial dispersion assumption in their equations. They reported that the dispersion model predicted nanofluid heat transfer behaviour accurately compared to their experimental data. The deviation in error to volume fraction variations was less than 2.5%, while the deviation in Reynolds number was less than 4%.

Akbaridoust et al. [188] investigated CuO-water nanofluids in helically coiled pipes under laminar flow both numerically and experimentally. They solved the governing equations in the 3D using the finite difference method. Using modified dispersion to model the algorithm reduced the deviation between the experimental and numerical results to just 4%. However, this approach was criticised as it did not account for two functional features of the nanofluid, volume concentration and nanoparticle diameter.

2.6.2 Two-phase Approach

In general, nanofluids are two-phase mixtures with both solid and liquid phases; in this type of model, it is inaccurate to assume a slip velocity equal to zero. The two-phase approach considers the nanoparticles and the base fluid to be two different phases with different temperatures and velocities. This approach can be classified into two main model types: Lagrangian-Eulerian and Eulerian-Eulerian.

2.6.2.1 Lagrangian–Eulerian model

In Lagrangian-Eulerian models (also called discrete phase models), the fluid phase is considered as a continuum described by solved time-averaged Navier-Stokes equations, while the dispersed phase is solved by tracking a large number of particles. The second phase is assumed to carry a low volume concentration.

Several numerical studies have been reported using similar methods. Moraveji and Esmaeili [189] presented a numerical investigation comparing single and two-phase models using a Lagrangian-Eulerian paradigm. The two models showed similar results, and the maximum deviation between the two models' predictions for average heat transfer coefficient was 11%.

The heat transfer improvement was studied numerically by Mirzaei et al [190] using the Eulerian–Lagrangian two-phase approach for Cu–water nanofluids. The two-phase approach results showed a slight enhancement compared to the conventional single-phase model. They highlighted that the Nusselt number predicted using the two-phase approach is slightly higher than the Nusselt number produced by a single-phase model. Bahremand et al. [191] numerically and experimentally investigated the flow of silver-water–nanofluids in helically coiled pipes. They adopted the Lagrangian–Eulerian model using ANSYS CFX software. Their results highlighted the fact that two-phase method calculations were slightly more accurate than those produced by the single-phase model, but was much more demanding from a computational point of view.

The same approach was also used by Mahdavi et al [192] in a vertical pipe when they studied the hydrodynamic features and heat transfer in three different nanofluids under laminar flow in 2D and 3D models. They made a comparison between the Lagrangian-Eulerian model and the mixture model. In their simulations, they considered the nanoparticles to be a discrete phase and the base fluid to be a continuous component in a discrete phase model (DPM). The mixture model treated the nanoparticles and the base fluid as two continuous components. For higher volume concentrations, the DPM was found to be inaccurate.

2.6.2.2 Eulerian-Eulerian model

Eulerian-Eulerian model is suitable for the two-phase mixture when the volume of fraction is large. However, this model can be used even for small volume concentrations. There are

three common Eulerian-Eulerian models for two phase approaches, the volume of fluid model (VOF), the mixture model, and Eulerian model.

2.6.2.2.1 The mixture model

The mixture model is recommended for studying two-phase turbulent flows [176]. The main advantage of this method is its simplicity and consequent reduced run time. However, one of its drawbacks is that it does not take into account any phase changes. Behzadrmehr et al [193] used with the mixture model to investigate turbulent flow in pipes for Cu-water nanofluids. The investigators reported that the mixture model was more accurate than the single-phase model when compared against experimental results. However, they highlighted the need to improve the accuracy of the mixture model by using proper effective thermophysical properties for nanofluids.

Mirmasoumi and Behzadmehr [194] studied the laminar mixed convection problem using the mixture model for Al_2O_3-water nanofluids. They compared their results with experimental data from the literature, and found that the skin friction factor predictions appeared overly high at the entrance region. Saberi et al [195] similarly presented a numerical study for Al_2O_3-water and Zicronica-water nanofluids in a vertical tube using both a single-phase model and two-phase mixture model; results from these were then compared with the experimental data. The mixture model prediction for the convective heat transfer coefficient displayed better agreement with the experimental data than the single-phase model. However, the prediction of the single-phase model for the bulk temperature distribution of the nanofluid was more accurate than that of the mixture model in comparison to the experimental data. The average deviation in the results for the convective heat transfer coefficient between single-phase model and experimental data was 13% for alumina-water, while the deviation for the mixture model was 8%.

2.6.2.2.2 The volume of Fluid

The volume of fluid model considers the following assumptions [196]:

- The continuity equation for the secondary phases is solved for the whole domain in order to track the volume fractions for all phases.
- The velocity components for all phases are calculated by the momentum equations in a single set for all phases.
- The energy equation is solved by one shared temperature.

- To calculate the thermophysical properties, the weight-average based on the volume fractions for all phases must be considered.

This approached has been used in investigating nanofluids by a limited number of researchers. Akbari et al [197] presented a comparative study of single- and two-phase approaches under turbulent flows. The predictions produced by the single-phase model were more accurate than those of the two-phase models. The researchers, therefore, suggested that the single-phase model is more suitable due to the need for less machine memory and its overall simplicity. Moraveji and Ardehali [198] presented a numerical simulation for Al_2O_3-water nanofluids using single-phase, VOF, mixture, and Eulerian models. They highlighted that the different two-phase models showed insignificant differences in terms of predicting the results. The single-phase model was found to have less accurate results compared to the experimental data.

2.6.2.2.3 Eulerian model

In this model, it is assumed that the nanoparticles and the water are of a continuum and that there is a difference in terms of temperature and velocity between the nanoparticle and the base fluid [199].

A comparative study between the three different two-phase models for Al_2O_3-nanofluid was presented by Akbari et al [196]. The study also included the single-phase approach. They highlighted the following issues:

- The two-phase models all had the same level of accuracy.
- The volume of fraction model was the least expensive model.
- The Nu number was over-predicted by the two-phase models.

Kalteh et al [200] investigated the heat transfer performance of a Cu–water nanofluid using the Eulerian two-phase model. They concluded that the relative velocity and temperature of the nanoparticle phase and the base fluid phase was insignificant. However, the single-phase model showed lower heat transfer enhancement compared to the two-phase model. Beheshti [201] presented a comparison study between the single-phase and Eulerian two-phase model for an annular channel using two different nanofluids. This work studied the effects of various parameters such as the types of nanoparticle and the nanoparticle volume

fraction on heat transfer enhancement. The results revealed that the two-phase models demonstrated better predictive power than the single-phase model in terms of the experimental data. Lotfi et al [202] investigated the heat transfer performance of Al_2O_3-water nanofluids. They implemented a two-phase Eulerian model, the single-phase approach and a two-phase mixture model. A comparison of the prediction results showed that the mixture model was the most accurate model among this group. According to these simulations, the single-phase model and the two-phase Eulerian model undervalued the Nu number.

2.6.3 Other CFD approaches

There are a few additional methods for modelling the nanofluids:

2.6.3.1 Lattice Boltzmann Method (LBM)

This method has recently attracted the attention of several researchers as it simulates the flow rather than the Navier-Stokes equations. Sheikholeslami et al [203] performed numerical simulations for Cu-water nanofluids in natural convection using LBM, and the results were verified against experimental data and found to provide good agreement. The researchers reported that the LBM is a powerful method for modelling nanofluid in natural convection. Nemati et al [204] applied the LBM method to investigate Cu-water and Al_2O_3-water nanofluids in mixed convection flows. They described the approach as suitable for modelling nanofluids under such conditions. According to their report, the LBM was found to be a simpler form of modelling compared to other CFD approaches.

This method has been modified by using multiple relaxation time as introduced by Nabavitabatabaya et al [205]. They showed that a multiple relaxation time LBM approach could become a powerful tool to simulate heat transfer. The natural convection problem for SiO2-water nanofluids was investigated using LBM by Kefayati et al [206]. The results compared to other CFD approaches and good agreement was observed.

Yang and Lai [207] studied heat transfer performance for Al_2O_3-water nanofluids using LBM. The predicted results were compared with the single-phase model and showed very good agreement. However, three different Nusselt number correlations were adopted in the LBM model, and the results showed large deviations between them.

2.6.3.2 Non-homogeneous two-component model

Various mechanisms were proposed by several researchers to model the special properties of nanofluids. For example, the influence of nanoparticle dispersion on the transfer of energy was investigated by Buongiorno [208] who suggested a new approach called a homogeneous two-component model. Different mechanisms of slips between the nanoparticles and the base fluid have been addressed in various ways, including Brownian motion, inertia, and thermophoresis. The effect of the Brownian motion mechanism was investigated by Sheikhzaden et al [209] using a homogenous two-component model; however, they reported that the transport model showed better agreement than the homogeneous approach in this instance.

2.7 Applications of nanofluids

2.7.1 Introduction

As a result of reports of their enhancement of thermophysical properties, nanofluid applications have attracted a significant number of researchers to investigate potential industrial applications. Various applications have been examined in this way, including industrial, commercial, and transportation applications. Areas of application for these fluids are wide-ranging, and include functions such as engine cooling, electronic cooling, generator cooling, vehicle thermal management, nuclear system cooling, machining coolant, refrigeration, cooling and heating in buildings, thermal storage, lubrication, solar heating, drug reduction, transformer cooling, heat pipes, biomedical applications, and maritime engineering [210-220]. The following sections will discuss nanofluid applications in microchannels and heat exchangers as an example of its utilisation

2.7.2 Heat exchanger

Heat exchangers are encountered in many industrial applications. Nanofluids can be used in many types of heat exchanger such as those used in power production, the chemical industry, the food industry, heat recovery, refrigeration, and air conditioning [215].

Pantzali et al. [221] presented a numerical and experimental study on the influence of CuO-water nanofluids on plate heat exchanger performance. Their observations revealed

that the thermal conductivity augmentation led to significant drop in specific heat and an increase in viscosity. Furthermore, the heat transfer rate was promoted when the flow rate was minimised. Chun et al [222] conducted an experimental investigation on the heat transfer coefficient of three different types of alumina-water nanofluids in a double pipe heat exchanger under laminar flow. The experimental results revealed that an increase in the volume fraction increased the average heat transfer coefficient of the heat exchanger. The researchers reported several key factors that affected this heat transfer enhancement, including nanoparticle size and shape, the properties of nanoparticles, and the volume fraction.

Huminic and Huminic [223] numerically studied the heat transfer performance of double-tube helical heat exchangers using Cu-water and TiO2-water nanofluids under laminar flow. They observed that for CuO-water at volume fraction 2% and same mass flow rate in an inner and outer tube, the heat transfer rate increased by 14% compared to water, as the base fluid. The simulations showed that the increase in the mass flow rate promoted the convective heat transfer coefficients of the nanofluids and water.

An experimental study on the convective heat transfer coefficient of Ag-water nanofluids in a double pipe heat exchanger was presented by Asirvatham et al. [172]. Their results indicated that, under a constant Reynolds number, the nanoparticles significantly enhanced heat transfer. At volume fraction 0.9%, the augmentation in the heat transfer coefficients was as much as 69.3%. The researchers also developed a correlation to predict the Nu number, and then compared experimental results with the results calculated by the correlation; an error of 10% was noted. Mousavi et al [224] studied the effects of a magnetic field on the heat transfer in a double pipe heat exchanger using nanofluids. Their results showed that the inner sinusoidal pipe considerably enhanced the heat transfer rate in the heat exchangers. Their findings showed that the Nusselt number increased by up to 25%. According to their predictions, heat transfer is enhanced by an increase in magnetic field intensity.

Goodarzi et al [225] conducted a numerical and experimental investigation on the heat transfer characteristics of NDG-water nanofluids in a double pipe heat exchanger. They observed an improvement in thermal conductivity of up to 37%. Viscosity decreased with an increase in the temperature by between 51.2 and 51.5%. On the other hand, an increase in Reynolds number and volume fraction could increase the friction factor and thereby

increase pressure drop. The main finding was that the key parameters in terms of heat exchanger efficiency enhancement are thermal conductivity and fluid density. Sarafraz et al [226] presented an experimental study on the thermal performance of multi-walled carbon nanotube nanofluids in a double pipe heat exchanger. They observed that that CNT nanofluid promoted convective cooling. The increase in the thermal conductivity due to fluid was found to be 56%, and heat transfer was significantly promoted by this increase in thermal conductivity; however, a marginal pressure drop was also noticed.

Sarafraz and Hormazi [227] investigated the forced convection problem in a double pipe heat exchanger using a novel biological nanofluid. Their results showed that the biological nanofluid changed the flow type from laminar to transient, and from transient to turbulent flow. Adding the nanoparticles improved the heat transfer coefficient by up to 67% with almost no penalty in terms of pressure drop. No agreement was found between the experimental results and the available correlations. The authors proposed a new formula in order to predict the heat transfer coefficient, and an average deviation of 17% was found between the experimental data and the proposed model.

Shakiba et al [228] investigated the effects of a magnetic field on thermal behaviour in a double pipe heat exchanger using Fe3O4-water nanofluids. The results showed that the magnetic field increased the Nusselt number, the friction factor, and the pressure drop.

2.7.3 Microchannels

Substantial developments in electronics, power stations, optical devices, transportation, and many other applications have led to a large number of applications requiring high heat flux dissipation. Such applications can be serviced by means of micro-heat exchangers, micro-heat sinks, micro-nozzles, and micro-reactors. These devices have many advantages, one of which is their larger complement parts. The most superior feature of micro-heat exchangers is their facility to work with close approach temperatures in a highly effective manner. Their other useful features can be summarised in three ways:

- High surface area per volume ratios;
- High heat transfer coefficients; and
- Low thermal resistances.

Microchannel heat sinks have attracted many researchers due to their interesting properties and demanding applications. Koo et al [229] studied laminar flow and aspect ratio in microchannel heat sinks, and they found that the channels with highest aspect ratios were most desirable. Chevallier et al [81] investigated the rheological properties of nanofluid flowing in microchannels, while Nguyen et al [230] investigated laminar flow in microchannel using single and two-phase models. The results revealed that the wall heat transfer enhanced with an increase in Re and an increase in volume fraction. Jie et al [231] studied entropy generation in microchannels, and they highlighted the fact that friction factor entropy generation becomes more important with any increase in inlet velocity.

Walchli et al [232] studied microchannel performance cooling. They proposed to limit the complexity of a three-dimensional CFD model to the modelling of only the unit cell of the heat exchanging meshes in microchannels for clarity.

Kalteh et al [233] conducted an experimental and numerical study to investigate heat transfer performance in microchannels. They found that nanofluid in these applications can be considered a homogeneous mixture and that the velocity and temperature profiles for two-phase results are flatter than the base water or homogeneous model profiles.

Mohammed et al [214] highlighted the deviations in some experimental and numerical results in microchannel applications using nanofluids while Vivekanand et al [234] studied evaporation heat transfer in a rectangular microchannel. These researchers showed that the vapour volume fraction varies substantially when the heat flux boundary condition is applied at the wall. Chein and Huang [235] investigated the heat performance of Cu-water nanofluid in a microchannel. They noted that heat performance is significantly improved due to the augmentation in thermal conductivity, and that adding nanoparticles to the base fluid showed no penalty in terms of pressure drop. The cooling performance of the nanofluid in a microchannel heat sink was also studied numerically by Jang and Choi [236]. The results showed that the cooling heat transfer was enhanced by up to 10% compared with water, the base fluid under consideration.

Chein and Chuang [237] theoretically and experimentally investigated the heat performance for CuO-water nanofluids in microchannel heat sinks. They reported that the nanofluid absorbed more energy than water, the base fluid, at low flow rates. At higher flow rates, an increase in nanoparticles did not show any additional heat absorption. The observed wall temperature variations were in agreement with the theoretical calculations at

low flow rates. However, at higher flow rates, the measured wall temperatures differed from the theoretical calculations. Only a marginal increase in pressure drop due to the presence of nanoparticles was detected.

The effect of the height of the microchannel and the volume concentration on the heat transfer performance was investigated experimentally by Manay and Sahin [238] for TiO2-water nanofluids under constant heat flux. Four different heights were tested (200, 300, 400, and 500 μm) for various volume fractions. The researchers observed an improvement in heat transfer for most volume concentrations tested; however, no enhancement was reported for volume concentrations greater than 2%. A decrease in the microchannel height increased the heat transfer under constant width. Among the microchannel heights tested, the channel with height 200 μm showed the highest heat transfer rate. On the other hand, an increase of 10 to 50% in the friction factor was reported when decreasing the microchannel height from 500 to 200 μm.

An experimental investigation on the enhancement of Al_2O_3-water nanofluid in a microchannel was carried out by Lee and Mudawar [239]. The augmentation in thermal conductivity enhanced the heat single-phase transfer. However, this enhancement was significantly observed only in laminar flow; in turbulent flow, insignificant enhancement was observed. The researchers attributed this weak enhancement to the non-dependence of the heat transfer on thermophysical properties in the turbulent region. The water-based fluid showed less heat transfer compared to the nanofluid; however, an enhancement in the heat transfer was observed only in the entrance region. In the fully developed region, the results indicated an insignificant heat transfer improvement.

Byrne et al [240] conducted an experimental investigation on the thermal performance of CuO-water nanofluids in a rectangular microchannel. An increase in the heat transfer rate of up to 17% was observed at a volume concentration of 0.01%. However, only insignificant increase in pumping power was reported. The researchers suggested that using appropriate surfactants is crucial for homogenous dispersion of the nanoparticles in the fluid. Hung et al [241] presented a numerical study on the enhancement of heat transfer by various nanofluids in a microchannel. The highest heat transfer calculated in the study was achieved when using an Al_2O_3–water nanofluid; this showed an increase of around 21.6% compared to the water base fluid. The researcher's calculations showed that, when the volume fraction increased, the thermal resistance first decreased and then increased.

According to their simulations, the heat transfer improved with a decrease in the nanoparticle diameter.

Jung et al [242] experimentally investigated the convective heat transfer performance of Al_2O_3-water nanofluids in a microchannel. Their measurement for the heat transfer coefficient in the laminar region showed an increase of up to 32% over the water base fluid. The Nusselt number measured increased with an increase in the Reynolds number in the laminar flow region. However, these results were not in agreement with conventional correlation calculations.

Heat transfer enhancement in a microchannel for SiO2-water nanofluid was investigated experimentally by Anoop et al [243]. The measured viscosity was enhanced by up to 7%, but the heat transfer deteriorated when the nanofluid flow rate increased beyond a critical value; before this critical value, the heat transfer was improved. Tokit et al [244] investigated heat transfer and fluid flow for three different nanofluids in a rectangular microchannel. The highest augmentation in thermal conductivity among the different nanofluids was 1.18% for Al_2O_3, and the relative Nu number improvement (Nu_{nf}/Nu_w) was 2.67%.

A three-dimensional numerical study on thermal performance in a microchannel with double layer was presented by Hung and Yan [245] for Al_2O_3-water nanofluid. Their predictions revealed that the maximum enhancement in the microchannel was achieved when Al_2O_3–water nanofluid was used. The thermal resistance was reduced by correctly altering the volume concentration under different pumping powers. Furthermore, the minimum thermal resistance was affected by the geometric parameters. They reported that the thermal performance can be enhanced by increasing the width ratio of the microchannel or decreasing the channel aspect ratio. At a given pumping power, the enhancement in thermal performance was 26% over that of pure water at a volume fraction of 1%.

Malvandi et al [246] theoretically investigated the influence of the migration of nanoparticles on convective heat transfer in a vertical microchannel for Al_2O_3-water nanofluids. They revealed that the effect of temperature-dependent buoyancy is minor; however, concentration-dependent buoyancy did demonstrate a significant effect on both flow and heat transfer characteristics. Malvandi et al [247] presented a theoretical study on the effect of nanoparticle migration on fully developed flow in the laminar region using

Al_2O_3-water in a microchannel. They reported that the buoyancy effect was improved; however, there was an acceleration in the velocity near the walls with no acceleration in the velocity in the core. They reported that the buoyancy influence had a negative impact on cooling performance, but that this negative effect significantly depended on nanoparticle diameter.

Different configurations of microchannels have been investigated by several researchers. Kuppusamy et al [248] studied the geometrical parameters for four different nanofluids in a trapezoidal microchannel. Their findings were that an increase in the maximum width and a decrease in the minimum width of the trapezoidal shape demonstrated the highest thermal performance; this suggests that a triangular cross section would be recommended in comparison to standard rectangular cross section microchannels.

The heat transfer enhancement in serpentine shaped microchannel was experimentally investigated by Sivakumar et al [249]. Four different configurations were tested using Al_2O_3-water for volume concentrations of up to 0.1 %. The researchers highlighted the fact that the pressure drop increased with a decrease in the microchannel hydraulic diameter. Furthermore, the heat transfer improvement was a function of the hydraulic diameter and the microchannel dimensions.

2.8 Conclusion

From this literature survey, several findings emerge:

- Natural convection with Brownian motion and the enhancement of heat transfer requires further investigation with a wider range of Rayleigh numbers
- The separations flows in backward-facing step with various face step inclinations are not investigated in depth in the literature; hence, further studies looking at the effect of the inclinations of the step are essential.
- There is as yet no unified model to predict the effective viscosity for the nanofluids, despite several models have been proposed for particular experimental configurations; in each case, model applicability is limited to that configuration.

- Increasing demand in the microchannel industry has attracted the attention of researchers looking to facilitate the enhancement of heat transfer using microchannels. Geometry parameters play a key role in this enhancement, so an understanding of the optimum parameters is crucial. Chapter seven discusses various configurations of microchannels under different scenarios.
- The enhancement of heat transfer in a double pipe heat exchanger is explored in the literature. However, all previous works used only one nanoparticle in their studies, while the current work will focus on using four different nanoparticles and their varying impacts on fluid flow and heat transfer characteristics.
- Consideration of the literature has shown that investigations on the heat transfer enhancement using nanofluid have been essentially focussed on the volume fractions on heat transfer improvement in several flow scenarios. It has also revealed the importance of the development of reliable, accurate and feasible CFD model.

3 Mathematical model and Numerical simulations

3.1 Introduction

In this chapter, the mathematical models and the numerical approaches employed in the present research are discussed. The governing equations of the flow, the numerical code and CFD solution method will be presented. The geometry creation, the mesh generation are also reported. A built in C-code incorporated in the CFD code is developed, this c-code known as user-defined function (UDF).

Computational fluid dynamic (CFD) is a robust tool for the analysis of systems comprising external or internal fluid flow and heat transfer. This analysis is made by computer-based simulation with higher accuracy. This method has been extended to a wide range of applications, such as aerodynamics, combustion, environment, medicine, agriculture and many other applications.

3.2 Governing differential equations of fluid flow and heat transfer

The governing equations of fluid flow and heat transfer describe the mathematical formulations of the laws of conservation of Physics [250, 251]. The equations of laws of conservations can be summarised as:

- Conservation of mass.
- Conservation of momentum.
- Conservation of energy.

The derivations of the equations will not be listed here assuming the reader is familiar with the field.

3.2.1 Continuity equation

The continuity equation resulted from applying the conservation of mass law to the fluid flow. The analysis made in an infinitesimal control volume, the form of the equation is expressed as:

$$\frac{\partial \rho}{\partial t} + \boldsymbol{\nabla}.(\rho \boldsymbol{V}) = 0 \tag{3.1}$$

where

ρ is the density of the fluid

V is the velocity of the fluid

The rate of the increase in the density is represented by the first term in equation (3.1), and the rate of mass flux per unit volume passing out the control surface is represented in the second term. For simplicity and using Lagrangian approach and by applying substantial derivative, equation (3.1) can be written as:

$$\frac{D\rho}{Dt} + \rho(\boldsymbol{\nabla}.\boldsymbol{V}) = 0 \tag{3.2}$$

For incompressible flows, the first term in equation (3.2) becomes zero, and the first term can be mathematically written

$$\frac{D\rho}{Dt} = 0 \tag{3.3}$$

The continuity equation can be written as:

$$(\boldsymbol{\nabla}.\boldsymbol{V}) = 0 \tag{3.4}$$

Alternatively, can be simplified in the Cartesian coordinate system to:

$$\frac{\partial u}{\partial x} + \frac{\partial v}{\partial x} + \frac{\partial w}{\partial x} = 0 \tag{3.5}$$

3.2.2 Momentum conservation equation

The momentum equation can be obtained by applying the Newton's second law on a fluid passing an infinitesimal control volume. The form of the equation can take the following:

$$\frac{\partial}{\partial t}(\rho \boldsymbol{V}) + \boldsymbol{\nabla}.\rho \boldsymbol{V}\boldsymbol{V} = \boldsymbol{\rho}\mathbf{f} + \boldsymbol{\nabla}.\mathrm{P}_{\boldsymbol{ij}} \tag{3.6}$$

The first term in equation (3.6) denotes the rate of increase of momentum in the control volume. The rate of momentum per unit volume lost by convection is represented by the second term in the equation and can be expressed as:

$$\boldsymbol{\nabla}.\rho \boldsymbol{V}\boldsymbol{V} = \rho \boldsymbol{V}.\boldsymbol{\nabla}\boldsymbol{V} + \boldsymbol{V}(\boldsymbol{\nabla}.\rho \boldsymbol{V}) \tag{3.7}$$

Substituting this term in equation (3.6), the momentum equation can be simplified to the following form:

$$\rho \frac{D\boldsymbol{V}}{Dt} = \rho\mathbf{f} + \boldsymbol{\nabla}.\mathrm{P}_{ij} \tag{3.8}$$

The body force per unit volume is expressed in the first term on the right-hand side. An example of common force is the gravitational force. The surface forces per unit volume are represented in the second term in equation (3.7). These forces are resulted from applying the external stresses on the fluid element.

For Newtonian fluids, the relation between the stress tensor and pressure and velocity can be written as:

$$P_{ij} = -p\delta_{ij} + \mu\left(\frac{\partial u_i}{\partial x_j} + \frac{\partial u_j}{\partial x_i}\right) + \delta_{ij}\acute{\mu}\frac{\partial u_k}{\partial x_k} \quad \text{i,j,k=1,2,3} \tag{3.9}$$

Where

u_1, u_2, u_3 represent the three components of the velocity vector **V**

x_1, x_2, x_3 represent the three components of the position vector

δ_{ij} is the Kronecker delta function ($\delta_{ij} = 1$ if $i = j$ and $\delta_{ij} = 0$ if $i \neq j$)

μ represents the coefficient of dynamic viscosity

$\acute{\mu}$ is the second coefficient of viscosity

Now the Navier-Stokes equation can be written as:

$$\rho \frac{D\boldsymbol{V}}{Dt} = \rho \mathbf{f} - \boldsymbol{\nabla} p + \frac{\partial}{\partial x_j}\left[\mu\left(\frac{\partial u_i}{\partial x_j} + \frac{\partial u_j}{\partial x_i}\right) - \frac{2}{3}\delta_{ij}\mu\frac{\partial u_k}{\partial x_k}\right] \tag{3.10}$$

In the Cartesian coordinate system, the Navier-Stokes equation can be written in three different scalar equations [252]:

$$\rho \frac{Du}{Dt} = \rho f_x - \frac{\partial p}{\partial x} + \frac{\partial}{\partial x}\left[\frac{2}{3}\mu\left(2\frac{\partial u}{\partial x} - \frac{\partial v}{\partial y} - \frac{\partial w}{\partial z}\right)\right] + \frac{\partial}{\partial y}\left[\mu\left(\frac{\partial u}{\partial y} + \frac{\partial v}{\partial x}\right)\right] + \frac{\partial}{\partial x}\left[\mu\left(\frac{\partial w}{\partial x} + \frac{\partial u}{\partial z}\right)\right] \tag{3.11}$$

$$\rho \frac{Dv}{Dt} = \rho f_y - \frac{\partial p}{\partial y} + \frac{\partial}{\partial y}\left[\frac{2}{3}\mu\left(2\frac{\partial v}{\partial y} - \frac{\partial u}{\partial x} - \frac{\partial w}{\partial z}\right)\right] + \frac{\partial}{\partial x}\left[\mu\left(\frac{\partial v}{\partial x} + \frac{\partial u}{\partial y}\right)\right] + \frac{\partial}{\partial x}\left[\mu\left(\frac{\partial v}{\partial z} + \frac{\partial w}{\partial y}\right)\right] \tag{3.12}$$

$$\rho \frac{Dw}{Dt} = \rho f_z - \frac{\partial p}{\partial z} + \frac{\partial}{\partial z}\left[\frac{2}{3}\mu\left(2\frac{\partial w}{\partial z} - \frac{\partial u}{\partial x} - \frac{\partial v}{\partial y}\right)\right] + \frac{\partial}{\partial x}\left[\mu\left(\frac{\partial w}{\partial x} + \frac{\partial u}{\partial z}\right)\right] + \frac{\partial}{\partial y}\left[\mu\left(\frac{\partial v}{\partial z} + \frac{\partial w}{\partial y}\right)\right] \tag{3.13}$$

For incompressible flow and constant viscosity equation (3.10) can be simplified to:

$$\rho \frac{D\boldsymbol{V}}{Dt} = \rho \mathrm{f} + \boldsymbol{\nabla} p + \mu \nabla^2 \mathbf{V} \tag{3.14}$$

3.2.3 Energy conservation equation

The energy equation can be obtained by applying the first law of thermodynamics to a fluid passing an infinitesimal control volume. Mathematically this can be written as:

$$\frac{\partial E_t}{\partial t} + \boldsymbol{\nabla}.\,\mathrm{E_t}\mathbf{V} = \frac{\partial Q}{\partial t} - \boldsymbol{\nabla}.\,\mathbf{q} + \rho \mathbf{f}.\,\mathbf{V} + \boldsymbol{\nabla}.\,(P_{ij}.\,\mathbf{V}) \tag{3.15}$$

The rate of increase of total energy is represented by the first term on the left-hand side in equation (3.15). The rate of total energy lost by convection is represented by the second term. On the right-hand side, the rate of heat produced by external forces is represented by the first term. While the second term represents the rate of heat lost by conduction. The work done body forces on the control volume is represented by the third term. The work done by the surface forces on the control volume is represented by the fourth term in equation (3.15). It is worth to mention that the first law of thermodynamics is simply the equation (3.15).

The total energy per unit volume E_t is given by:

$$E_t = \rho\left(e + \frac{V^2}{2} + \text{potential energy} + \cdots\right) \tag{3.16}$$

Where

e is the internal energy per unit mass

For Cartesian coordinate system, equation (3.15) can be written as:

$$\begin{aligned}\frac{\partial E_t}{\partial t} - \frac{\partial Q}{\partial t} - \rho\left(f_x u + f_y v + f_z w\right) \\ + \frac{\partial}{\partial x}\left(E_t u + pu - u\tau_{xx} - v\tau_{xy} - w\tau_{xz} + q_x\right) \\ + \frac{\partial}{\partial y}\left(E_t v + pv - u\tau_{xy} - v\tau_{yy} - w\tau_{yz} + q_y\right) \\ + \frac{\partial}{\partial z}\left(E_t w + pw - u\tau_{xz} - v\tau_{yz} - w\tau_{zz} + q_z\right) = 0\end{aligned} \tag{3.17}$$

Using the continuity equation, the left-hand side of equation (3.15) can be expressed as:

$$\rho\frac{D}{Dt}\left(\frac{E_t}{\rho}\right) = \frac{\partial E_t}{\partial t} + \boldsymbol{\nabla}.E_t\mathbf{V} \tag{3.18}$$

Equation (3.18) can take the following form:

$$\rho \frac{D}{Dt}\left(\frac{E_t}{\rho}\right) = \rho \frac{De}{Dt} + \rho \frac{D}{Dt}\left(\frac{V^2}{2}\right) \tag{3.19}$$

If considering only the kinetic energy and internal energy in equation (3.16) and using the scalar product in equation (3.7), yields the flowing equation:

$$\rho \frac{D\boldsymbol{V}}{Dt}.\mathbf{V} = \rho \mathbf{f}.\mathbf{V} - \boldsymbol{\nabla}\mathrm{p}.V + \left(\boldsymbol{\nabla}.t_{ij}\right).\mathbf{V} \tag{3.20}$$

After some manipulation the following equation can be obtained:

$$\rho \frac{De}{Dt} + p(\boldsymbol{\nabla}.\mathbf{V}) = \frac{\partial Q}{\partial t} - \boldsymbol{\nabla}.\mathbf{q} + \boldsymbol{\Phi} \tag{3.21}$$

Where $\boldsymbol{\Phi}$ called the dissipation function which defined as the rate where mechanical energy is expended in the deformation of fluid because of the viscosity.
Equation (3.20) can be rearranged to the following:

$$\rho \frac{Dh}{Dt} = \frac{Dp}{Dt} + \frac{\partial Q}{\partial t} - \boldsymbol{\nabla}.\mathbf{q} + \boldsymbol{\Phi} \tag{3.22}$$

Where h is the enthalpy and can be calculated from the following equation:

$$h = e + \frac{p}{\rho} \tag{3.23}$$

In the Cartesian coordinate system, the dissipation function takes the following form:

$$\boldsymbol{\Phi} = \mu\left[2\left(\frac{\partial u}{\partial x}\right)^2 + 2\left(\frac{\partial v}{\partial y}\right)^2 + 2\left(\frac{\partial w}{\partial z}\right)^2 + \left(\frac{\partial v}{\partial x} + \frac{\partial u}{\partial y}\right)^2 + \left(\frac{\partial w}{\partial y} + \frac{\partial v}{\partial z}\right)^2 + \left(\frac{\partial u}{\partial z} + \frac{\partial w}{\partial x}\right)^2 - \frac{2}{3}\left(\frac{\partial u}{\partial x} + \frac{\partial v}{\partial y} + \frac{\partial w}{\partial z}\right)^2\right] \quad (3.24)$$

If the flow is incompressible and the thermal conductivity is constant, energy equation can take the form:

$$\rho\frac{De}{Dt} = \frac{\partial Q}{\partial t} + k\boldsymbol{\nabla^2}T + \boldsymbol{\Phi} \quad (3.25)$$

3.3 Discretization method

The discretization method is defined as the approach of approximating the differential equations by a set of algebraic equations for the variables at some set of discrete locations in space and time [253].

The governing equations discussed in the previous section can be discretised using several methods such as:

- Finite difference method
- Finite volume method
- Finite element method

The CFD code used in the present research is based on the finite volume approach. The next section will discuss this method and its implementation.

3.4 The finite volume method (FVM)

The finite volume is a numerical approach for solving the partial differential equations; these partial differential equations calculate the conserved variables averaged values in the control volume. What distinguishes the finite volume method from the finite difference is the using the control volume.

The finite-volume method principal is local conservation thus the method gains its success in CFD applications. The advantages of this method can be summarised in:

- Can be implemented in unstructured grids
- Integral formulation of conservation laws is used in finite volume method.
- Based on cell averaged values.

3.4.1 The FVM steps

The general procedure of the FVM can be summarised into the flowing steps:

i. The problem domain decomposed into control volumes.
ii. For each control volume, the integral balance equations are formulated.
iii. The integrals are approximated by numerical integrations.
iv. The function values and derivatives are approximated by interpolation with nodal values.
v. Assembling and solving the discrete algebraic systems

The above steps are used when discretising any flow domain; the next section will focus on the mathematical formulations of the FVM.

3.4.2 The FVM Procedure

In order to solve the equations numerically employing the finite volume method, the whole computational domain is divided into small volumes. These small volumes called the cells, the partial derivatives expressing a conservation principle using Gauss' law, such as div *u*, can be rewritten at each cell as an algebraic equation. The governing equation, expressed in the partial differential equations, is expressed in each computational cell as a set of linear algebraic equations; these equations are solved numerically in an iterative mode. An error arises in the solution due to the discretization of the domain. It is vital to minimise the error value after a solution has been achieved. It can be shown that this error can be eliminated when the cell size reduced to zero. As a result of an extra decrease in the cell size, the error will be reduced well enough. However, decreasing the cell size significantly will generate a needlessly huge number of cells, which will result an extra computational effort required and probably produce excessive simulation times.

3.4.3 The FVM mathematical formulations

The divergence theorem can be written as:

$$\iiint_R \frac{\partial u}{\partial x} dR = \oiint_S \boldsymbol{V}.\boldsymbol{n} dS \tag{3.26}$$

Where the vector **V** has one component *u* in the *x* direction. The divergence is the derivative of the vector **V**in 1-D. The purpose of the divergence is to find the finite volume representation of $\frac{\partial u}{\partial x}$ at point *i*. The control volume boundaries are selected as halfway between point *i* and its neighbours.

When approximating the averaged derivative at point i, we get the following form:

$$\frac{\partial u}{\partial x}\Big)_i \cong \frac{u_{i+1/2} - u_{i-1/2}}{\Delta x} \tag{3.27}$$

The values are approximated as:

$$u_{i+1/2} \cong \frac{u_{i+1} + u_i}{2} \tag{3.28}$$

$$u_{i-1/2} \cong \frac{u_{i-1} + u_i}{2} \tag{3.29}$$

Equation (3.27) can be modified for equally spaced points as:

$$\frac{\partial u}{\partial x}\Big)_i \cong \frac{u_{i+1} - u_{i-1}}{2\Delta x} \tag{3.30}$$

In the same manner, the control volume for the second derivative $\frac{\partial^2 u}{\partial x^2}$ can be represented at point *i*. in this case the vector **V** has one component in the x direction which is $\frac{\partial u}{\partial x}$. The divergence theorem can be written as:

$$\iiint_R \frac{\partial^2 u}{\partial x^2} dR = \oiint_S \boldsymbol{V}.\boldsymbol{n} dS \tag{3.31}$$

The conservation form can be expressed as:

$$\iiint_R \rho c \frac{\partial T}{\partial t} dR + \oiint_S \boldsymbol{q}.\boldsymbol{n} dS = 0 \tag{3.32}$$

The first term in the above-mentioned equation represents the time rate of increase in the energy stored in the volume and also known as the integral over the control volume.
The net rate at which energy is conducted out through the surface is represented by the second term in equation (3.32), and also known as the integral over the surface of the volume.
For 2-D heat equation, one can write:

$$\rho c \frac{\partial T}{\partial t} = \frac{\partial}{\partial x}\left(k \frac{\partial T}{\partial x}\right) + \frac{\partial}{\partial y}\left(k \frac{\partial T}{\partial y}\right) = \boldsymbol{\nabla}.(k\boldsymbol{\nabla T}) \tag{3.33}$$

The heat flux vector can be given as:

$$q = -k\nabla T \tag{3.34}$$

Equation (3.33) can be integrated over the control volume to get

$$\iiint_R \left(\rho c \frac{\partial T}{\partial t} + \boldsymbol{\nabla}.\boldsymbol{q}\right) dR = 0 \tag{3.35}$$

For the 2-D problem, equation (3.32) can be rewritten as:

$$\iiint_R \rho c \frac{\partial T}{\partial t} dR + \oiint_S \left(q_x d_y - q_y d_x\right) = 0 \tag{3.36}$$

Where the term $\oiint_S \left(q_x d_y - q_y d_x\right)$ represents the net flow of heat through the surface of the volume and q_x , q_y are the heat flux components in x and y directions respectively.
The time derivative term (on the left) can be calculated by assuming the temperature T at a point (*i, j*), the left term in equation (3.36) can be modified to:

$$\rho c \frac{\left(T_{i,j}^{n+1} - T_{i,j}^{n}\right)}{\Delta t} \Delta x \Delta y$$

The thermophysical properties of the base fluid (which is water in this case) were modelled as temperature dependent as reported by Minkowycz [254] as follows
The density of water is written as:

$$\rho_f = 1000\left(1 - \frac{(T + 15.7914)}{508928.2.\,(T - 205.0204)}(T - 277.1363)^2\right) \tag{3.37}$$

Where T is non-dimensional temperature.
The specific heat of water is expressed as:

$$C_{pf} = 9616.873445 - 48.73648329T + 0.1444662T^2 - 0.000141414T^3 \tag{3.38}$$

The viscosity of water is modelled as:

$$\mu_f = 0.02165 - 0.0001208T + 1.7184 \times 10^{-7}T^2 \quad (3.39)$$

The thermal conductivity of water can be written as:

$$K_f = -1.1245 + 0.009734T - 0.00001315T^2 \quad (3.40)$$

3.5 The CFD Code

The CFD code used in the present study is ANSYS WORKBENCH 15.0 [255]. FLUENT CFD code (which works under the ANSYS WORKBENCH environment) is a common commercial software package. As discussed earlier in the literature survey, it has been used in many numerical applications and provided comprehensible results by solving 3D Navier-Stokes continuity, momentum and energy equations. In this study, FLUENT was selected as a computational tool to perform the numerical Fluid and heat transfer analysis.

Throughout this research, each model was analysed by three main solution steps namely; ANSYS pre-processing, ANSYS solution and ANSYS post-processing.

3.5.1 Geometry Creation

All geometries for the problems investigated in the present research were created by ANSYS Design modeller. The Design modeller is an application that designed to be employed as a geometry editor for all kind aspects of shapes in 2-D and 3-D problems.

The Design modeller is well-known for its flexibility in creating and editing and complex geometry without almost any penalty on the solution accuracy.

The CFD code used in the present study can be simplified in the following flow chart in Figure 1.3.

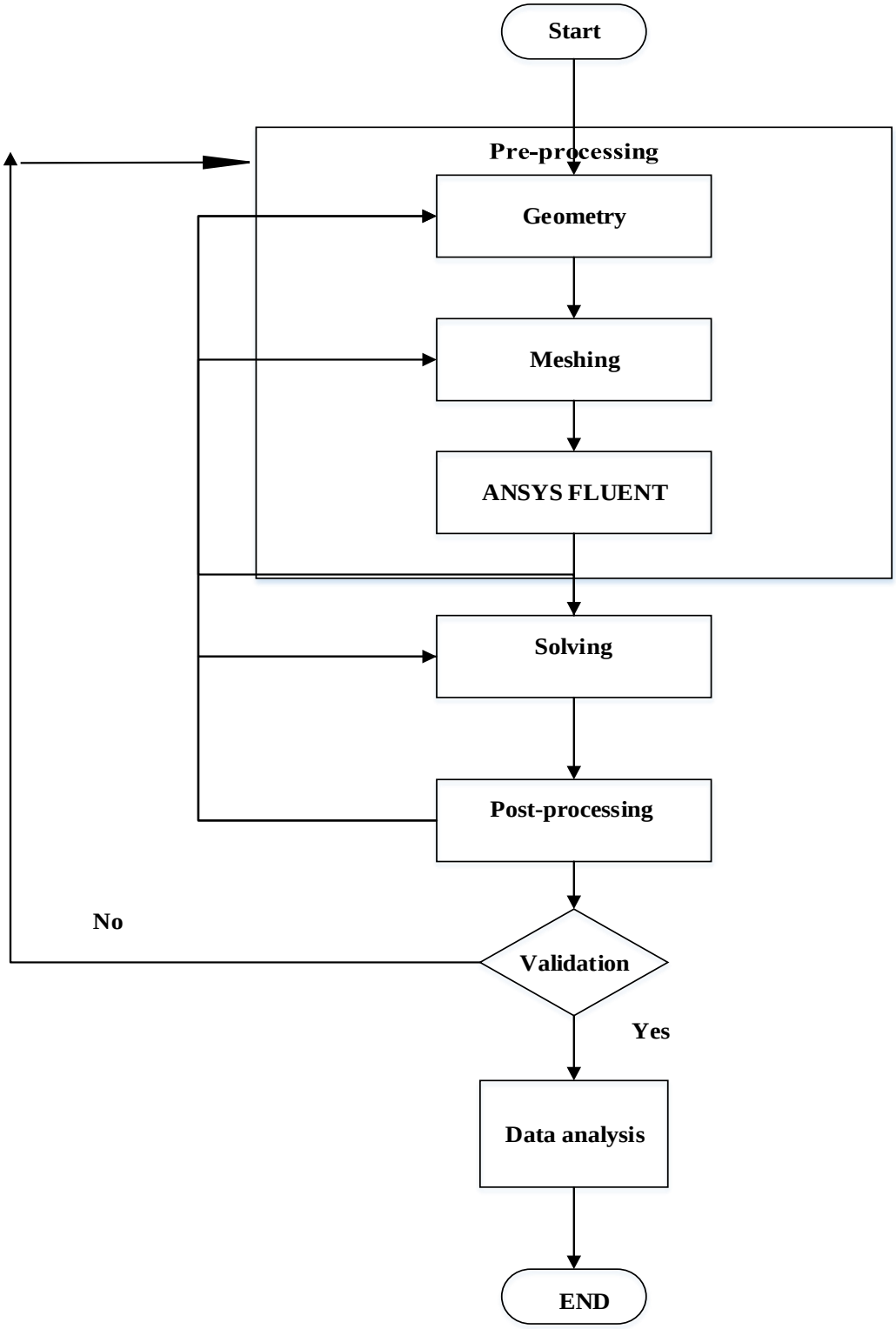

Figure 3-1 CFD flow chart

3.5.2 Mesh Generation

The mesh studied in this research was generated by ANSYS Mesh 15. The aim of this application is to deliver a robust, flexible and easy to use meshing tool. This tool is designed for the discrete representation of the domain geometry. The ANSYS mesher designated the cells or the control volumes on which the flow is solved.

The flow domain is divided into cells or elements. The cells are grouped into boundary zones; the boundary conditions are applied on these boundary zones.

The mesh has a significant impact on the accuracy of the solution as well as the rate of convergence. The CPU time is also directly affected by the quality of the mesh.

The solution should not depend on the mesh, in other word, all solutions obtained in this research was tested by the so-called mesh dependency test. In this test, the number of cells is increased to the level where any extra refinement does not affect the solution accuracy. Full details on this test are described in the following chapters.

3.5.3 Results Verification and Validation

All results obtained for tested cases in this research are validated with data from the literature. At least one or two validation tests have been carried out to ensure the model performs well and the results are reliable. The validations for all different scenarios in the present study are listed in the relevant Chapters.

3.5.4 Calculating surface heat transfer coefficient

To calculate the heat transfer coefficient in the solver FLUENT, the temperature is calculated in two lines in a reference line, the heat flux is calculated and the heat transfer coefficient can then be calculated from the equation:

$$h = \frac{Q}{A\Delta T} \tag{3.41}$$

3.6 Modelling nanoparticles using a user-defined function (UDF)

The user-defined function (UDF), is a function written in C language that can be dynamically loaded with the ANSYS Fluent solver to promote its standard features. For example, you can use a UDF to do the following:

- Modify the boundary conditions, surface and volume reaction rates, material property definitions, source terms in the transport equations, source terms in user defined scalar (UDS) transport equations, diffusivity functions.
- Initialize the solution.
- Execute at the end of the iteration, at the exit from ANSYS Fluent, or upon loading of a compiled or interpreted UDF library.
- Enhance the post-processing process.
- Enhance built-in Fluent models (such as discrete phase model, multiphase mixture model, discrete ordinates radiation model).

UDF is recognised by a (.c) extension (for example, udf.c). The source file can contain a single UDF or multiple UDFs, and even can define multiple source files.

In the present research, the UDF will be used to customise the thermophysical properties of the nanofluids. The full discussion will be presented in Chapter 4, Chapter 5, Chapter 6 and Chapter 7. An example of UDF is presented below; the full UDF codes will be attached to the present research as appendices.

```
#include "udf.h"
#define fi 0.04
#define ro_s 3950

DEFINE_PROPERTY(cell_density, cell, thread)
{
real ro_nf;
real ro_f;
real tt= C_T(cell, thread);
ro_f=-0.00357*tt*tt+1.88*tt+753.2;
ro_nf=((1-fi)*(ro_f))+(fi*(ro_s));
return ro_nf;
}
DEFINE_SPECIFIC_HEAT(cell_specific_heat, T, Tref, h, yi)
{
real cp;
real cp_f;
real cp_s;
real ro_f;
real ro_nf;
ro_f= -0.00357*T*T+1.88*T*T+753.2;
ro_nf=((1-fi)*(ro_f))+(fi*(ro_s));
cp_f= 9616.873445-48.73648329*T+0.1444662*((pow((T) ,2)))-0.000141414*((pow((T)
,3)));
cp_s= 765;
cp=(((1-fi)*(ro_f*(cp_f))+(fi*(ro_s*(cp_s)))))/(ro_nf);
```

```
*h = cp*(T-Tref);
return cp;
}
DEFINE_PROPERTY(thermal_conductivity, cell, thread)
{

real k_eff;
real ks;
real kf;
real tt= C_T(cell, thread);
kf=-1.1245+0.009734*tt-0.000013158*tt*tt;
ks= 35;
k_eff=(kf*(ks+2*kf-2*fi*(kf-ks)))/(ks+2*kf+fi*(kf-ks));

return k_eff;

}
DEFINE_PROPERTY(viscosity, cell, thread)
{

real mu_f;
real mu_eff;
real tt= C_T(cell, thread);
mu_f=(2.414e-5)*(pow((10) ,(247.8/(tt-140))));
mu_eff =(1+5*fi+80*fi*fi*120*fi*fi*fi)*mu_f;

return mu_eff;
```

4 Natural convection with Brownian motion

4.1 Introduction

The natural convection heat transfer arises within an enclosure due to the temperature difference and buoyancy force, one of the limitations of enhancing the heat transfer of the natural convection is the intrinsically low thermal conductivity of the conventional fluids. The investigation of the enhancement of heat transfer due to the use of nanofluids has recently attracted the attention of many researchers [256]-[257]. Putra et al [258] observed the natural convective characteristics of water-based Al_2O_3 nanofluids; they reported that adding nanoparticles to base fluid systematically worsen the natural convective heat transfer with the increase in nanoparticle concentration. However, they did not give an acceptable reason for the decrease of the natural convective heat transfer in a cavity with the increment of the volume fraction of nanoparticles. According to many investigations, the thermal conductivity is found to have the most significant role in the enhancement utilising nanofluids; the effective thermal conductivity was modelled using theoretical and experimental models of nanofluids. Saleh et al. [259] investigated the natural convection in trapezoidal filled with nanofluids. Nasrin et al. [260] investigated the heat transfer performance in a vertical closed enclosure, and it is found that the nanoparticle volume fraction plays a significant role in the temperature field. Ghasemi and Aminossadati [261] carried out a numerical study and investigated on natural convection heat transfer in an inclined enclosure filled with CuO–water nanofluids. Ho et al. [262] investigated experimentally the natural convection heat transfer of Al_2O_3-water based nanofluid. Ghasemi et al. [263] studied the effect of the Brownian motion in a triangular enclosure with natural convection.

The aim of this Chapter is to investigate the heat transfer enhancement in natural convection in a square enclosure with different nanoparticles types and incorporating the Brownian motion.

4.2 Problem Description

A schematic diagram of the physical domain is shown in Fig. 1. The model consists of a square enclosure with length and height equal to L. the upper and bottom walls are thermally insulated, the left wall is heated at temperature T_H and the right wall is maintained at lower temperature T_C. The enclosure is filled with water-based nanofluid, the nanoparticle investigated are Al_2O_3, Cu and TiO_2 with a spherical diameter of 25 nm. The water and the nanoparticle are assumed to be in thermal equilibrium, fluid is considered to be Newtonian, and the flow is laminar. The thermophysical properties are assumed to be temperature dependent and shown in the following section. The thermal properties of Al_2O_3, Cu and TiO2 particles are shown in Table 4.1.

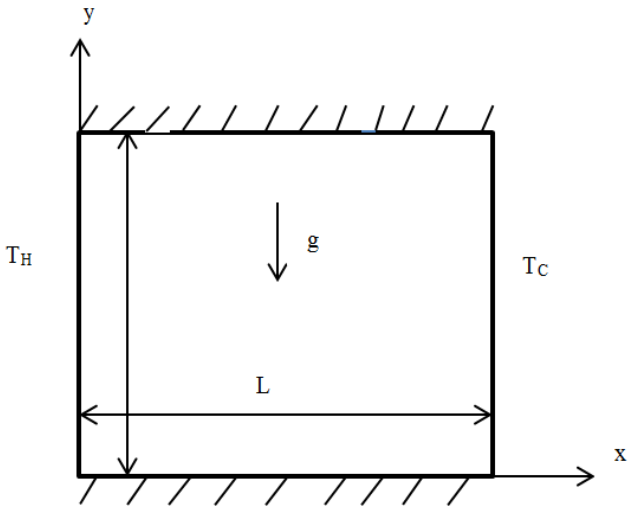

Figure 4-1 Schematic diagram of the physical model

4.3 Governing Equations

The fundamental governing equations are essentially the same as those discussed in section 3.2. However, the treatment of Brownian motion for the slow moving fluid needs special attention. Here the set of governing equations is discussed in this section and a matter of:

The continuity equation and written as:

$$\frac{\partial \rho}{\partial t} + \boldsymbol{\nabla}.(\rho \boldsymbol{V}) = 0 \tag{4.1}$$

The momentum equation as expressed as:

$$\frac{\partial}{\partial t}(\rho \boldsymbol{V}) + \boldsymbol{\nabla}.\rho \boldsymbol{V}\boldsymbol{V} = \boldsymbol{\rho}\mathrm{f} + \boldsymbol{\nabla}.\mathrm{P}_{\boldsymbol{ij}} \tag{4.2}$$

The energy equation

$$\frac{\partial E_t}{\partial t} + \boldsymbol{\nabla}.\mathrm{E_t}\mathbf{V} = \frac{\partial Q}{\partial t} - \boldsymbol{\nabla}.\mathbf{q} + \rho \mathbf{f}.\mathbf{V} + \boldsymbol{\nabla}.(P_{ij}.\mathbf{V}) \tag{4.3}$$

The thermophysical properties of the nanofluid are expressed as follows:

The density is calculated as

$$\rho_{nf} = (1-\phi)\rho_f + \emptyset\rho_s \tag{4.4}$$

The specific heat is written as:

$$C_{pnf} = \frac{(1-\emptyset)\left(\rho C_p\right)_f + \emptyset\left(\rho C_p\right)_s}{\rho_{eff}} \tag{4.5}$$

The thermal conductivity is calculated as Corcione [264]

$$\frac{K_{static}}{K_f} = 1 + 4.4Re^{0.4}Pr^{0.66}\left(\frac{T}{T_{fr}}\right)^{10}\left(\frac{K_s}{k_f}\right)^{0.03}\emptyset^{0.66} \tag{4.6}$$

Where K_f and K_s are the thermal conductivities of the base fluid and particle respectively. T_{fr} is the freezing temperature of the base fluid.

$$K_{eff} = K_{static} + K_{Brownian} \tag{4.7}$$

The Brownian thermal conductivity is calculated in the present work as proposed by [52]:

$$K_{Brownian} = 5 \times 10^4 \beta \emptyset \rho_f C_{pf} \sqrt{\frac{K_b T}{\rho_s d_s}} f(T, \emptyset) \tag{4.8}$$

K_b is the Boltzmann constant=1.3807x10^{-23}

$$\beta = 0.0011(100\emptyset)^{-0.7272} \tag{4.9}$$

Re number is calculated by equation (4.6) as:

$$Re = \frac{2\rho K_b T}{\pi \mu_f^2 d_p} \tag{4.10}$$

Where d_p s the particle diameter; Pr is the Prandtl number for base fluid and written as:

$$Pr = \frac{\mu C_p}{K} \tag{4.11}$$

The temperature function in equation (4.8) is given by:

$$f(T,\emptyset) = (-6.04\emptyset + 0.405)T + (1722.3\emptyset - 134.63) \tag{4.12}$$

The viscosity in this investigation is modelled as proposed by Corcione [61]:

$$\mu_{static} = \frac{\mu_f}{\left(1 - 34.87\left(\frac{d_s}{d_f}\right)^{-0.3}\emptyset^{1.03}\right)} \tag{4.13}$$

The effective viscosity is calculated as:

$$\mu_{eff} = \mu_{static} + \mu_{Brownian} \tag{4.14}$$

Where d_f and d_s are the equivalent diameter of the base fluid and nanoparticle diameter respectively. The equivalent diameter of the base fluid is given by:

$$d_f = 0.1\left(\frac{6M}{N\pi\rho_{fo}}\right)^{\frac{1}{3}} \tag{4.15}$$

M is the molecular mass weight of the base fluid, N is the Avogadro number, ρ_{fo} is the mass density of the base fluid calculated at T=293 K. The Brownian viscosity is calculated as

$$\mu_{Brownian} = 5 \times 10^4 \beta \emptyset \rho_f \sqrt{\frac{KT}{\rho_s d_s}} f(T, \emptyset) \tag{4.16}$$

The convective heat transfer coefficient is given by:

$$h = \frac{Q}{A\Delta T} \tag{4.17}$$

Where Q is the heat flux and ΔT is T_H-T_C

Nu number is written as:

$$Nu = \frac{hL}{K_{eff}} \tag{4.18}$$

Where L is the characteristic length

Rayleigh number is defined as:

$$Ra = \frac{g\beta L^3 \Delta T}{\alpha \nu} \tag{4.19}$$

Where β is the thermal expansion, α is the thermal diffusivity and ν is the kinematic viscosity = $\frac{\mu}{\rho}$, $\alpha = \frac{K}{\rho C_p}$

The thermophysical properties of the nanoparticles are shown in Table (4.1)

Table 4-1 Nanoparticles thermophysical properties

Nanoparticle	Density kg/m^3	Thermal conductivity $w.m^{-1}.k^{-1}$	Specific heat $J.kg^{-1}.k^{-1}$
Al_2O_3	3950	35	765
Cu	8933	400	385
TiO2	4250	8.93	686.2

4.4 Numerical Simulation

4.4.1 Numerical procedure

The CFD code used in this investigation is ANSYS 15 as described in Chapter 3. The nanofluid is modelled as single phase model. Equations (4.4), (4.5), (4.7) and (4.17) have been used to model the density, specific heat, thermal conductivity and viscosity respectively. The laminar model was used in the natural convection simulation. For pressure-velocity coupling, Courant number=200, under relaxation factor was chosen 1 for density, body force and energy. Explicit relaxation factor 0.75 for momentum and pressure, body force weighted for pressure spatial discretization, the time step=0.021 s, number of time steps=17000, the transient formulation is first order implicit, the hot and cold temperature for boundary conditions are 274 K and 273 K respectively

4.4.2 Grid independency study

A grid independence test was carried out in order to ensure that the solution obtained is mesh independent. The simulations were first done for various meshes with different number and arrangement of cells and the average Nu was calculated for each mesh. The five meshes tested with Nu results are shown in Table 4.2. As it can be seen that Nu number for mesh 4 with 10700 cells found remain unchanged, and hence mesh 4 was selected for the present numerical simulations.

Table 4-2 Mesh dependency test results

Mesh	Number of cells	Nu
Mesh 1	6400	1.864
Mesh 2	8400	2.013
Mesh 3	10200	2.212
Mesh 4	10700	2.323
Mesh 5	11200	2.324

4.4.3 Validation of Results

The present CFD code results for the average Nusselt number for various Ra numbers along the hot wall are validated with results available in the literature for natural convection in an enclosure filled with nanofluids as presented in Tables 4.3

Table 4-3 Results Validations

Ra	Nu			
	Cu-water (ϕ=5%)		Al_2O_3-water (ϕ=2%)	
	Present study	Kahveci	Present study	Ho et al
$Ra=10^4$	2.431	2.461	2.323	2.372
$Ra=10^5$	5.072	5.136	4.769	4.700
$Ra=10^6$	9.946	10.04	9.389	9.314

The present code is further validated against the numerical simulation of Khanafer et al. [3] as shown in Fig. 4.2. It can be clearly seen that the obtained CFD results are in excellent agreement with the work published in the literature.

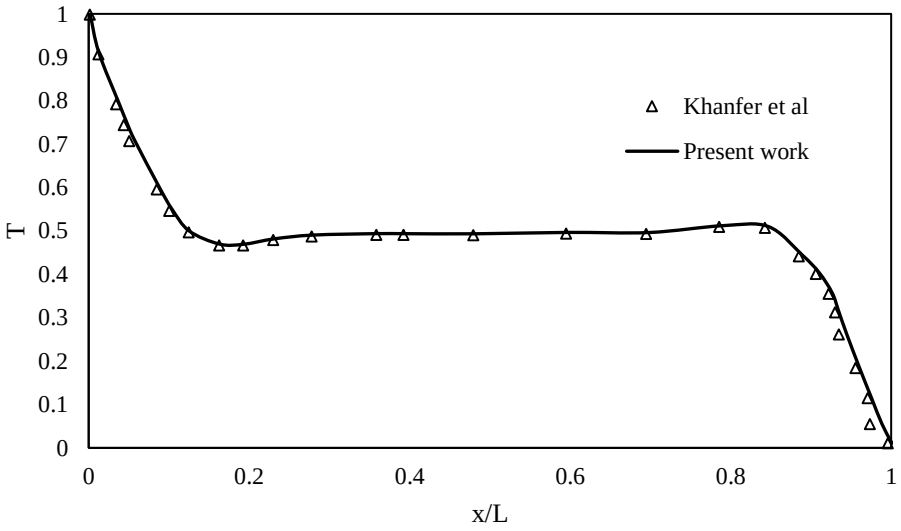

Figure 4-2 Results Validations

4.5 Results and Discussion

The effect of the volume fraction on the heat transfer rate is investigated for a range of Ra numbers. The four Ra number tested were Ra 1×10^4, 1×10^5, 1×10^6 and 1×10^7. The volume fractions tested were between 2% and 6 %. The Nu was calculated based on two scenarios: The first scenario where Brownian motion is taken into account. The second scenario, no Brownian motion effect was considered. The results of these investigations are shown in Fig 4.3. The figure shows the variation of Nu number as Y-axis against the volume fraction ϕ as X axis. The Nu number as shown in the figure decreases as the volume fraction increses for all Ra numbers. This agrees well with many previously work reported in the literature [265]. This decrease is not in favour of heat transfer convection as the increase in Nu number is an indication of the heat transfer enhancement.

This deterioration in the heat transfer is clearer in higher Ra number. This decline is less significant in Ra number 1×10^4 and 1×10^5. However, the increase in Ra number led to an increase in Nu number. As shown in the figure, Ra $1x10e^7$ showed the highest Nu and subsequently the highest heat transfer rate, while Ra $1x10e^4$ had the lowest Nu number.

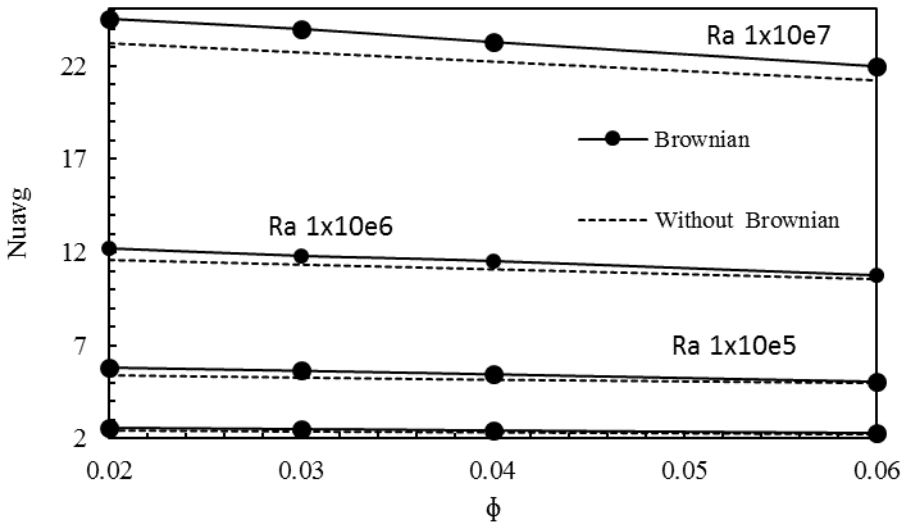

Figure 4-3 Change of Nu vs volume fraction

The effect of the Brownian motion was also investigated further, and the results are shown in the Figure. The Nu number calculated with Brownian motion is higher, this due to the increase in the thermal conductivity as a result of Brownian effect. This is attributed to the increase in thermal conductivity in equation (4.7), as it is well established that the increase in thermal conductivity results in an increase in Nu number. This increase is obvious in Figure 4.3 for Ra numbers, 1×10^6 and 1×10^7, the higher Ra numbers is accompanied with higher velocities in the near wall region, these higher velocities promote the heat transfer rate.

The figure shows that the effect of the volume fraction on Nu number is noticeable at high Ra number than at low Ra number. This is associated with the conduction dominated mechanism for heat transfer at low Rayleigh number compared to convection mechanism at higher Rayleigh number. However, the buoyancy force increases and exceeds the viscous forces, and hence, heat transfer is dominated by convection at high Rayleigh number

In order to have a better understanding of the effect of the nanoparticles on the heat performance, the variation of Nu number with Ra number for various nanoparticles was investigated, and the results are depicted in Figure 4.4. The investigations were done for

three nanofluids with water base fluid and three different nanoparticles Cu, TiO2 and Al_2O_3. The results are shown for constant volume fraction (2%) and aspect ratio 1

The Nu number was found to increase moderately with the increase in Ra number for all the nanoparticles tested, the difference between the nanoparticles is presented in thermophysical properties which are shown in Table 4.1. All the nanofluids showed similar results. However, the heat transfer rate of Al_2O_3-water nanofluid was 2 % higher than TiO_2 where Cuo showed the lowest heat transfer rate of 4% when compared to the Al_2O_3-water nanofluid. It is worth mentioning that all the Ra numbers tested were are in the laminar flow as turbulent flows are in the range > 10^8

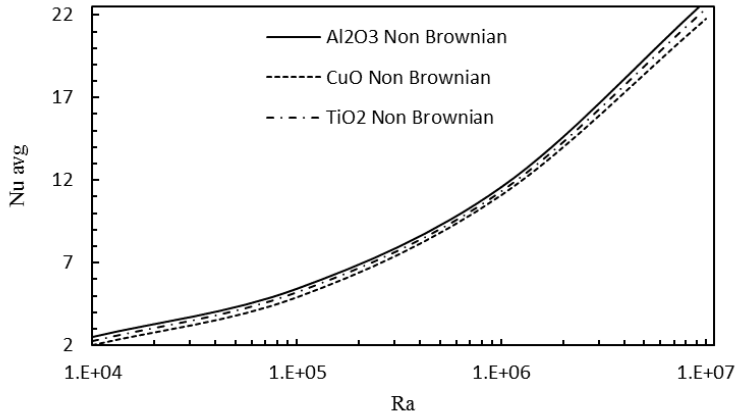

Figure 4-4 Effect of Nanoparticles on the heat transfer rate

The results clearly indicate that the heat transfer is less sensitive to the nanoparticle material compared to the Ra number effect. As shown in Fig 4.3 and 4.4 the increase in Ra number lead to increase in the heat transfer rate. This increase in heat transfer is due to the sensitivity of the boundary layer thickness to the higher Ra number, where for lower Ra numbers, the boundary layer thickness is insensitive to Ra number.

The effect of the Brownian motion along with the nanoparticle type on the heat transfer for a range of Ra numbers is also investigated, and the results are presented in Fig 4.5.

The three different nanoparticles Cu, TiO2 and Al_2O_3 are used with water as nanofluids. The Brownian motion is considered and incorporated through the effective thermal

conductivity of the nanofluids tested. The results highlight that the Nu number is enhanced moderately with the increase in Ra number and this increase is evident for all nanoparticles tested. However, when considering the Brownian motion the variation of Nu is almost the same for all nanofluids at low Ra numbers, where for Ra number higher than 1×10^6.

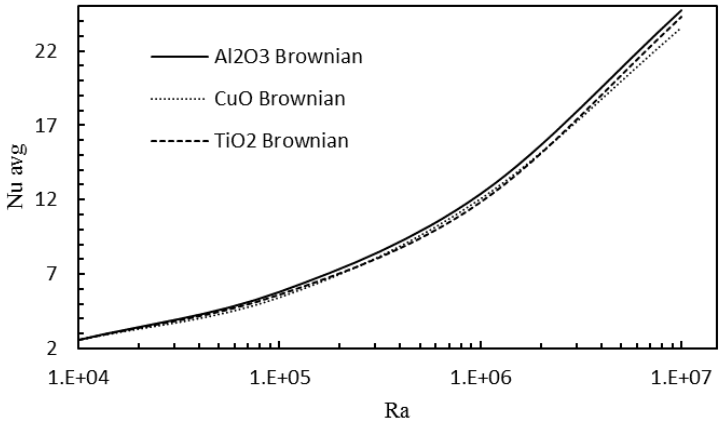

Figure 4-5 The effect of Brownian motion and the nanoparticle on Nu

As seen in Fig 4.5, at Ra number 1×10^7 the change in Nu is up to 4.6% compared to Tio_2 This increase could be attributed to the high thermal conductivity of Al_2O_3 nanoparticle compared to TiO2 (35 to 8.93), and also to the high specific heat of Al_2O_3 compared to Cu (765 to 385). By comparing results in Fig 4.4 and 4.5, it is evident that the Nu number is higher when considering the Brownian motion; however, the heat transfer enhancement is less sensitive to the nanoparticle material when taking Brownian motion effect into account.

In natural convection, the understanding of the velocity change is essential. The flow velocity variation is investigated thoroughly for all Ra numbers. The investigations covered four volume fractions (ϕ 2, 3, 4 and 6%) for Al_2O_3-water nanofluid. The results are shown in Fig 4.6, Fig 4.7, 4.8 and 4.9.

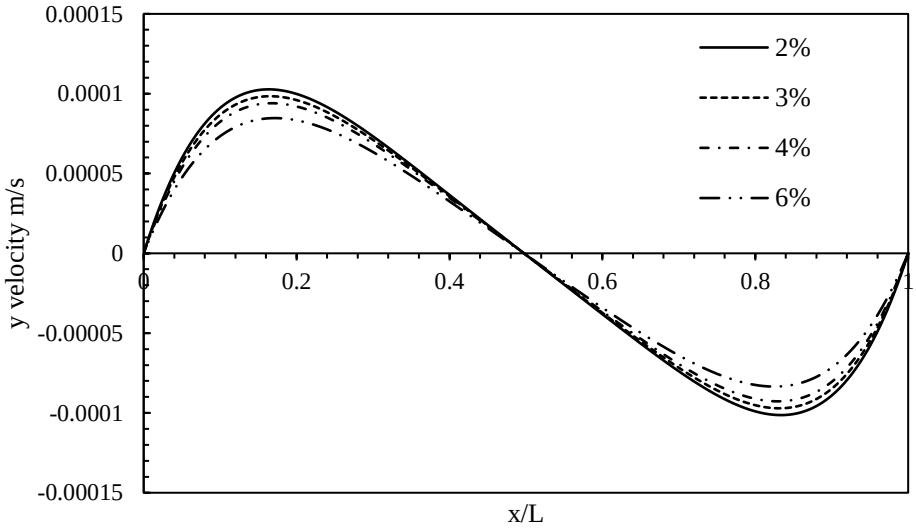

Figure 4-6 Velocity variation for Ra 1x10^4

The distribution of the vertical velocity component with the normalised distance x/L for Ra 1x10^4 is plotted in Fig 4.6. The trend is consistent with the expected behaviour in the natural convection phenomenon in an enclosure. The origin of the graph represents the middle of the hot wall which is located on the left of the square enclosure. The middle of the cold wall located at a normalised distance equal to 1. The flow accelerates from the hot wall to the cold wall due to the buoyancy forces which are the main influence of the natural convection. This buoyancy force is resulted from the temperature difference between the hot and cold walls. The volume fraction 2% showed the highest velocity among the other volume fractions tested. It can be clearly seen that the increase in the volume fraction decreased the vertical velocity component. This finding is explained by the deterioration of the heat transfer due to the increase in volume fraction, as the increase in the velocity in the thermal boundary layer region is accompanied by an increase in the heat transfer rate.

This is further investigated for other Ra number. Fig 4.7 illustrates the variation of the vertical velocity component with the volume fractions 2,3,4,6 % for Ra 1x10^5.

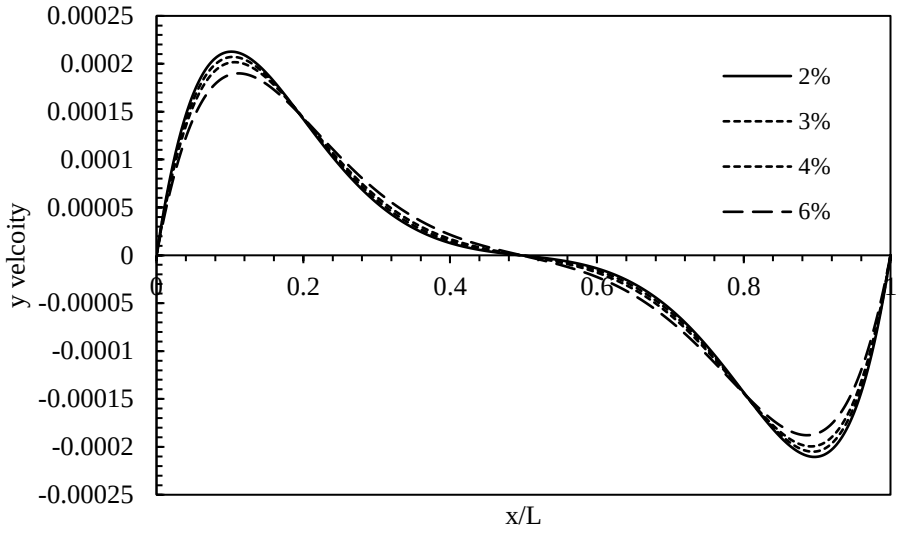

Figure 4-7 Velocity variations with volume fraction for Ra 1x10^5

The velocity profile as depicted in Fig 4.7 is found to decrease with the increase in the volume fraction. This has a negative impact on the heat transfer performance as the effective viscosity is more pronounced in natural convection as seen in equation 4.13 where viscosity is increased with the increase in volume fraction. Despite the increase in thermal conductivity which promotes heat transfer, the augmentation in viscosity is significant, and hence the Nu number is affected by the increase in the viscosity.

A similar finding is reported in Fig 4.8 and 4.9. The vertical velocity component shows a parabolic variation near the isothermal wall due to the buoyant flow inside the enclosure.

It was also found that the vertical velocity profile is insensitive to the nanoparticle material, as the three nanofluids tested showed similar vertical velocity component profile. This is attributed to the influence of the volume fraction on the effective viscosity where the nanoparticle effect has no influence on it

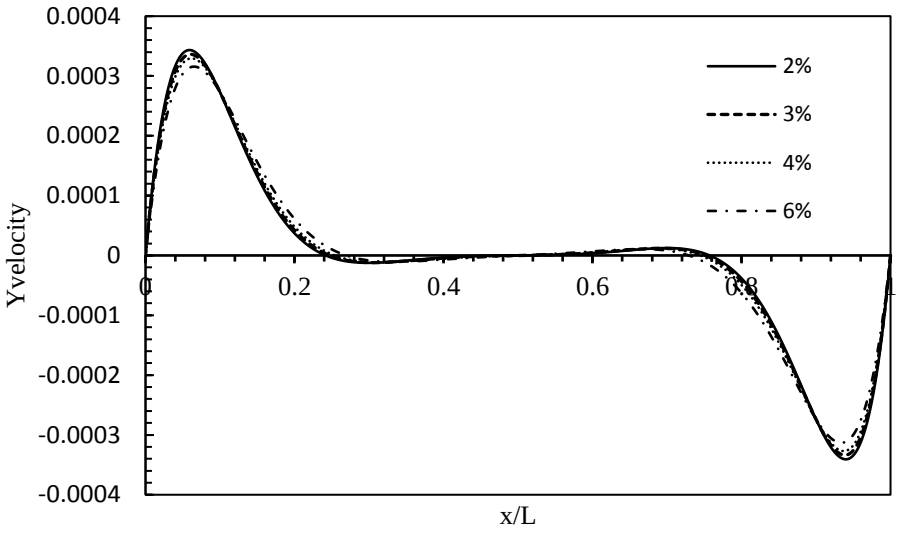

Figure 4-8 Variation of velocity with volume fraction for Ra 1x10^6

Although the higher volume fraction showed less velocity on the hot wall, its corresponding velocity on the cold wall is higher. This change in the flow field is directly affected by the particle suspension; however, the flow velocity in the cavity centre is almost zero. This vertical velocity component profile helps in the understanding of the direction of the flow rotation.

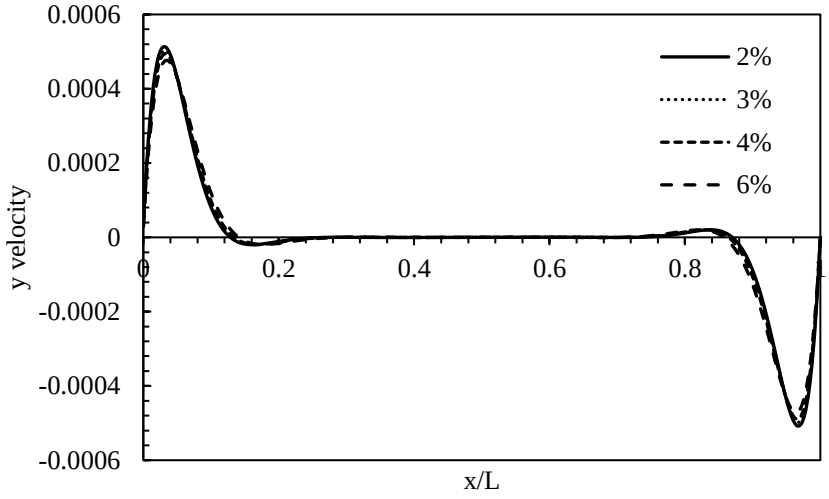

Figure 4-9 Velocity variation with volume fraction for Ra 1x10^7

It should also be noted that as the Ra number increase, the velocity increase. The results in Fig 4.10 show clearly this velocity change. The volume fraction used in the graph shown is 2%, the Brownian effect was considered in this case. From the graph shown, it can be seen that the convection term is more pronounced at higher Ra number in the isotherm walls, i.e. in the near wall region, where the velocity is almost zero in the normalised distance in the enclosure in the range 0.2-0.8

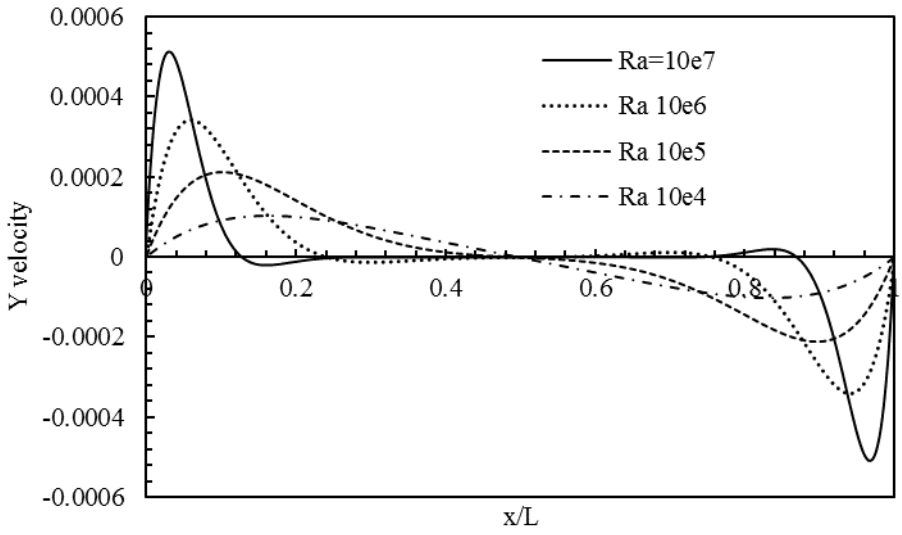

Figure 4-10 The velocity change with Ra number for volume fraction 2%

The change in the velocity for various Ra number tested in the present investigation can lead to a better understanding of the enhancement of the heat transfer due to the Ra growth. As the velocity is more pronounced in the viscous layer in the higher Ra number, so the viscosity increase effect becomes less and subsequently promoting the heat transfer. On the other hand, when the volume fraction effect on the heat transfer rate was negative, the heat transfer rate deteriorated with the increase in the volume fraction as reported by many previous works in the literature. However, with no solid explanations for this influence, some researchers attributed this to the strong effect of the viscosity in the natural convection where viscosity increases with the increase in the volume fraction as can be seen in equation 4.13. This augmentation in viscosity is accompanied by an increase in thermal conductivity due to the increase in volume fraction.

The shear stress effect was also investigated in this study. In order to gain a good understanding, the velocity gradient du/dx and dv/dy are studied for different Ra numbers. The effect of the volume fraction was also investigated. The results are presented in Fig 4.11, 4.12 and 4.13 for Ra= 10^4, 10^6 and 10^7 respectively. The simulations are devoted to Al_2O_3-water nanofluid only as the nanoparticle type effect on the velocity was neglected as discussed earlier.

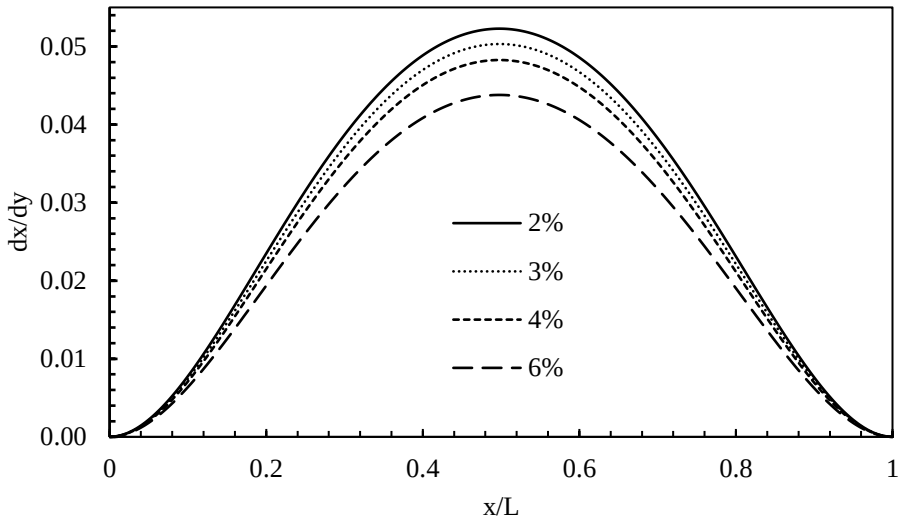

Figure 4-11 The variation of velocity gradient with volume fraction for Ra 1x10^4

The vertical velocity gradient is zero at the hot and cold wall and its maximum value located at the centre of the enclosure. This implies that the axial velocity is zero at the isothermal wall. As noted in the graph, the velocity gradient increases with the decrease in the volume fraction. This is explained by the increase in the viscous effect due to the particle suspension. This variation applies to all Ra number tested. However, it was also noted that the increase in Ra number led to decrease in the axial velocity gradient at constant volume fraction. Another interesting finding, which represents in the variation of the axial velocity gradient at the middle of the enclosure, as the increase in Ra number, the peak of the parabola gradually, goes down as the Ra grows. At Ra 1x10^7 two peak values were noticed for the axial velocity gradient. These two values are explained by the significant change in the velocity in the middle of the enclosure.

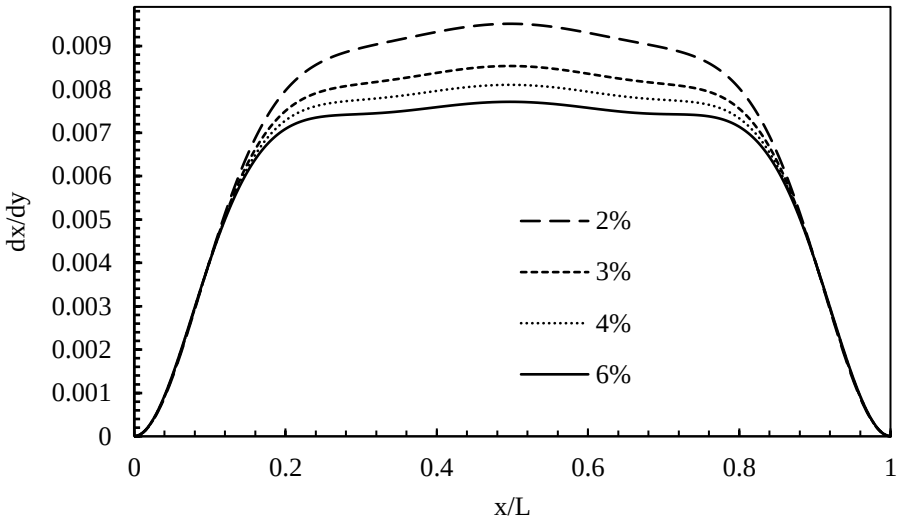

Figure 4-12 The variation of velocity gradient with volume fraction for Ra 1x10^6

It is also worthy to mention that the effect of the volume fraction is more pronounced at the centre of the enclosure, whereas at the isothermal walls, the axial velocity gradient is insensitive to the volume fraction, this is attributed to the sharp fall in the velocity in the near wall region.

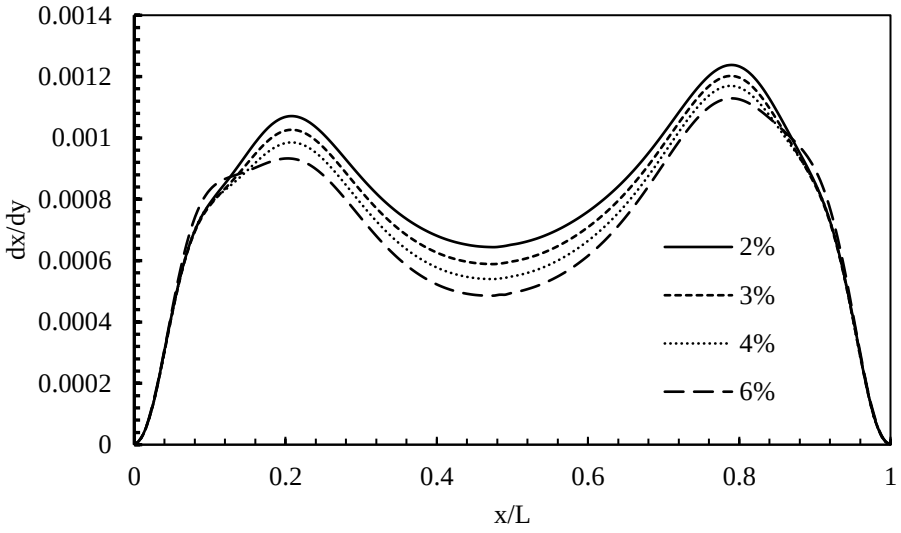

Figure 4-13 The variation of velocity gradient with volume fraction for Ra 1x10^7

The Fig 4.14, 4.15, 4.16 and 4.17 illustrate the change of the velocity gradient for the vertical component at the centre line of the enclosure for a range of volume fractions for Ra $1x10^4$, $1x10^5$, $1x10^4$, $1x10^6$ and $1x10^7$ respectively. It was found that the velocity gradient increase with the increase in the volume fraction at the isotherm walls (the hot and the cold) and decreases with the increase in the volume fraction in the middle of the enclosure and this agrees well with the previous finding where the velocity has a minimum value at this location.

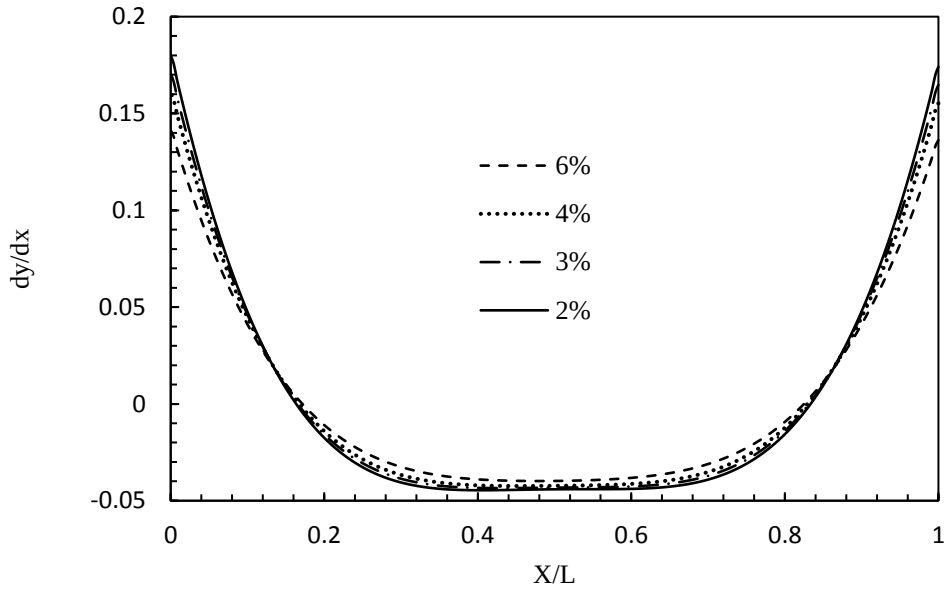

Figure 4-14 The velocity gradient variation with the volume fraction for Ra $1x10^4$

The vertical velocity gradient has the maximum value at the isothermal walls. The explanation for this is when looking the shear stress equation (4.20) as the maximum shear stress is located at the walls. As a result at the thin fluid layer, the velocity gradient and shear stress are large, where out the boundary layer both the shear stress and the velocity gradient are negligible.

$$\tau = \mu \frac{dv}{dx} \tag{4.20}$$

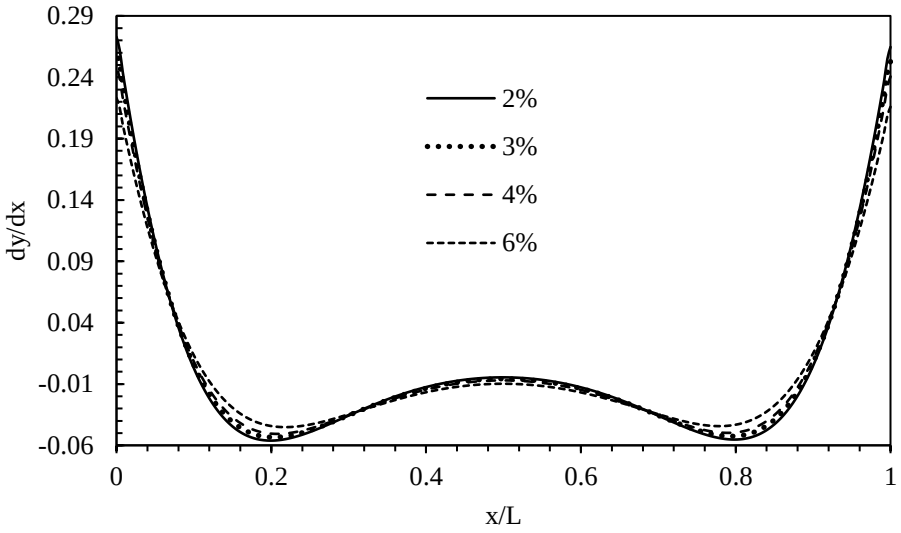

Figure 4-15 The variation of velocity gradient with volume fraction for Ra 1x10^5

As the Ra number rise, the vertical velocity component becomes less sensitive to the volume fraction of the particles. At which case the convection effect is more prominent where the viscous effect is declined considerably.

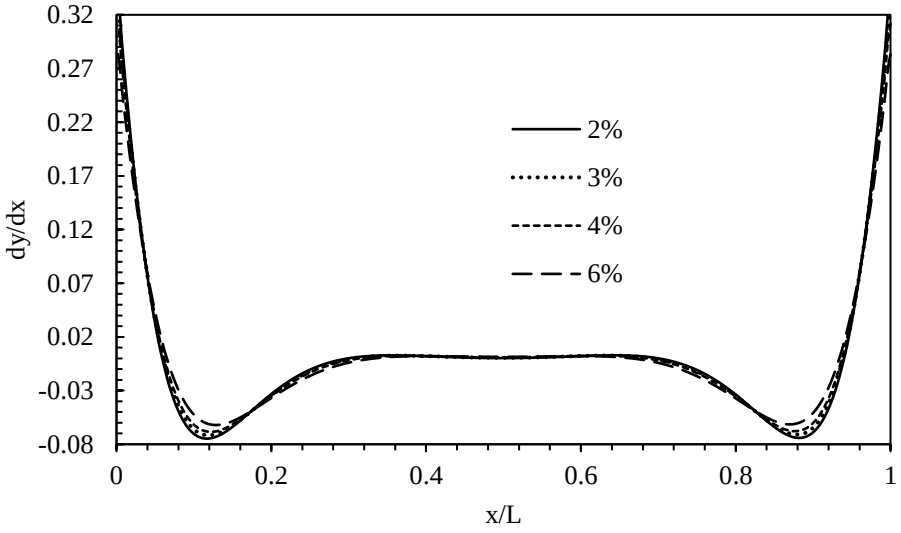

Figure 4-16 The variation of velocity gradient with volume fraction for Ra 1x10^6

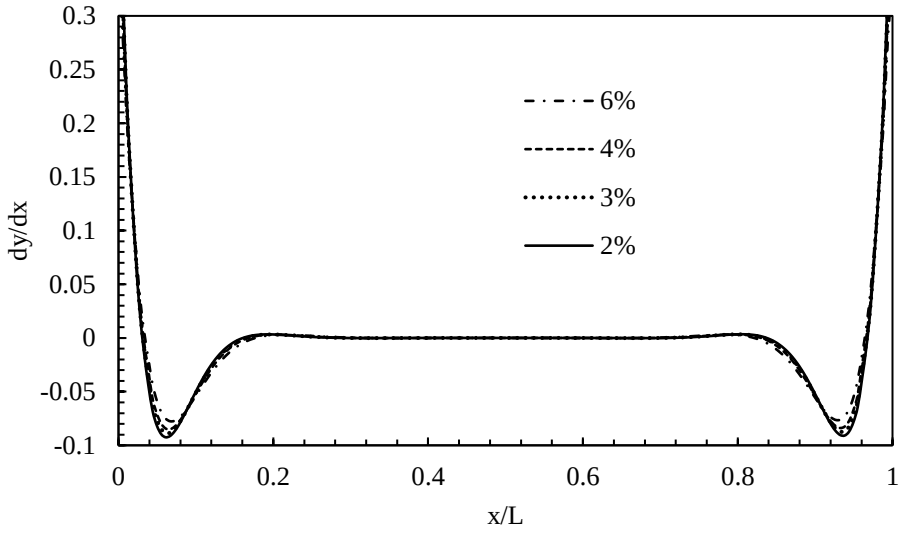

Figure 4-17 The variation of velocity gradient with volume fraction for Ra 1x10^7

In order to understand the relation between the velocity gradient and Ra, Figure 4.18 is introduced, and it depicts the variation of different Ra numbers at the middle line of the enclosure with velocity gradient at a constant volume fraction (ϕ=2%). It is clearly seen that as Ra increases the velocity gradient increases in the near wall region where shear stress has the maximum value. However, when the boundary layer increases, the velocity gradient decreases with the increase in the Ra number particularly in the normalised distance ranges (0.056-0.196) and (0.844-0.984). This opposite effect is attributed to the declining viscous effect with the growth in the boundary layer thickness.

With increasing distance from the isothermal walls, the viscosity effect vanishes gradually to the location where the velocity gradient increases again with an increase in the Ra Number. This augmentation is explained by the dominant of the buoyant forces over the viscous forces in the circulation inside the enclosure.

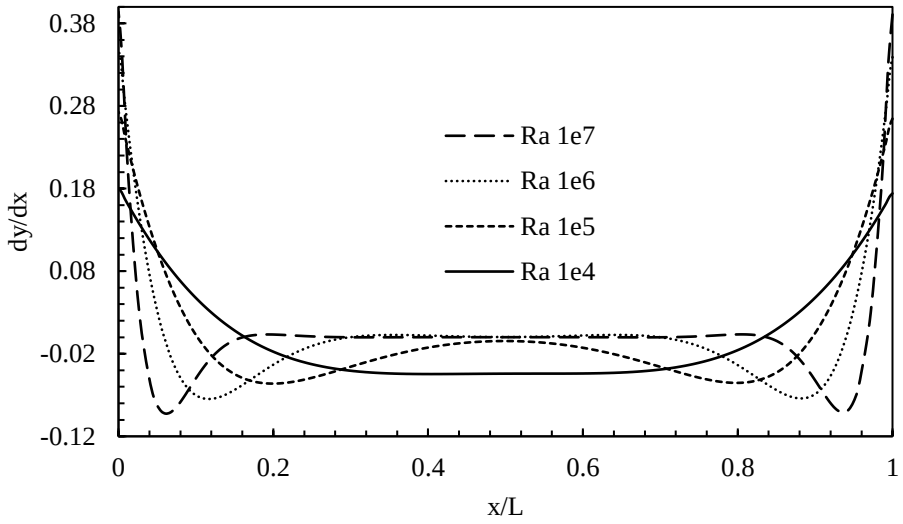

Figure 4-18 Ra number change with velocity gradient

In order to give a better understanding of the flow circulation and how the heat performance affected, the contours of the temperature are presented for Ra 1x104, 1x105, 1x106 and 1x107 in Fig 4.19 a, b, c and d respectively. It is well established that due to the buoyancy effect and the gravitational force the flow moves in the enclosure from the hot wall to the cold wall

a b

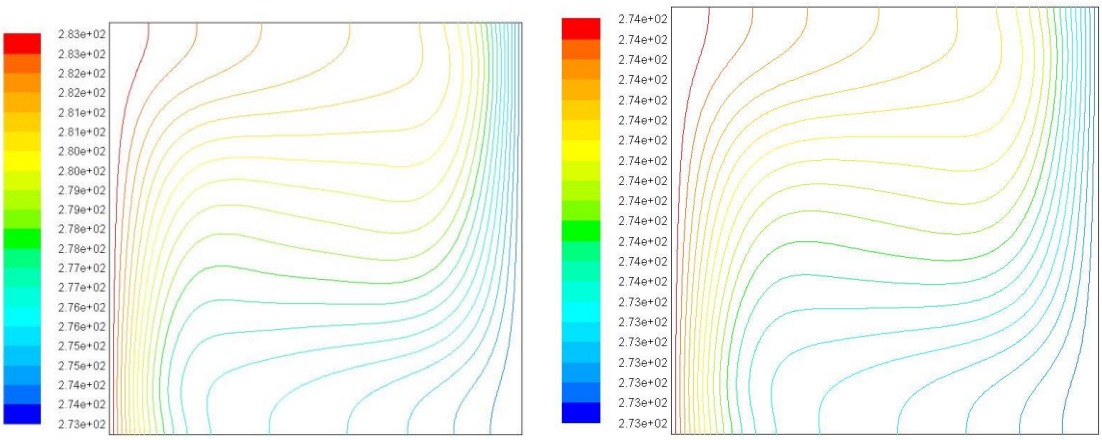

This motion can be visibly seen in the different Ra contours. However, it was noted that with the increase in Ra number, the flow advances steeply which proved by the increase in

the vertical velocity component as discussed earlier. This rise is accompanied by a heat transfer enhancement.

c d

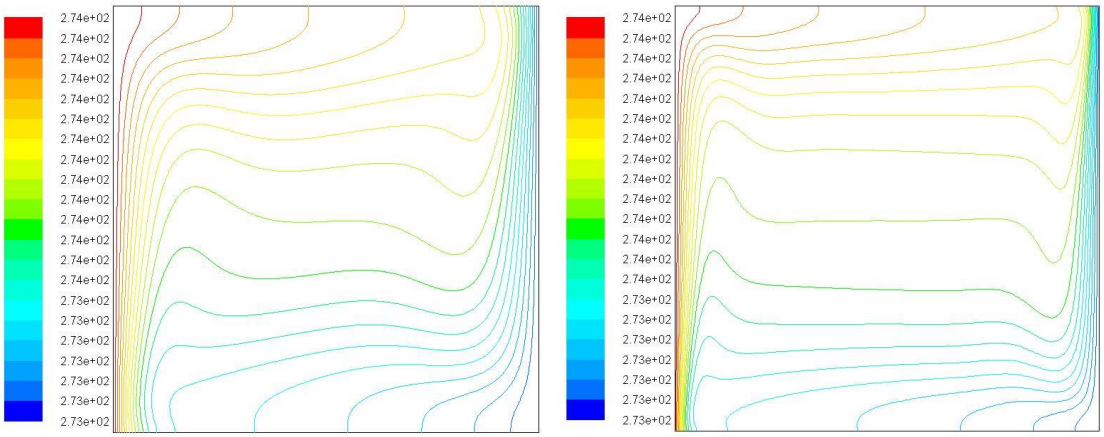

Figure 4-19 Isotherm contours for a) Ra1x10^4. b) Ra 1x10^5. c) Ra 1x10^6. d) Ra 1x10^7

5 Investigation of Backward-Facing Step flows

5.1 Introduction

Separations in flows due to the adverse pressure gradient can be encountered in many industrial applications such as electronic cooling, the passage of turbine blades, combustors, and many heat exchangers. Backward-facing step is one of the basic configurations where flow separation takes place. The separation and reattachment of the flow play a vital role in determining the flow structure and affect the heat transfer performance. A significant amount of high fluid energy occurs in the reattachment region of these devices. There are several ways to enhance heat transfer, one of which is to employ nanofluids. There were many studies focused on the flow separation and reattachment in the past decades, and the BFS geometry received much attention.

Armaly et al [266] conducted an experimental work on the backward-facing step to investigate the reattachment length. Biswas et al [267] investigated Laminar backward-facing step flow for a broad range of Reynolds numbers and expansion ratios in two and three-dimensional simulations. The finding was that this primary recirculation length increases non-linearly with increasing expansion ratio. Abu-Nada [268] presented a numerical study of entropy generation over a 2D backward facing step with various expansion ratios, and the results showed that total entropy generation increases with the increase in Reynolds number. Mohammed et al [269] studied the effect of Nanofluids on heat transfer performance in Backward-facing step and found that there is a primary recirculation region for all nanofluids behind the step, and the skin friction coefficient is sensitive to the recirculation flows.

Pour and Nassab [270] has numerically studied the convective flow of nanofluids with different volume fractions over a BFS under bleeding condition. They found that the recirculation zones and the reattachment length increase as bleed coefficient increases. Tougan et al [271] investigated numerically the effect of volume fraction on the heat transfer rate using nanofluid, the results showed that the recirculation flow as created by the backward-facing step enhanced heat transfer. Erturk [272] presented a comprehensive numerical work of the 2-D steady incompressible backward-facing step flow; the results

showed that for an inlet channel that is at least five step heights long is required for accuracy, he also found that the size of the recirculating regions grows almost linearly as the Reynolds number increases. Lan et al [273] reported the effect of aspect ratio and the Re number on the flow and the heat transfer performance and showed that the effect of Re on the flow reattachment is minimal in the range of the parameters.

Mohammed et al [274] carried out a Numerical simulation of laminar and turbulent mixed convection heat transfers of nanofluid flow over backward facing step placed in a horizontal duct having a baffle. They reported that Nusselt number and velocity distribution increased gradually by increasing the Reynolds number of laminar and turbulent flows. Kherbeet et al [275] and et al Kherbeet [276] studied numerically and experimentally the heat transfer characteristic of nanofluid laminar flow over the microscale backward facing step. They also carried out a simulation of three-dimensional laminar mixed convection to study the effect of step height on the flow and heat transfer characteristics. They found that the Nusselt number increase with increases volume fraction. Water–SiO2 nanofluid showed a higher enhancement of the average Nusselt number in comparing to the pure water and water– Al_2O_3 nanofluid. The finding was also revealed that the increasing of the step height increases the reattachment length and thus Nusselt number, the size of the sidewall reverse flow region. Chen et al [277] presented simulations of three-dimensional laminar forced convection adjacent to inclined backward-facing step in a rectangular duct, the finding was that the friction coefficient inside the primary recirculation region increases with the increase of the step inclination angle.

The aim of the present Chapter is to investigate the effect of the inclination of the facing step on the heat transfer performance in the backward facing step geometry using Al_2O_3/water as a working fluid and investigate the entropy generation as well as the heat and fluid flow performance.

5.2 Problem Description

The problem geometry considered in this work is shown in Figure 1. A channel with a backward facing step with length L1 is considered filled with Al_2O_3 -water nanofluid. The fluid is assumed to be Newtonian, incompressible and there is no slip velocity between the particle and the base fluid. The thermal properties of the nanoparticle are presented in Table 1. The step size of backward facing step is h and channel height H and expansion ratio ER= (H/h) equal to 1.5 and the bottom length is L2. At the inlet of the channel, a velocity U and a uniform temperature (T = 300 K) are imposed. The downstream length starting from the edge of the step to the exit of the channel is 20H to ensure that the exit boundary does not affect the flow in the zone of interest. The downstream bottom surface of the backward facing step is maintained at T=274 K, while the other walls of the channel are assumed to be adiabatic, the outlet is assumed to be outlet boundary condition. These boundary conditions have been previously used by other authors and the present work is an extension in line with those works. L1=1400 mm, L2=800 mm and h=20 mm. Five inclination angles were tested, 90º, 97º, 105º, 115º and 125º, the schematic diagram for these angles are shown in Fig 5.4

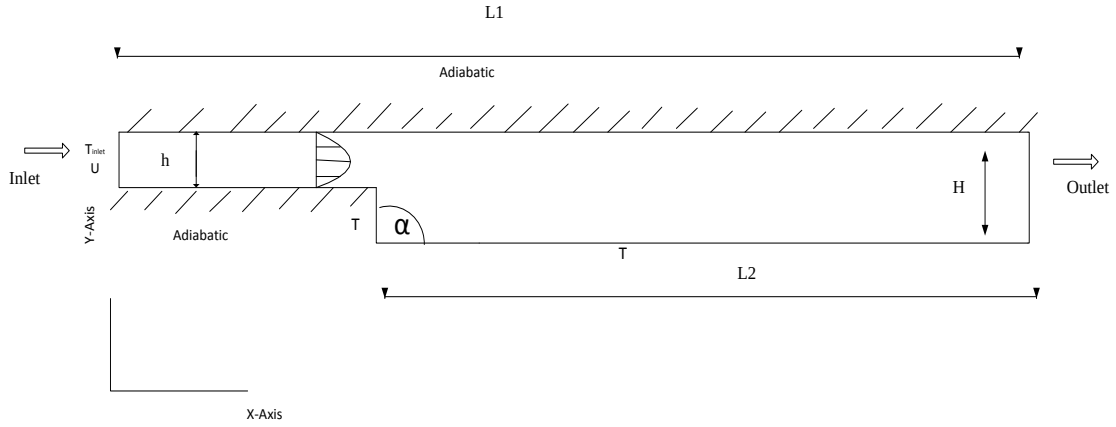

Figure 5-1 Problem Geometry

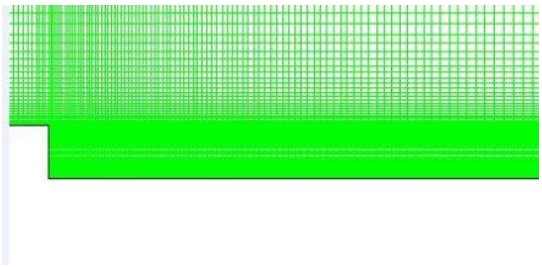

Figure 5-2 Mesh

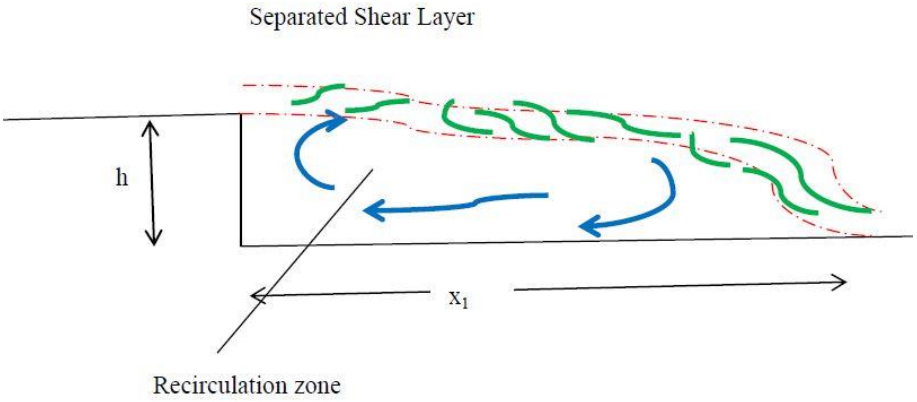

Figure 5-3 Detailed flow feature of the backward facing flow Kostas et al.[278]

Table 5-1 Thermophysical properties of the nanoparticle

Physical property	Al_2O_3
Heat Capacity(J/kg K)	765
Density (kg/m^3)	3950
Thermal conductivity (W/m K)	35

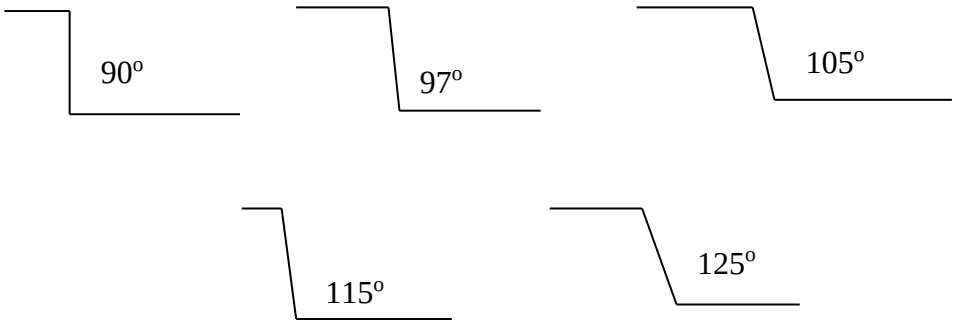

Figure 5-4 inclination angles of the step face

5.3 Governing Equations

The governing equations are continuity, momentum and energy equation. The mathematical formulations for these equations were presented in Chapter 3. The thermophysical properties can be modelled using the following mathematical formulations: The density is written as

$$\rho_{nf} = (1-\phi)\rho_f + \emptyset\rho_s \tag{5.1}$$

The specific heat is modelled as:

$$C_{pnf} = \frac{(1-\emptyset)\left(\rho C_p\right)_f + \emptyset\left(\rho C_p\right)_s}{\rho_{eff}} \tag{5.2}$$

The thermal conductivity is modelled as

$$\frac{K_{eff}}{K_f} = 1 + 4.4Re^{0.4}Pr^{0.66}\left(\frac{T}{T_{fr}}\right)^{10}\left(\frac{K_s}{k_f}\right)^{0.03}\emptyset^{0.66} \tag{5.3}$$

Where Re, Pr and T_{fr} are defined as introduced in Chapter 4.

The viscosity is written as:

$$\mu_{eff} = \frac{\mu_f}{\left(1 - 34.87\left(\frac{d_s}{d_f}\right)^{-0.3} \emptyset^{1.03}\right)} \tag{5.4}$$

Where d_s and d_f are defined as in Chapter four

Nu number is calculated as:

$$Nu = \frac{hL}{K_{eff}} \tag{5.5}$$

Where L is the characteristic length and in this investigation is taken as H.

The pressure coefficient is written as:

$$C_p = \frac{\left(P - P_{ref}\right)}{\frac{1}{2}\rho_{ref} v_{ref}^2} \tag{5.6}$$

The entropy generation is modelled by Mahian et at[279] as

$$S_{gen}^{///} = \frac{K}{T^2}\left[\left(\frac{\partial T}{\partial x}\right)^2 + \left(\frac{\partial T}{\partial y}\right)^2\right] + \frac{\mu}{T}\left\{2\left[\left(\frac{\partial v_x}{\partial x}\right)^2 + \left(\frac{\partial v_y}{\partial y}\right)^2\right] + \left(\frac{\partial v_x}{\partial x} + \frac{\partial v_y}{\partial y}\right)^2\right\} \tag{5.7}$$

The entropy generation number is given by Abu-Nada [280]

$$N_s = \frac{S_{gen}^{///} H^2}{K} \tag{5.8}$$

5.4 Numerical Simulation

In the present study the conservation equation (1 to 3) are solved numerically using finite volume scheme, the Ansys Workbench 15 package was used. A source code written in C

language was developed to introduce the thermophysical properties of the nanofluids as a user defined function. The geometry was created using ANSYS Workbench design modeller; the mesh created using ANSYS Mesh. Explicit relaxation factor 0.75 for momentum and pressure, standard for pressure spatial discretization. A convergence criterion of $1X10^{-6}$ is chosen for continuity, x-velocity and y-velocity

5.4.1 Grid independency study

Extensive grid test was carried out. The aim of the test is to ensure that the solution is gird independent. Refined mesh is adopted in the near wall region as shown in Figure 2. A grid independence test was performed for five meshes as shown in Table 5.2. The Nu number results were used as a parameter to check the solution independency. The number of cells was increased until the change in Nu is less than 0.1%, so any further refinement in the mesh does not affect the accuracy of the solution. As seen in Table 5.2 the final calculations were obtained for mesh 4 with 240000 cells.

Table 5-2 Mesh independency test

Mesh	Number of cells	Nu
Mesh 1	160800	6.869
Mesh 2	192600	8.082
Mesh 3	210500	8.4192
Mesh 4	**240000**	**8.591**
Mesh 5	260400	8.598

5.4.2 CODE validation

This simulation is validated by comparing the present results with experimental results from Armaly [266] for Re=800 and other numerical published results as shown in Table 5.3. The present results have good agreement with the other numerical results. However, most of the numerical published works, including the present work, underestimate the

reattachment length. According to Armaly et al the flow at Re = 800 has three-dimensional features, this feature arises when using Reynolds number equal to or greater than 400. The reason for the underestimation of x_1 (as shown in Fig 5.3) and x_2 which are the reattachment lengths for first and second circulation zones respectively is the assumption of the two-dimensional assumption by all numerical published data.

Table 5-3 Results validation at Re=800

Authors	Work Type	x_1	x_2
Armaly	Experimental	7.2	5.3
Vradis	Numerical	6.13	4.95
Pepper	Numerical	5.88	4.75
Abu-Nada	Numerical	6.03	4.81
Present simulation	Numerical	5.94	4.79

Further simulation comparison between present results and available data in the literature, for Re number variation with $x_1$is given in Figure 5.5. The figure shows excellent agreement between the present predictions and the experiment of Armaly et al.

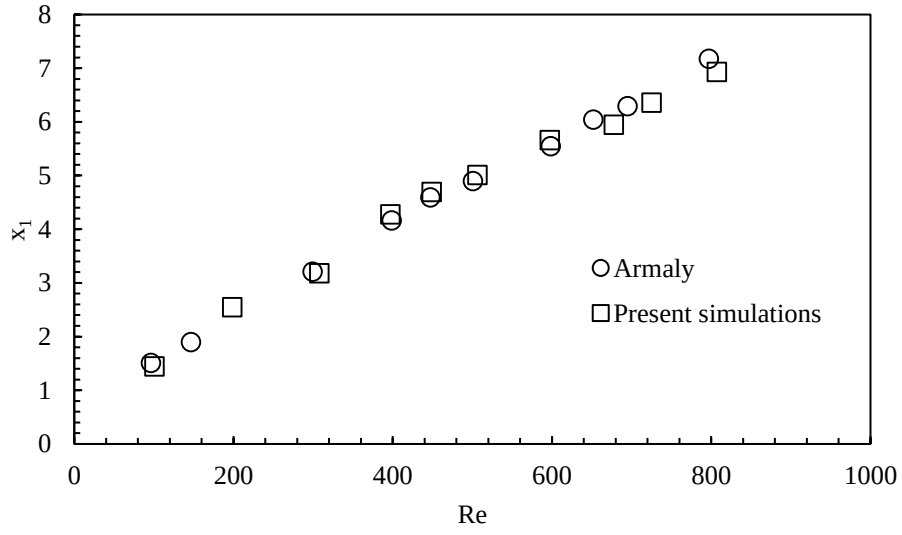

Figure 5-5 Variation of the reattachment length with Re number for present and previous data

5.5 Results and Discussion

The Backward-facing step problem with nanofluid is studied in the present Chapter, and the results are shown and discussed in this section.

5.5.1 The inclination angle effect

The effect of inclination angle α of the face step using nanofluid is investigated numerically, and the results of this effect is shown in Figure 5.6, four angles of facing step are investigated 90º, 97.5º, 105º, 115º and 125º and four expansion ratios (ER) were tested, 1.66, 2, 2.5 and 3.

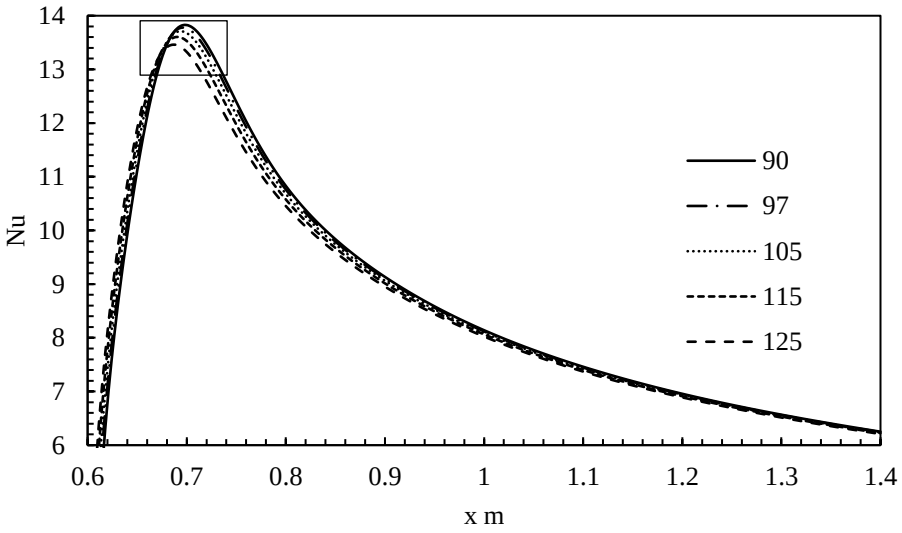

Figure 5-6 Nu variation with inclination angle

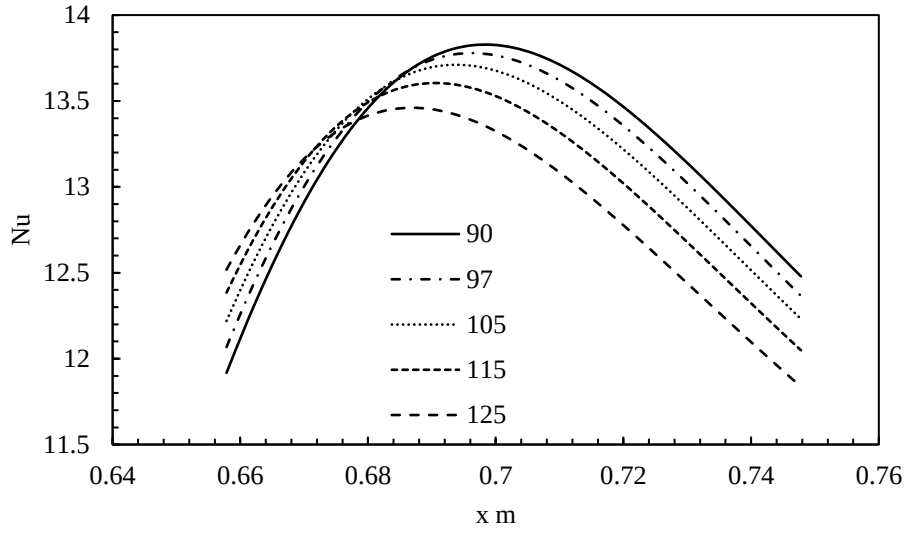

Figure 5-7 zoom of Nu variation with inclination angles for ER1.66

The increase in angle of the face step was found to slightly decrease Nu number. The heat transfer rate for ER 1.66 as shown in Fig 5.6 and the area zoomed in Fig 5.7 shows that the angle 90 was 3% higher than that of 125^{o}. It can be clearly seen that on the bottom wall, Nu number has the peak value at the reattachment point. Nu number is located in the separation region where the generated recirculation flows. The flow in the separating region is impinged on the stepped wall and it is responsible for developing the peak values in Nusselt number. As a result of adding the nanoparticle to the base fluid, the thermal conductivity is increased. This is the reason for the reduction in temperature gradient at the bottom wall, developing in thermal conductivity is accompanied by increase in thermal diffusivity. The surface Nu number on the bottom wall increases linearly from zero (just before the bottom wall) up to a peak value which lies in the circulation zone(coincide with the point of reattachment), after this point the value of Nu decreases due to the temperature gradient decreases. It is clearly seen that the five angles 90^{o}, 97.5^{o}, 105^{o}, 115^{o} and 125^{o} have an almost identical variation of Nu number in the bottom wall except in the circulation zone, where 90^{o} angle of face step has the higher Nu number. The reason for this is the change of the shear stress in this area as well as the thermal diffusivity is pronounced in the circulation zone.

The change of the thermal conductivity, although very small for the different inclination angles is also studied and the results are depicted in Fig 5.8

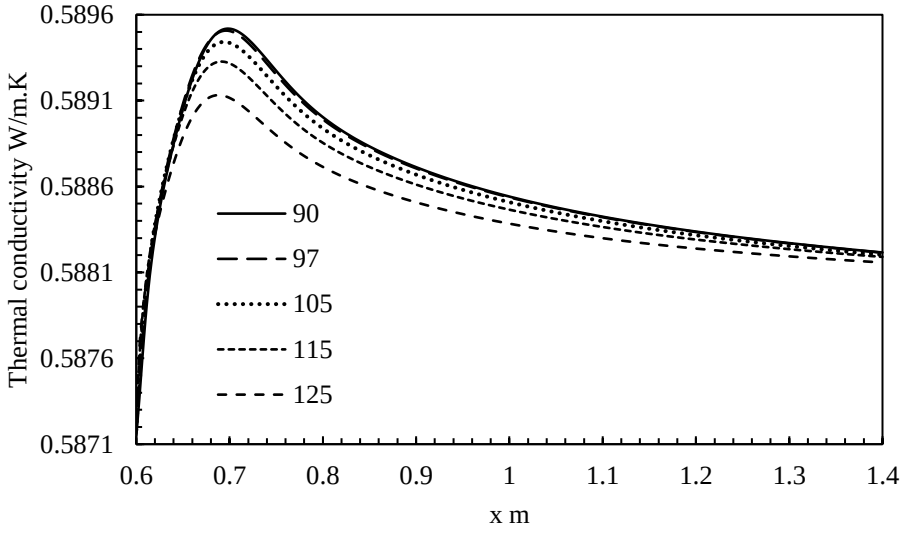

Figure 5-8 Thermal conductivity change with inclination angle for ER 1.66

The graph shows the variation of the thermal conductivity along the lower wall for five inclination angles for ER 1.66 at volume fraction 2%. However the increase in thermal conductivity was no more than 0.06%, it is obvious that the enhancement in the heat transfer is not attributed only to the increase in thermal conductivity but also to the recirculation zone where the peak Nu number is recorded. It was also noticed that the thermal conductivity for the various inclination angles is not identical out of the circulation zone. The reason for this is due to the change of the temperature as the thermal conductivity is a function of temperature.

In order to understand the thermal change in the backward facing step, the variation of the thermal conductivity on a vertical line in the circulation zone is calculated and the results are presented in Fig 5.9.

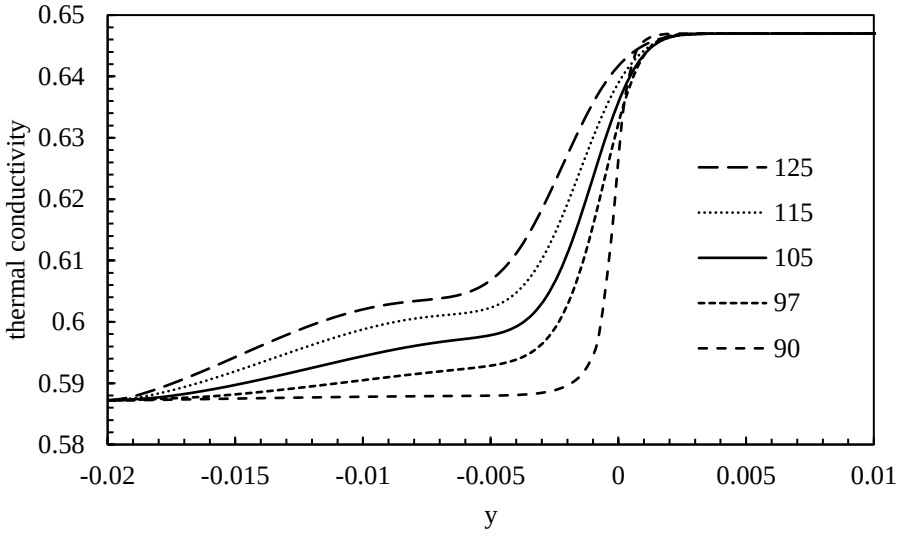

Figure 5-9 Thermal conductivity variation with inclination angle at recirculation zone for ER 1.66

The thermal conductivity is increased with the increase in the inclination angle as can be seen from the graph. The effect of temperature on the thermal conductivity is more pronounced in the circulation zone; however no change in the thermal conductivity for all inclination angles outside of the circulation zone. The opposite effect of the inclination angle on the thermal conductivity on the lower wall and the vertical line in the circulation zone is attributed to the temperature dependent property of all thermophysical properties. As the temperature in the circulation zone is higher when increasing the inclination angle, the explanation for this is due to the increase in temperature gradient with the increase of the inclination angle.

To have a better understanding of the heat transfer enhancement in the backward facing problem, the Prandtl number is investigated on the lower wall for a range of inclination angles. The results are shown in Fig.5.10.

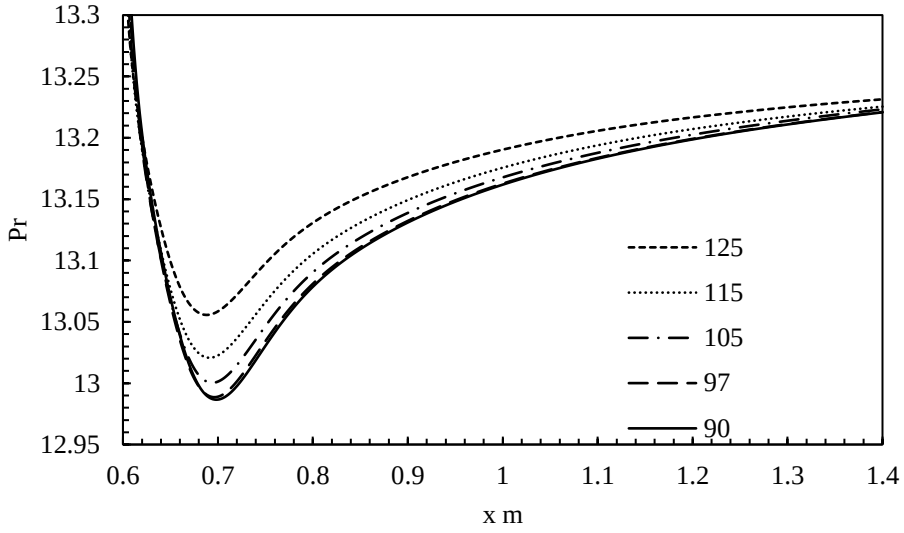

Figure 5-10 Variation of Pr number with inclination angle on the lower wall for ER 1.66

The Pr number increases with the increase in the inclination angle; the minimum value is located in the circulation zone. However, all the inclination angle showed similar Pr numbers away from the circulation zone. The maximum change in the value of the various angles was found in the circulation zone; the highest Pr corresponds to 125^{o}, the minimum value of Pr number in the circulation zone is explained by the decrease in the viscosity which is located in the circulation zone. It is worth mentioning that all parameters used to calculate Pr number (viscosity, specific heat and thermal conductivity) are thermal dependent which is directly affected by temperature.

For more clarification, the viscosity change with the inclination angle is calculated, and the results are depicted in Fig 5.11. The graph illustrates the viscosity for ER 1.66 on a vertical line in the separation zone.

The Figure shows clearly that the viscosity is identical for all angles above the separation zone. However, the variation is obvious in the circulation are where angle 90 showed the highest value of viscosity.

The viscosity for angle 90 is constant in the circulation zone and drop sharply just above the zone; this is due to the sharp inclination of the 90^{o} face step. As the angle increases the viscosity is no longer constant in the circulation zone, however just above the circulation zone, all inclination angles have the same viscosity.

The viscosity results presented here are for volume fraction 2%. The viscosity is a function in the volume fraction, so as the volume fraction increases, the viscosity increase and this can be found from equation (5.4), this means that the water viscosity has lower value than results shown in Fig.5.11

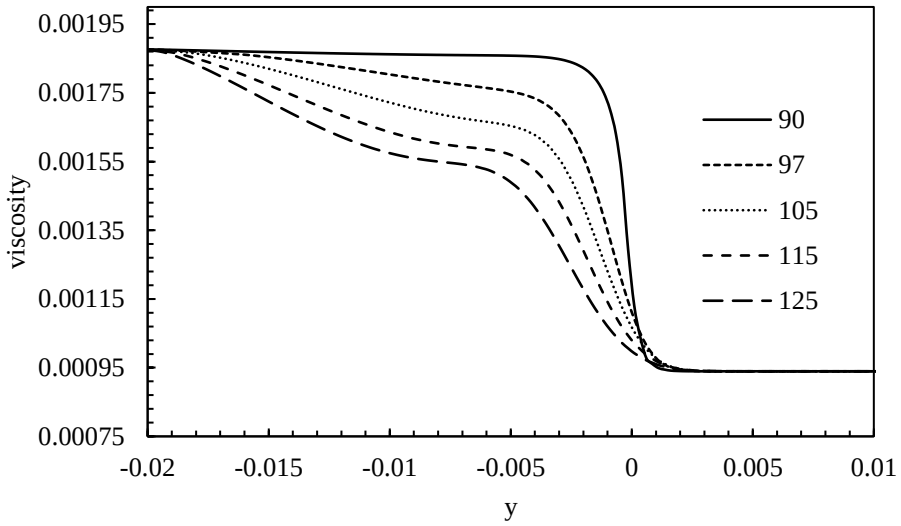

Figure 5-11 Viscosity change with inclination angle at circulation zone for ER 1.66

5.5.2 The effect of velocity gradient

The flow characteristics in the backward-facing geometry were also investigated, and the results for the velocity and velocity gradients are presented. The vertical velocity component for ER 1.66 at volume fraction 2% and Re number 100 is shown in Fig 5.12.

The graph demonstrates the variation of the vertical velocity along a vertical line in the separation region. The X-axis represents the vertical line from the lower wall to the top wall in the recirculation zone, while the y-axis represents the vertical component of the velocity.

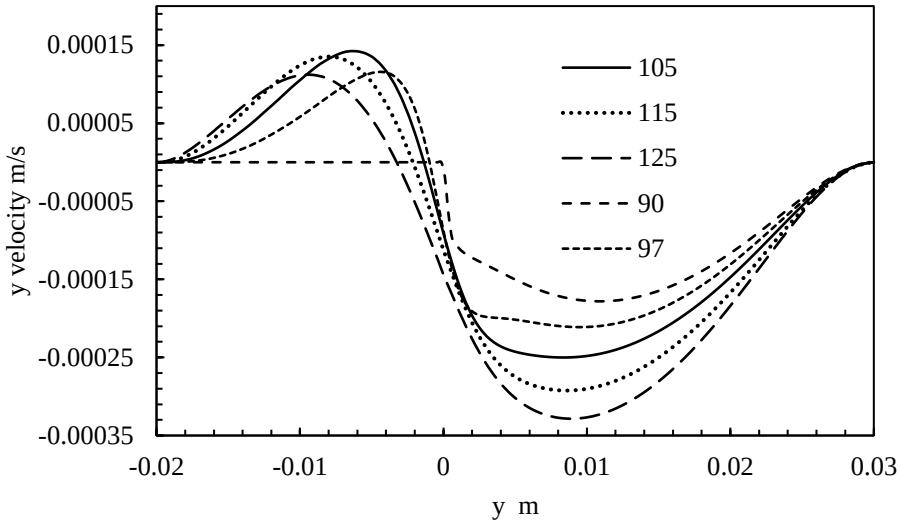

Figure 5-12 Vertical velocity component variation with inclination angle for ER 1.66

The vertical velocity component increases with the increase in inclination angle in the circulation zone. However, this trend is opposite just above the recirculation zone. This contrary behaviour is attributed to the change of the shear stress in the recirculation zone. The vertical velocity is zero at the walls, and as a result, the vertical velocity for angle 90^o is zero at the vertical line. The velocity drops above the circulation zone which is anticipated in this region. The vertical velocity gradient was also investigated, and the results for this case is illustrated in Fig 5.13

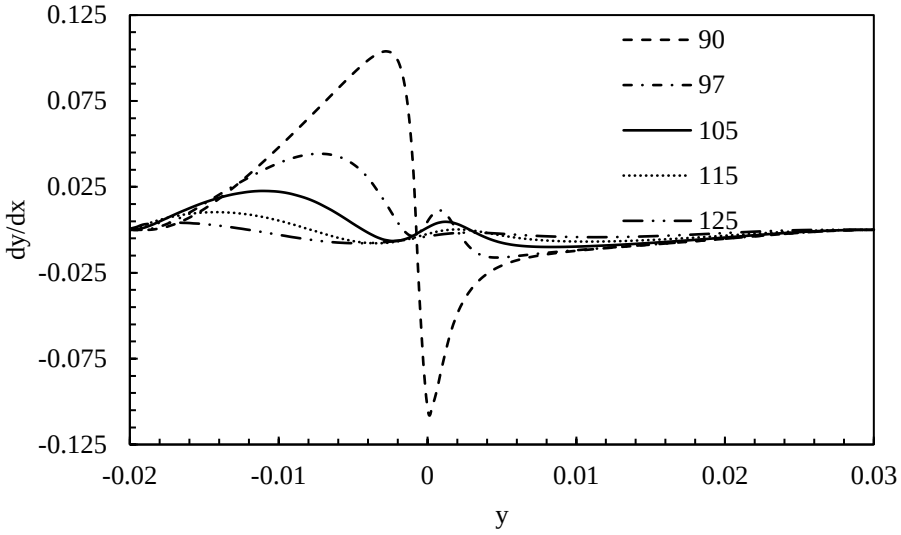

Figure 5-13 Vertical velocity gradient change with inclination angle for ER 1.66

From Fig 5.13 it can be seen that the vertical velocity gradient has insignificant change above the circulation region for all inclination angles as there is no change in the x direction. On the other hand, in the circulation zone, the velocity gradient increased with the decrease in the inclination angle, this is due to the sharp drop in the step wall where the circulation takes effect. For 125^{o} angle, the velocity gradient was almost constant as the velocity component does not change in the x-axis, this velocity vector direction will be discussed later.

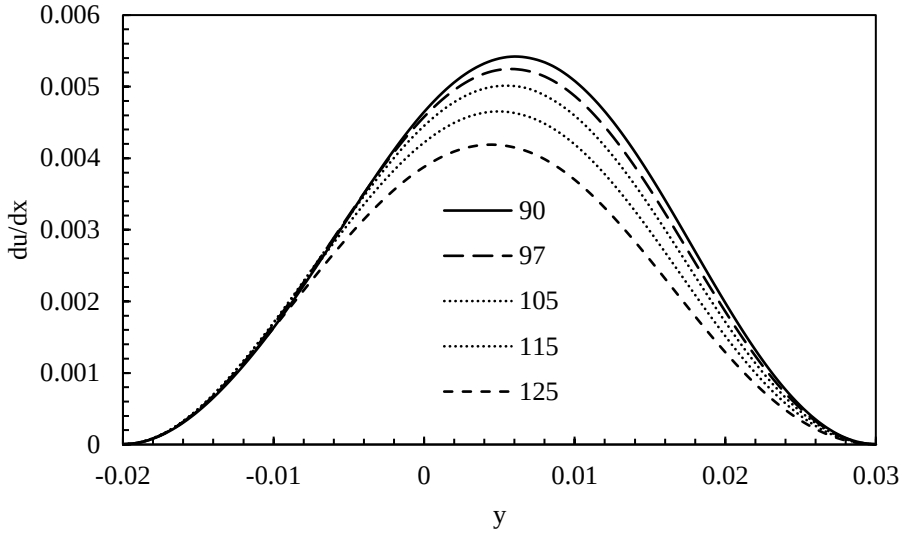

Figure 5-14 vertical velocity gradient change with inclination angle out of the circulation ER 1.66

The vertical velocity component gradient was also studied after the circulation zone(x=0.7m) and the results are shown in Fig 5.14. It is evident that the velocity gradient increases with the decrease in the inclination angle, this increase is more noticeable in the middle of the channel. However, as the flow approaches the wall the velocity gradient is insensitive to the inclination angle, and this is due to the decrease in the velocity near the wall. It was also noticed that the velocity gradient is symmetric so there is no change whether it is above or inside the circulation zone and this is only valid at x=0.7, as there was a change at x=0.6 as seen previously in Fig 5.13.

The axial velocity gradient was investigated for different locations; Fig 5.15 presents the axial velocity gradient for ER 1.66 at the lower wall for five inclination angles. The results are shown for Re 100 and volume fraction 2%.

The graph shows that the velocity gradient increases with the decrease in the inclination angle in the circulation gradient (0.6-0.67) where at the end of the circulation region the axial velocity gradient tends to zero. However after the circulation zone, the variation is opposite till x=0.8, the velocity gradient onward is insensitive to the inclination angle.

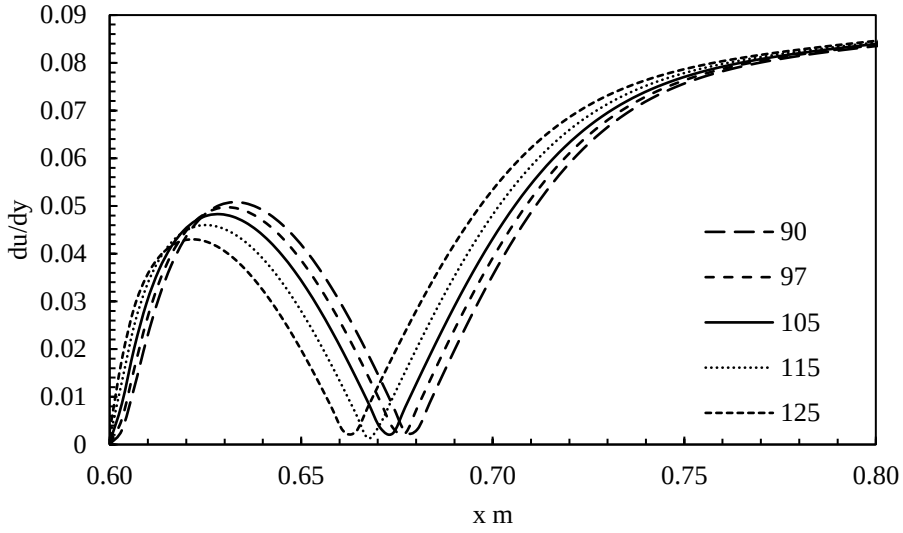

Figure 5-15 Axial velocity gradient variation with inclination angles for ER 1.66

On the lower wall

The axial velocity gradient on the vertical line in the circulation zone is studied, and the results are shown in Fig 5.16. The velocity gradient increases gradually with the increase in the inclination angle in the separation zone. The peak value is at 90^{o} in the middle of the channel, the variation of the velocity gradient above the circulation zone slightly change with the inclination angle. This contradicts effect is attributed to the change in the x-shear stress in the recirculation zone, as it is well known that the shear stress is proportional to the axial velocity gradient.

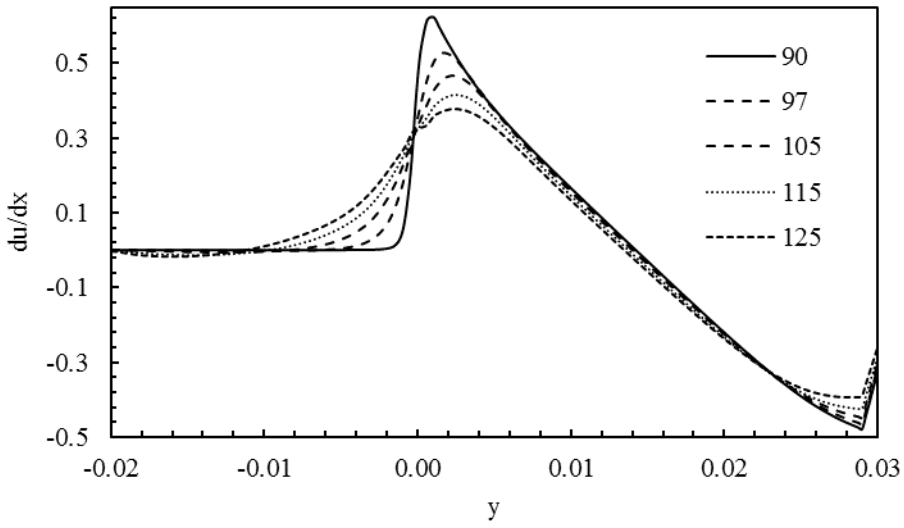

Figure 5-16 Axial velocity gradient variation with inclination angle for ER 1.66 at vertical line x=0.6

The same parameter was studied at x=0.7 m (just after the recirculation region) at the same operating conditions. The results are introduced in Fig 5.17 for the five inclination angles tested. It can be seen from the graph that the velocity gradient is insensitive to the angles tested.

As the velocity gradient does not change with the inclination angles, so it is anticipated that the shear stress is no longer affected by any changes in these angles.

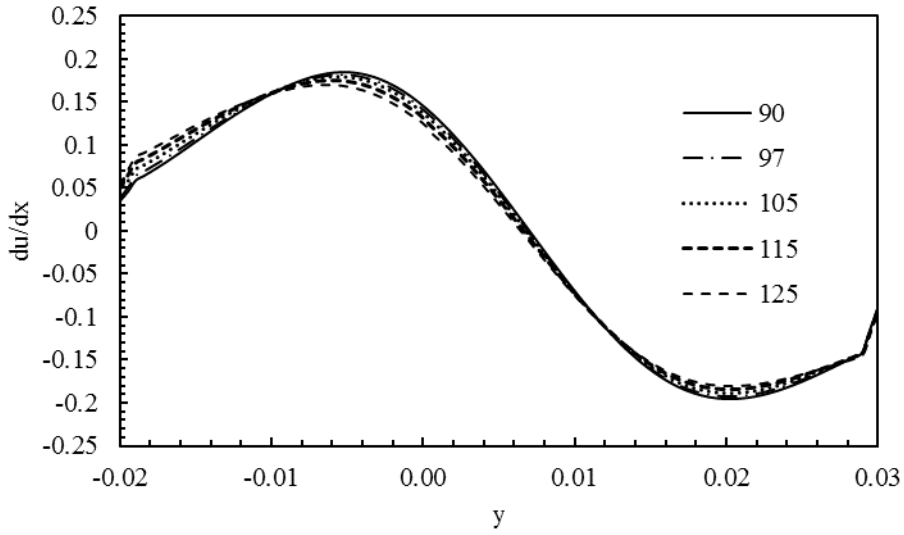

Figure 5-17 Axial velocity gradient variation with inclination angle for ER 1.66 at vertical line x=0.7

5.5.3 Effect of Expansion ratio (ER)

The ER 2.5 was also investigated for the various inclination angles. The thermal conductivity on the lower wall is calculated and the results are shown in Fig 5.18

The thermal conductivity starts from a minimum value at the corner where the temperature value is minimum in the flow domain and the value increases sharply as the temperature grows in the circulation zone. It is noticed from the graph that the thermal conductivity increases with the decrease in the inclination angle; this variation is pronounced in the circulation region. This effect becomes insignificant as the flow advances towards the channel exit.

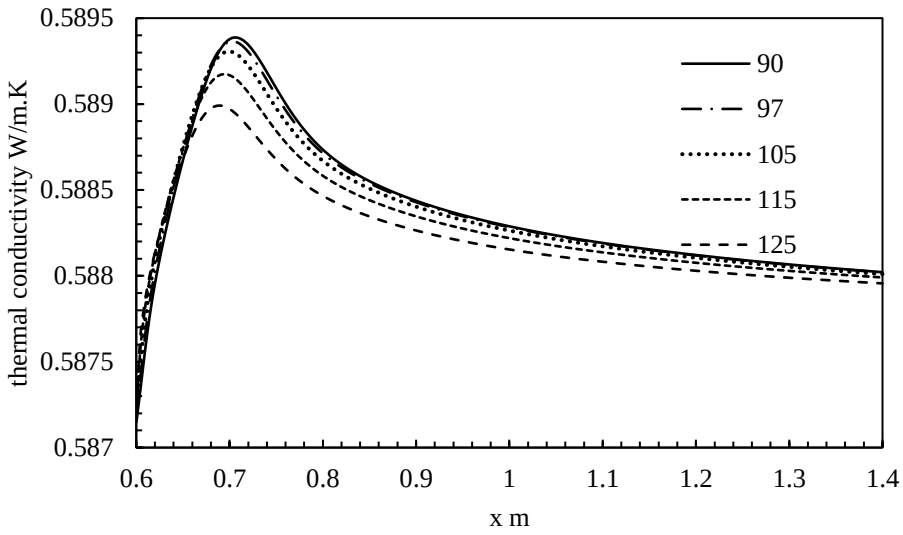

Figure 5-18 The thermal conductivity on the lower wall ER 2.5

These changes support the finding discussed earlier regarding the enhancement of heat transfer with the decrease in the inclination angle. As can be seen, the angle 90^o showed the highest thermal conductivity among the angles tested in the present study.

The results shown in this Fig for ER 2.5 is similar to that in Fig 5.8 for ER 1.66. As a result to that, it can be concluded that the expansion ratio has on effect of the variation of

the thermal conductivity with the inclination angles on the lower wall. The same results were found for ER 2 and ER 3

The viscosity change with the inclination angle for ER 2.5 at the lower wall was studied, and the results are portrayed in Fig 5.19. The graph shows that the viscosity drops sharply at the start of the circulation zone and has its minimum value where the viscosity is very sensitive to the inclination angle as the temperature of the flow varies according to the configuration of the step face, and hence the temperature is higher at that point.

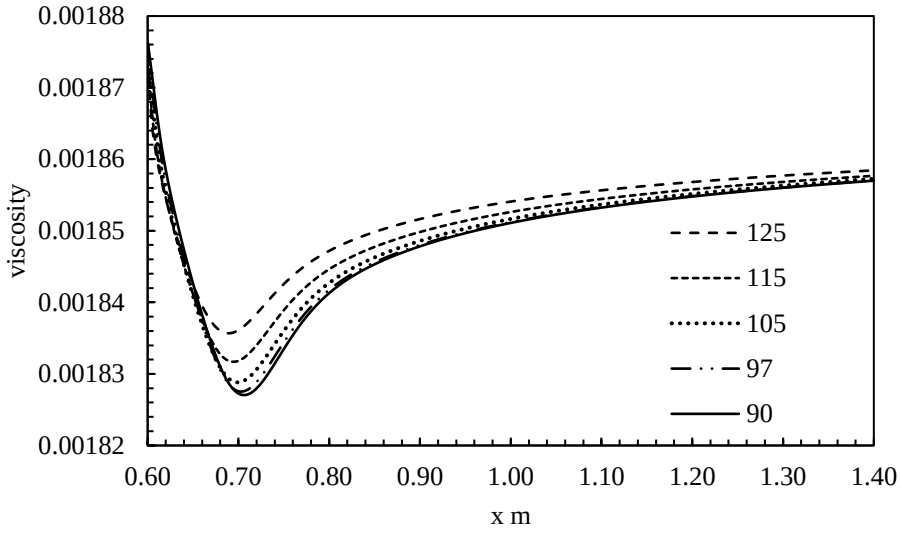

Figure 5-19 Viscosity variation with inclination angle for ER 2.5

This variation for ER 2.5 is similar to that for ER1.66, 2 and 3. These results prove that the expansion ratio has an insignificant effect on the change of the inclination angle with the viscosity.

A similar trend was observed on the Prandtl number calculations for ER 2.5 as seen in Fig 5.20 for Re 100 and volume fraction 2%. Pr number increases with the increase in the inclination angle in the circulation zone, however at the beginning of the circulation zone, the Pr number is insensitive to the inclination angle, and after the circulation region, the effect of the inclination angle becomes less pronounced compared to that in the circulation area. By comparing the Pr number results in Fig 5.10 and Fig 5.20, it is evident that the

variation of the inclination angle with the Pr number is independent of the expansion ratio. This behaviour is similar to the viscosity variation discussed earlier.

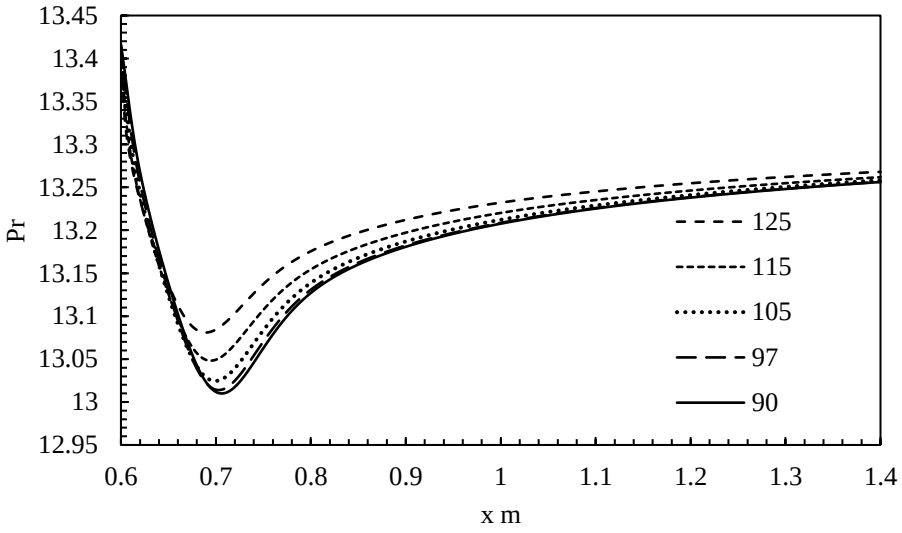

Figure 5-20 Pr number change with inclination angle for ER 2.5

The pressure coefficient and its variation with the inclination angle is studied for ER 2.5, and the results are illustrated in Fig 5.21. The graph shows the variation along the lower wall of the backward-facing step problem. It can be seen that the inclination angle affects the pressure coefficient only in the separation zone as expected from the slope of the step face for various inclination angles. The pressure coefficient increases with the increase in the inclination angles. However, this increase applies only to the circulation region as all tested angles after the recirculation region showed the same pressure coefficient.

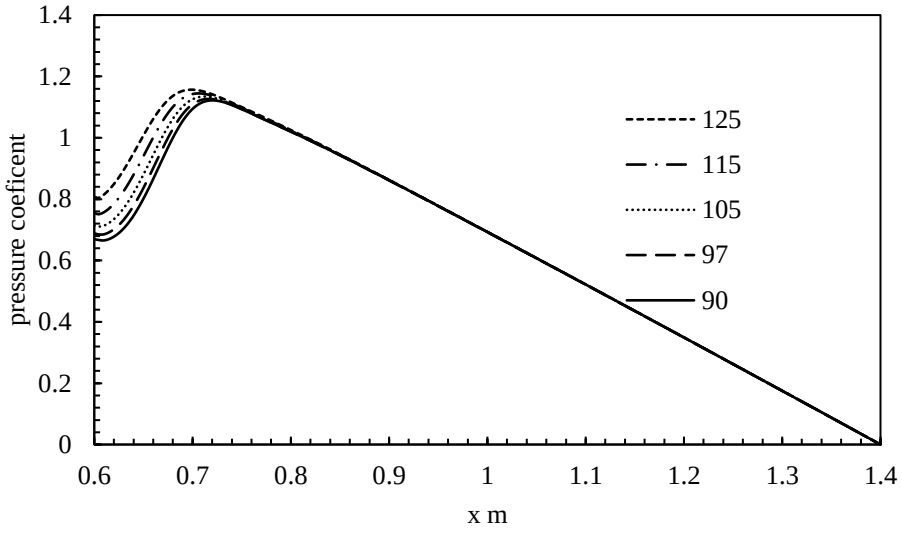

Figure 5-21 Pressure coefficient variation with the inclination angle ER 2.5

The effect of the inclination angle on the heat transfer rate for ER2 was investigated, and the results are shown in Fig 5.22 and Fig 5.23

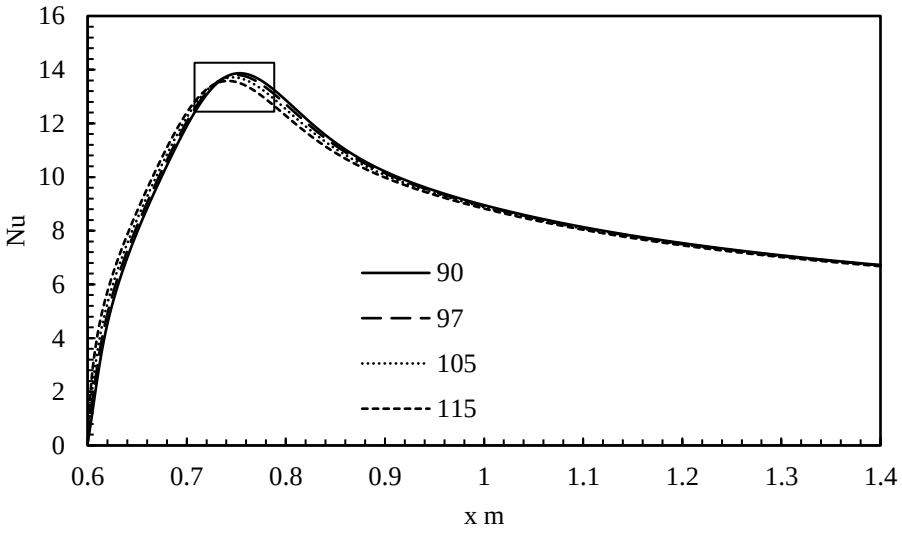

Figure 5-22 Nu variation with inclination angle for ER 2

As discussed earlier, the inclination angle decrease promoted the heat transfer rate, in ER2 the increase was up to 3.5%. This increase is located in the separation region where the

most of the heat transfer takes place. The area on the graph highlighted in Fig 5.25 is expanded and shown in Fig 5.23. The increase in the angle enhances the heat transfer.

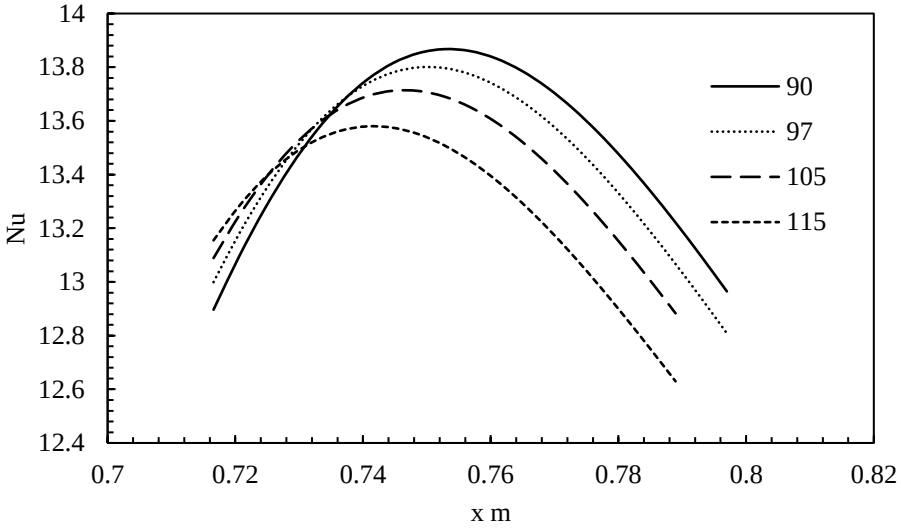

Figure 5-23 zoom of the Nu change with inclination angle ER 2

The effect of the expansion ratio and the inclination angles on the heat transfer enhancement was studied and the results are shown in Fig 5.24 ,a , b, c and d

a b

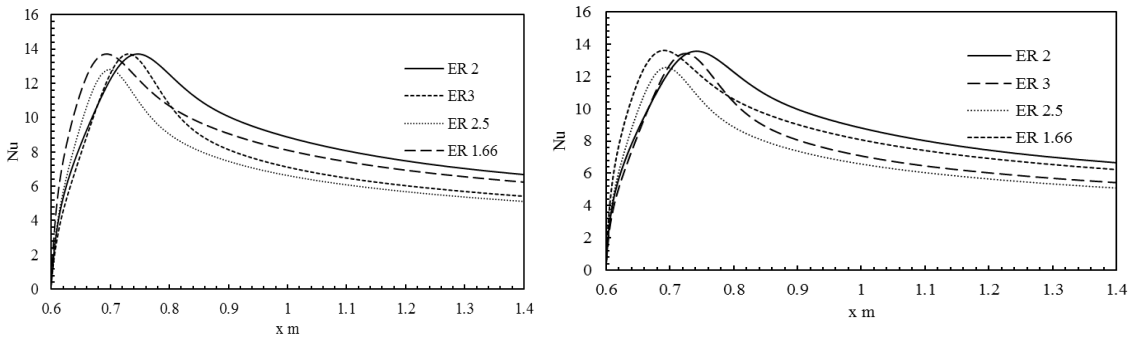

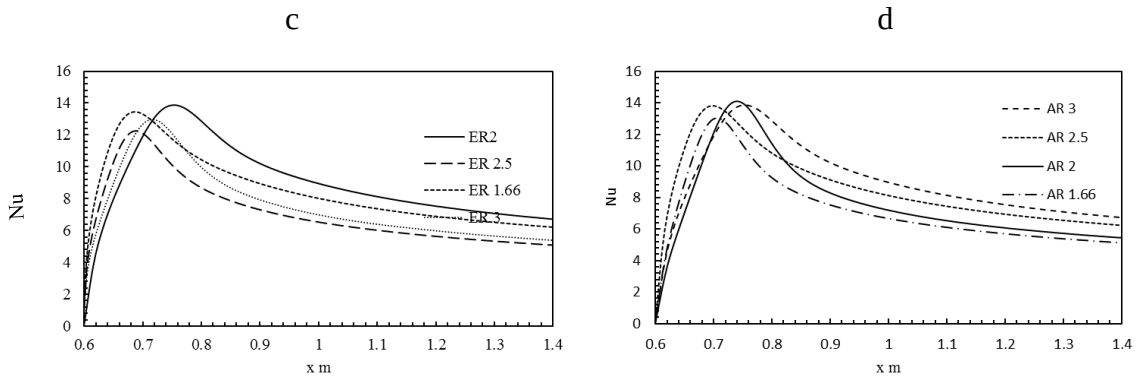

Figure 5-24 Expansion ratio effect on the Nu for inclination angles, a) 105 b) 115 c) 125 d) 90

The variation of heat transfer rate with expansion ratio for four inclination angles on the lower wall are calculated and the results are shown in Fig 5.24 a, b, c and d for 105^o, 115^o, 125^o and 90^o angles respectively. The Nu number increased with the increase in the expansion ratio. The increase was found to be applicable to all inclination angles tested.

This is in agreement with previous published works for 90^o angle because of the limited published information on the enhancement with the other inclination angles are.

5.5.4 Effect of volume fraction

The effect of the volume fraction on the heat transfer enhancement was also studied and the results are introduced in Fig 5.25

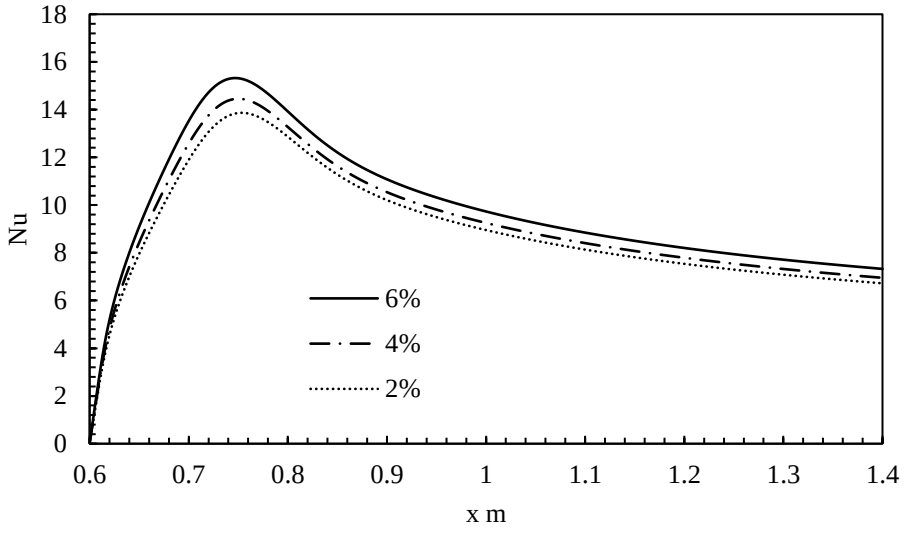

Figure 5-25 volume fraction effect on the heat transfer rate

The figure shows the variation of Nu number on the lower wall for three volume fractions tested, 2%, 4% and 6%. The graph shows an improvement in the heat performance with the increase in the volume concentration, 6% showed the highest Nu number tested, as a result to this, water has poor heat transfer rate (assuming the volume fraction is lower in water).

As seen in the graph, a remarkable increase in Nu number is located in the reattachment point as anticipated in this kind of configurations. The increase in the nanoparticles leads to an increase in the temperature gradient at the lower wall, which implies an increase in the inertia forces. Moreover, the increase in the volume fraction results in an augmentation in the thermal conductivity.

Both the increase in the temperature gradient and the increase in the thermal conductivity improved the heat transfer at the lower wall. The thermal conductivity is accompanied by higher thermal diffusivity, this high thermal diffusivity results in a reduction in the temperature gradient. The improvement in thermal diffusivity requires a better nanoparticle density and thermal capacity.

The variation of the heat transfer with Reynolds number is studied thoroughly, and the results are depicted in Fig 5.26.

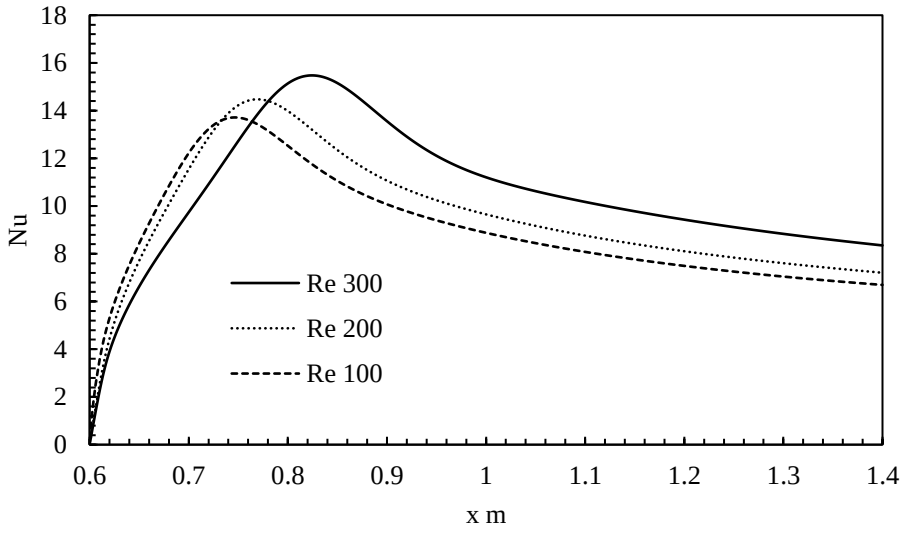

Figure 5-26 Variation of Nu with Re at the lower wall

The heat transfer improved with the increase in the Re number on the lower wall, as can be seen in the graph. The increase due to the Re number rise is more pronounced out of the circulation zone. This is due to the increase in the inertia forces which is noticeable out of the circulation zone. A remarkable increase was also observed along the wall out of the circulation zone.

5.5.5 The entropy generation

The entropy is also investigated for Re number 100,200,300 and 400 for $\alpha=90^{o}$ and volume fraction 2%. The results are presented in Fig 5.27. As shown in equation (5.6) and (5.7) entropy is a function of thermal conductivity and viscosity, these two thermal properties are the most important properties among the nanofluid thermal properties. Entropy generation determines the level of the gained irreversibilities during a thermal process. Therefore, entropy production can be employed as a measure to evaluate the performance of engineering devices. For proper optimisation of engineering systems in terms of operation and design, entropy has to be minimised as well as maximising the heat transfer. It is clearly seen that the increase in Re number results in an increase in entropy generation number, which implies that increasing Re number has an advantage of enhancing the heat transfer rate. Re number 100 has minimum entropy generation number compared with Re 200 and 300. The entropy generation number at the bottom wall starts from zero and increases to a peak value in the recirculation zone, the entropy increases with Re number up to circulation zone and has the maximum value at 0.352 m from the corner of the geometry, i.e. coincides with the reattachment point. The same trend applies to the 200 and 300 Re numbers; the only change is the point of the minimum entropy, the explanation for this is that decreasing Re number will result in decreasing the reattachment length which was one of the findings from [266] experimental work.

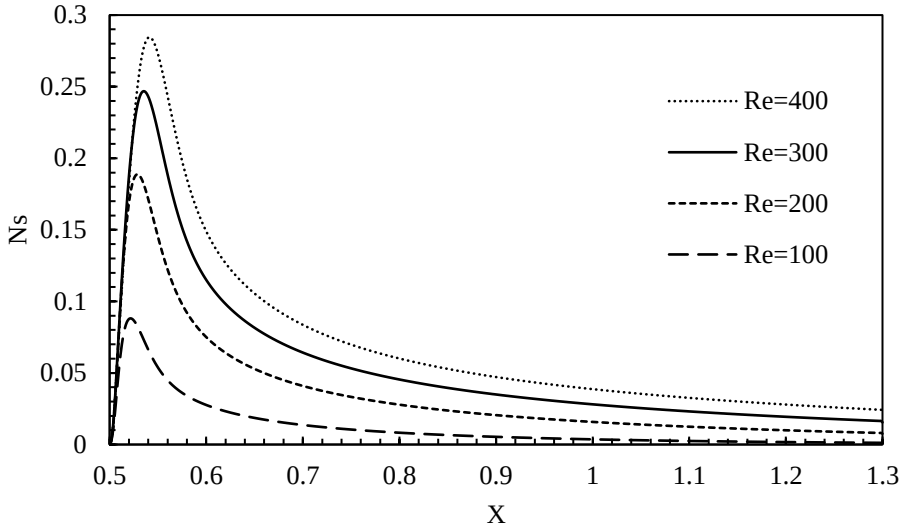

Figure 5-27 Effect Re on the entropy generation number on the bottom wall

The contours of velocity in various inclinations angles are shown in Figure 5.27; it can be seen in the contours the growth in the recirculation zone. The flow enters fully developed as can be seen in the velocity variation.

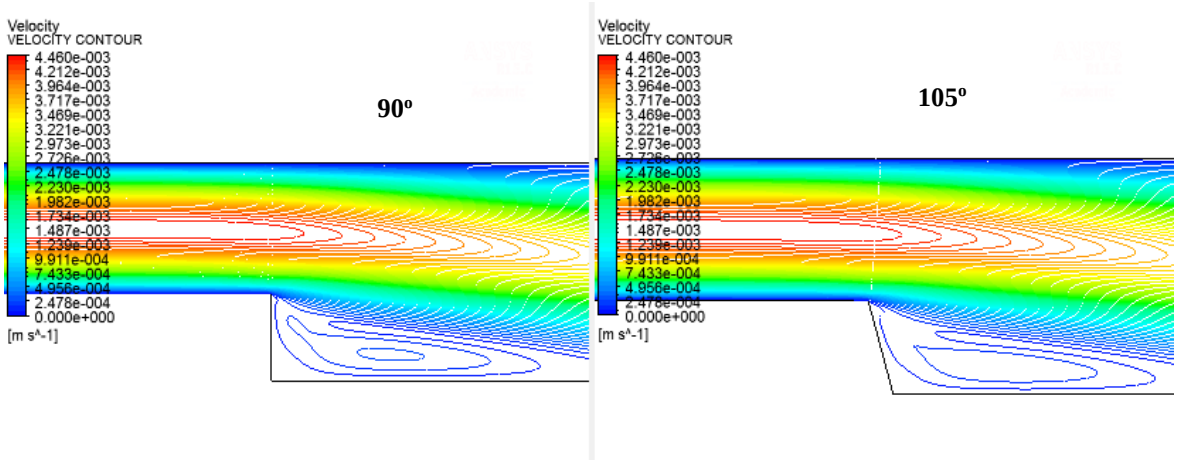

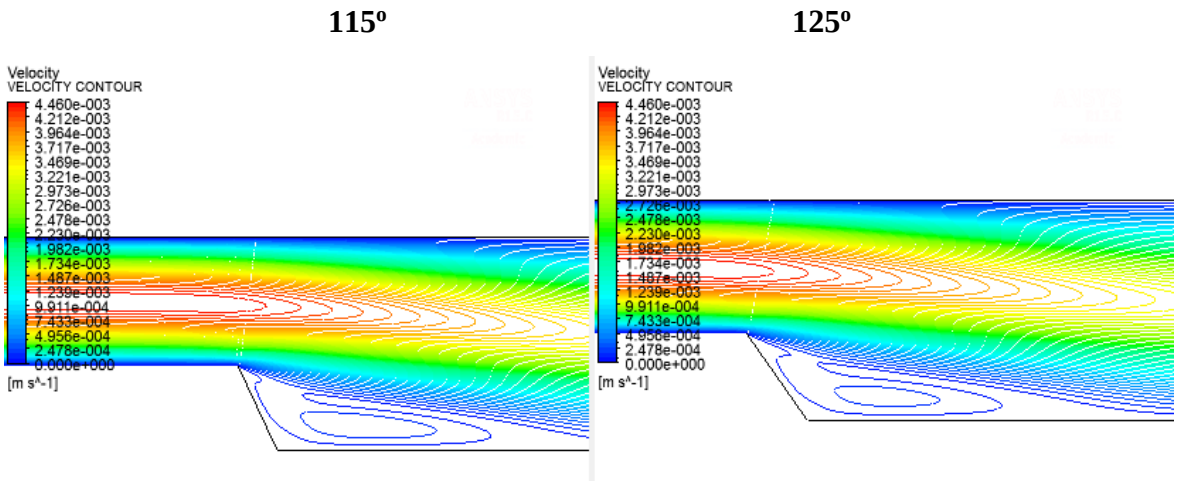

Figure 5-28 Velocity contours for several inclination angles

5.6 Summary and conclusion

In this Chapter, the Backward-facing step problem with nanofluid as the working fluid has been investigated numerically, in particular, the effect of the inclination angle of the step face and the expansion ratio on the heat transfer performance and the flow characteristics. Four inclination angles have been studied; four expansion ratios have been considered in these simulations.

Several parameters have been tested such Re number, volume fraction. Pr number, pressure coefficient and velocity gradient have been investigated thoroughly. All results were shown and discussed. This chapter addresses the influence of the inclination angle on the fluid flow and heat transfer rate in backward-facing step

6 A new correlation for effective viscosity

6.1 Introduction

Since introducing the nanofluids in the heat transfer applications, many researchers proposed models to predict thermophysical properties for nanofluids. Much research has been carried out for modelling the thermal conductivity. However, only limited number of investigations were focused on the effective viscosity models. Viscosity is an important flow property of fluids. Pumping power, the pressure drop in laminar flow and convective heat transfer are directly affected by the viscosity of fluids. The understanding of viscosity change is vital for predicting the heat transfer performance of nanofluids.

Einstein [62] developed the first viscosity formula for micro colloids in 1906. The model was based on the assumption of viscous fluid containing spherical particles. His model was found to be valid for volume concentrations up to 2%. Brinkman[64] introduced a formula to predict the viscosity of the particles at a very low volume fraction. The model was based on the assumption of spherical particles.

Batchelor [281]developed Einstein's model and proposed a new model for rigid and spherical particles with Brownian motion. The model was investigated by many researchers and found to be working well with low concentrations. Boungiorno [282]developed a mathematical model for colloids made of a base fluid and nanoparticles and showed that the nanofluid properties might vary significantly within the boundary layer because of the effect of the temperature gradient and thermophoresis. He attributed the convective heat transfer enhancement to the reduction of viscosity within and consequent thinning of the laminar sub-layer. Tseng [106]conducted an experimental investigation for TiO2. The number of data used in his experiment was only four volume concentrations. He derived a curve fit model for effective viscosity. Maiga [283] proposed a model for effective viscosity in forced convection using Al_2O_3 water nanofluid. Saito[284] implemented a theoretical model for very small particles with rigid spherical particles.

Nguyen[285] conducted an experimental study for Al_2O_3 and CuO particles nanofluid; he derived a curve fit equation for predicting the effective viscosity for nanofluids.

Grag et al[286] measured the viscosity of copper nanoparticles in Ethylene glycol. They found that the viscosity increase was almost four times of that predicted by the Einstein law of viscosity. The number of data used for introducing their model is only five readings. Wang and Xu[46] measured the viscosity of Al_2O_3-water; they highlighted that the enhancement of viscosity was between 20-30% for 3% volume fraction. Three volume fractions were used to measure the thermal conductivity and viscosity. The list of viscosity models can be found in Table 2.2

The aim of this Chapter is to bridge the gap in modelling effective viscosity and propose a new generalised and applicable effective viscosity model.

6.2 Model formulation

The earliest study on the rheological behaviour of the colloid dispersion introduced by Einstein was written in the form

$$\frac{\mu_{eff}}{\mu_f} = 1 + [\mu]\emptyset + 0\emptyset^2 \tag{6.1}$$

Where $[\mu]$ is called intrinsic viscosity which gives an indication of the contribution of the particles to suspension viscosity. This factor was expressed in many different values by many researchers.

The intrinsic viscosity was proposed in his work is 2.5, so equation (6.1) can be written as:

$$\frac{\mu_{eff}}{\mu_f} = 1 + 2.5\emptyset + 0\emptyset^2 \tag{6.2}$$

Since equation (6.2) has been introduced, many attempts of works have been proposed to take into consideration the hydrodynamic interactions effect, which arises in the suspension due to the higher volume concentrations.

In most of the expressions developed, the equation takes the following form:

$$\frac{\mu_{eff}}{\mu_f} = 1 + a\emptyset + b\emptyset^2 + c\emptyset^3 + \cdots. \tag{6.3}$$

An example of these equations, the expression developed by Brinkman :

$$\frac{\mu_{eff}}{\mu_f} = 1 + 2.5\emptyset + 4.375\emptyset^2 + 0\emptyset^3 \quad (6.4)$$

In a later work by Lundgren [68], the equation takes the form:

$$\frac{\mu_{eff}}{\mu_f} = 1 + 2.5\emptyset + (2.5\emptyset)^2 + 0\emptyset^3 \quad (6.5)$$

Bachelor added the Brownian motion so the form developed to the expression developed to the following form:

$$\frac{\mu_{eff}}{\mu_f} = 1 + 2.5\emptyset + 6.2\emptyset^2 + 0\emptyset^3 \quad (6.6)$$

In general, these equations rigorously underestimated the effective viscosity as reported by several experimental studies. Accordingly, some expressions have been developed, nonetheless some of which have limited applicability due to the narrow range of experimental data used to develop these equations.

The equation proposed in this study is based on a carefully selected data from literature as well as theoretical models; the equation is written in the form of Taylor series expansion such as equation (6.6) as follows

$$\frac{\mu_{eff}}{\mu_f} = 1 + A\emptyset + B\emptyset^2 + C\emptyset^3 \quad (6.7)$$

The models and experimental data in this study are summarised in Table 6.1. A regression analysis was used to calculated the variables $A,\ B$ and C. The coefficient of determination R^2 found to be 95.8%, the maximum error is 5%. The constants were determined from the trend of the equation as shown in Figure 6.1

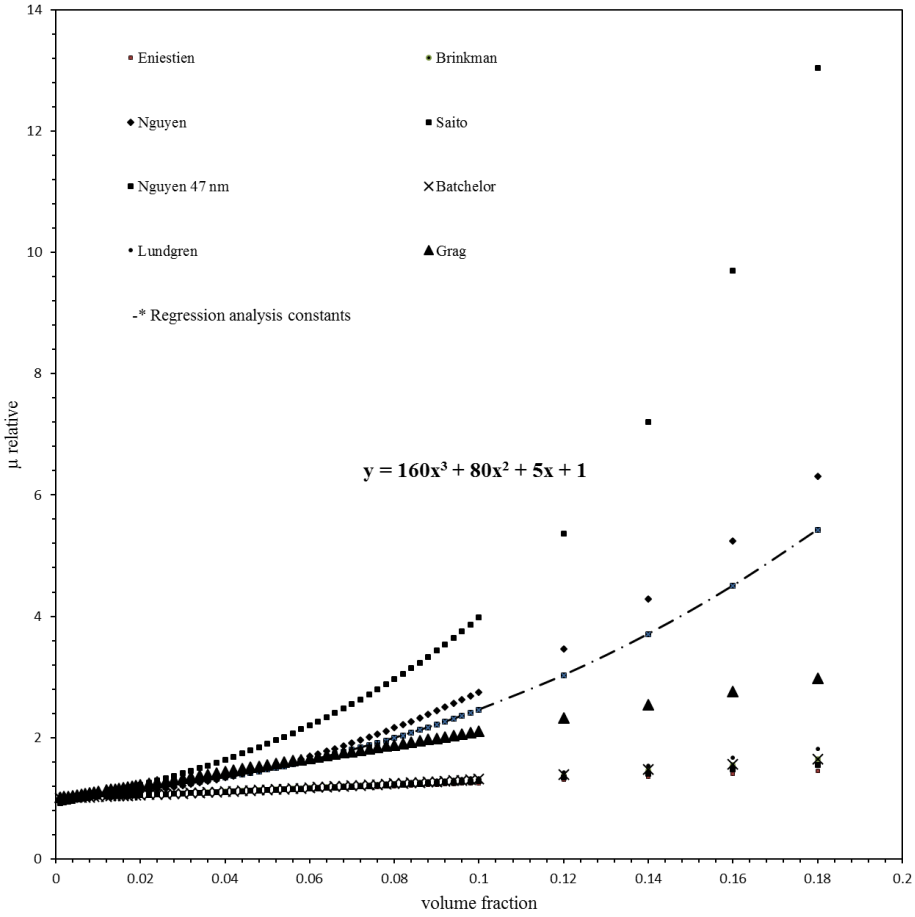

Figure 6-1 Regression analysis constants

Table 6-1 Data and models used for regression analysis

Model		Theo/ Exp.	Notes
Einstein	**1906**	Theoretical	Infinitely dilute suspension
Brinkman	**1952**	Theoretical	Spherical particles
Maiga	**2005**	Numerical	Al203-water
Buongiorno	**2006**	Mathematical	Tio2-water
Tseng	**2003**	Experimental	Tio2-water
Nguyen	**2007**	Experimental	Al203-water
Batchelor	**1977**	Theoretical	Rigid and spherical particles
Saito	**1950**	Theoretical	Spherical particles
Grag	**2008**	Experimental	Cu-EG

From the regression analysis, the values of a, b and c were 5, 80 and 120 respectively so equation (6.7) can be written as:

$$\frac{\mu_{eff}}{\mu_f} = 1 + 5\emptyset + 80\emptyset^2 + 120\emptyset^3 \tag{6.8}$$

The base fluid viscosity is temperature dependent, and in this study, water is used as the base fluid. The viscosity of water can be written as a function of temperature as presented by the following expression as reported by [74]

$$\mu_f = 2.414 \times 10^{-5} \times 10^{247.8(T-140)} \tag{6.9}$$

Where T is the fluid temperature in K

The next section will discuss the results and the performance of the proposed model.

6.3 Problem Description

The geometry considered in this work is shown in Fig 6.2, a pipe with length 1 meter and a diameter 10 mm with constant external heat flux. The fluid enters the pipe with temperature T_o=293 K and uniform axial inlet velocity. At the pipe exit a fully developed flow condition is considered. The fluid considered in this study is Al_2O_3 water nanofluid. The properties of the nanoparticles are shown in Table 1.

Table 6-2 Nanoparticle Properties

Nanoparticle	ρ (kg/m^3)	k (W/m-K)	C_p (J/kg-K)
Al_2O_3	3950	35	765

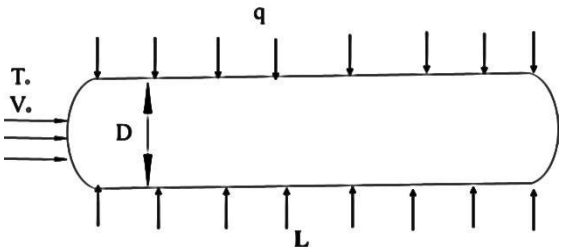

Figure 6-2 Problem Geometry

Problem Geometry

6.4 Governing Equations

The governing equations are continuity, momentum equation and energy equation. The mathematical formulation can be found in Chapter three.

6.4.1 The thermophysical properties of nanofluid

The density is modelled as

$$\rho_{nf} = (1 - \phi)\rho_f + \emptyset\rho_s \tag{6.10}$$

The specific heat is written as:

$$C_{pnf} = \frac{(1 - \emptyset)\left(\rho C_p\right)_f + \emptyset\left(\rho C_p\right)_s}{\rho_{eff}} \tag{6.11}$$

The thermal conductivity is expressed as

$$K_{eff} = K_f \left(\frac{K_s + 2K_f - 2\emptyset\left(K_f - k_s\right)}{K_s + 2K_f + \emptyset\left(K_f - k_s\right)}\right) \tag{6.12}$$

6.5 Numerical Simulation

The governing equations were solved numerically with the boundary conditions using ANSYS 15.0. The geometry was created in ANSYS design modeller; the computational domain was discretized in ANSYS meshing and solving the governing equations together with the boundary conditions in ANSYS FLUENT. The CFD code is based on the finite

volume method and SIMPLE algorithm that solves the governing equations. Second-order upwind schemes were used for the convective fluxes. Convergence was obtained with residuals less than 10^{-6} for the continuity equation, the momentum equations and the energy equation. To ensure an independent mesh solution, the maximum Nu number at the outer surface was used. The solution was taken to be mesh independent when the percentage change in maximum Nu remained less than 1% to give a mesh-independent solution for all simulations in this study. Table 2 shows the mesh dependency test for maximum Nu and it is clearly seen that for the mesh with 281000 elements the maximum Nu becomes insensitive to further refinement and hence mesh was selected for the solution

Table 6-3 Mesh dependence test

Mesh	No. of Elements	Nu_{max}
1	39500	3258
2	152000	4761
3	**281000**	**4821**
4	360500	4823

6.5.1 Results validations

The present simulations were validated, and the results are shown in Fig 6.3. The Figure illustrates the change of the surface heat transfer coefficient at the wall. As there is an external heat flux applied on the wall and the flow enters the pipe with constant temperature, it is expected that the heat transfer coefficient will decrease from a peak value at the inlet of the pipe until a point where becomes almost unchanged at the wall. The results as seen from the graph show there is a good agreement with Bianco et al [178] results.

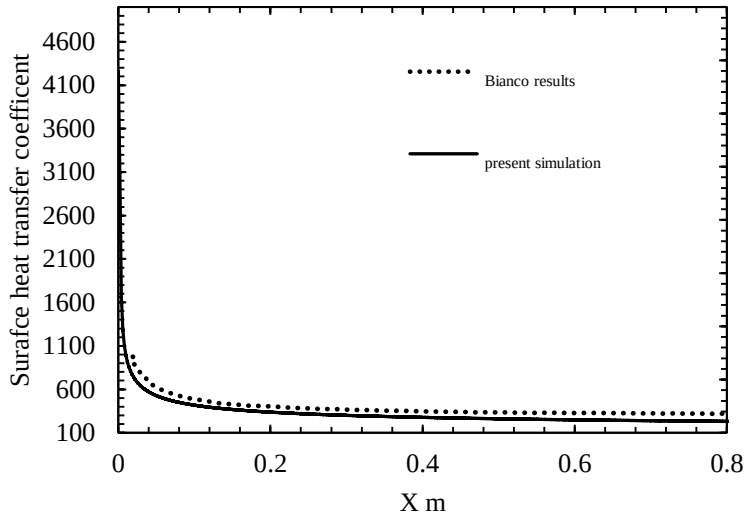

Figure 6-3 Results Validation of surface heat transfer coefficient

Further simulation validations were carried out. The presents simulations were compared with Bianco et al [287] for the relationship between Re number and average Nu number. The results are shown in Fig 6.4, and as can be seen in the graph the present simulations showed good agreement with the Bianco et al results.

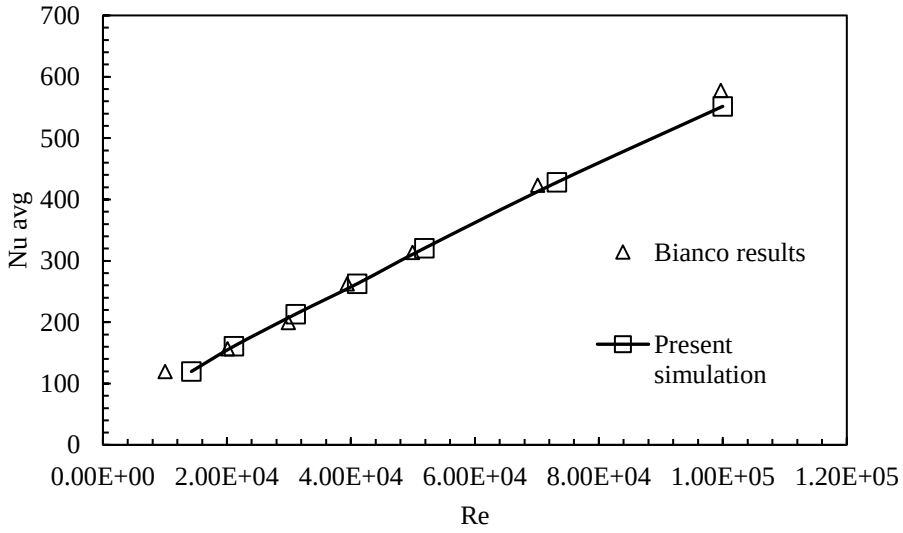

Figure 6-4 Results validation Nu vs Re with Bianco et al

6.6 Results and Discussion

The viscosity is calculated using the proposed model and the results are depicted in Fig 6.5. The graph shows the variation of the viscosity with temperature for different models. The results of all viscosity models are for volume fraction 1%, the temperature range tested was between 273 K and 330 K.

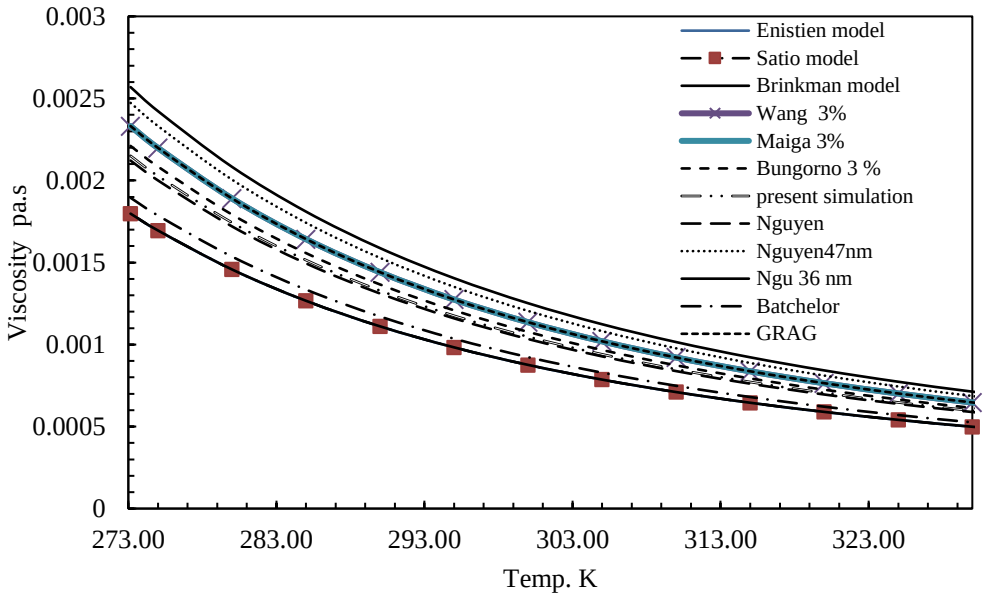

Figure 6-5 Viscosity change with temperature for different models

The viscosity decreases with the increase in temperature. This trend is observed in all models tested as shown in the graph. The reason behind this is that all models are presented as a function of the viscosity of the base fluid which is water in this case. As reported in the literature, water viscosity declines with a rise in temperature.

The prediction of viscosity shows clearly the underestimation of classical models such as Einstein and Brinkman. However few empirical models based on experimental observations for viscosity demonstrated higher value such as Nguyen compared to other models predictions. The explanation for the augmentation of viscosity relative to the base fluid viscosity is the stability of the nanofluid as it is reported in the literature in chapter two plays a vital role in the accurate prediction of the thermophysical properties of the nanofluid.

The model was also tested with some experimental data for Tiamsawas, Nguyen 47 nm, Nguyen 36 nm, Grag, Chen and Duang. The results are shown in Fig 6.6

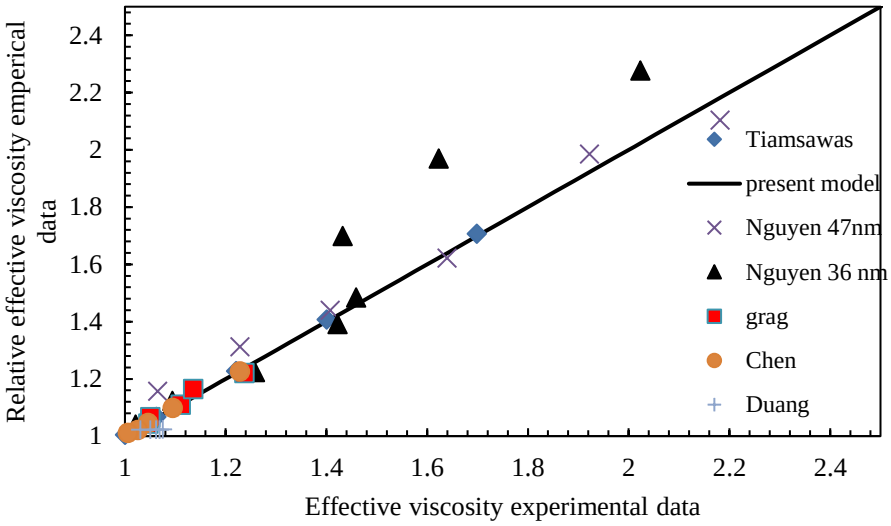

Figure 6-6 Relative viscosity comparison for various models

The graph represents the relation between the effective viscosity to base fluid viscosity ratio empirical data and the effective viscosity ratio experimental data.

The effective viscosity ratio is defined as the ratio between the effective nanofluid viscosity to the base fluid viscosity. It is worth mentioning that the effective viscosity ratio is always greater than unity as the effective viscosity of the nanofluid is always higher than the base fluid. This is attributed to the augmentation of the effective viscosity due to the existence of the nanoparticle which is explained by the effect of the volume fraction in the formula used to calculate the effective viscosity such as equation (6.8). However there are few contradictory studies in the literature where the nanofluid effective viscosity is below that of the base fluid. This behaviour of viscosity is in discrepancy to most of the published work where effective viscosity is greater than that of the base fluid.

In terms of data comparison to the present model, it should be noted that the model has fairly accurately captured most of the data. However, some of the data reported by Nguyen for nanoparticle with 36 nm diameter is relatively higher than data reported by other experimental studies. This is possibly attributed to the preparation method used to synthesise the nanofluid sample in their work.

In order to evaluate the applicability of the present model, the relative viscosity change with volume fraction for various viscosity models has been studied, and the results are shown in Fig 6.7.

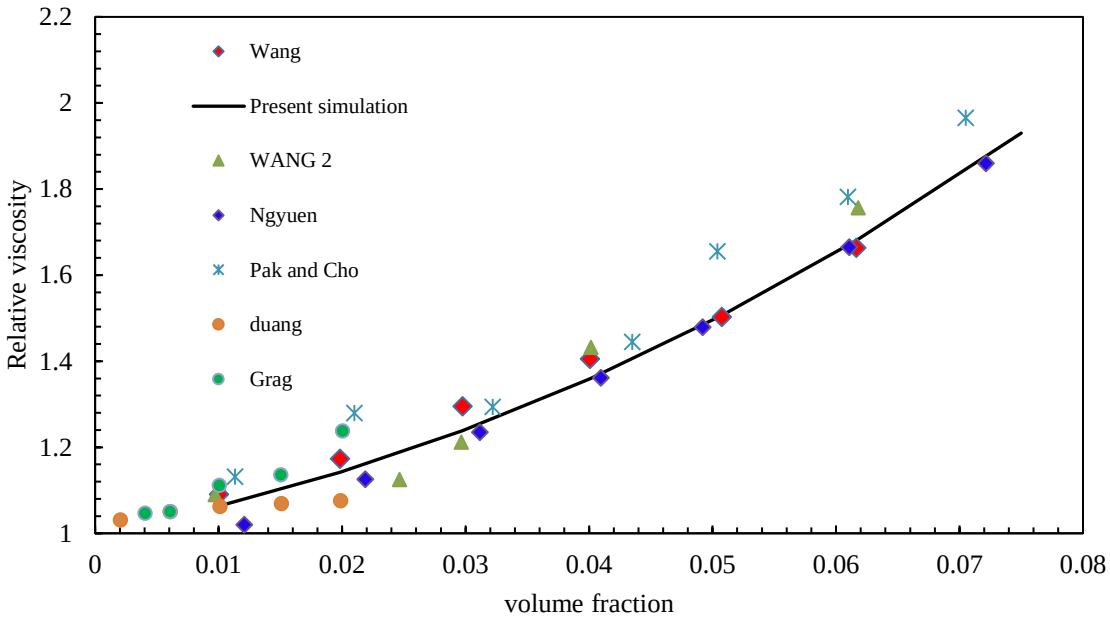

Figure 6-7. The relative viscosity model change with volume fraction for various models.

As mentioned earlier that the effective viscosity increases with the increase in the volume fraction, the graph shows clearly that the viscosity rises gradually with volume fraction growth. This variation is observed in all models tested in the present study.

The relative viscosity predicted by the present model matches up fairly closely to ϕ=0.075. However, the data presented by Park and Cho showed slightly higher values; this is possibly attributed to experimental error due to the constant temperature when the viscosity results were recorded. They developed their viscosity model based on particle volume fraction taking room temperature as a reference [288]. It is well known that the viscosity decreases with the increase in temperature, so it is anticipated that the three high readings for Pak and Cho would be slightly lower if temperature effect was taken into account.

The performance of the proposed model has been tested at higher volume fractions. The effective viscosity has been studied when the volume fraction rises to 10%. The results of this study are introduced in Fig 6.8.

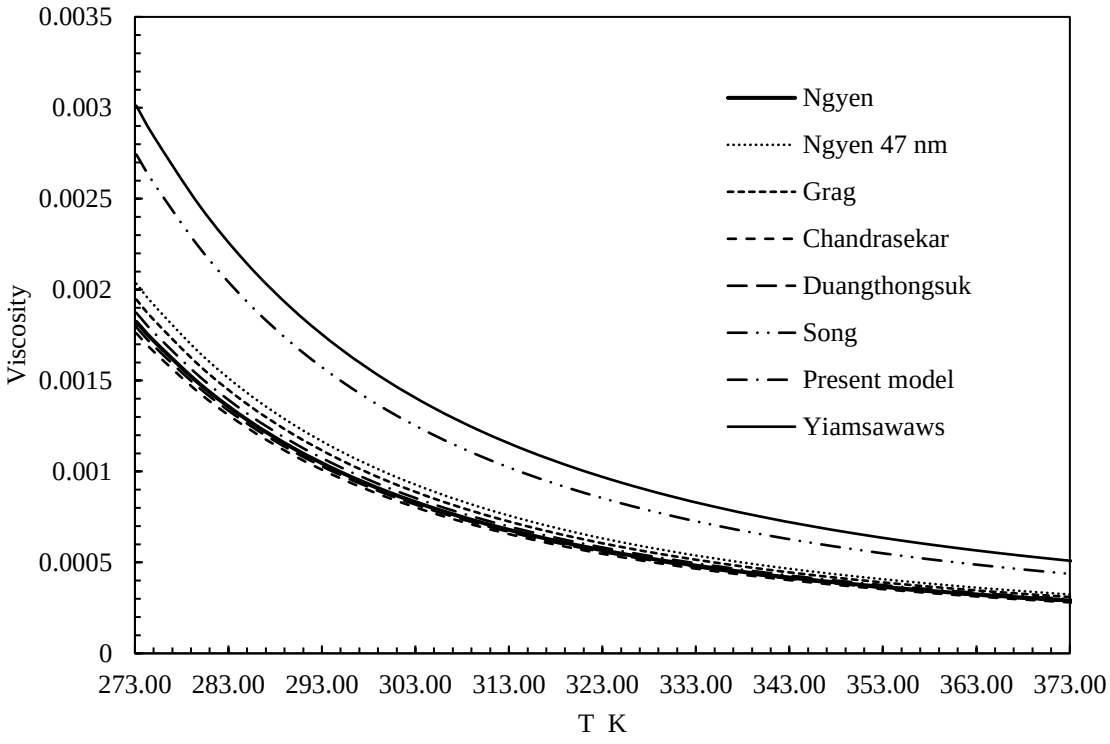

Figure 6-8 The viscosity change with temperature at 10% volume fraction

The decrease in temperature was also noticed when increasing the volume concentration dramatically. Two models among the tested model showed over-predicted viscosity. These two models are Yiamsawaws and Song. The gap between the predictions of these two models and the other models is pronounced when the temperature is low (273-313 K). However the proposed model proved a reliable prediction even at higher volume fractions.

It should be noted that many of the empirical models are based on limited recorded data of individual experiment. This assumption makes the applicability of such models to be restricted to a narrow range of either volume fraction or temperature range.

The performance of various models tested including the present model showed smaller difference in viscosity at very high temperature (353-373 K), compared to the difference at lower temperature (273-303 K)

The viscosity model was also tested rigorously with theoretical and experimental models. The relative viscosity was calculated for a range of volume fractions, and the results are depicted in Fig 6.9.

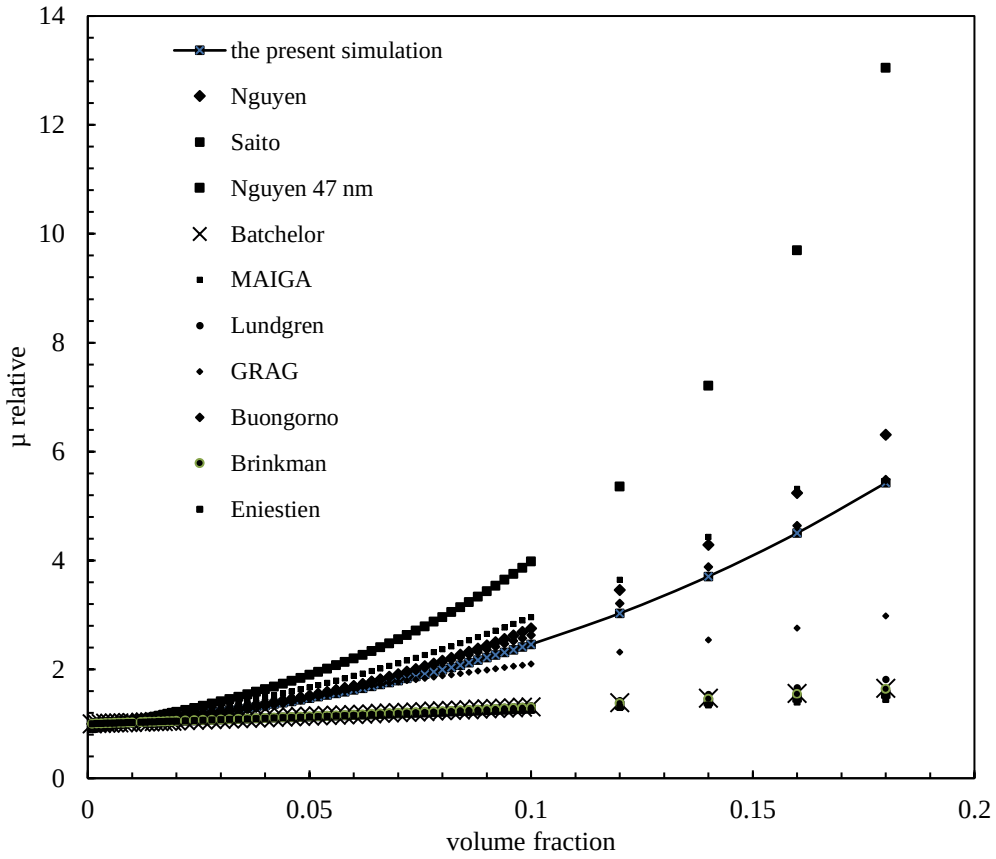

Figure 6-9 Relative viscosity change with volume fraction for theoretical and empirical models

Several classical and empirical models have been studied along with the proposed viscosity model to understand the variation with a wide range of volume fractions.

From the graph shown, it is evident that the relative viscosity increases with the increase in the volume fraction. However, this increase is noticeable in the empirical and presented model for all volume fractions tested.

For all classical and theoretical models, the relative viscosity is massively underestimated at high volume fractions (ϕ>2%), where the viscosity can be predicted with acceptable accuracy at lower volume fractions. The present model predicted the relative viscosity in the middle of most models tested and hence justifies that the model shows promise for wider applicability.

The proposed model was tested with a set of selected data to ascertain the validity of the model; the results are shown in Figure 6.10.

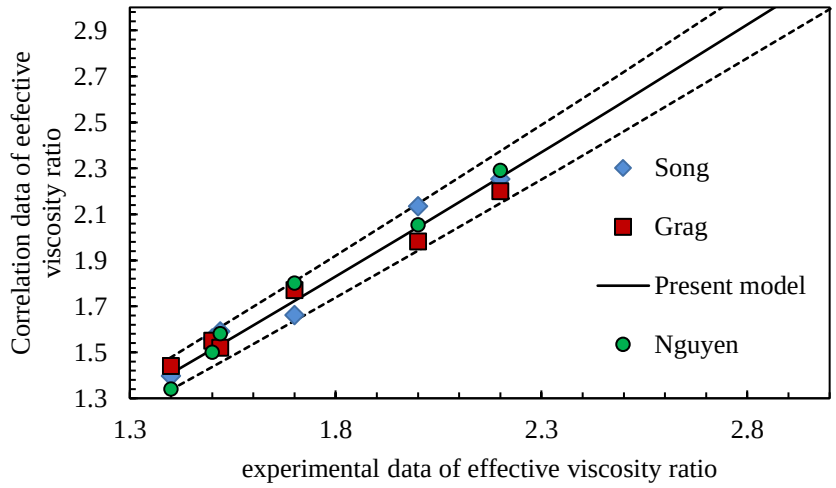

Figure 6-10. Comparison of the proposed model and set of experimental data

The graph shown represents the relation between the experimental data and the data predicted by correlations developed by several researchers. The suggested equation for predicting the effective viscosity fits all the selected data in this study with 95% level of accuracy. This level can give a high confidence of the credibility of the proposed model.

The selected data used in Figure 6.10 varied between different nanoparticles, such as data from Nguyen, Grag and Song.

The level of accuracy bridges the low and high relative viscosity predicted by experimental data and correlations presented by a certain number of researchers. Figure 6.10 also highlights the minimal error (<5%) in a wider range of volume fractions, as it is obvious that the higher relative viscosity ratio is resulted from the rapid increase in volume fraction of the nanoparticles.

The presented model also provides simplicity in use as the correlation proposed in equation (6.11) only include the base fluid viscosity and the volume fraction. Unlike some other correlation which involves parameters such as the nanoparticle diameter or freeze temperature of the base fluid where in some cases it would be difficult to predict the viscosity with high accuracy without recalculations of these parameters. This advantage can promote the applicability and the credibility of this correlation.

The variation of the viscosity predicted by the present model with other models on the diameter of the pipe is investigated, and the results are described in Figure 6.11.

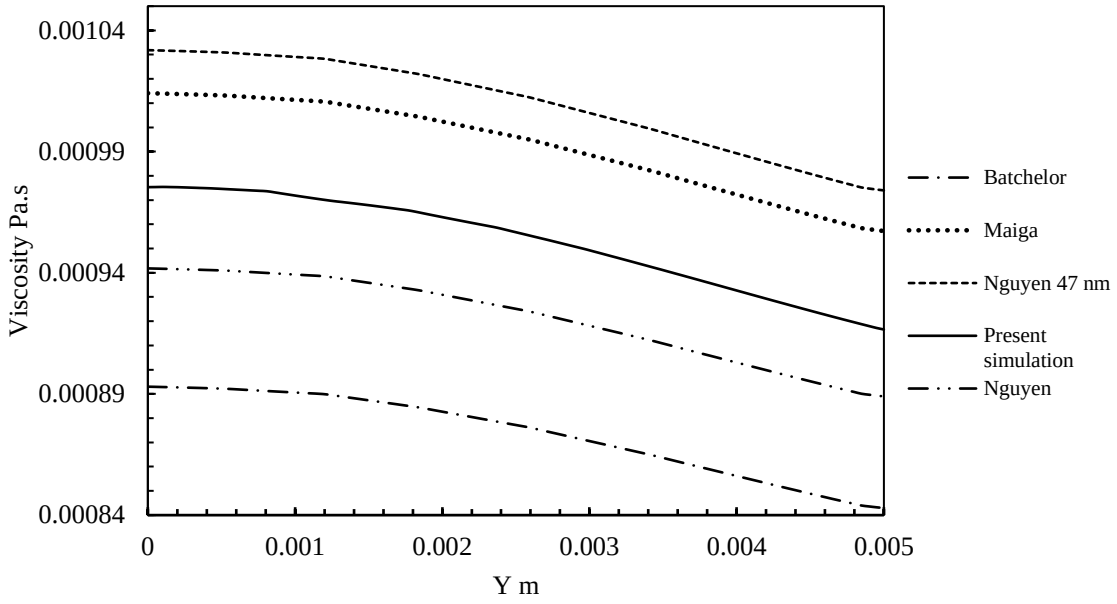

Figure 6-11 the viscosity change along the radius of the pipe for various models.

The graph represents the variation of the effective viscosity of the nanofluid along the radius of the pipe for different viscosity models. The x-axis represents the radius of the pipe. It can be seen that the viscosity decreases when approaching the wall, this is attributed to the higher temperature at the wall as mentioned in the boundary conditions that there is a constant external heat flux applied on the wall.

It is also worth noting that the viscosity predicted by the present model is in the middle of the results predicted by other correlations. The lowest predicted viscosity was for that calculated by Brinkman model. Again this is another indication of the gross underestimation of the viscosity by classical models.

The highest viscosity was calculated by Nguyen correlation, as it was obvious that the viscosity evaluated by this model is slightly higher than other models predictions. This can be explained by the single set of data used to develop the model presented by Nguyen, the limited available data used to build such a model can restrict the credibility in a wide range of applications for different scenarios of flows.

Fig 6.12 shows the viscosity prediction along the wall for proposed correlation and compared with a selection of these models.

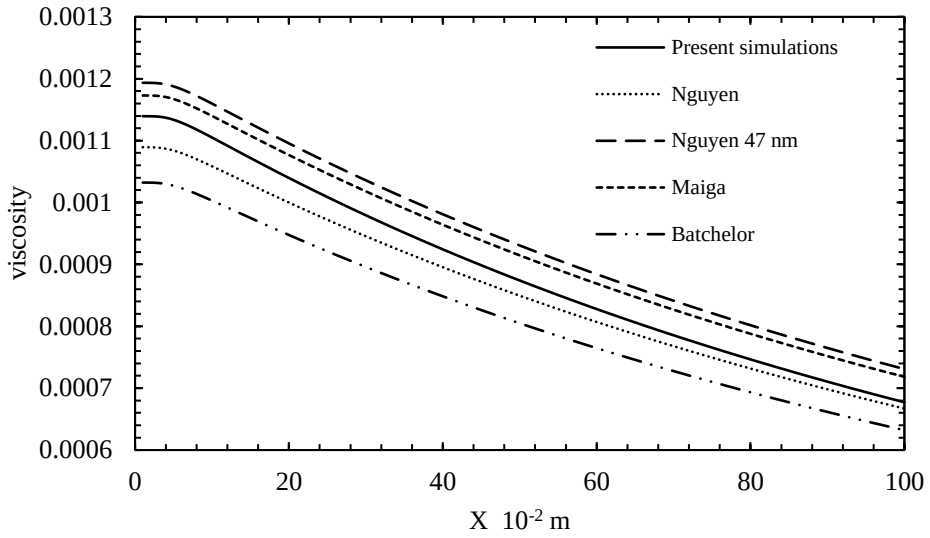

Figure 6-12 viscosity predictions on the wall by various models

It can be seen that the viscosity significantly drops along the wall as the temperature rises remarkably due to the external heat flux. This decline in viscosity is observed in all viscosity models tested.

However, there is a gap in the viscosity predicted by these different models. The gap reached up to 16% at the pipe inlet and up to 12% at the pipe exit.

It can be established that the viscosity predicted by Nguyen model was the highest whereas the classical Batchelor model showed the lowest viscosity prediction. The effective viscosity predicted by the proposed model are shown in the graph. It is evident that from the evaluation of the viscosity that the present simulation is located in the middle of the different correlations. This emphasise that the present model is far from the theoretical model which underestimate the viscosity value and on the other hand it is not giving a high value for calculated viscosity as that obtained by Nguyen model.

This realistic estimation obtained by the present model can enhance the validity of this model so the gap in various models developed by several researchers can be bridged by employing the proposed model and testing it under different fluid flows.

The heat transfer rate is investigated by incorporating the proposed correlation for viscosity, the volume fraction effect is studied, and the results are depicted in Figure 6.13.

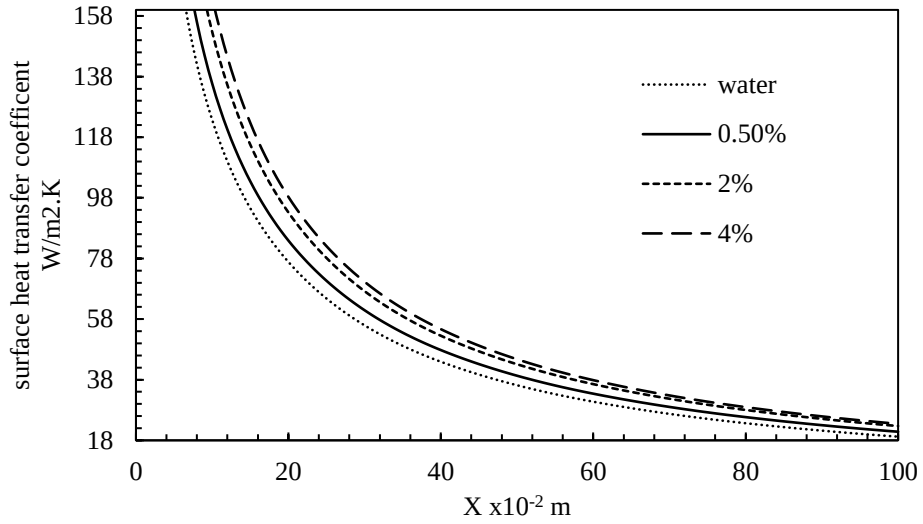

Figure 6-13. Effect of volume fraction on surface heat transfer coefficient

The graph shows the variation of the surface heat transfer coefficient on the wall of the pipe for three volume fractions as well as with water as the base fluid.

In general, the surface heat transfer coefficient drops rapidly along the wall from a peak point which is located at the pipe inlet.

This drop is noticed in all volume fractions tested. However, the volume fraction increase was found in favour of surface heat transfer coefficient, as it can be clearly seen that the volume fraction 4% has the highest surface heat transfer coefficient. On the other hand, the lowest value was for the water base fluid. This finding endorses previously published works where it was reported that the heat transfer rate is enhanced with the increase in the volume fraction.

Exploratory calculations were also carried out for the pipe (ϕ=2%) for four Re numbers, and the predicted Nu number variation are shown in Figure 6.14.

In the graph shown, the Nu number decreases dramatically starting from a peak value at the pipe inlet to a monotonically decreasing value for $x > 0.04$ m.

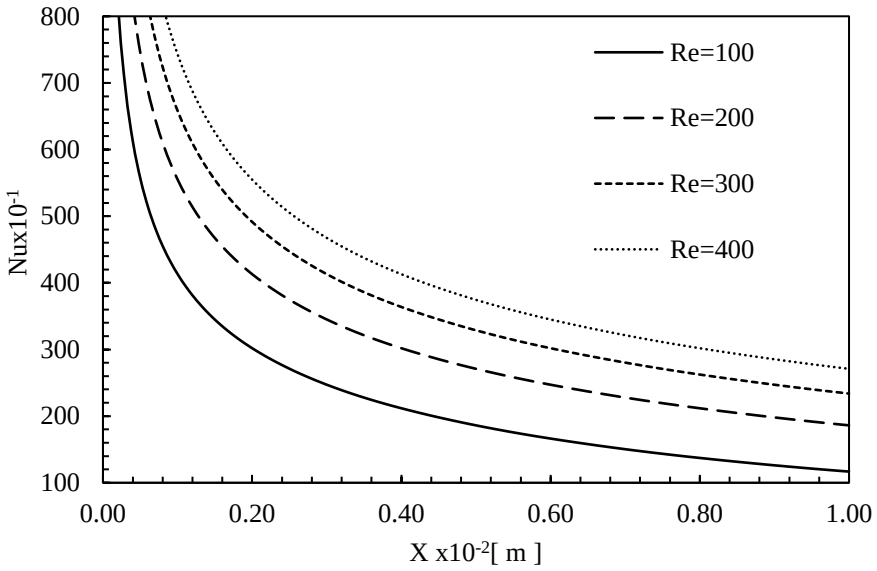

Figure 6-14 Re number variation with Nu number

From the results, it can be seen that the Nu number increases significantly with the increase in Re number.

The increase in Re number was reported by several previous works that it is one of the tools to enhance and improve the heat transfer rate due to the increase in the inertia force.

6.7 Summary and Conclusion

In this Chapter, a new effective viscosity was proposed based on a chosen set of expressions available in the literature. The suggested model was compared with theoretical and empirical correlations for viscosity. The model was validated with experimental data from the literature.

The present model showed reliable results and the predictions of viscosity were in good agreement with experimental results from previous work. The model was scrutinised for its viscosity predictions, and the results show promise for wider applicability. It is believed that the ease of use of this model as well as the good level of accuracy of attained results can give the proposed model wider range applicability.

7 Investigation of microchannel flows

7.1 Introduction

Recent growths in nanofluid applications and the approaches for improving cooling technology for electronic devices with high heat application have attracted the need for possible production of effective and compact cooling components.

The applications of microchannels are in increasing demand for their high heat flux, due to their advantages such as compactness, light weight and high heat transfer surface area to fluid volume ratio in comparison to other macro-scale systems.

In his comprehensive review, Kandlikar et al [289] classified channels based on flow considerations. They proposed that conventional channels are identified according to the hydraulic diameter as follows

Conventional Channels: $D_h > 3$ mm

Minichannels: 3 mm $\geq D_h >$ 200 μm

Microchannels: 200 μm $\geq D_h >$ 10 μm

Transitional Channels: 10 μm $\geq D_h >$ 0.1 μm

Transitional Microchannels: 10 μm $\geq D_h >$ 1 μm

Transitional Nanochannels: 1 μm $\geq D_h >$ 0.1 μm

Molecular Nanochannels: 0.1 μm $\geq D_h$

Several works have been reported in the literature to study the microchannel with nanofluid as working fluid. In addition to what has been discussed in chapter two, this section will highlight the previous studies on the enhancement of the heat transfer and fluid flow characteristics for microchannels. Salman et al [290] investigated numerically the enhancement of heat transfer of various nanofluids with micro-tube with constant heat flux. They concluded that the friction factor was not influenced by the volume fraction of the nanoparticle. The same authors [291] presented a numerical and experimental study for the forced laminar flow of nanofluids. They reported an enhancement in heat transfer rate by up to 22% compared to water base fluid. However, the maximum deviation between the numerical and experimental in Nu number was found 10.5%.

Chai et al [292] presented three-dimensional numerical investigation to study the laminar flow in an interrupted microchannel with different configurations. They reported an improvement in the heat transfer coefficient. They attributed this enhancement to the

mixing of hot and cold water in micro-chamber and the much higher redeveloping level of the thermal boundary layer in the microchannel areas. Moahmmadian et al [293] investigated numerically the single-phase heat transfer in the microchannel. They highlighted that increase in volume concentration increased the effectiveness and pumping power of the system. They also highlighted that the frictional contribution of entropy increased with the increase in Re number and volume fraction.

This Chapter will explore the heat transfer enhancement in microchannels using nanofluids with various configurations. The test cases which are presented here are:

I. Flow through the circular cross-sectional horizontal microchannel.
II. Flow through rectangular channels of various aspect ratios
III. Flow through a circular cross-section U-bend
IV. Flow through a rectangular cross-section U-bend

7.2 Circular cross section microchannel

This section will investigate, and the discuss heat transfer rate and the flow characteristic of the nanofluid in a circular cross section horizontal microchannel under constant temperature

7.2.1 Problem Description

The geometry considered in this study is shown in Figure 7.1, a microchannel with length 4 cm and a diameter 106 μm with constant external temperature. The nanofluid enters the channel with temperature T_o=300 K and uniform axial inlet velocity. At the channel exit, a fully developed flow condition is considered. The fluid considered in this study is Tio_2-water nanofluid. The properties of the nanoparticles are shown in Table 1.

Table 7-1 Nanoparticle thermophysical properties

Nanoparticle	Density kg/m^3	Thermal conductivity $w.m^{-1}.K^{-1}$	Specific heat $J.kg^{-1}.K^{-1}$
TiO2	4250	8.93	686.2

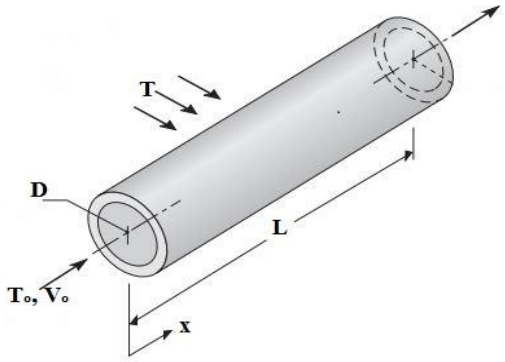

Figure 7-1 Geometry of the microchannel considered

7.2.2 Governing Equations and thermophysical properties of nanofluid:

In the governing energy conservation equation, it is well known that the viscous dissipation terms are generally and neglected for describing conventional flow characteristics. However, in microchannel flows, emerge of a large velocity gradient, may result in major errors when the effects of viscous dissipation are ignored. Hence, incorporating the viscous dissipation effects into the governing equation, in this case is essential.

The term that appeared as a result of kinetic energy change per unit volume, this term is the rate at which the work (against viscous forces) is converted into internal energy, this term is known as the viscous dissipation and expressed as:

$$\boldsymbol{\tau}.\boldsymbol{\nabla u} = \mu\phi_v \tag{7.1}$$

Where ϕ_v is defined in Cartesian coordinates as:

$$\begin{aligned}\phi_v = 2\left[\left(\frac{\partial u_x}{\partial x}\right)^2 + \left(\frac{\partial u_y}{\partial y}\right)^2 + \left(\frac{\partial u_z}{\partial z}\right)^2\right] + \left(\frac{\partial u_x}{\partial y} + \frac{\partial u_y}{\partial x}\right)^2 \\ + \left(\frac{\partial u_y}{\partial z} + \frac{\partial u_z}{\partial y}\right)^2 + \left(\frac{\partial u_z}{\partial x} + \frac{\partial u_x}{\partial z}\right)^2 - \frac{2}{3}(\nabla.\boldsymbol{u})^2\end{aligned} \tag{7.2}$$

The mathematical formulation of the governing equations can be found in Chapter three

The governing equations solved are continuity, momentum equation and energy equation. The thermophysical properties for the nanofluid are expressed as a function of the volume fraction, nanoparticle properties and the thermophysical properties of the base fluid which is water in the present investigation.

The nanofluid density is written as

$$\rho_{nf} = (1 - \phi)\rho_f + \emptyset\rho_s \tag{7.3}$$

The specific heat of the nanofluid is expressed as

$$C_{pnf} = \frac{(1 - \emptyset)\left(\rho C_p\right)_f + \emptyset\left(\rho C_p\right)_s}{\rho_{eff}} \tag{7.4}$$

The thermal conductivity was modelled as:

$$K_{eff} = K_f\left(\frac{K_s + 2K_f - 2\emptyset\left(K_f - k_s\right)}{K_s + 2K_f + \emptyset\left(K_f - k_s\right)}\right) \tag{7.5}$$

The effective viscosity was modelled using the present viscosity model used in Chapter 6 as:

$$\mu_{eff} = \mu_f(1 + 5\emptyset + 80\emptyset^2 + 160\emptyset^3) \tag{7.6}$$

The heat transfer coefficient, Re number, Nu number, the heat flux, friction factor and Pr number formulations were presented in Chapter3, 4, 5 and 6.

7.2.3 Numerical Simulation and Results validations

The governing equations were solved with the boundary conditions(described in section 7.2.1) numerically using ANSYS 15.0. The computational domain was discretized in ANSYS meshing, and the governing equations were solved together with the boundary conditions in ANSYS FLUENT. The CFD code is based on the finite volume method and

SIMPLE algorithm that solves the governing equations. The approach is well known for the solution stability. Second-order upwind schemes were used for the convective fluxes. Convergence was achieved with residuals less than 10^{-6} for all governing equations. To ensure the solution is mesh independent, the maximum Nu number at the outer surface was used. The solution is chosen to be mesh independent when the percentage change in maximum Nu remained less than 1% to ensure a mesh-independent predictions for all simulations in the present investigation. Table 2 shows the mesh dependency test for maximum Nu, and it is clearly seen that for the mesh with 1015454 elements the maximum Nu becomes insensitive to any further refinement and therefore the mesh was selected for the solution.

Table 7-2 Mesh dependency test

Mesh	No. of Elements	Nu_{max}
1	926408	113.26
2	1010200	116.65
3	**1015454**	**119**
4	1020040	119.24

The computational model is first validated with the numerical and experimental data from Lee [294]. The volume fraction in equations (7.1) to (7.4) goes to zero. The results are shown in Figure 7.2. The graph shown represents the relation between Re number and Nu number. As the Re number increases, the Nu number increases. It can be clearly seen the present predictions agree well with the numerical and experimental work by Lee.

Further simulation validations were carried out; the results were compared to the results by Salman et al [291]. The comparisons are shown in Figure 7.3, the results are shown for Re=90, Al_2O_3-water with 1% volume fraction. The comparison shows good agreement between the present simulation and Salman's results.

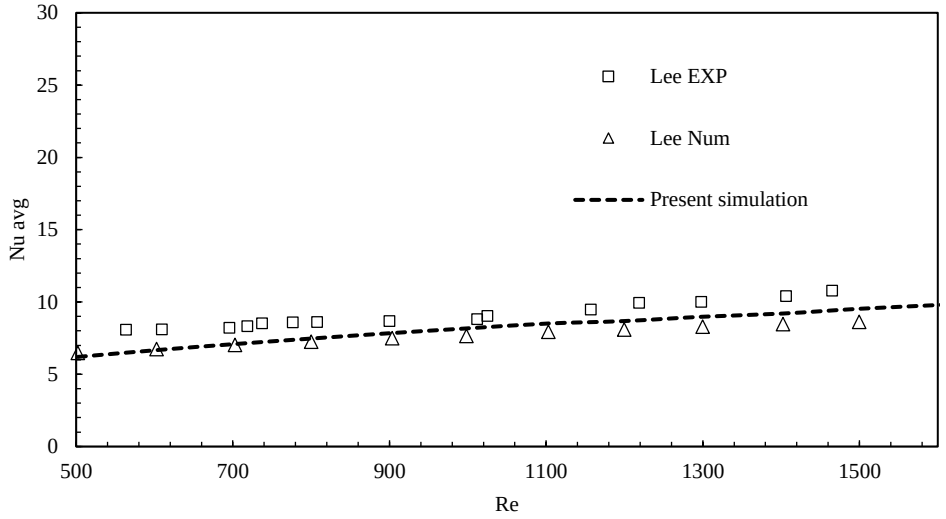

Figure 7-2 Results validations with Lee experiment

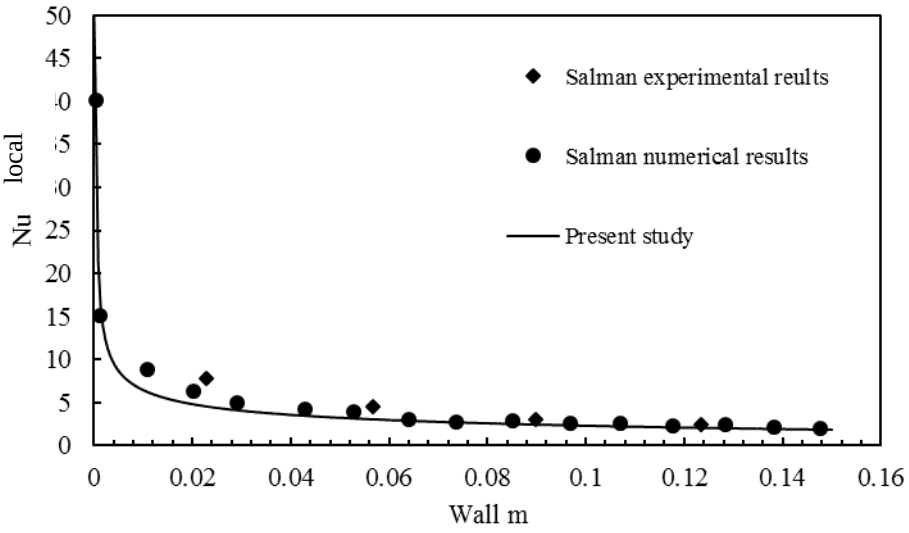

Figure 7-3 Results validations with Salman et al

After the simulations validations have been confirmed, the results of the present investigations are presented and discussed in the next section.

7.2.4 Results and Discussion

The numerical simulations were performed, and the results and the discussions are presented in this section.

The change of the velocity profile in the entrance region is investigated; the results are shown in Figure 7.4. The graph depicts u velocity profile at a different distance from the microchannel inlet. The profile of the velocity is tested at 0.8 mm, 4 mm, 9 mm and 20

mm from the entrance region. The y-axis represents u velocity and x-axis represents a vertical line in the microchannel entrance at a certain distance as shown in Fig 3. The change of the velocity at the end of the entrance region is a parabola, at that point, the flow is fully developed, i.e., the velocity becomes constant at that point onward. However, the velocity at x=0.8 mm from the entrance shows the minimum velocity, which is resulted from the inlet boundary conditions. The more the flow departs from the inlet, the more the magnitude of the velocity until the flow becomes fully developed.

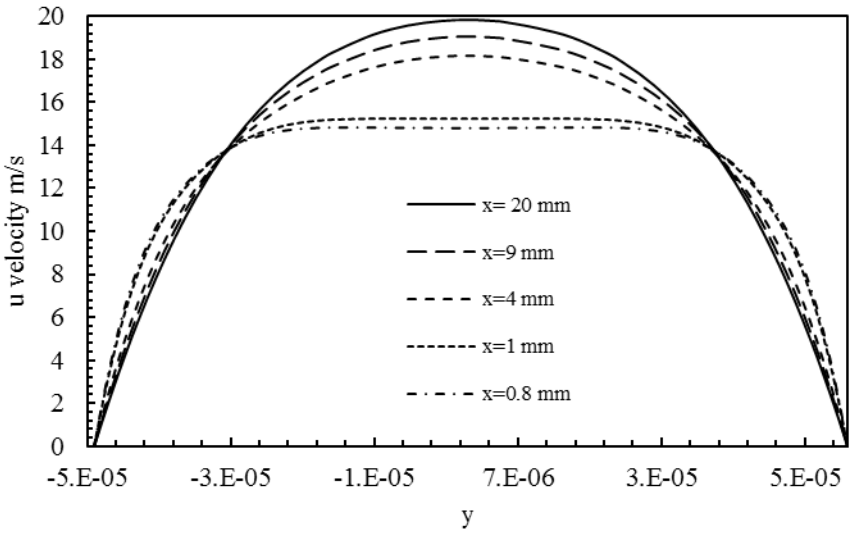

Figure 7-4 velocity change in the entrance region

The viscosity change in the entrance region was also investigated. The understanding of the viscosity change in the microchannels is essential as the viscous dissipation is reported several times in the literature.

The change of the viscosity is illustrated in Figure 7.5. As the viscosity decreases with the increase in the temperature, it can be seen that the viscosity has the maximum value in the entrance of the microchannel. The viscosity is calculated at various distances from the entrance ranging from 0.5 mm to 20 mm where the temperature is constant from that point towards the x-axis of the channel. The reason for this is attributed to the increase in the temperature as a result of the external constant temperature which was assumed as an external boundary condition.

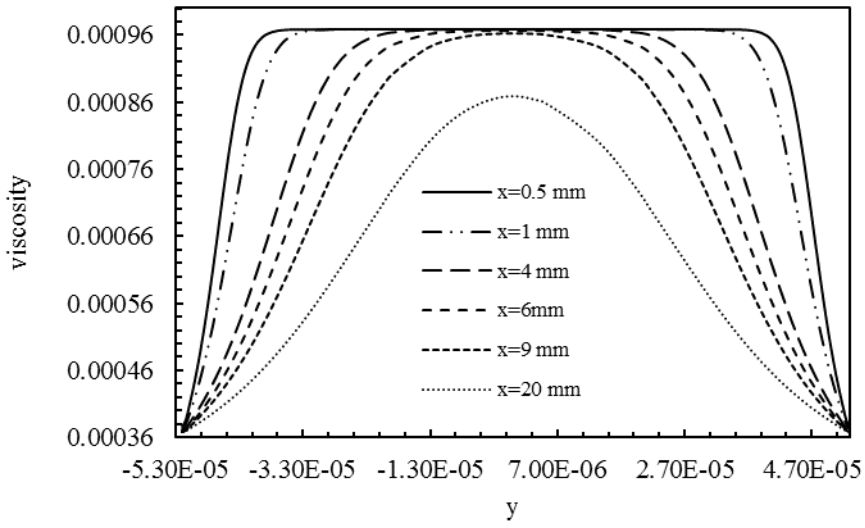

Figure 7-5 Viscosity change in the entrance of the microchannel

The vertical line where the viscosity predicted is located at the diameter of the microchannel. By looking at the constant viscosity at a distance 0.5 mm at the vertical line along the y-axis, this constant value changes suddenly at the near wall region of the microchannel. This sudden change is a result of the viscous layer which has the maximum value near the wall.

In order to investigate the heat transfer enhancement, Nu predictions were also studied. The calculations of Nu values for various volume fractions are shown in Figure 7.6. The range of volume concentrations tested in the present investigations ranges from 0% (pure water) to 6% as well as water.

It is found that Nu begins with a maximum value and decreases along the microchannel wall where it remains unchanged. Also from Figure 7.6, the effect of the volume fraction on the Nu was found in favour of the heat transfer rate. The increase in the volume fraction shows a positive effective on heat transfer. The weakest heat performance was shown in the case of water working fluid. The reason behind the enhanced heat transfer rate as the volume fraction increases is the augmentation in the thermal conductivity due to the presence of the nanoparticles in the fluid. As the thermal conductivity of the working fluid increased rapidly, the nanofluid demonstrated an improvement in the heat transfer.

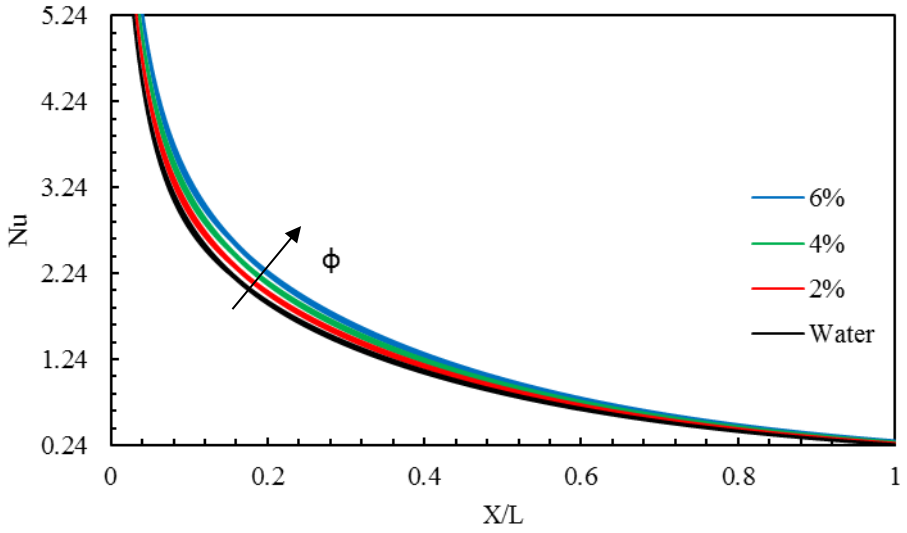

Figure 7-6 The effect of volume fraction on Nu along the microchannel

The drop in the pressure is also investigated for several Re numbers. The understanding of this change is crucial for optimum pump design. The change in the pressure along the microchannel for different Re numbers from 200 to 1800 is shown in Figure 7.7. The pressure decreased along with the microchannel where at the end of the channel zero gauge pressure was assumed. It can be seen that the increase in the Re number will result in the increase in the pressure. This has a negative impact on the pump power. On the other hand, it is that increase in the Re number which promotes the heat transfer

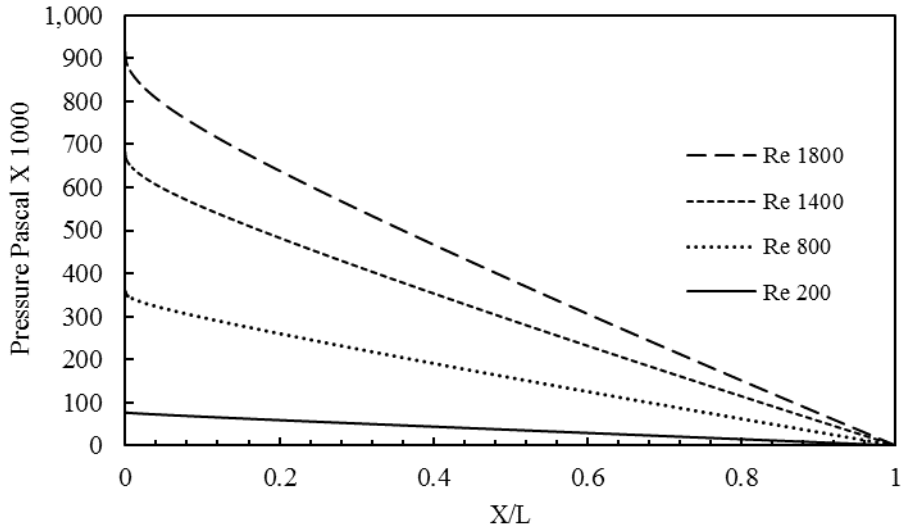

Figure 7-7 The pressure drop in the microchannel

The change of the temperature in the microchannel was also studied in the entrance region. The temperature variation at certain distances is shown in Figure 7.8. The temperature has

the minimum value at the entrance where the fluid enters the microchannel with constant temperature 300 K. As a result of the heat transfer, the temperature of the fluid increased gradually with the x-axis until the flow becomes fully developed where the temperature remained unchanged. At x=0.5 mm the temperature has the lowest value (300 K) which is the same temperature of the inlet boundary condition. At X=20 mm the temperature increased to the maximum value at the centre line of the microchannel. This graph is in line with viscosity distribution presented in Figure 7.5

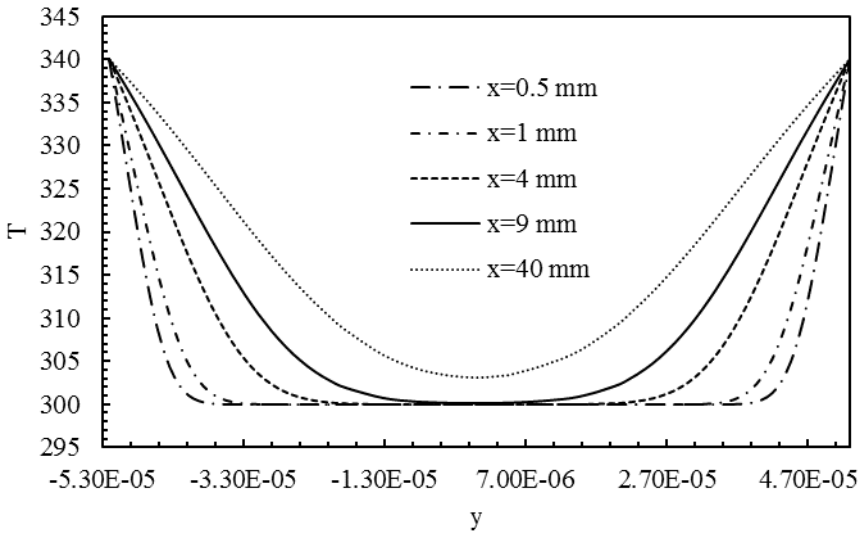

Figure 7-8 The temperature change in the entrance region

The effect of the hydraulic diameter of the microchannel on the heat transfer rate was also investigated, and the results are shown in Figure 7.9

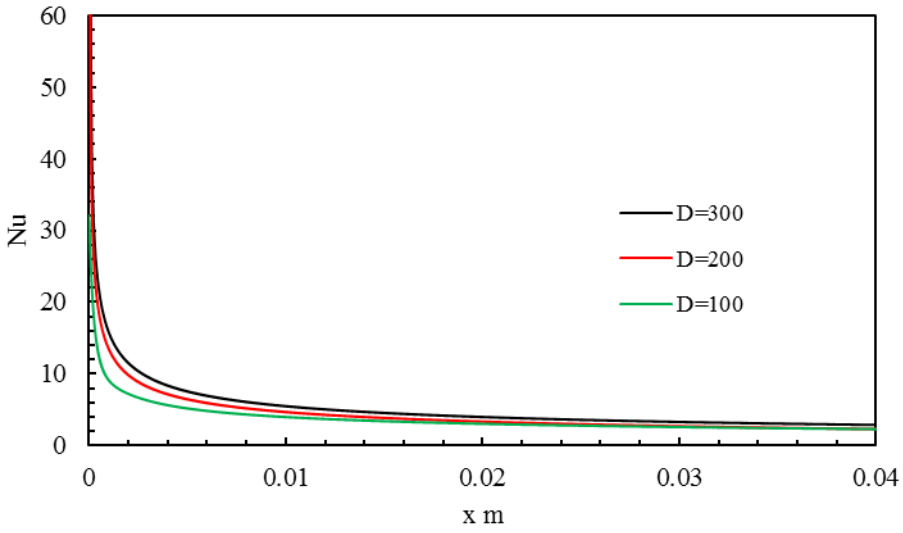

Figure 7-9 Effect of hydraulic diameter on Nu

The graph illustrates the variation of Nu number on the wall of the channel with three hydraulic diameters 106, 200 and 300 μm at constant Re number. From the Figure, it is clearly seen that the Nu number enhanced with the increase in the hydraulic diameter as the tested diameter 300 μm showed the highest heat transfer rate among the diameters tested. The improvement in Nu was remarkable in the developing region as anticipated. The reason behind this is the significant temperature change in this area.

The present study explored the velocity gradient change in the microchannel. The u-velocity gradient change in the vertical line located at the diameter of the microchannel at several locations from the flow entry is calculated, and the results are shown in Figure 7.10.

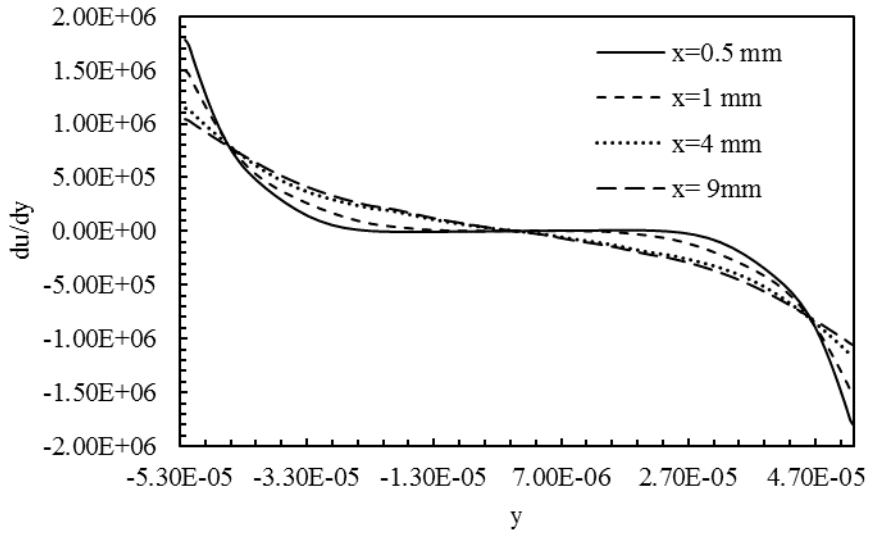

Figure 7-10 The velocity gradient at vertical line in the entrance region.

At the fully developed region the velocity gradient becomes constant where at x=0.5 mm, the u-velocity gradient has the value change in the vertical line, particularly near the wall. However, the value is constant far from the wall. This illustrates that the change of the velocity gradient is significant in the near wall region.

The effect of external temperature on the surface heat transfer coefficient for four Re numbers 200, 500, 1000 and 1600 has been investigated, and the results are shown in Figure 7.11

A

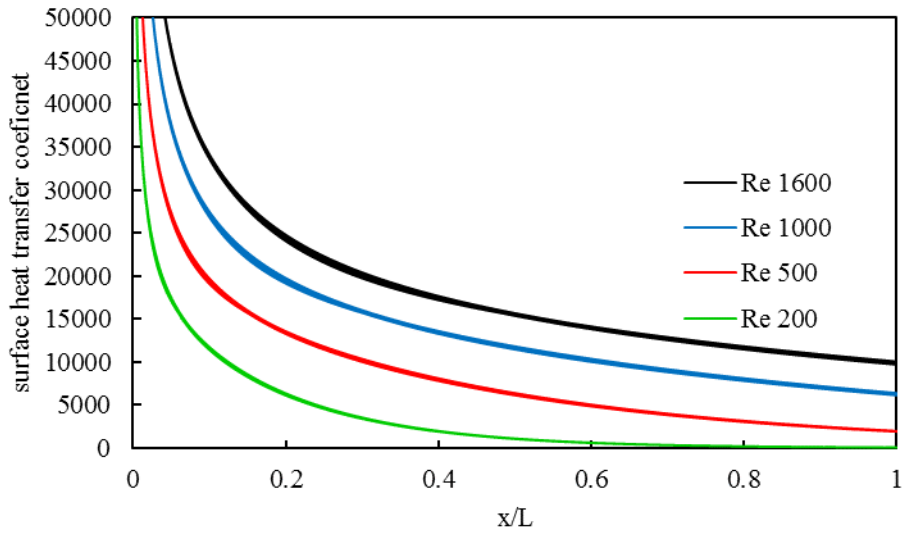
surface heat transfer coeficnet
50000
45000
40000
35000
30000
25000
20000
15000
10000
5000
0
0
0.2
0.4
0.6
0.8
1
x/L
Re 1600
Re 1000
Re 500
Re 200

B

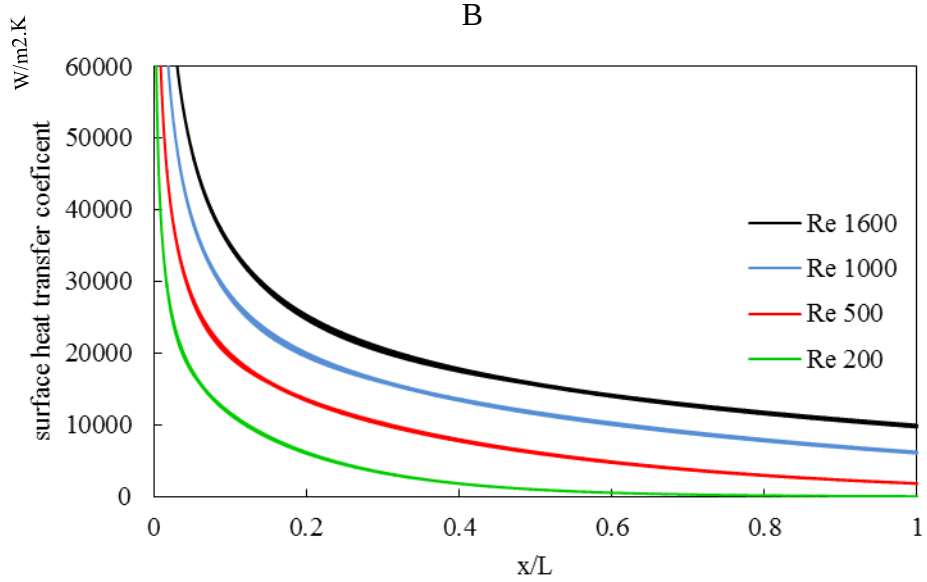
W/m2.K
surface heat transfer coeficent
60000
50000
40000
30000
20000
10000
0
0
0.2
0.4
0.6
0.8
1
x/L
Re 1600
Re 1000
Re 500
Re 200

C

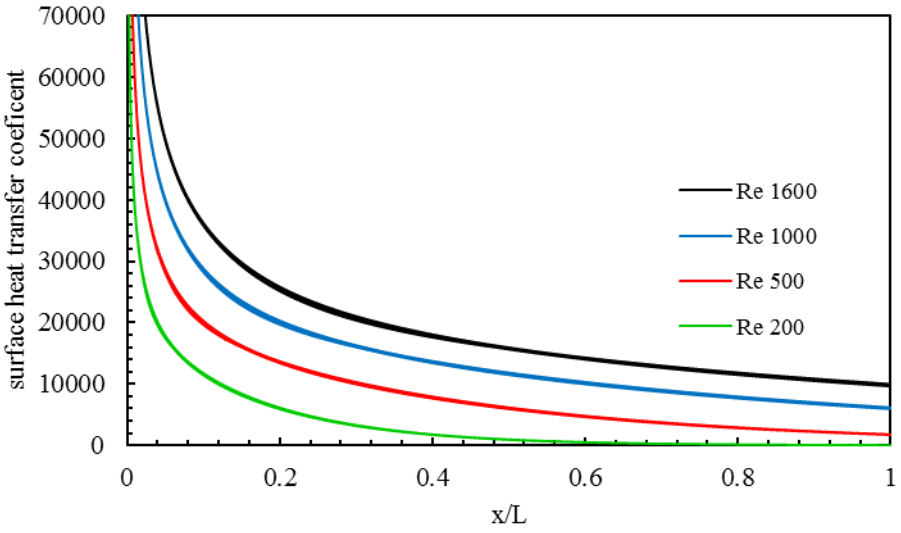

Figure 7-11 Effect of external temperature on surface heat transfer coefficient for a range of Re numbers, A)320 k, B)340 K and C) 360 K

The surface heat transfer coefficient was found to increase with the increase in Re number, and this increase is encountered in all external temperatures tested. However, the increase in the external temperature also increased the surface heat transfer coefficient as seen in Figure 7.11 A, B and C. From the graphs it can be seen that using the nanofluid as a coolant will improve the heat transfer even with increasing the external heat temperature applied on the wall.

7.3 Rectangular cross section with different aspect ratios microchannel

In this section rectangular cross-sectional microchannels with five aspect ratios have been tested with various parameters to get a better understanding of heat transfer enhancement in microchannels.

7.3.1 Problem Description

The problem considered in this section is illustrated in Figure 7.11. The aspect ratio (b/a), tested in this investigation are 1, 1.5, 2, 3 and 4. The hydraulic diameter of the microchannel is 300µm for all aspect ratios tested. The length of the channel is 40 mm, and the upper wall is insulated while the other three walls are maintained at constant heat flux (20 w/cm^2). The flow enters at a uniform velocity and the same as temperature. The working fluid considered is TiO_2, the thermophysical properties were presented in Table 7.1.

A

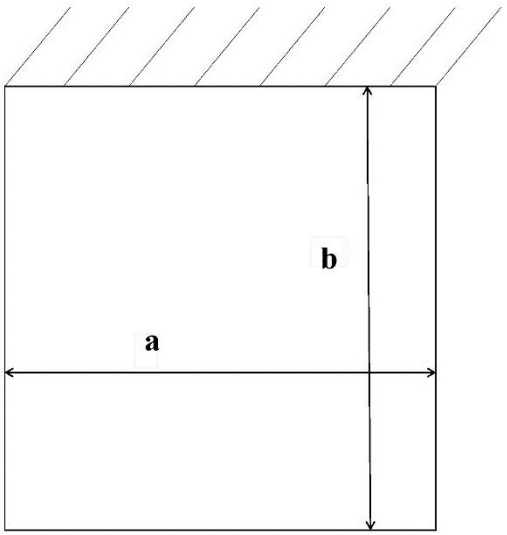

B

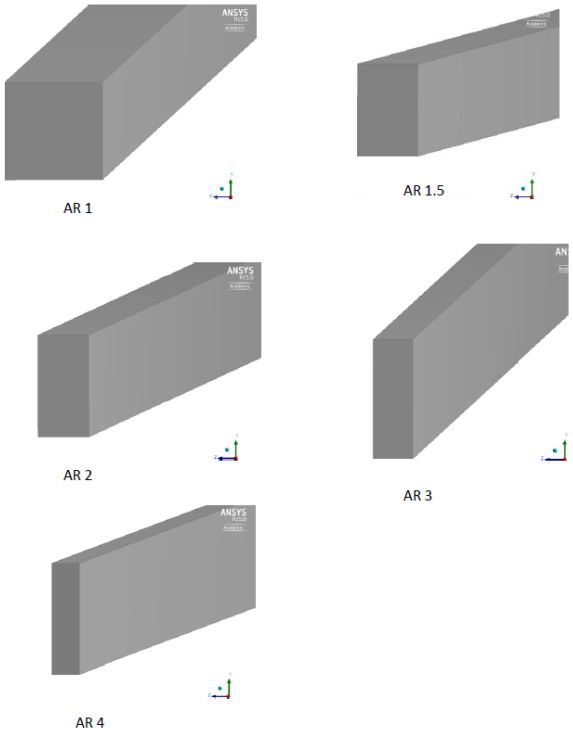

Figure 7-12. Schematic diagram for rectangular microchannel, A) geometry description) Aspect ratios

The microchannel was tested under different volume fractions and various Re numbers. The results are presented and discussed in the following section.

7.3.2 Results and Discussion

The temperature change on the microchannel is investigated, and the results are depicted in Figure 7.12. The graph shown represents the variation of temperature on the wall for various volume fractions. The fluid enters the microchannel as uniform temperature of 300 K, and insignificant change is noticed for the volume fractions tested at the entrance region (up to 0.0035 m). However, as the flow advances in the microchannel, a considerable change in the temperature due to the volume fraction is noticed. The more the fluid advances in the channel, the more change in the temperature is observed.

7.3.2.1 Temperature and thermophysical properties effect

The explanation of the increase in the temperature, in general, is the external heat flux applied on the microchannel wall, though the influence of the nanoparticles is substantial at higher temperature, it can be seen from the graph that the water showed higher wall temperature compared to the nanofluid, the increase in the volume fraction decreases the wall temperature, this is attributed to the adding of the nanoparticles which improved the thermal properties of the fluid as reported by many previous works.

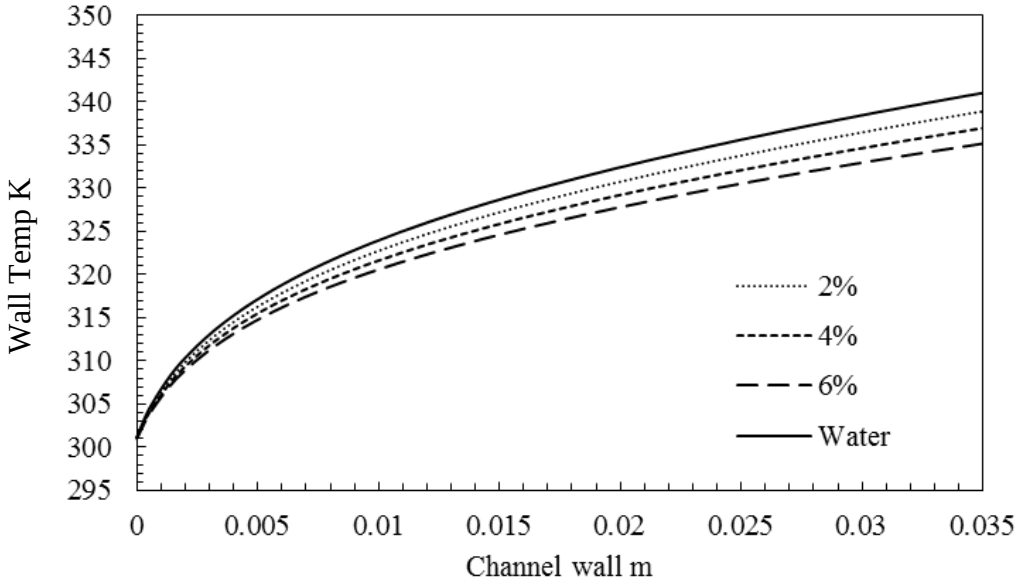

Figure 7-13 Wall temperature change for various volume fractions

To understand the improvement in the thermal properties of the nanofluid due to the suspended nanoparticles, the thermal conductivity of the fluid at the wall for AR 1 and

various volume fractions at Re 100 has been investigated, and the results are illustrated in Figure 7.14.

The thermal conductivity at the wall increases when flow departs the inlet; this increase is due to the increase in the temperature as the thermal conductivity is a temperature dependent property. It was also found that the thermal conductivity improved with the increase in the volume fraction. This increase is explained by equation (7.5) in which the thermal conductivity is improved by the rise in the volume fraction; this improvement is responsible for the heat transfer rate as will be discussed later.

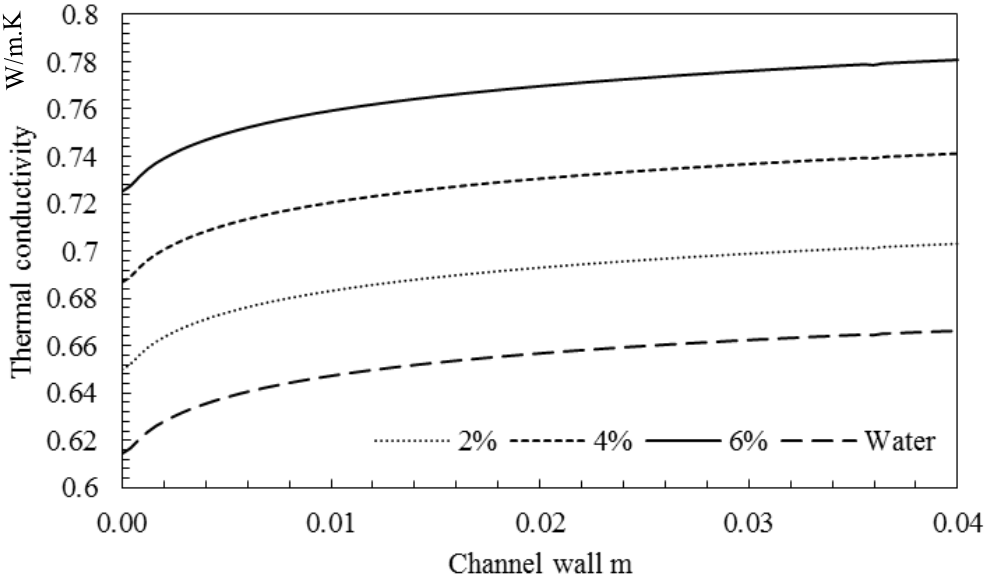

Figure 7-14. Thermal conductivity variation on the wall for various volume fractions

The heat performance is also influenced by another important thermophysical property which is the effective viscosity. The flow in microchannels is remarkably affected by the viscosity due to the viscous dissipation in microchannels.

The effective viscosity variation with the volume fraction of the fluid at the wall has been studied, and the results are portrayed in Figure 7.15.

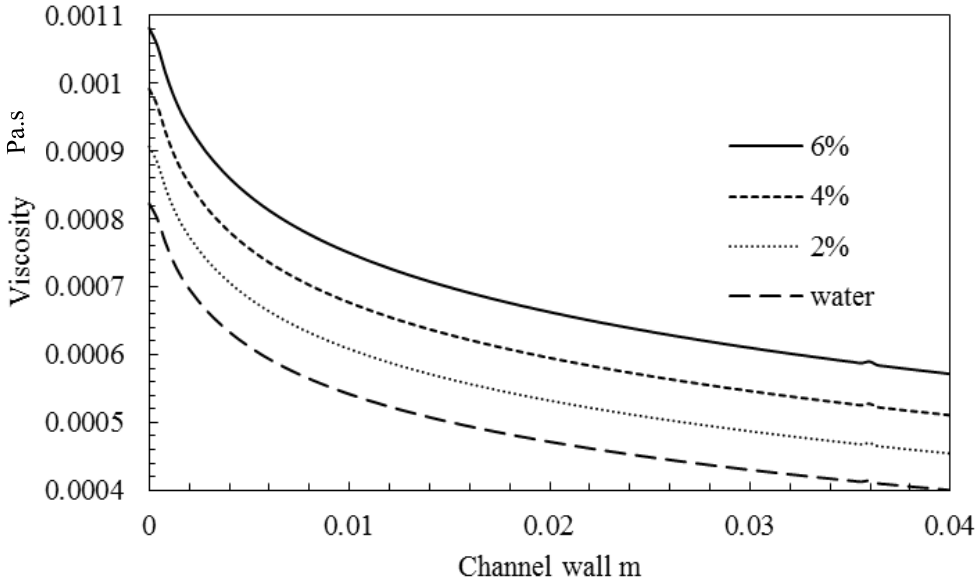

Figure 7-15 Viscosity change on the wall for a range of volume fractions

It can be seen that the viscosity decreases along the wall; the decrease is resulted from the increase in the temperature on the wall as shown in Figure 7.12, water has the lowest viscosity among the cases tested. The decline in the viscosity is also attributed to equation (7.4) which indicates that the effective viscosity is directly influenced by the volume fraction.

The effective viscosity plays a vital role in the flow characteristics and the heat transfer rate in the microchannel as it affects the shear stress and Nu number significantly.

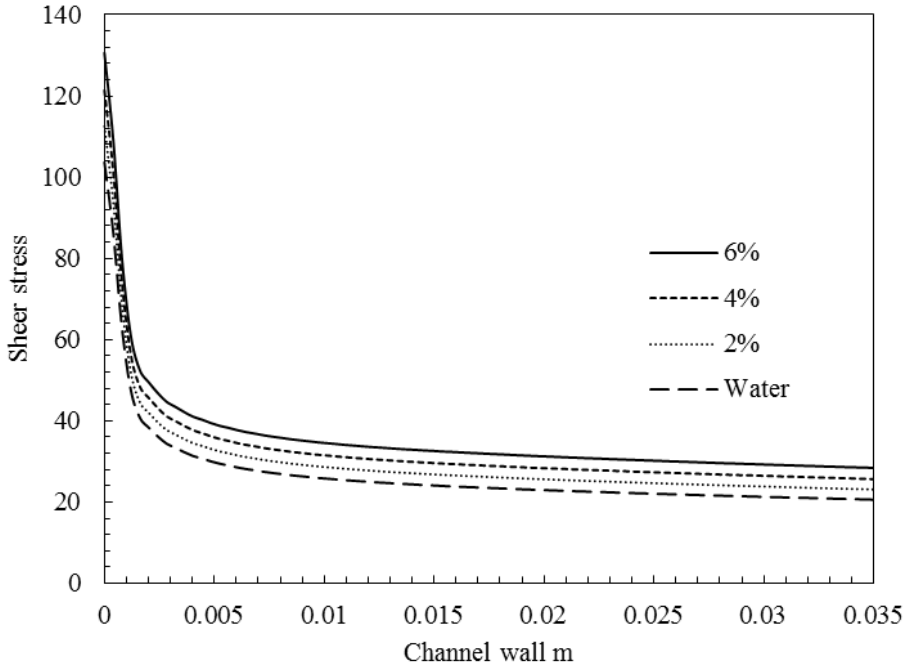

Figure 7-16 Shear stress variation with volume fraction on the wall

The shear stress was studied, and the results for a range of volume fractions are depicted in Figure 7.16. The graph represents the variation of shear stress on the wall of the microchannel for three volume fractions.

It is evident from the graph that the shear stress increases with the increase in volume fraction. As discussed earlier that the heat transfer enhanced with the increase in volume fraction, this enhancement is also accompanied with an increase in wall shear stress which is resulted from the rise in the nanoparticle suspension.

7.3.2.2 Aspect Ratio Effect

The effect of the aspect ratio on the wall temperature was also investigated to give a better understanding of the aspect ratio on various parameters. The results of the temperature variation on the wall for a range of aspect ratios (1, 1.5, 2, 3 and 4) are shown in Figure 7.17. The calculations presented in this section for Re =500 and ϕ=2%.

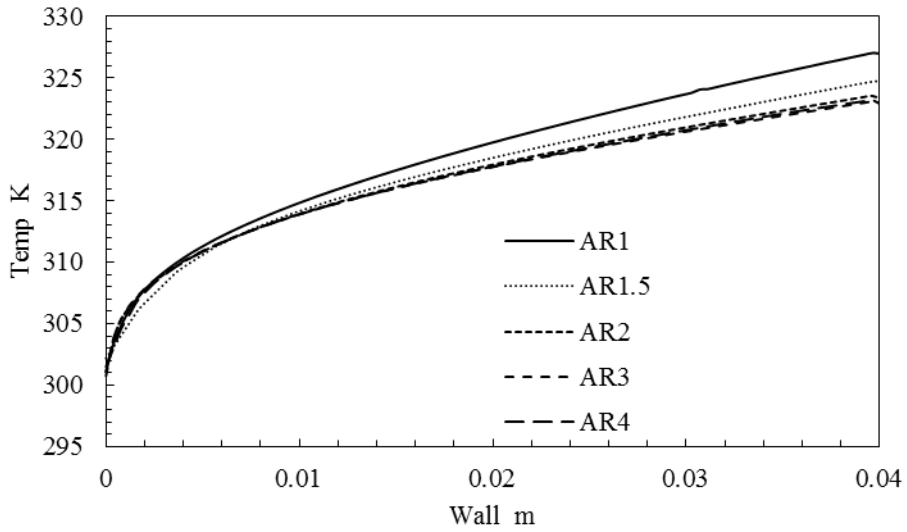

Figure 7-17 Aspect ratio effect on the right wall temperature

It can be noticed from the graph that the wall temperature increases with the flow direction due to the external heat flux applied on the wall as a boundary condition as discussed earlier. Part of the heat is transferred as a results of the flowing the nanofluid as a coolant in this investigation.

It can be seen from Figure 7.17 that the increase in the aspect ratio decreases the wall temperature of the microchannel; however, this variation is almost negligible in the entrance region of the microchannel (up to 1 cm from the inlet).

The noticeable decrease in the temperature can be found between AR 1 and AR 1.5 from 0.1 mm onward, though the decrease is insignificant at AR2, AR3 and AR4. This decrease in the temperature with the aspect ratio is explained by the improvement in the heat transfer with the increase in the wall temperature as well be discussed later.

The influence of the aspect ratio on the viscosity was tested, and the results are illustrated in Figure 7.18. The graph shows the variation of viscosity on the wall at a constant external temperature and constant Re number at fixed volume fraction for a range of aspect ratios.

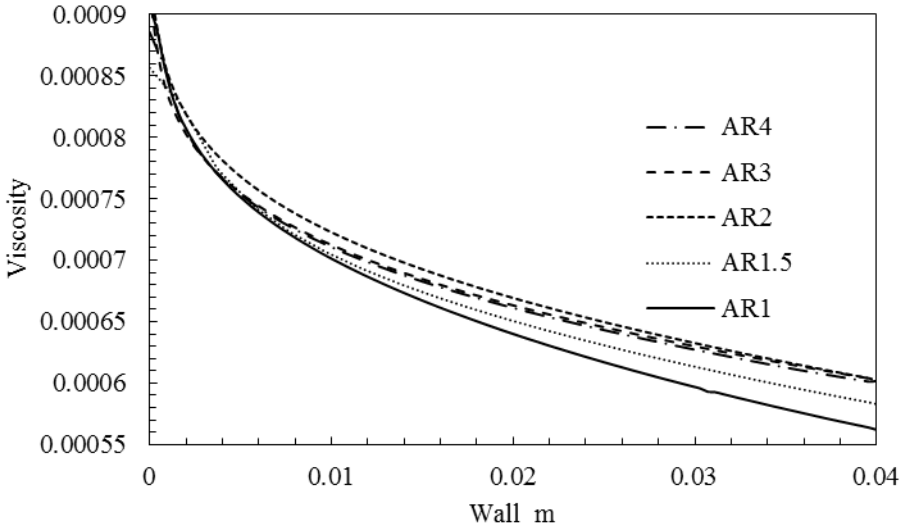

Figure 7-18 Viscosity variation on the wall for a range of aspect ratios

The viscosity of the fluid decreased at the wall as discussed earlier when the volume fraction effect was discussed. However, this decrease in temperature is directly influenced by the aspect ratio of the cross section microchannel. The effect of the aspect ratio on the effective viscosity is negligible in the entrance of the microchannel; this is attributed to the marginal temperature variation in the entrance region for the aspect ratio tested.

However, the viscosity decreased significantly with the increase in the aspect ratio along the length of the microchannel. This variation is more pronounced in aspect ratios AR1 and AR1.5 compared to AR 2, AR3 and AR4.

The effect of Re number on the effective viscosity on the wall and at the vertical line at the right wall was investigated at constant heat flux, and fixed volume fraction at AR4 and the results are depicted in Figure 7.19 and Figure 7.20. Five Re numbers have been tested from 300 to 1600 at constant volume fraction (ϕ=2%).

As reported earlier that the viscosity decreases along the microchannel length due to the external heat flux. This decrease is noticed in all Re numbers tested. However it was found that the increase in Re number increased the viscosity along the microchannel length. This increase in viscosity is explained by the increase in the inertia force which is accompanied by an increase in the viscous force and hence increasing the effective viscosity.

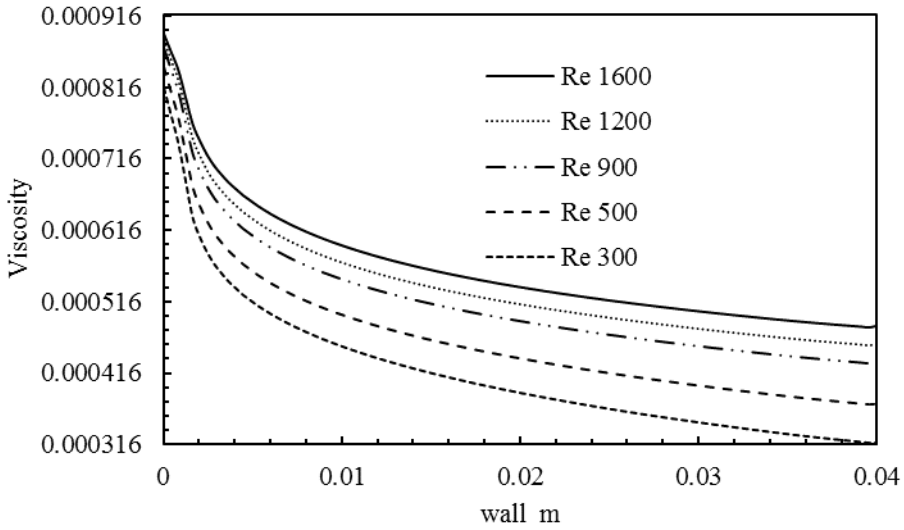

Figure 7-19 Effect of Re number on viscosity at the wall

The effect of Re number on the viscosity on a vertical line on the side wall of the microchannel for AR4 at volume fraction 2% was also investigated, and the results are shown in Figure 7.20.

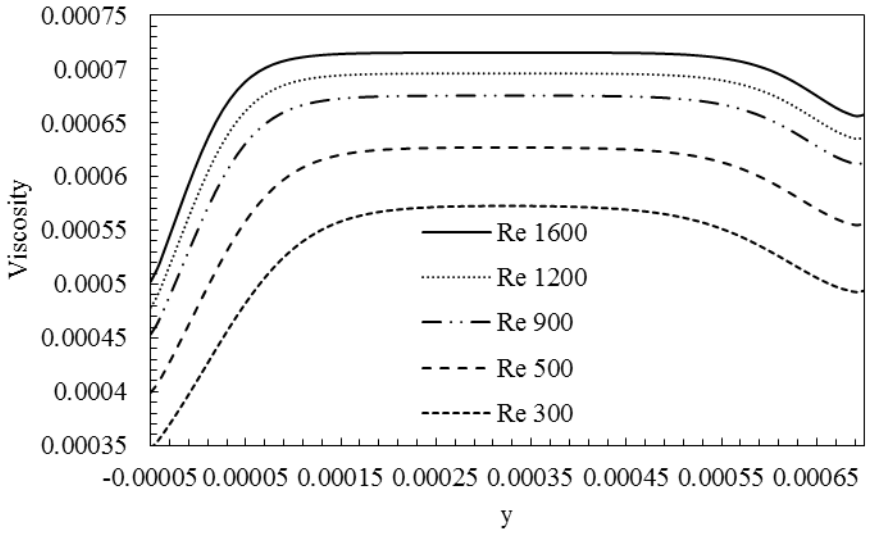

Figure 7-20 Effect of Re number on viscosity at vertical line at wall for AR4

It is evident that the increase in Re number increased the viscosity on the vertical line on the right wall, it can be seen that the viscosity has the minimum value at the lower side of the microchannel due to the higher temperature. However, the viscosity remains unchanged in the middle region as temperature is constant and the viscosity declined again at the top side of the microchannel as it is assumed adiabatic wall.

The variation of Nu along the wall of the microchannel was calculated and the results are portrayed in Figure 7.21.

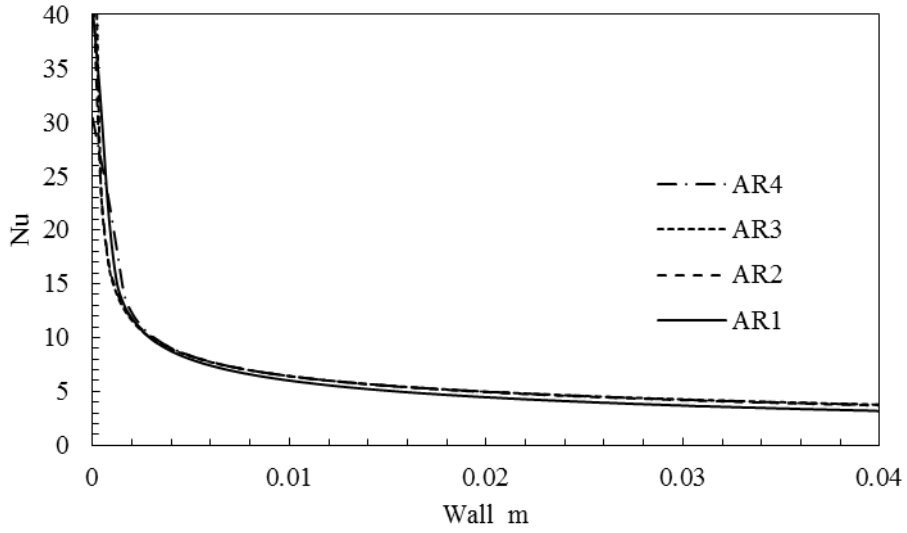

Figure 7-21 Aspect ratio effect on Nu number

From the graph shown it can be seen that Nu number showed an insignificant increase due to the increase in the aspect ratio. To give a clear representation of the heat transfer rate, the average Nu number was calculated over the whole length and the results are introduced in Table 7.3.

Table 7-3 Aspect ratio effect on Nu_{avg}

Aspect ratio	**Nu_{avg}**
1	5.964
2	6.112
3	6.288
4	6.493

It is evident from Table 7.3 that the average Nu number increases with the increase in the aspect ratio; the rise in AR4 compared to AR1 was found 8%. This performance can be employed to enhance the heat transfer rate by increasing the aspect ratio. This finding endorses that the increase in the aspect ratio as well as the increase in the volume fraction can enhance heat transfer rate.

The local skin friction factor was studied for a range of Re numbers and the results are shown in Figure 7.22.

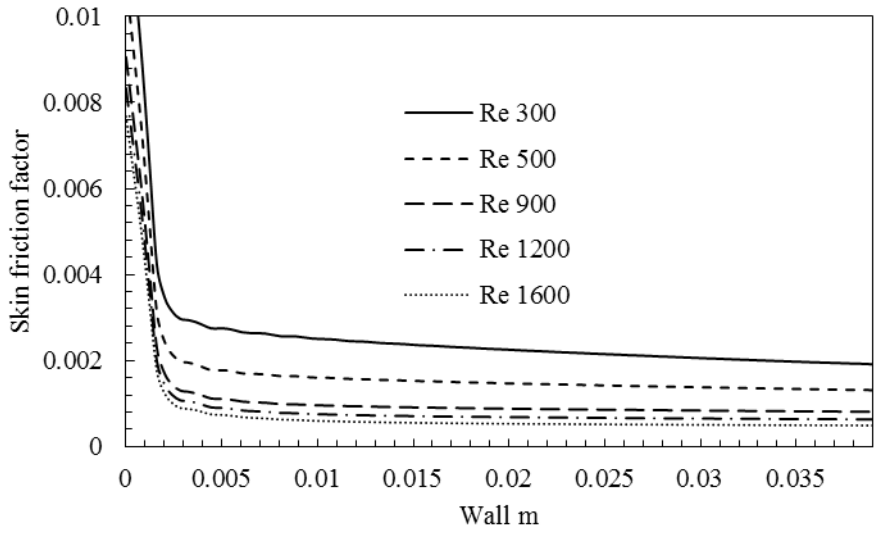

Figure 7-22 Re number effect on the local skin friction factor

From the figure it can be seen that the local skin friction factor increases with the decrease in Re number, this is in agreement with what is anticipated by the relation between Re number and the skin friction factor.

The wall shear stress at the vertical side at different locations was studied, and the results are shown x=0.5 mm from the inlet and at x=20 mm from the inlet, the first represents the entrance region where the flow is developing and the later in the middle of the flow stream in the microchannel. The results are depicted in Fig 7.23 and 7.24 respectively.

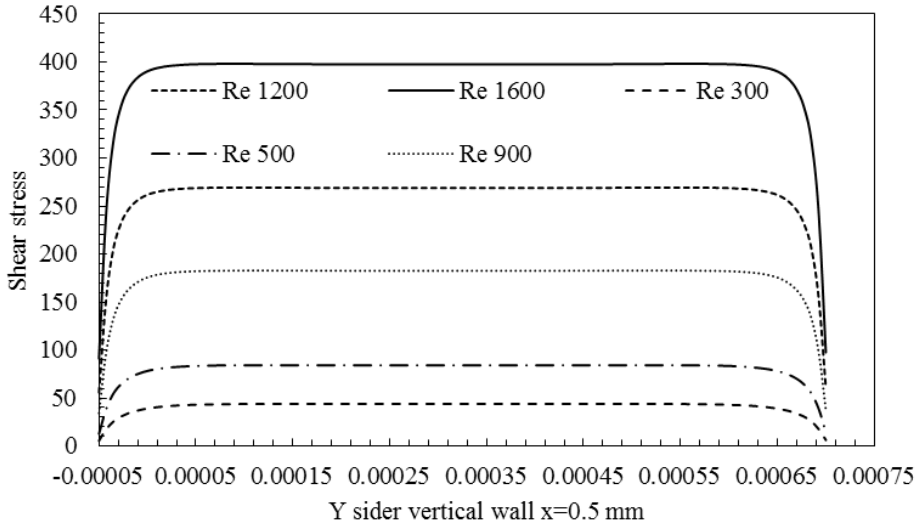

Figure 7-23 wall shear stress at vertical side wall x=0.5 mm

The understanding of the shear stress behaviour in the microchannel is crucial for a better design of the microchannel industry. Hence the variation of the wall shear stress along the

horizontal wall and the vertical side of the microchannel was also tested and investigated thoroughly for a range of Re numbers.

The graph illustrates the change of the shear stress at the side wall of AR4 microchannel at 0.5 mm from the inlet at volume fraction 2% for a range of Re numbers. It is evident that the shear stress increases with the increase in Re number, this increase applies to Figure 7.24 where x=20 mm as well.

However, it was noticed that the shear stress is much higher in the entrance region as it can be seen when comparing the results in the two graphs. The increase is due to the higher the velocity gradient.

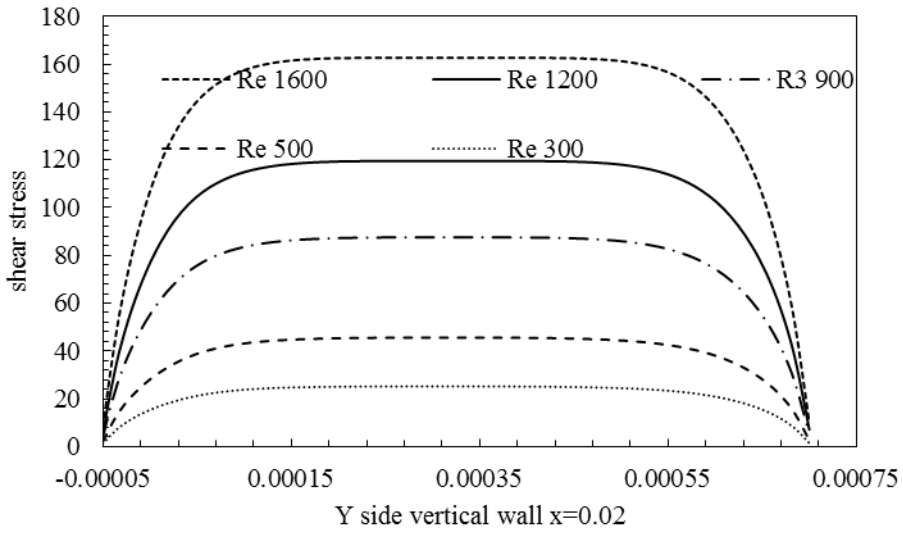

Figure 7-24 wall shear stress at vertical side wall x=20 mm

The increase in the wall shear stress with the increase in Re number in the entrance region is explained by the fact that the shear stress is proportional to the viscosity, and it is known that the viscosity is increased by the increase in Re number as shown and discussed earlier in Figures 7.19 and 7.20.

7.3.2.3 Flow contours

The contour of the thermal conductivity, velocity and temperature at different locations are shown to give a better understanding of the temperature and flow characteristics for various Re numbers in the in the microchannel cross section.

The temperature contours for Re numbers 500, 300, 900 and 700 are shown in Figure 7.25 a, b, c and d respectively. It can be seen from the figure that with the increase in Re the

temperature of the fluid decreases as a result of the improvement in the heat transfer rate which is resulted from the temperature difference between the fluid and the wall as discussed earlier.

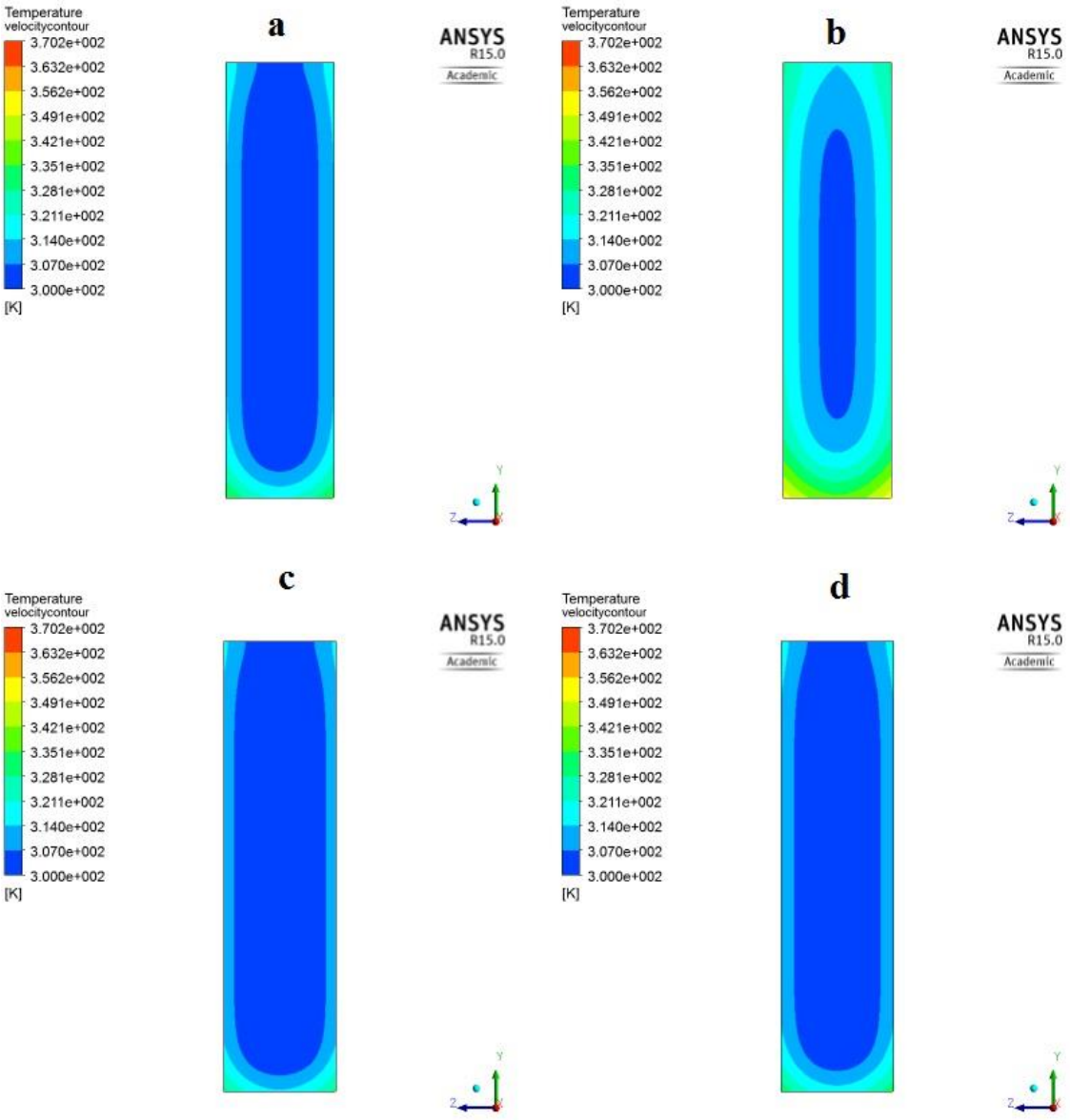

Figure 7-25 Temperature contour for AR4 at :) a Re500 b) Re300 c) Re900 d) Re 700

The thermal conductivity and its change in the microchannel was studied, and the contours for four Re numbers are shown in Figure 7.26. This thermophysical property was calculated based on 2% volume fraction at four Re number as listed in the temperature contours.

As the thermal conductivity is a temperature dependent property, the thermal conductivity reduced with the rise in Re number as shown in the contour in Figure 7.26. The contour is

taken at x=3 mm from the inlet, i.e. the entrance region where the temperature of the inner fluid has not grown yet.

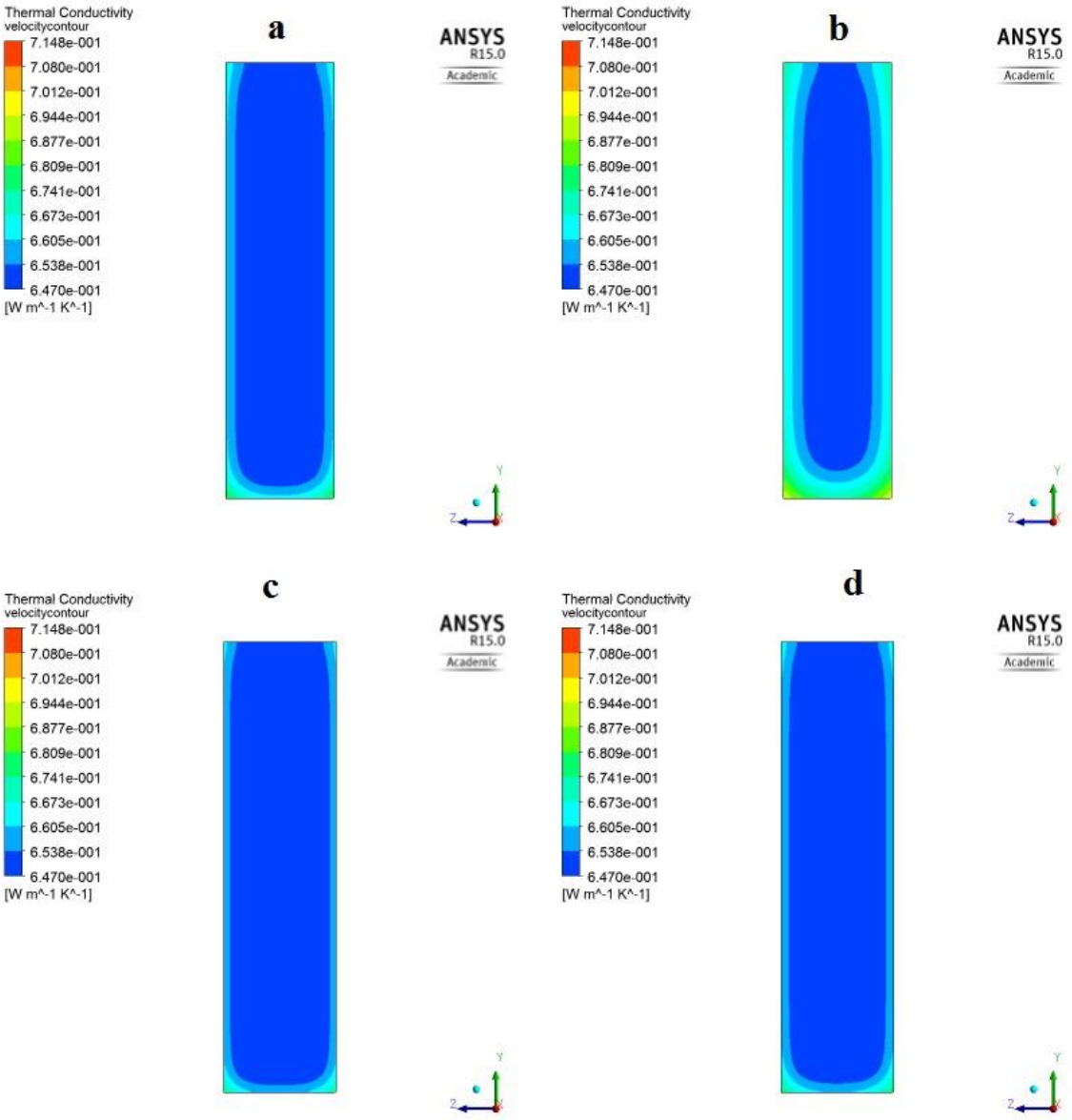

Figure 7-26 Thermal conductivity contour for AR4 at :) a Re500 b) Re300 c) Re900 d) Re 700 at x=3 mm

The contour of the thermal conductivity at the middle of the microchannel(x=0.02 m) is shown in Figure 7.27 for four Re numbers. The figure shows the thermal conductivity for Re numbers 300, 500, 700 and 900 in a, b, c and d respectively.

By looking at Figures 7.26 and 7.27 it can be seen that the thermal conductivity developed due to the augmentation in temperature. The increase in the temperature and hence the thermal conductivity in the developed region is caused by the external heat flux applied on the microchannel wall.

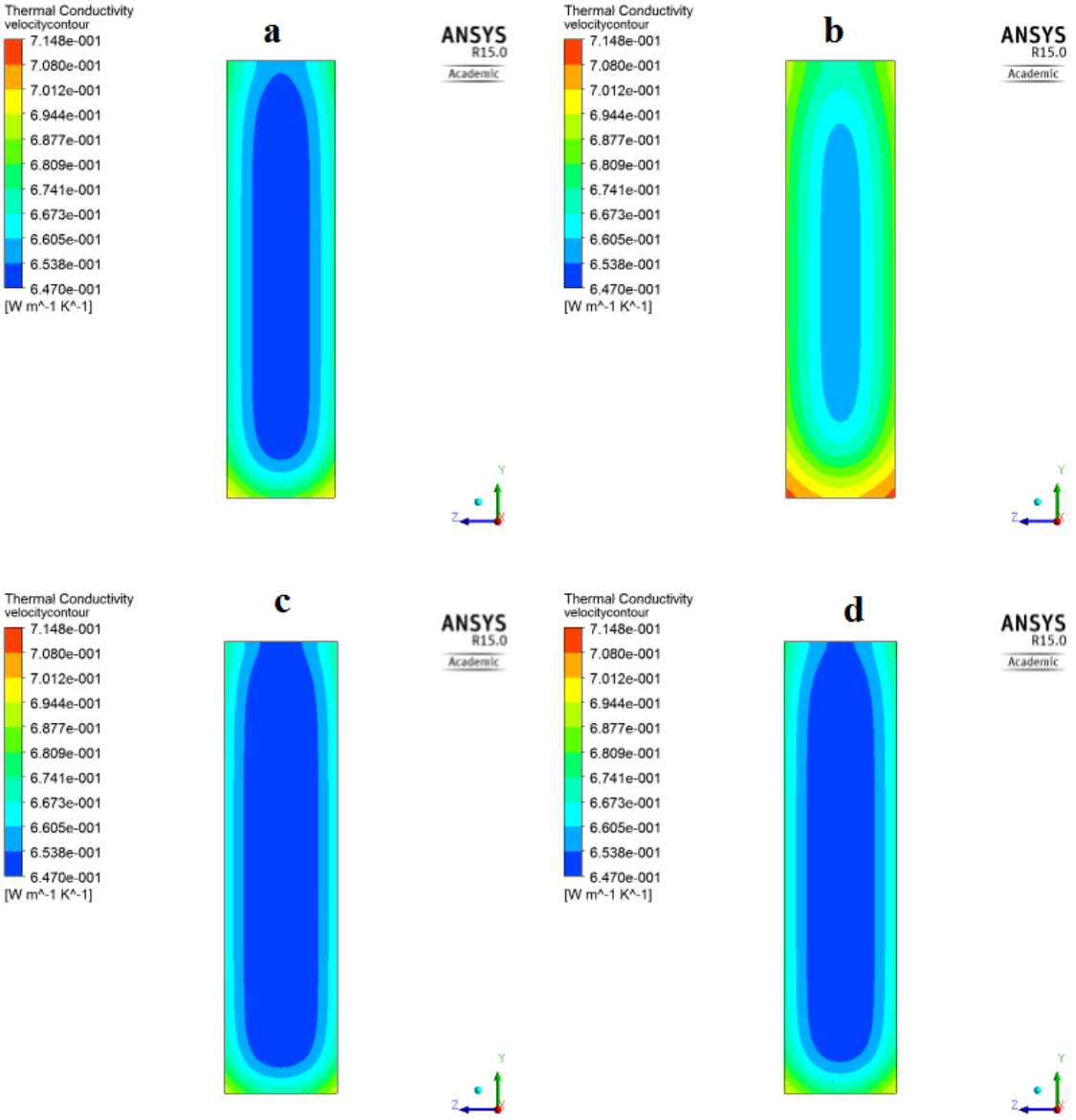

Figure 7-27 Thermal conductivity contour for AR4 at :) a Re500 b) Re300 c) Re900 d) Re 700 at x=20 mm

The velocity contour was also investigated and the contour in portrayed in Figure 7.28. As Re number is a function of velocity, so it is anticipated that the Re number is increased with the rise in velocity. This rise which implies that the inertia force escalates is in favour of heat transfer rate. This is in agreement with previously reported suggestion of improving the heat transfer by increasing Re number. It is evident that the velocity for Re number 900 is the highest among other Re numbers in the fully developed region (in the middle of the microchannel, x= 20 mm)

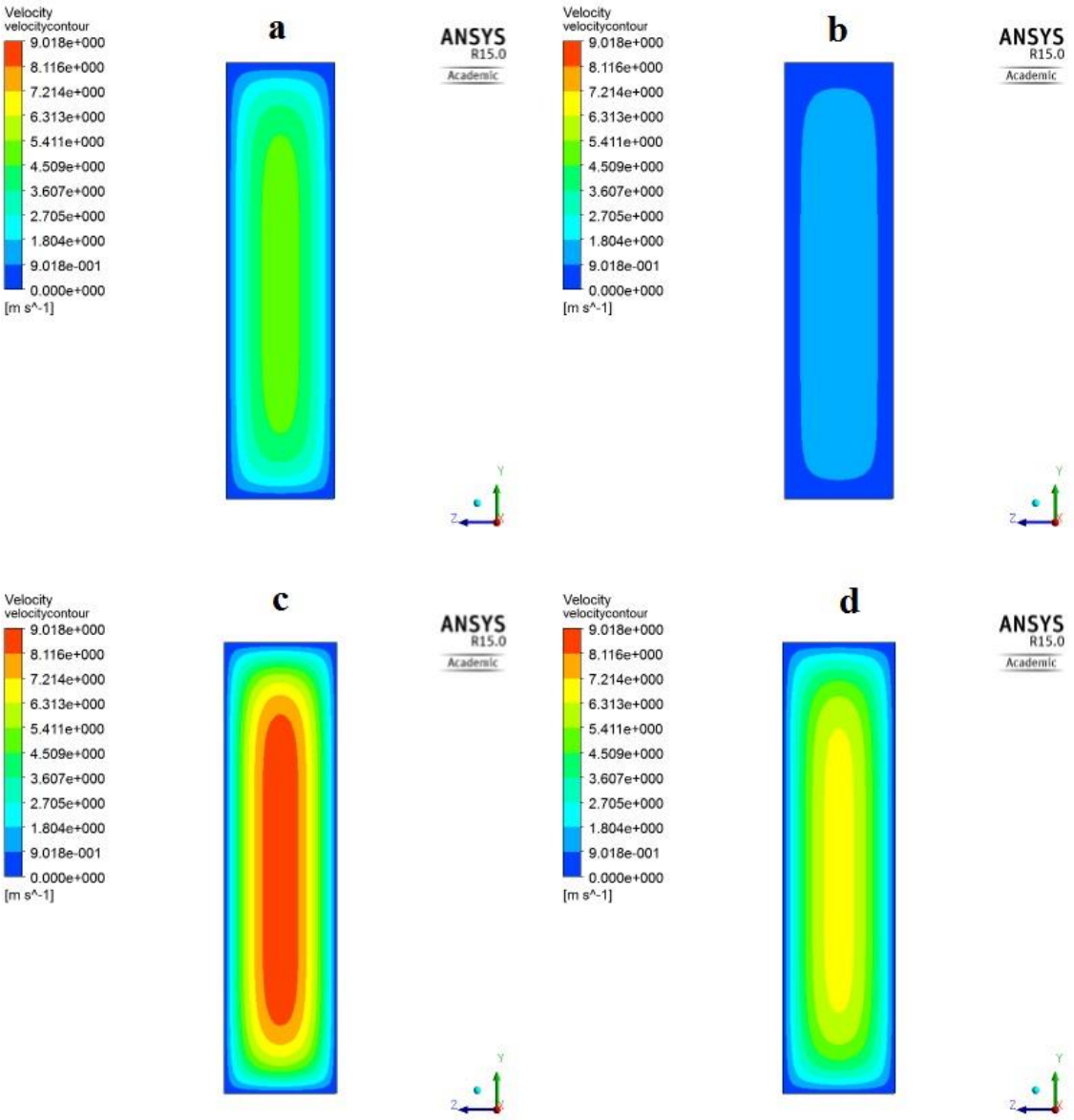

Figure 7-28 Velocity contour for AR4 at :) a Re500 b) Re300 c) Re900 d) Re 700 at x=20 mm

7.4 U-bend microchannel

The flow inside microchannel using nanofluid was studied for an additional configuration of geometry configuration. In this section, the flow in a circular cross section U-bend microchannel is studied, and the results of the heat transfer enhancement and flow characteristics are presented and discussed.

The main objective of studying the U-bend microchannel is to investigate the pressure coefficient and shear stress at the bend of the microchannel. The temperature, Nu number and the thermophysical properties such as thermal conductivity and viscosity were tested at the upstream pipe, downstream pipe and the bend of the microchannel. Knowledge of

the fluid flow and heat transfer will be useful in designing complex electronic systems for efficient heat transfer.

7.4.1 Problem Description

The geometry considered in the present investigation is shown in Fig 7.29. The flow inters the inlet with uniform temperature T_i=300 K and initial velocity V_i and leaves the exit with zero pressure gauge. An external heat flux is applied on the wall, the working fluid is TiO2-water nanofluid, the thermophysical properties of the nanofluid was presented in Table 7.1. The fluid is assumed homogenous and there is no slip between the particles and the base fluid.

The microchannel diameter is 100 µm, the axial lengths of upstream and downstream pipes are 40 mm and the distance between inlet and outlet centres is 500 µm. The domain was discretised using ANSYS meshing, and grid independent solution was obtained with 835624 cell which was used in the whole investigation for this section.

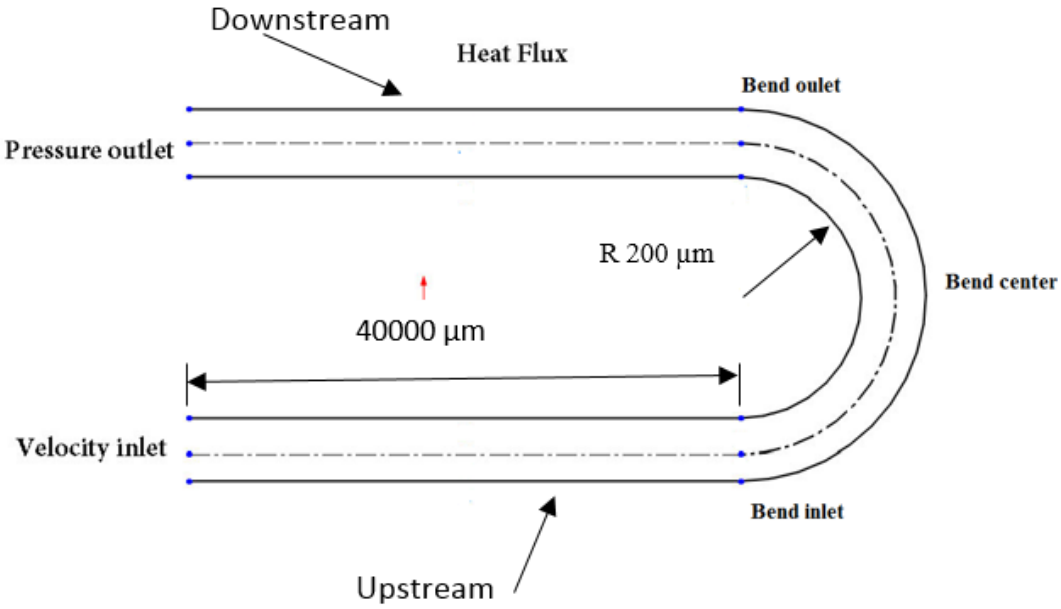

Figure 7-29 Circular U-bend microchannel

7.4.2 Results and Discussion

This section presents results of the investigation of the enhancement of heat transfer and fluid flow characteristics in a U-bend microchannel.

The variation of Nu number at various volume fractions in the upstream pipe of the microchannel was investigated, and the results are described in Figure 7.30. The results are shown for four volume fraction 2%, 4%, 6% and water base fluid at Re number 500. The Nu number drops sharply at the microchannel inlet till the point where the temperature becomes steady, and the flow becomes fully developed, at which point, the Nu number remains unchanged along the microchannel upstream. It can be seen that the local Nu number increases slightly with the increase in the volume fraction.

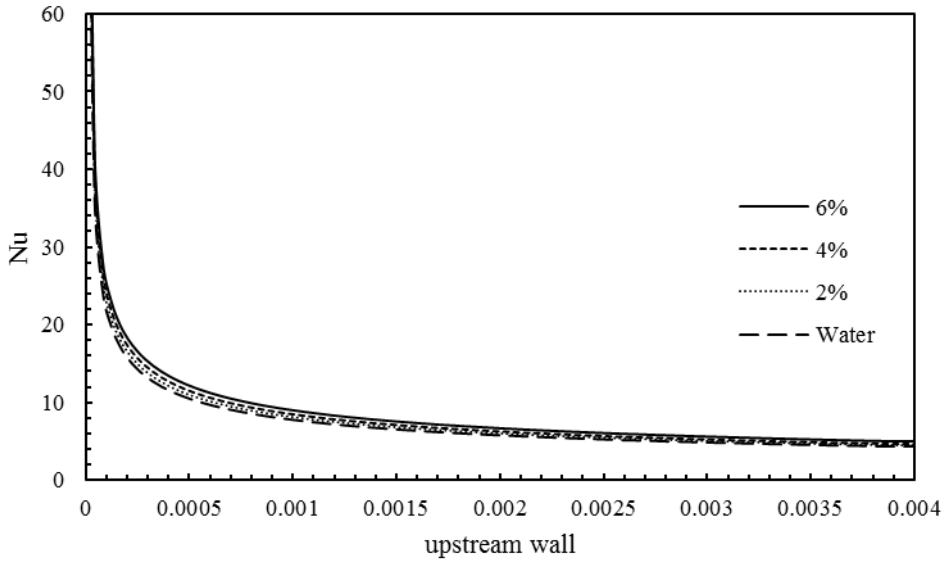

Figure 7-30 Nu variation at upstream wall with volume fraction

The average Nu number for the whole length was also calculated along the wall, and the results are shown in Table7.4. From the table, it was found Nu number enhanced by up to 14% when using 6% volume fraction compared to water as the base fluid.

Table 7-4 Average Nu number in the upstream pipe

Volume fraction ϕ	**Nu_{avg}**
water	8.152
2%	8.604
4%	9.067
6%	9.539

The improvement in the heat transfer in the downstream pipe was also investigated at the same conditions discussed earlier and the results are shown in the Figure 7.31. The Nu number decreases gradually at the inlet of the downstream pipe where the wall temperature increases and the fluid temperature increases due to the external heat flux. However, it was

noticed that Nu number in the downstream pipe is much less than that of the upstream pipe. The Nu improved with the rise in volume fraction in both the upstream and downstream pipe.

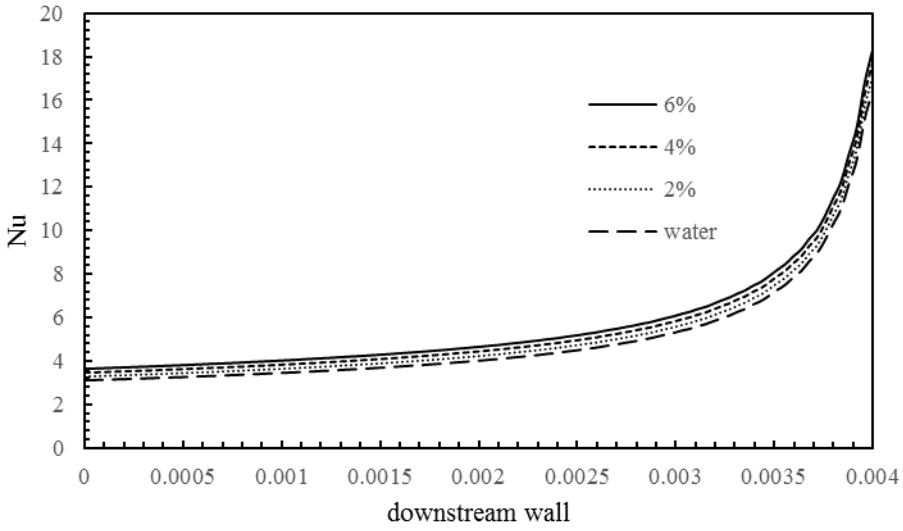

Figure 7-31 Nu number change with volume fraction at the downstream pipe

The average Nu number in the downstream pipe was predicted, and the results are presented in Table 7.5 for various volume fractions. The average Nu number increased up to 11% which is slightly less than that of the upstream pipe.

From this investigation it was found that most of the heat transfer occurred in the U-bend microchannel took place at the upstream pipe, this can be explained by the initial uniform velocity and the higher shear stress in the U-bend as will be discussed later.

Table 7-5 Average Nu number for various volume fraction at the downstream wall

Volume fraction ϕ	downstream Nu_{avg}
water	4.992
2%	5.214
4%	5.443
6%	5.669

To understand how the heat transfer in the U-bend, the variation of Nu in this area was studied in both x-direction and y-direction and how it is affected by the volume fraction.

The change of Nu number in the x-direction with the volume fraction is investigated, and the results are illustrated in Figure 7.32.

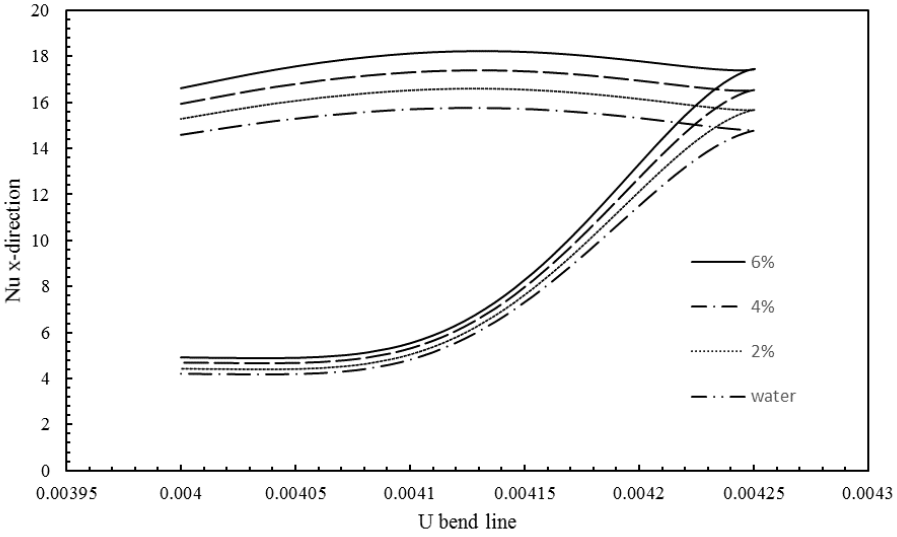

Figure 7-32 Nu variation with volume fraction in U-bend x-direction

It can be seen from the Figure that the heat enhanced in the lower half of the U-bend than that of the upper half of the U-bend. The Nu increased from 4 to 14 when the flow leaves the upstream pipe and enters the U-bend. At x=0.0045 m which represents the point at the middle of the U-bend, the heat enhancement was the peak, after which, the Nu shows an insignificant decline. This decline continues till the value which represents the start of Nu at the downstream pipe which was shown earlier in Figure 7.31 where Nu drops again from 16-18 to 2-4.

It was also noticed that the heat transfer improved significantly with the augmentation of the nanoparticle, this improvement is valid at all locations investigated, however, this improvement is more pronounced in the upper half of the U-bend which is ultimately entering the downstream pipe. This noticeable improvement is attributed to the lower local shear stress.

From the Figures 7.30, 7.31 and 7.32, it can be seen that the Nu number increases in the x-direction only when the flow enters the lower half of the U-bend, whereas Nu decreases in upstream pipe, downstream pipe and the upper half of the U-bend

The change of Nu number with the volume fraction in the y-direction was investigated, and the results are depicted in Figure 7.33. The Nu improved rapidly with the increase in the y-direction up to the middle of the U-bend (the direction of the flow), after which, the Nu number remains unchanged till it leaves the U-bend and enters the downstream pipe, it

can be seen that the flow leaves the bend with Nu 16-18 which the same value of Nu number where the flow enters the downstream pipe as shown in Figure 7.31

The heat performance was improved with the increase in the volume fraction and water showed the weakest Nu in the cased tested. It was also noticed that this increase in pronounced in the range (167-467 μm) which represents the end on the lower half of the U-bend.

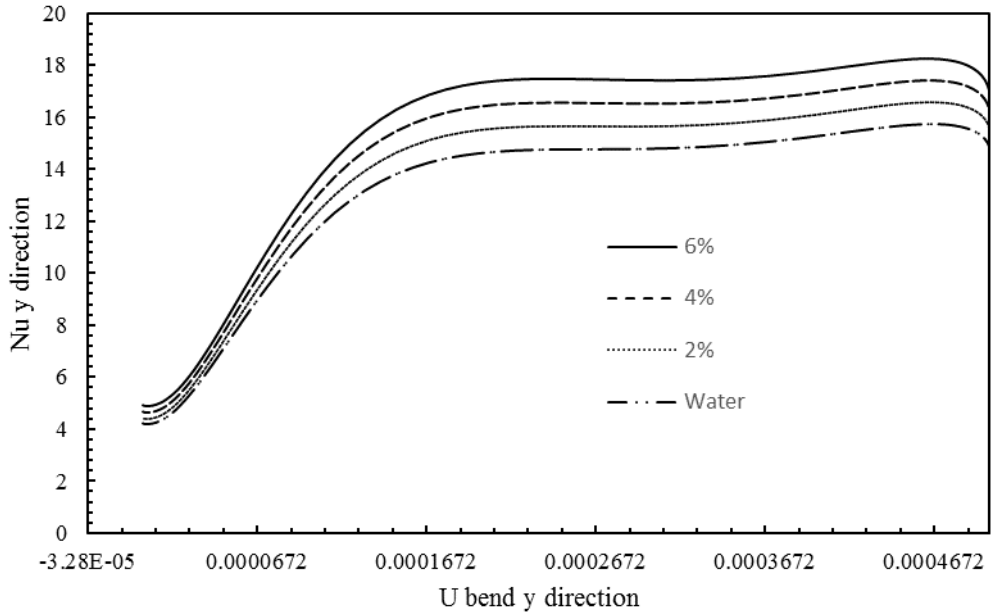

Figure 7-33 Nu change with volume fraction in U-bend y-direction

The change of the temperature at the wall was investigated for a range of volume fractions in the upstream wall and the results are illustrated in Figure 7.34. The temperature at wall starts with value 300 K which is the temperature of the inlet fluid and increases in the x direction which represents the flow direction. This rise in temperature is resulted from the external heat flux, and it continues until the end of the upstream pipe where the temperature reached 320 K.

It is evident from the graph that the wall temperature increases with the decreases in the volume fraction, this increase in more noticeable at the end of the upstream pipe.

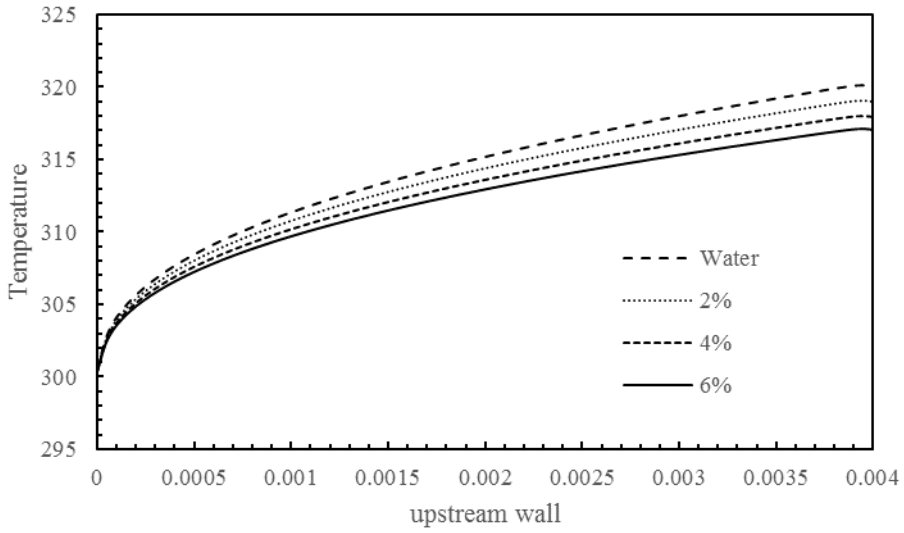

Figure 7-34 Wall temperature variation with volume fraction in the upstream pipe

The variation of the wall temperature in the downstream wall is shown in Figure 7.35. The temperature increases sharply again from 304 K to 327 K at the downstream pipe exit. This rise is attributed to the external heat flux applied to the downstream pipe as well.

The increases in the volume fraction decreased the wall temperature of the microchannel, this decrease in more pronounced when increasing the temperature which located in the downstream pipe exit. It was noticed that water showed the highest wall temperature among various volume fluids tested. This is in agreement with the enhancement of Nu number due to the increase in volume fraction which implies that the heat exchanged profoundly as a results of the nanoparticle suspension.

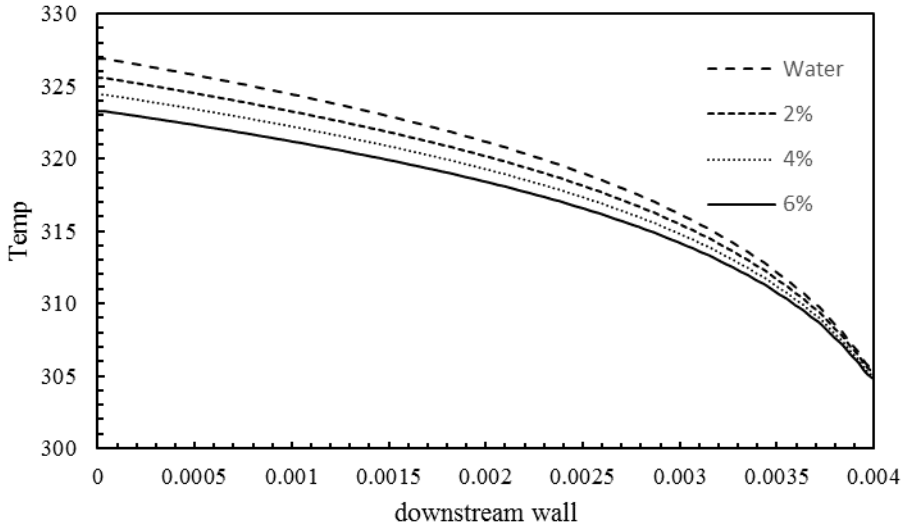

Figure 7-35 Wall temperature change with volume fraction in downstream pipe

In order to understand the heat and flow characteristics in the U-bend in both x and y-direction, the prediction of the change of the temperature along the U-bend is needed. The change of temperature in the x direction in the U-bend is depicted in Figure 7.36.

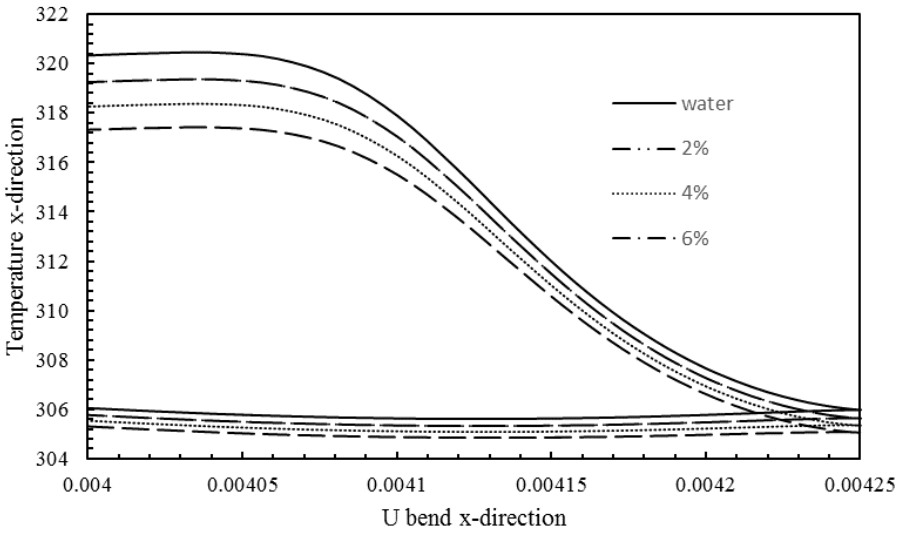

Figure 7-36 Temperature change with volume fraction in the U-bend x-direction

The flow leaves the upstream pipe at temperature 315-320 K as shown previously in Figure 7.34 and enters the lower half of the U-bend then drops rapidly in x direction to 305 K where it becomes insensitive to the location and leaves the U-bend at that temperature which then enters the downstream pipe as shown in Figure 7.35.

It is evident that the temperature increase with the decrease in the volume fraction, so water has the highest temperature as the volume fraction in this case is zero. The increase in wall temperature denotes less heat exchange between the wall temperature and the working fluid temperature.

This temperature trend is noticed in all locations tested in the U-bend in the x direction for all volume fractions investigated, the lower temperature at the wall indicates a higher rate of heat transferred from wall to the working fluid which implies better heat transfer rate.

The change of the wall temperature in the U-bend in the y direction is also studied, and the results are shown in Figure 7.37. The graph represents the variation of wall temperature in the y-direction if the U bend for three volume fractions as well as water. All cases tested at the same conditions of Re number. The temperature drops sharply from the inlet of the U-bend in the y direction from 318-322 K to 304-306 K; it is noticed that the temperature does not change in this direction at y>67 μm, this location is just higher than the upstream

pipe. The flow leaves the U bend with the temperature 304-306 K which then the flow enters the downstream pipe at this temperature.

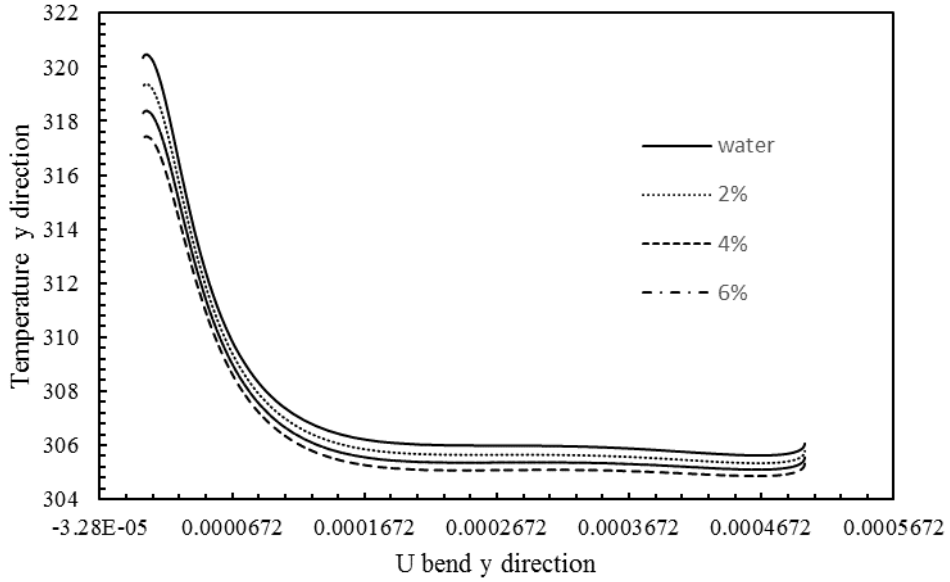

Figure 7-37 Temperature change with volume fraction in the U-bend y-direction

As the thermal conductivity of the nanofluid is the most significant thermal property due to its augmentation with the adding of nanoparticles and enhancing the heat transfer rate, this property was studied in the upstream pipe, downstream pipe and U-bend in both x and y-direction. The variation of the thermal conductivity in the upstream pipe is calculated, and the results are depicted in Figure 7.38.

It can be seen from the graph that the thermal conductivity increases with the rise in the volume fraction of the nanoparticle. This increase is in favour of the cooling purpose of engineering applications. Water was the poorest among cases tested in terms of thermal conductivity.

It was also noticed that the thermal conductivity rises gradually with the advance of the flow in the upstream pipe of the microchannel. This rise is attributed to the increase in the wall temperature of the upstream pipe. It was mentioned earlier that the thermal conductivity is a temperature dependent, so any increase in temperature results in an increase in thermal conductivity. The enhancement in thermal conductivity at the wall in this case was found up to 9% for 6% volume fraction compared to water.

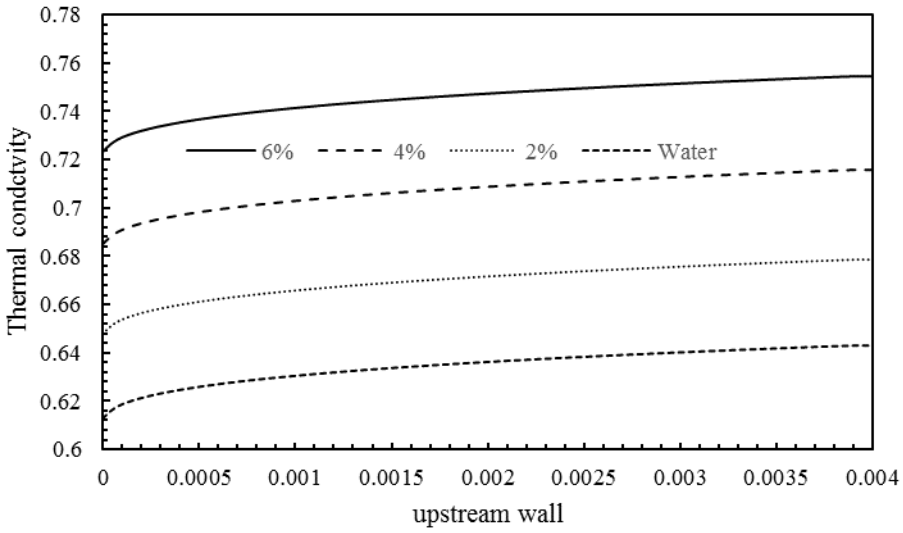

Figure 7-38 Variation of thermal conductivity with volume fraction in the upstream pipe

A similar trend for thermal conductivity was seen in the downstream pipe in terms of the increase with the volume fraction as shown in Figure 7.39. However, the thermal conductivity enters the downstream pipe with lower value due to the lower temperature entering the downstream part pf the microchannel.

It was found that the average thermal conductivity in the upstream pipe is slightly lower than that of the downstream pipe despite that the heat transferred in the upstream pipe more than that of the downstream pipe.

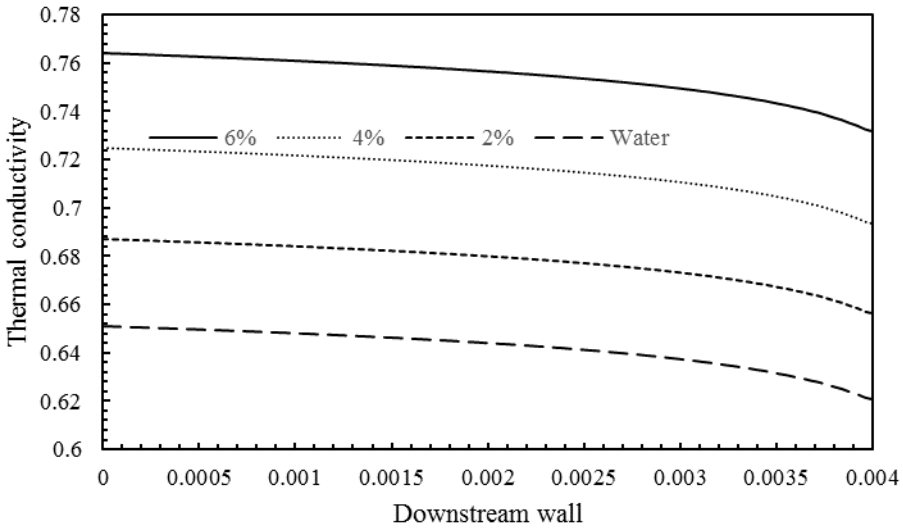

Figure 7-39 Variation of thermal conductivity with volume fraction in the downstream pipe

The variation of the thermal conductivity with volume fraction is investigated in the U-bend in x and y-direction. The change in the x direction is shown in Figure 7.40.

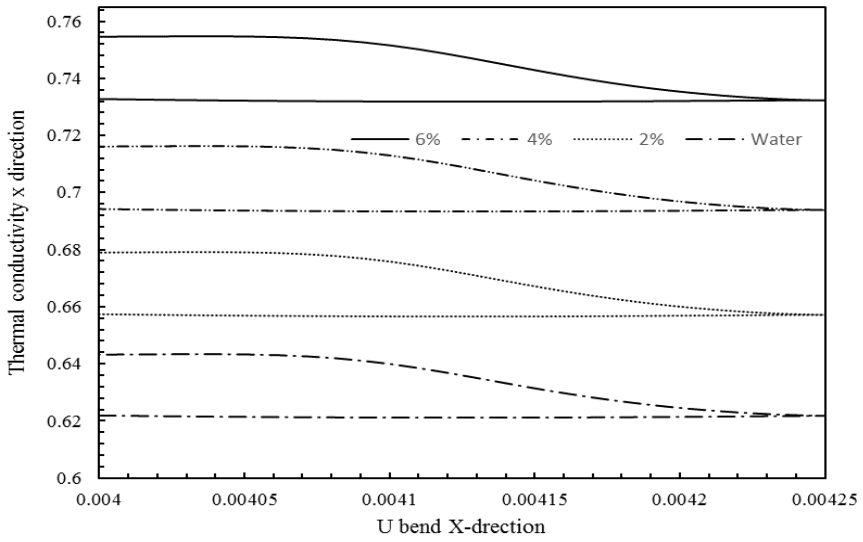

Figure 7-40 Variation of thermal conductivity with volume fraction in U-bend x direction

The thermal conductivity is almost constant in the lower half of the U-bend in x-direction, this is due to the constant temperature at this region, although it rises slowly in the upper half of the U-bend in the x direction.

It was also found that the thermal conductivity increases with the rise in volume fraction in all locations, in the lower and upper half of the U-bend. This is in agreement with the wall temperature variation at this region as shown previously in Figure 7.36.

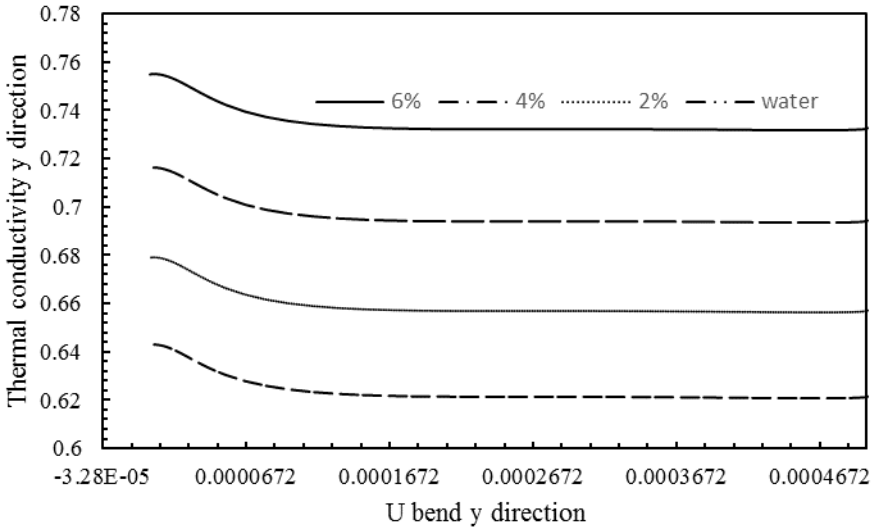

Figure 7-41 Variation of thermal conductivity with volume fraction in U-bend y direction

The variation of thermal conductivity with the volume fraction in the U-bend y direction is portrayed in Figure 7.41. The graph shows the steady thermal conductivity in the y direction, however, in origin a small decline was noticed.

The volume fraction enlarged the thermal conductivity massively in the y direction in the same manner which was shown previously in the x direction. This increase in thermal conductivity is the main reason for the improvement in the heat performance.

The viscosity change in the upstream wall is investigated in the upstream pipe for a range of volume fractions, and the results are shown in figure 7.42, all cases studied were tested under the same conditions such as Re number, external heat flux and nanoparticle type.

It can be seen from the graph that the viscosity decreases steadily with the advance of the flow inside the upstream pipe of the microchannel. This decrease is explained by the increase in the temperature at this wall as discussed earlier that the viscosity decreases with the increase in temperature.

It can also be noticed that the viscosity developed with the rise in nanoparticle volume fraction, this augmentation is attributed to the volume fraction dependent as presented in equation (7.4). It is worth to mention that the intensification in viscosity is not preferable due to its drawback in engineering applications.

From the graph, it can be found that the water exhibited the lowest viscosity in all cases tested in the present investigations. The rise in viscosity using 6% volume fraction is 27% higher than that of water.

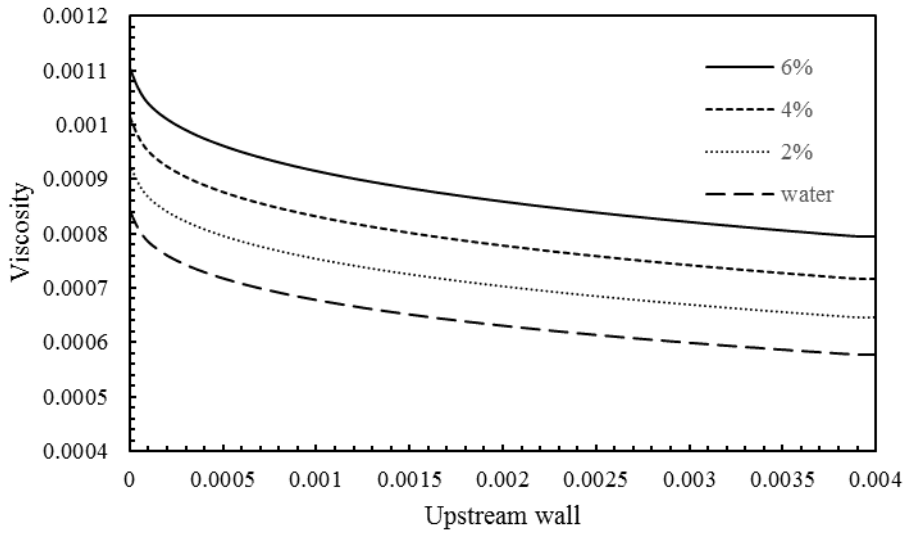

Figure 7-42 Viscosity variation with volume fraction in the upstream pipe

The flow in the downstream pipe was investigated to predict the effective viscosity, and its variation with volume fraction and the results are introduced in Figure 7.43.

The viscosity decreased along the downstream pipe wall; this decrease was 25% for 6% volume fraction. The explanation of this decrease is due to the rise in temperature along the downstream wall temperature as higher temperature worsens the viscosity as mentioned earlier.

It can be seen also that the viscosity developed with the volume concentration rise. The effective viscosity jumped up to 28% when employing 6% volume fraction compared to water base fluid. This prediction is consistent with previous findings as discussed earlier in section 2.3.2.3

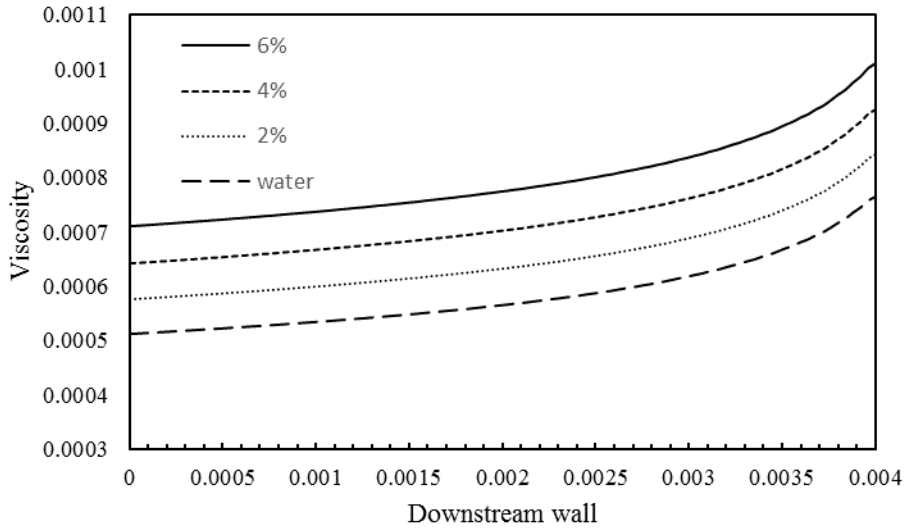

Figure 7-43 Variation of viscosity with volume fraction along the downstream wall

The variation of effective viscosity in the U-bend in both x and y-direction have been investigated to give a better understanding to this important thermophysical property in such a configuration. The effective viscosity in the U-bend x direction is calculated, and the results are illustrated in Figure 7.44.

The effective viscosity in the U-bend x direction increased in the lower half of the U-bend in the x direction for all volume fractions tested, this increase in attributed to the decrease in the temperature in that region as discussed earlier. In the upper half of the U-bend the viscosity is constant as the temperature does not change in x-direction as shown in Figure 7.36. The volume fraction increased the effective viscosity remarkably along the U-bend in x-direction, this increase was up to 25% for 6% in the upper half and 32% in the lower half

respectively compared to water. Indeed, this enlargement in viscosity is undesirable in engineering devices.

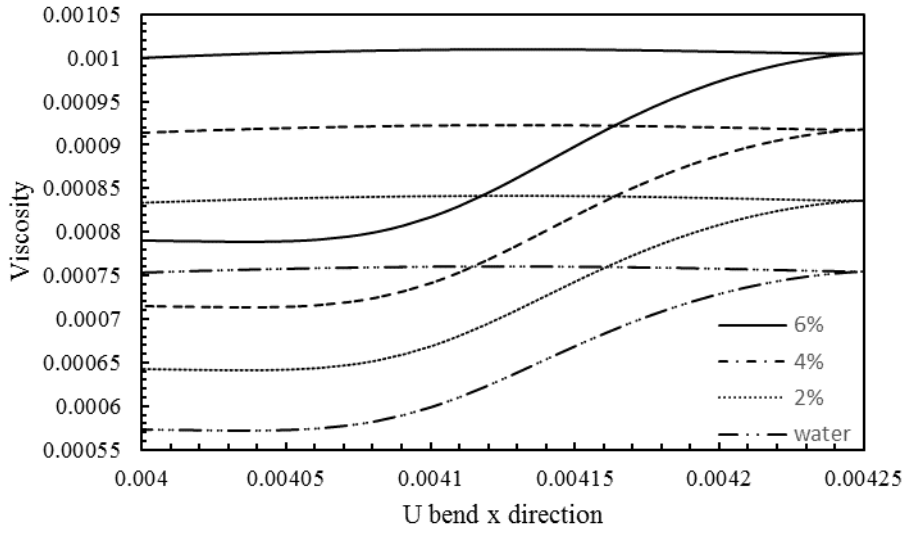

Figure 7-44 Viscosity variation with volume fraction in the U-bend x direction

The viscosity change in the U-bend y-direction is calculated, and the results are shown in Figure 7.45. The viscosity had prominent increase till y = 67 µm, after which, it remained unchanged, this trend is noticed in all volume fractions tested.

The increase in the effective viscosity was found 31.4% when 6% volume fraction was used compared to water. This increase will subsequently enlarge the wall shear stress as a result.

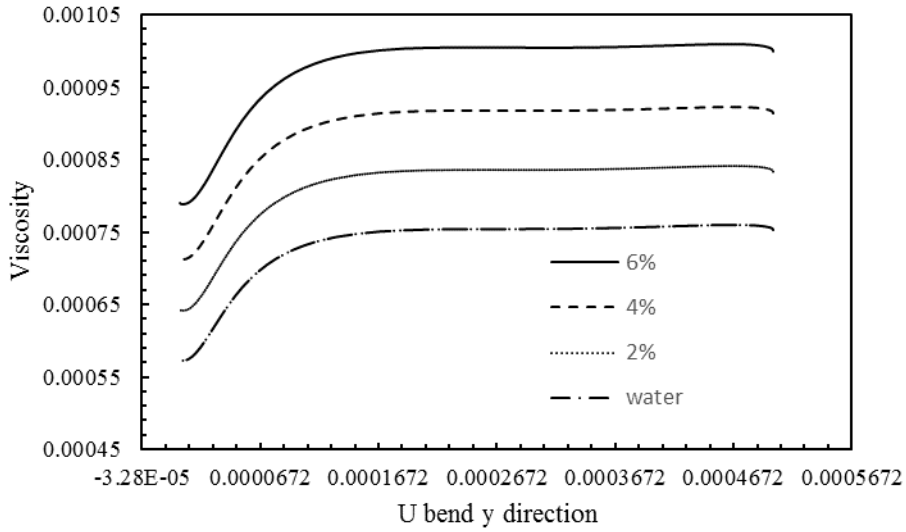

Figure 7-45 Viscosity variation with volume fraction in the U-bend y direction

The pressure coefficient in the upstream pipe is investigated, and the results are shown in Figure 7.46. The variation of the pressure coefficient with the volume fraction is tested,

and the graph illustrates that the pressure coefficient declines sharply in the upstream pipe at the wall. The pressure coefficient increases with the increase in the volume fraction, this increase found up to 10.7% when using 6% volume fraction compared to water.

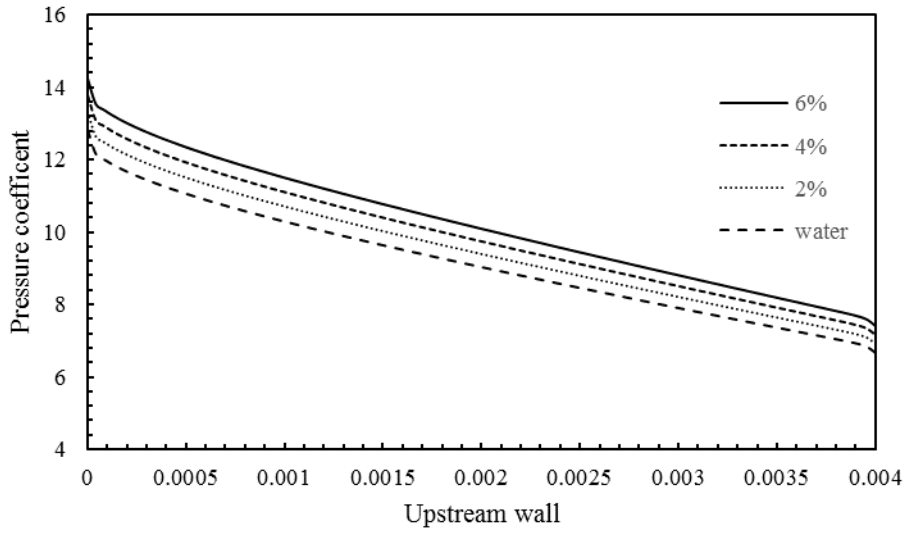

Figure 7-46 Pressure coefficient variation with volume fraction in the upstream wall

The downstream pipe was tested for a range of volume fractions, and the pressure coefficient declined severely with the advance of flow in the downstream wall and the results are shown on Fig 7.47. The rise of the pressure coefficient when testing 6% volume fraction was up to 20% compared to water. It is worth to mention that the pressure coefficient in the upstream pipe is higher than that of downstream pipe.

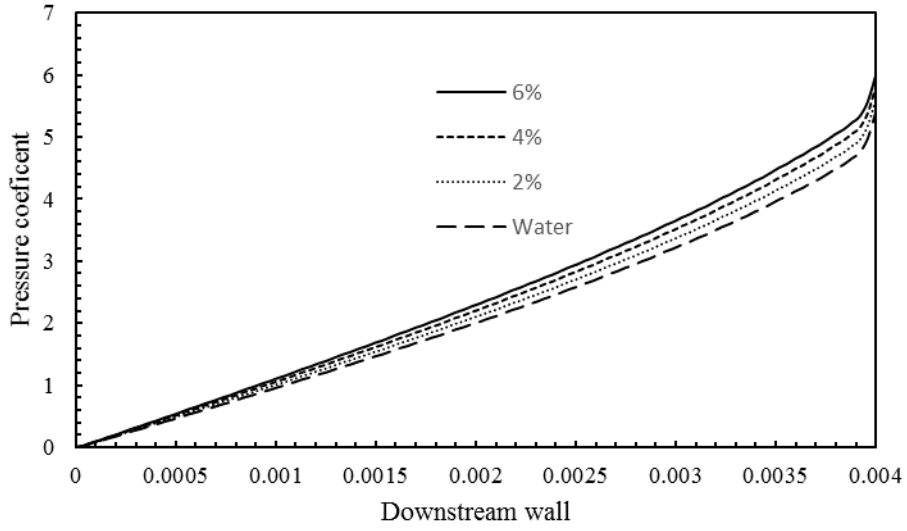

Figure 7-47 Pressure coefficient variation with volume fraction in the downstream wall

The change of the pressure coefficient in the U-bend x-direction and its relation with volume fraction is investigated, and results are illustrated in Figure 7.48. The pressure

coefficient increases when the flow enters the U-bend in the x direction until the end of the lower half of the U-bend and then increases again as the flow approaches the upper half in the U-bend x-direction, this increases continues till the flow enters the downstream pipe.
It was also noticed that the pressure coefficient enlarged with the volume fraction increase, an increase up to 10.5% is found in comparison to water.

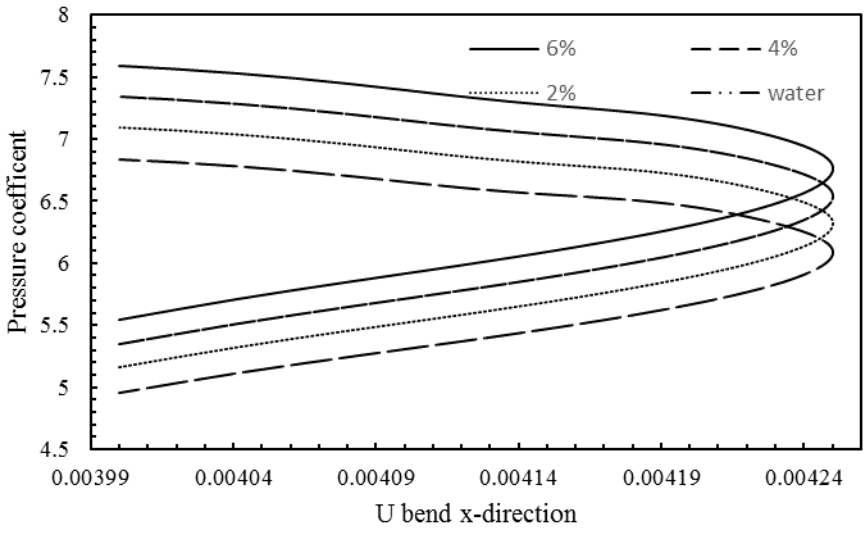

Figure 7-48 Variation of pressure coefficient with volume fraction in U-bend x direction

The variation of pressure coefficient with the volume fraction in the U-bend y-direction is investigated, and the results are depicted in Figure 7.49.
The pressure coefficient increases linearly in the U-bend in y direction, the rise was up to 26.3% at the end of U-bend compared to the inlet. The increase in volume fraction was found not preferable in terms of the pressure coefficient as the volume fraction augmentation increased the pressure coefficient in y-direction up to 10.52% when 6% volume fraction used compared to water.
It can be seen for this investigation that despite the enhancement of the heat transfer by means of developing the volume fraction, the pressure coefficient increased as a penalty due to this augmentation in nanoparticles. It is worth to mention here that this investigation used only one type of nanoparticles which is Titanium oxide, the thermophysical properties are listed earlier in Table 7.1.

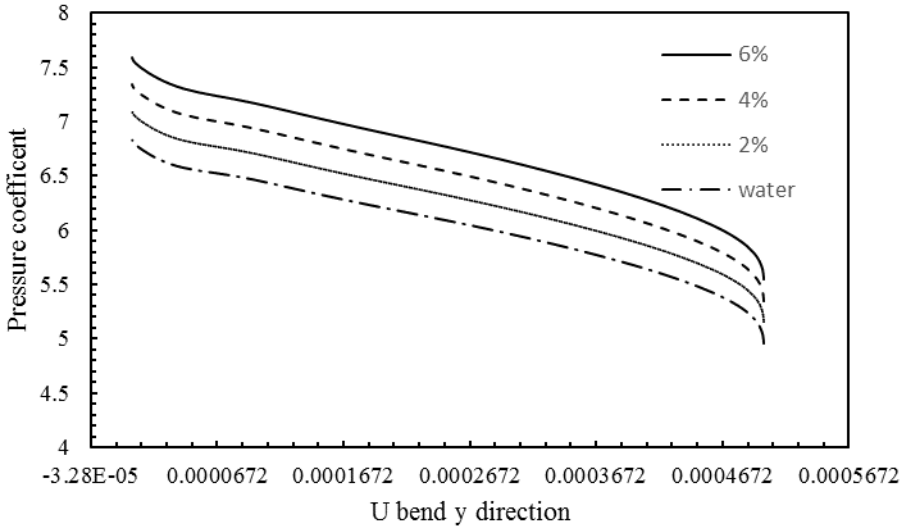

Figure 7-49 Variation of pressure coefficient with volume fraction in U-bend y-direction

The shear stress change in the U-bend x-direction was tested and analysed, and the results are presented in Figure 7.50. The wall shear stress showed insignificant variation in the U-bend entry in x direction, however, when the flow rises in the upper half of the U-bend, the wall shear stress slumps dramatically, the explanation for this is due to the drop in the effective viscosity as the wall shear stress is directly proportional to the effective viscosity as well as velocity gradient. The percentage in the rise in the wall shear stress between the inlet and the exit of the U-bend was up to 62% when using 6% volume fraction.

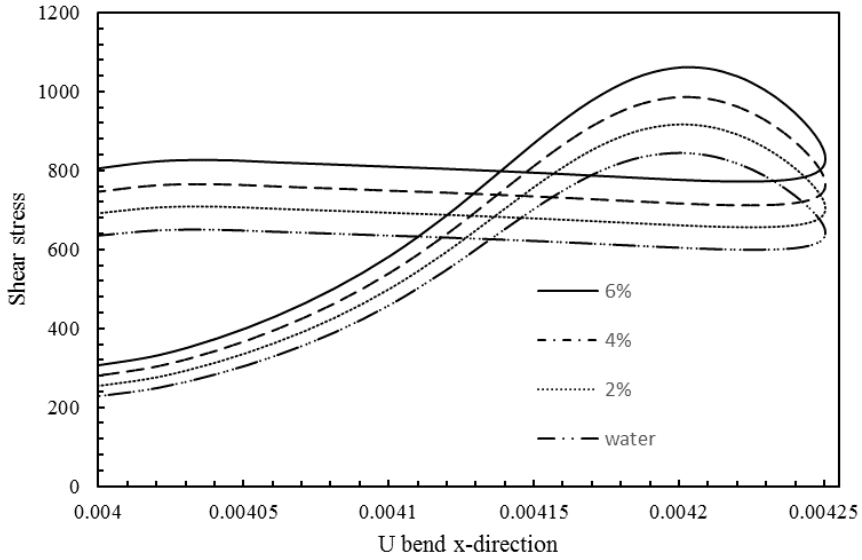

Figure 7-50 shear stress change with volume fraction in the U-bend x-direction

From Figure 7.50 it can also be seen that the shear stress increased with the increase in the nanoparticle volume fraction. This behaviour was noticed in all locations for all volume fractions tested. The increase in shear stress due to nanoparticle suspension was found up to 20% when using 6% volume fraction compared to water.

The shear stress and its change with volume fraction in the U-bend in the y-direction was calculated, and the results are detailed in Figure 7.51. The graph shows a jump in the shear stress in the exit of the upstream pipe and the entry of U-bend, this rise is attributed to the increased effective viscosity of the nanofluid. Moreover, the velocity gradient is increased in this region.

The shear stress drops slowly in the y-direction after entering the U-bend. This variation is noticeable in all volume fractions tested. However, the shear stress developed remarkably with the increase in the volume fraction, this increase is less pronounced in y<0.099 µm.

The rise in the shear stress due to the rise in volume fraction was found up to 20% when 6% of volume fraction was used compared to water. It is worth to mention that all cases tested under the same conditions of Re number and external heat flux.

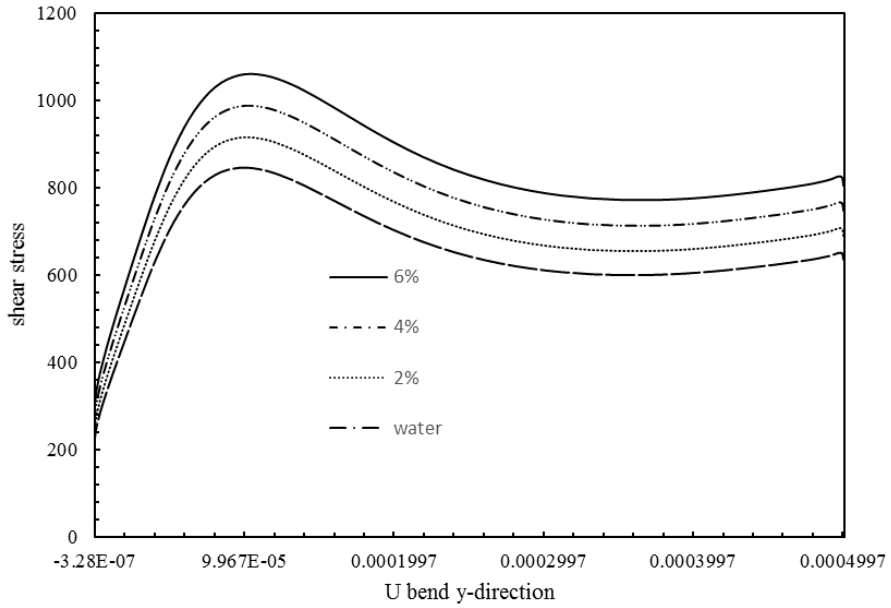

Figure 7-51 shear stress change with volume fraction in the U-bend y-direction

The skin friction factor was studied in all locations in this configuration of the microchannel, the results of the variation of skin friction factor with volume fraction in the upstream pipe are portrayed in Figure 7.52.

The skin friction factor declined sharply at the entrance of the microchannel in the upstream pipe when the flow is fully developed, the skin factor remained almost unchanged, and this behaviour is seen for all volume fractions investigated.

The volume fraction of the nanoparticle increased the skin friction factor in the upstream pipe, the rise in skin friction was up to 12.89% when the volume fraction 6% was employed compared to water.

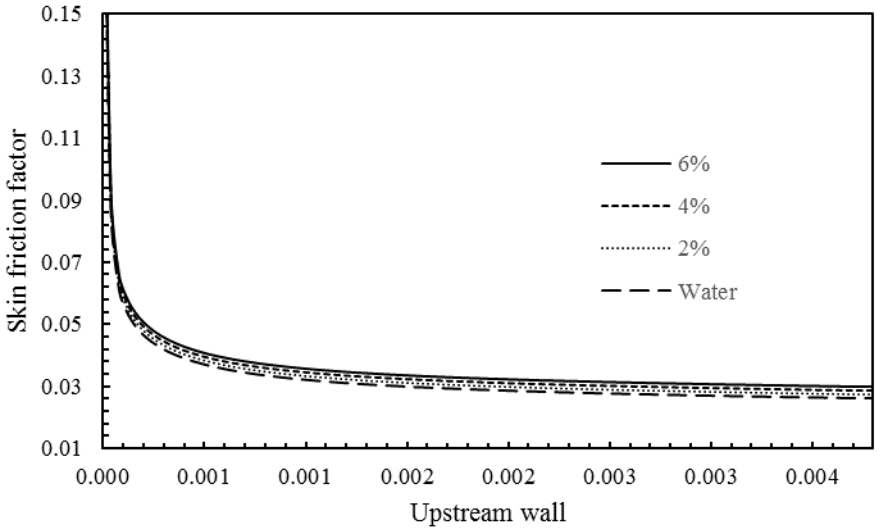

Figure 7-52 Skin friction factor variation with volume fraction in the upstream pipe

The variation of the skin friction factor with the volume fraction in the downstream pipe was also tested under the same conditions, and the results are illustrated in Figure 7.53.

The friction factor slumped significantly at the entrance of the downstream pipe in the microchannel, and as the flow advances in the downstream pipe, the skin friction factor becomes steady, and no changes were noticed. It was also found that the skin friction factor increased with the increase in the volume fraction of the nanoparticles. The increase in the skin friction factor due to the augmentation of volume concentration was up to 13.11%.

This finding shows that the increase in the skin friction factor in the downstream pipe was higher than that of the upstream pipe despite the superior of the skin friction factor in the upstream pipe than that in the downstream pipe.

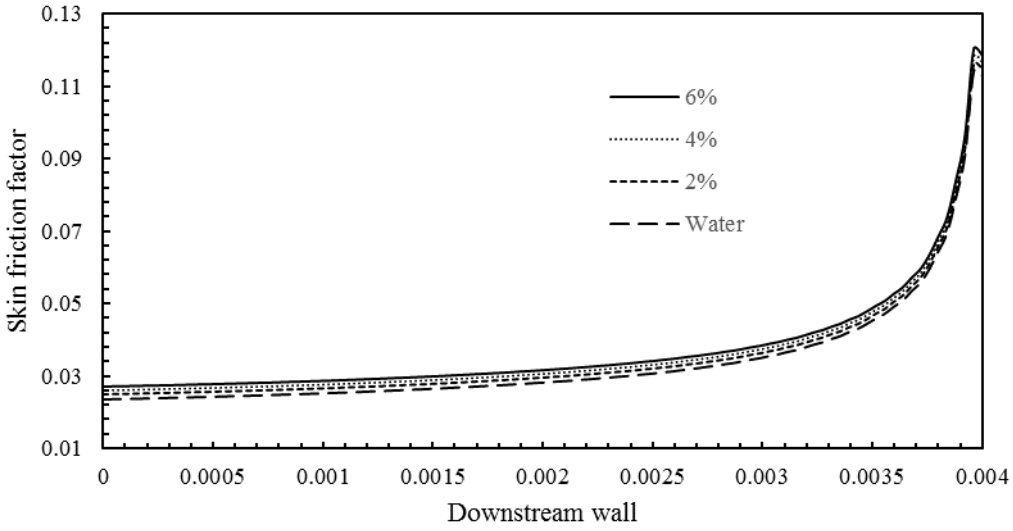

Figure 7-53 Skin friction factor variation with volume fraction in the downstream pipe

The skin friction coefficient variation with volume concentration in the U-bend was studied in both x and y-direction. The variation in U-bend x direction is shown in Figure 7.54. The skin friction is constant in the entrance of the U-bend due to the constant shear stress in this region, the skin friction rises and drops again suddenly as it is a function of the shear stress. It was also found that the skin friction coefficient increases with the increase in the volume concentration of the nanoparticle. The volume fraction 6% showed skin friction coefficient 4.78% higher than water.

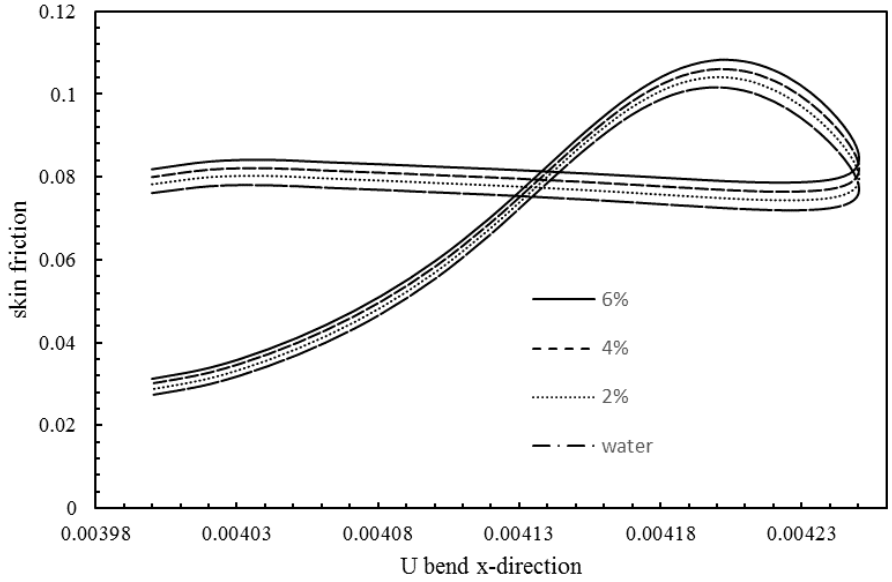

Figure 7-54 Skin friction coefficient variation with volume fraction in the U-bend x-direction

The change of skin friction in the y-direction in U-bend is calculated, and Figure 7.55 depicts the change of the skin friction in the U-bend y-direction. Skin friction rises sharply in the y direction until y>100 µm which represents the middle of the lower half of the U-bend. The skin friction developed by the rise in the volume fraction by up to 8.52% when 6% volume fraction is used compared to water.

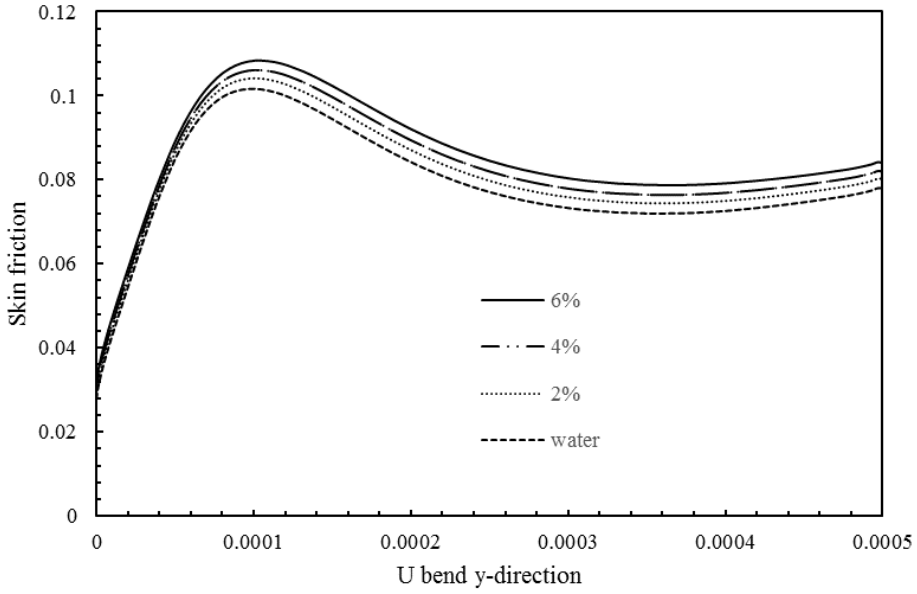

Figure 7-55 Skin friction variation with volume fraction in U-bend y-direction

The u-velocity gradient in the U-bend x-direction was studied to give a better understanding of the effect of the volume fraction on the velocity gradient in the U-bend, this variation is portrayed in Figure 7.56.

The velocity gradient declines gradually at the entrance of the U-bend in the lower half in x-direction until x>20 µm from the entrance of the U-bend. After which, the velocity gradient drops significantly to the location where the flow enters the upper half of the U-bend where velocity gradient develops again; it was noticed that the rise in velocity gradient in the entrance of the U-bend was up to 50% compared to the exit of the U-bend.

It is worth to mention that the velocity gradient is increased with the decrease in the volume fraction, this trend is seen particularly in the lower half of the U-d. However, the insignificant effect was detected in the upper half. This decrease was found up to 4.34% when 6% of volume fraction was tested compared to water. This decrease was found in the entry of the lower half of the U-bend.

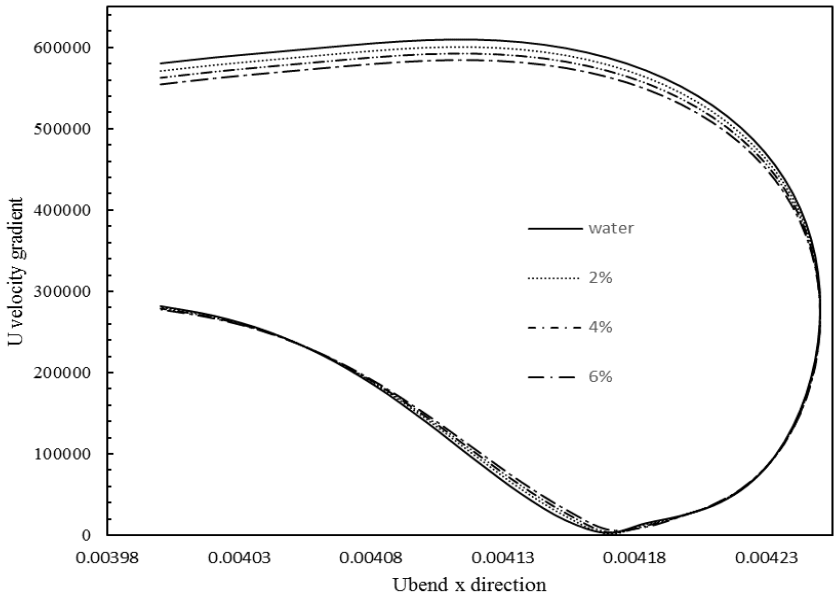

Figure 7-56 Axial velocity gradient in x-direction in U-bend

In order to understand how temperature changes in the U-bend, the temperature contour was taken and the image is illustrated in Figure 7.57. It can be seen that the maximum temperature occurs in the near wall region and the entrance of the bend. However, as the flow moves more towards the bend, temperature distribution changes drastically, and the area near the inner radius shows higher temperature. It can be seen from the Figure that the temperature is slightly higher in the vicinity of the left wall of the U-bend. In the previous Figure, it was noticed that the velocity is lower in this particular area. This contrast in the behaviour is anticipated as the velocity accelerates, the temperature at the wall is lower due to the decrease in the cooling process where the heat exchange is worsened due to the poor change in temperature between the working fluid and the temperature at the wall.

The temperature rises gradually as the flow leaves the U-bend and enters the downstream pipe, where the temperature distribution is very similar to that observed in the upstream pipe as shown in Figure 7.34.

This observation in temperature is in line with the velocity contours as shown in Figure 7.58.

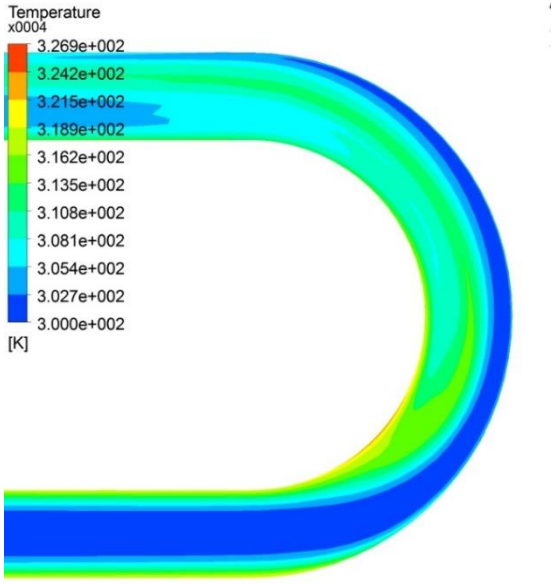

Figure 7-57 Temperature contour in the U-bend

Due to the effect of the centrifugal forces, the flow is forced more towards the outer radius and region of high temperature exists near the inner radius. The image depicted here is for Re number 500 and 2% volume fraction as shown in Fig 7.58. The velocity leaving the upstream pipe is fully developed as seen in the contour. The velocity decelerates at the U-bend entry as discussed earlier, the highest velocity can be seen at the right side of the U-bend section, at the left side, the velocity reduces significantly.

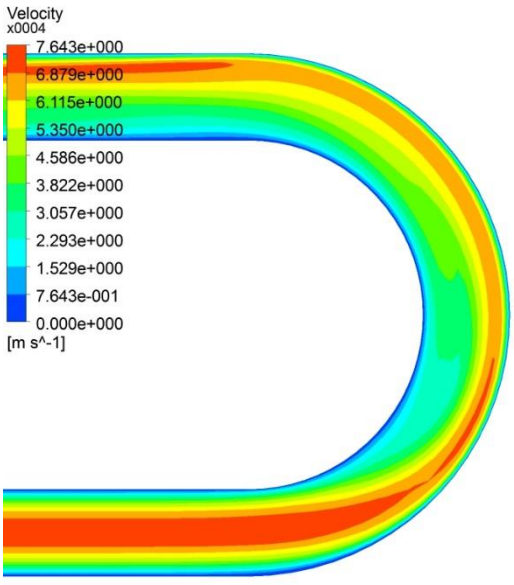

Figure 7-58 Velocity contour in the U-bend

The contour of Prandtl number in U-bend cross section is illustrated in Figure 7.59. It is evident that the Pr number is maximum at the outer radius. This maximum value implies that the momentum diffusivity is higher at the outer radius. However, on the other hand, a higher thermal diffusivity is noticed in the inner radius of the bend, this is in line with the thermal predictions as reported earlier.

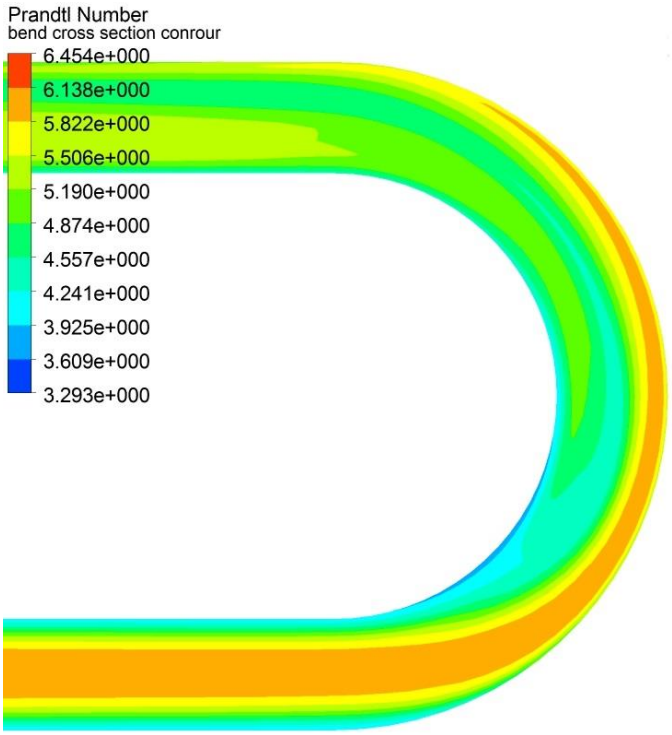

Figure 7-59 Contour of Prandtl number in the U-bend

A cross section in the U-bend in y-direction is taken, and the temperature and velocity contours are shown in Figure 7.60 (a) and (b) respectively. It is obvious from the Figure that the temperature is minimum in the upper, lower and left side of the cross-section and maximum in the right and the core of the U-bend. On the other hand, velocity is vanishing when approaching the near wall region and maximum on the left side of the U-bend section.

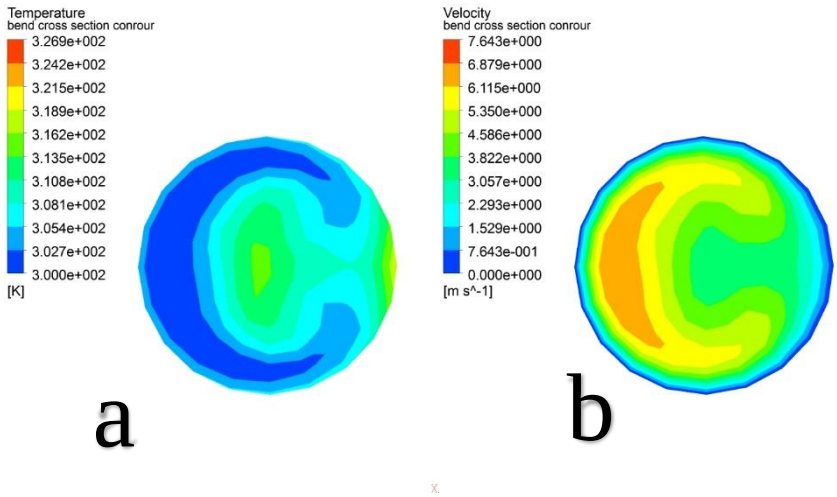

Figure 7-60 Temperature and velocity contours in U-bend cross section y-direction

The velocity contour is depicted in Figure 7.61 for upstream and downstream pipe in various locations. The velocity distribution is shown for the velocity in the upstream and downstream pipe at x=0.0004, 0.0019, 0003 and 0.004 m respectively. The contour demonstrates clearly how velocity develops in the upstream and downstream pipe when the flow advances in the microchannel. It is evident that the flow is fully developed in the upstream and downstream pipe at x=0.0019, the velocity does not change in the upstream until the flow leaves the upstream pipe. However, unlike the flow in the upstream pipe, in the entrance of the downstream pipe, variant velocity values were found at $x \geq 0.003$.

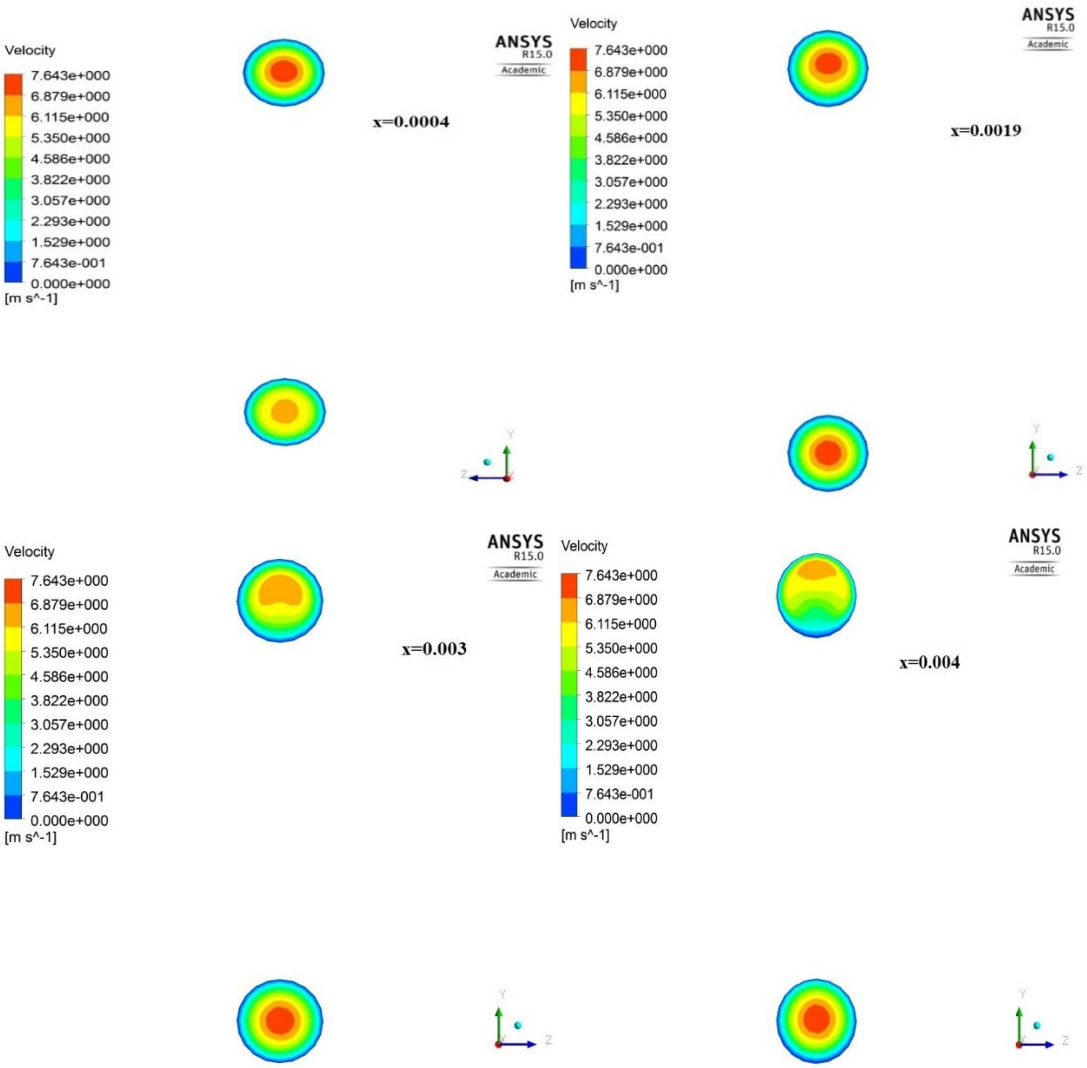

Figure 7-61 Velocity contour in the upstream and downstream pipe at different locations

In the same manner, the temperature contours in various locations in the upstream and downstream pipe were studied, and the contours are portrayed in Figure 7.62. The temperature isotherms are presented in the cross section of the upstream and downstream pipe at x=0.0004, 0.0019, 0.003 and 0.004 m. As can be seen in the upstream pipe, the temperature is minimum at x=0.0004 m where the heat transfer process is at an early stage, and the effect of the external heat flux is still insignificant. However, as the flow advances in the upstream pipe, the temperature at the wall increases gradually. At the downstream pipe, lower temperatures can be found in the entrance region.

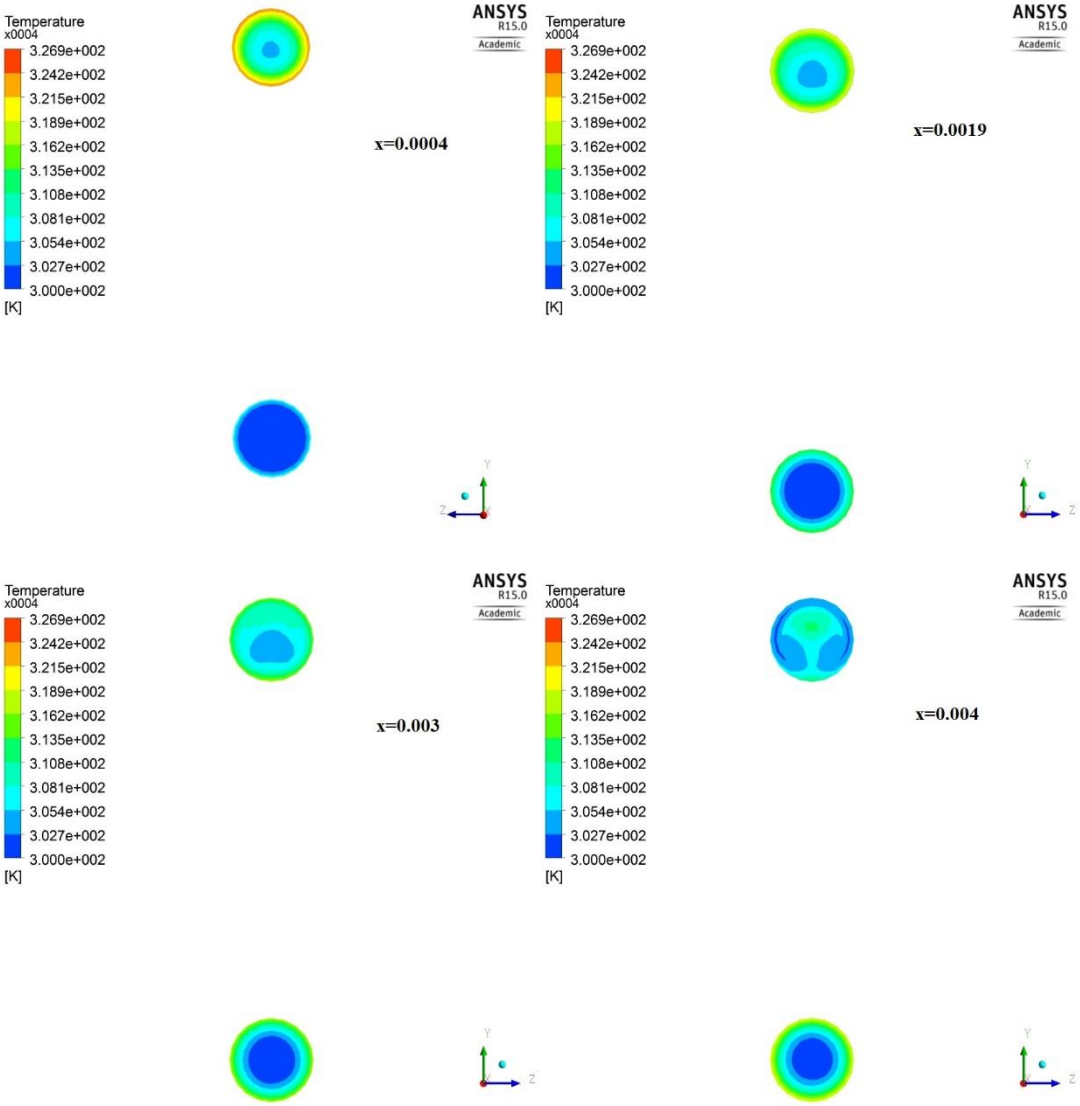

Figure 7-62 Temperature contour in the upstream and downstream pipe at different locations

7.5 Triangular U-bend microchannel

Microchannels geometry can take various cross sections shapes. This section will explore the flow in a rectangular cross section U-bend microchannel. The investigation in such a configuration in the literature using nanofluids is very limited.

7.5.1 Problem Description

The geometry considered in this investigation is shown in Figure 7.63. The flow enters a triangular U-bend microchannel with a uniform temperature T=300 K and initial velocity V in the upstream pipe channel and leaves downstream channel at the exit with zero

pressure gauges. The cross-section is an isosceles triangle with a dimension of 240 µm, resulting in a hydraulic diameter of 138.5 µm. The lengths of the upstream and downstream straight sections are 40 mm.

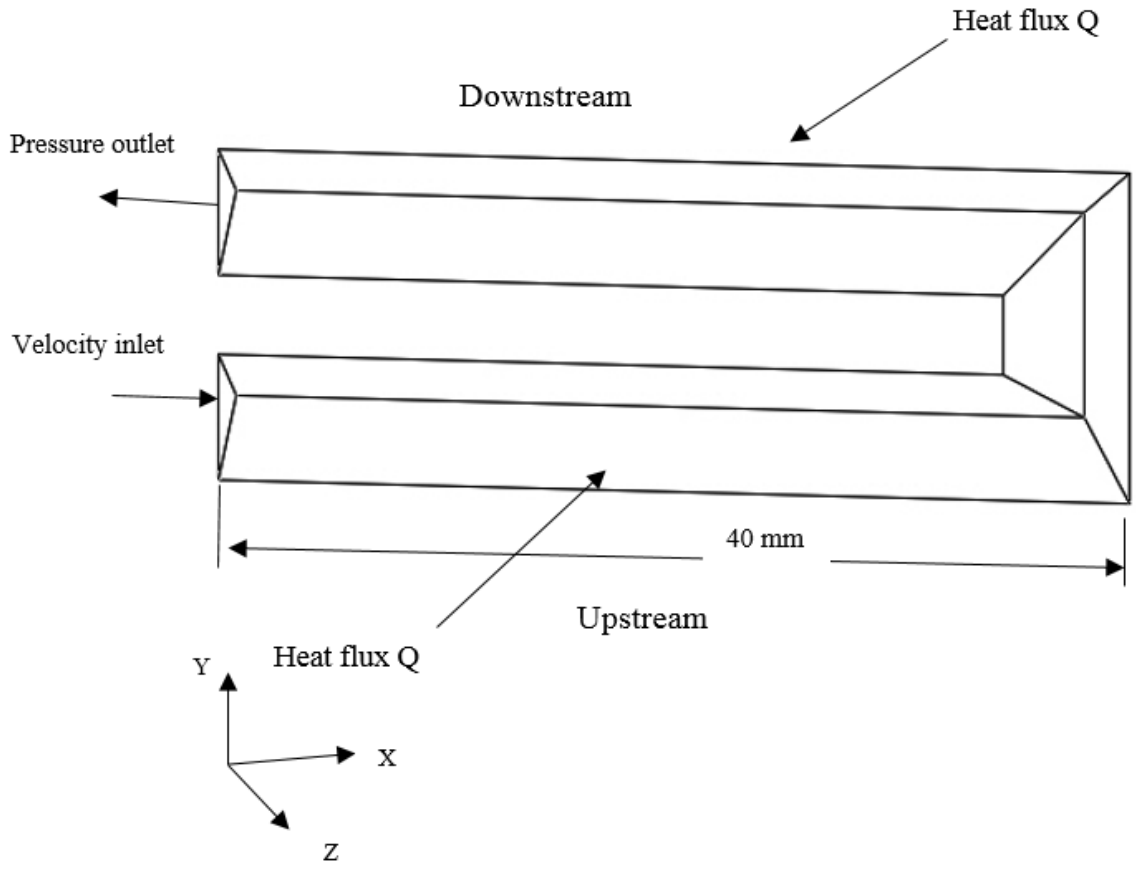

Figure 7-63 Triangular U-bend microchannel geometry

7.5.2 Results and Discussion

In the present section, the results are introduced and discussed for the heat transfer enhancement, and the flow characteristics of Titanium oxide nanofluid in a rectangular shape microchannel is exposed to an external heat flux of 25 w/cm^2. The Nu number along the upstream pipe is studied, and the results are illustrated in Figure 7.64.

The Nu number drops sharply at the entrance of the microchannel until the flow becomes fully developed, at that point onward, the Nu number decreases slowly along the upstream pipe. Various volume fractions (2%, 4% and 6%) were tested as well as water, the influence of the volume fraction was studied and found that the increase in volume fraction is in favour of heat transfer. The average Nu number at the upstream wall was calculated for the different volume fractions, and the results are presented in Table 7.6.

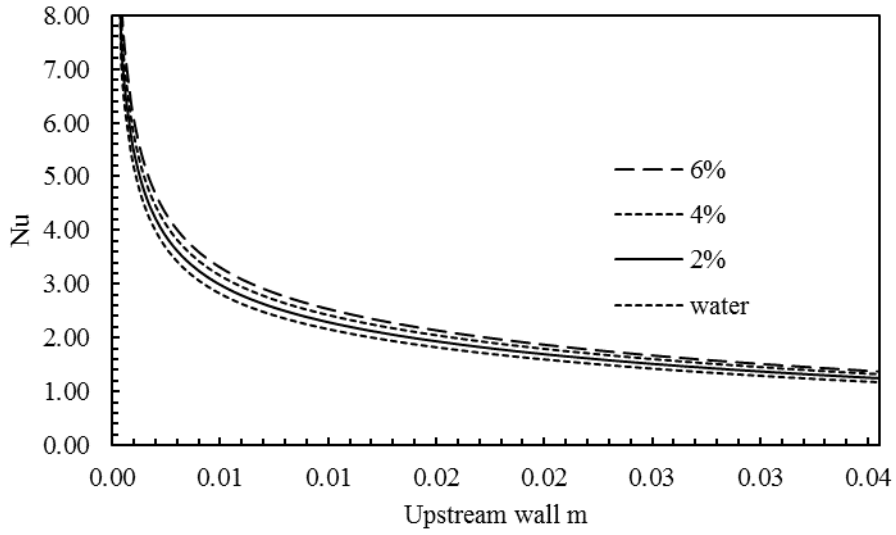

Figure 7-64 Nu at wall for upstream wall

It can be seen in Table 7.6 that the average Nu number over the length of the upstream increases with the increase in volume fraction. It was found that the heat transfer enhanced up to 14.73% when 6% volume fraction was tested compared to water. This emphasises that the nanofluids showed a substantial improvement in the heat transfer rate.

Table 7-6 Nu average at upstream wall

Volume fraction ϕ	Nu_{avg}
water	2.193
2%	2.317
4%	2.443
6%	2.572

The thermal conductivity variation with the volume concentration is investigated on the wall of the upstream pipe, and the results are shown in Figure 7.65. The graph shown represents the gradual increase in thermal conductivity along the wall. The increase in thermal conductivity is resulted from the increase in temperature on the wall due to the external heat flux. The thermal conductivity improved at the upstream pipe exit by up to 14.75% when utilising 6% volume fraction compared to water base fluid.

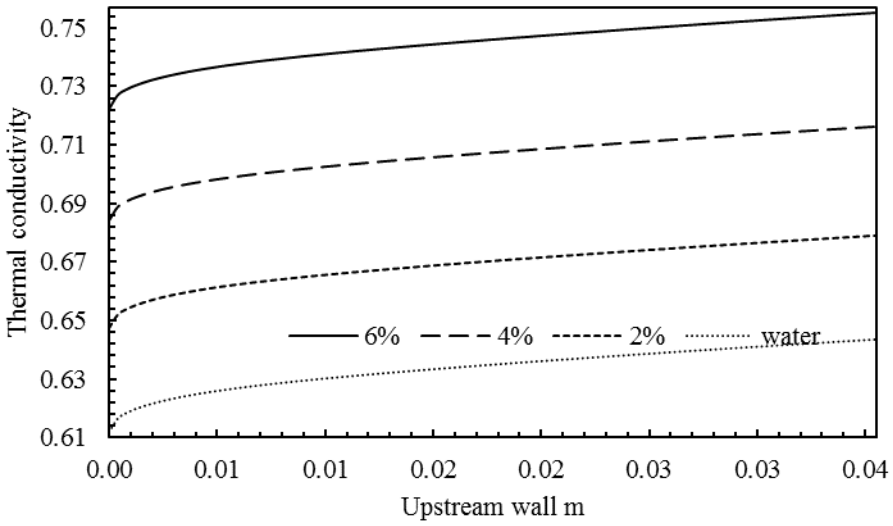

Figure 7-65 Thermal conductivity at wall for upstream wall

The pressure coefficient in the upstream pipe was investigated, and the variation with the volume fraction is depicted in Figure 7.66. The pressure coefficient drops linearly along the wall of the upstream pipe of the microchannel. The volume fraction showed a negative influence on the pressure coefficient, as the volume fraction increases, the pressure coefficient increase. The rise in pressure coefficient was up to 10.9% when 6% volume fraction was employed compared to water at the upstream pipe exit, whereas this rise was up to 11.33% at the entry of the microchannel upstream pipe.

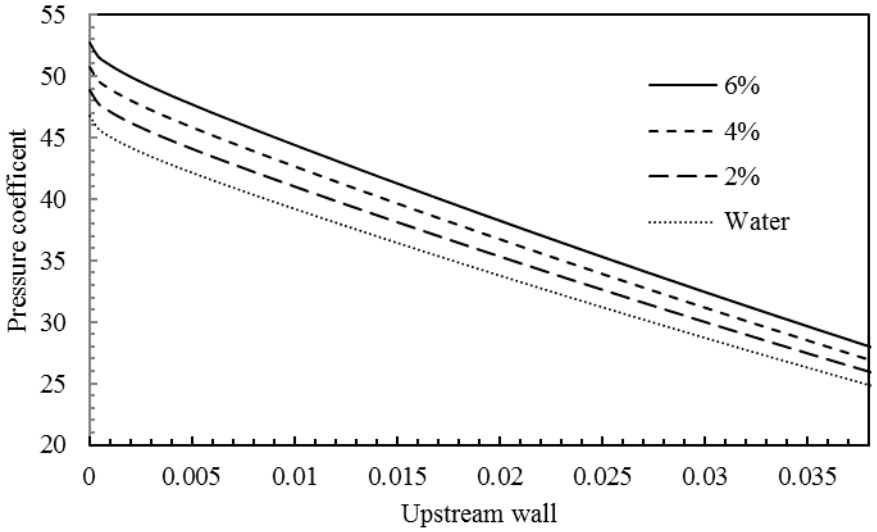

Figure 7-66 Pressure coefficient at upstream wall

The skin friction coefficient in the upstream pipe is investigated, and the influence of the volume fraction was studied, and the results are demonstrated in Figure 7.67.

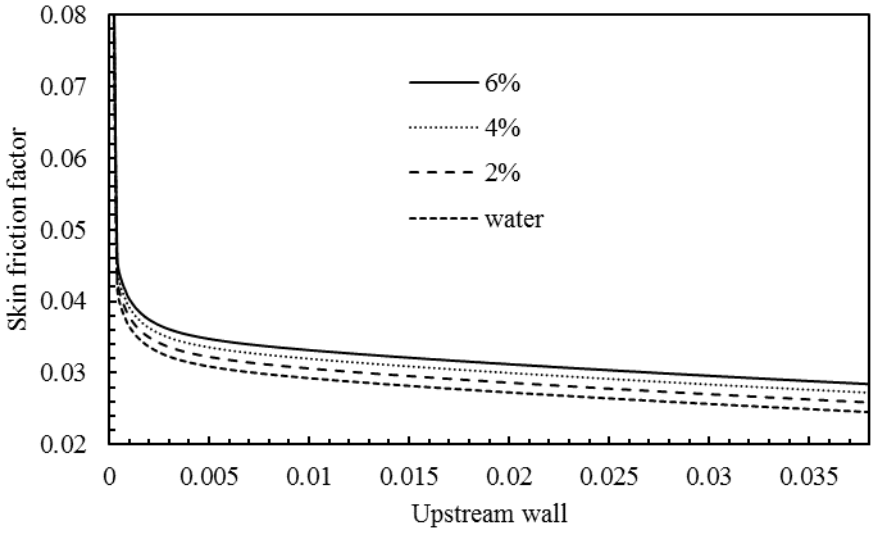

Figure 7-67 Skin friction coefficient

The skin friction coefficient drops rapidly at the entrance of the upstream pipe microchannel; this drop is anticipated as the skin friction is the ratio of the shear stress to the pressure. The skin friction is found to increase with the increase in the nanoparticle volume fraction, the rise at the upstream pipe exit was found up to 13.67% when the volume fraction 6% is used compared to water. This is in line with the variation of pressure coefficient and is important to calculate the pump capacity.

The temperature variation along the upstream pipe wall is studied, and the results are presented in Figure 7.68.

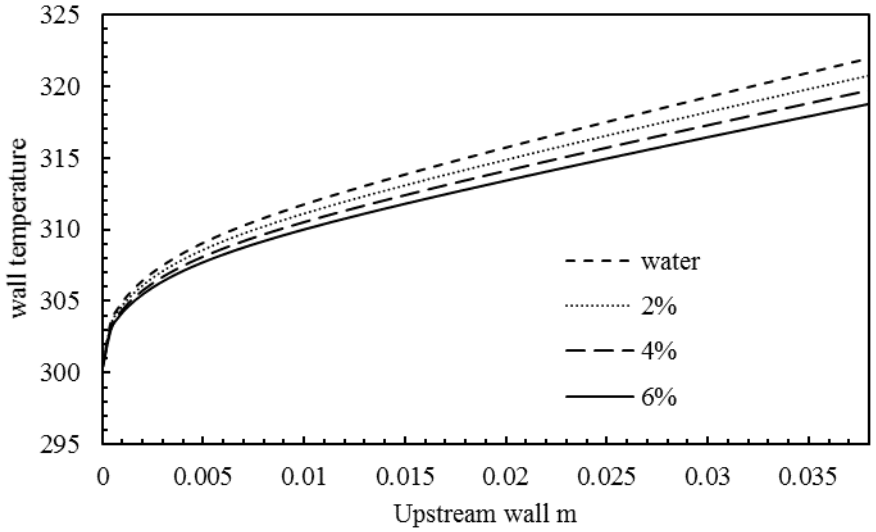

Figure 7-68 Wall temperature in the upstream wall

The wall temperature starts at 300 K when the flow enters the upstream pipe in the microchannel, the temperature rises rapidly at the entrance region, and a linear increase is

seen at x≥0.005 m, this increase is explained by the applied external heat flux. The temperature increases for all volume fractions tested. However, the increase in the volume fraction resulted in a decrease in the wall temperature. The rise in wall temperature was found up to 1.03% at the exit when 6% volume fraction was tested compared to water.

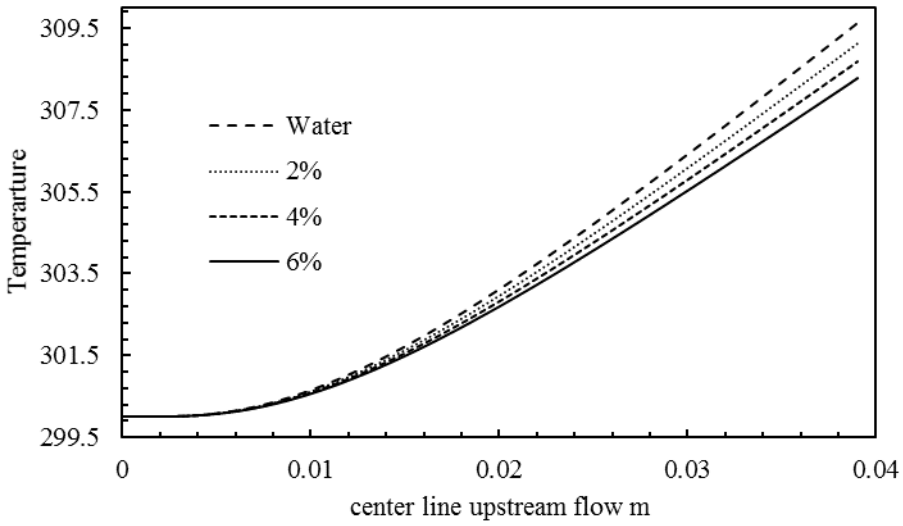

Figure 7-69 Temperature at centre line upstream pipe

The temperature variation with volume fraction in the centre line of the upstream pipe in the microchannel. It was found that the temperature is steady in the entrance region up to x≥0.01 m, after that point, the temperature increases significantly, the highest value was found at the upstream pipe exit.

The volume fraction influence on the temperature was also investigated, and it was found that the temperature at the wall is deteriorated with rise in nanoparticle volume concentration. The rise in temperature in the centre line due to the nanoparticle suspension was up to 0.43 % when the volume concentration 6% was utilised in comparison to water. This finding indicates that the influence of the volume fraction in the wall temperature is more pronounced than that at the centre line. The explanation to this effect is due to the higher temperature at the wall (322 K) than that at the centre line (309 K), this implies that the higher the temperature, the more the effect of the volume fraction on temperature.

The effective viscosity variation on the upstream pipe wall is investigated, and its change with volume fraction is studied, and the results are depicted in Figure 7.70. The viscosity decreases gradually till the upstream pipe exit where the minimum value was found. The

decrease in viscosity is attributed to the increase in temperature as discussed earlier in Figure 7.68; this is in agreement with the previously discussed results which refers to the opposite effect of temperature on the viscosity.

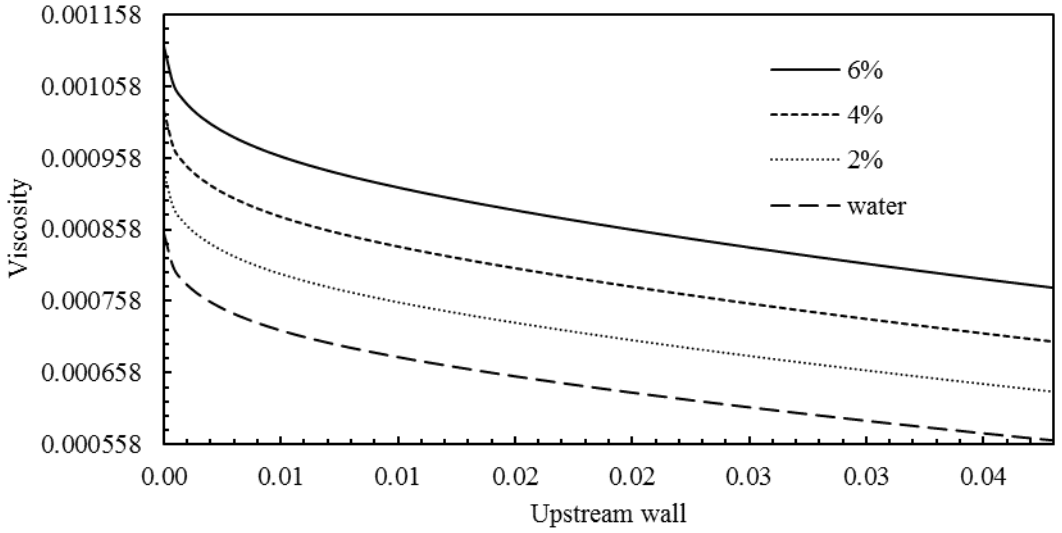

Figure 7-70 Viscosity change at the wall for upstream wall

The viscosity change in the centre of the microchannel upstream pipe was investigated, and the results are illustrated in Figure 7.71. It should be mentioned that the present case is investigated under Re number 500.

The effective viscosity showed insignificant change up to $x \geq 0.01$ m where it decreases slowly, this trend is explained by the temperature change discussed in Figure 7.69, as the effective viscosity drops with the increase in temperature.

The volume fraction impact on the effective viscosity in the centre line of the upstream pipe is studied, and it was found that the viscosity is enhanced with the rise in volume fraction suspension. This enhancement was up to 25.5% when 6% volume fraction was tested compared to water. It is worth to mention that this enhancement was 27.61% at the upstream wall. This proves that the enhancement of the effective viscosity at the upstream pipe wall is more pronounced than that at the upstream pipe centre line. This is explained by the higher temperature difference in the upstream pipe wall.

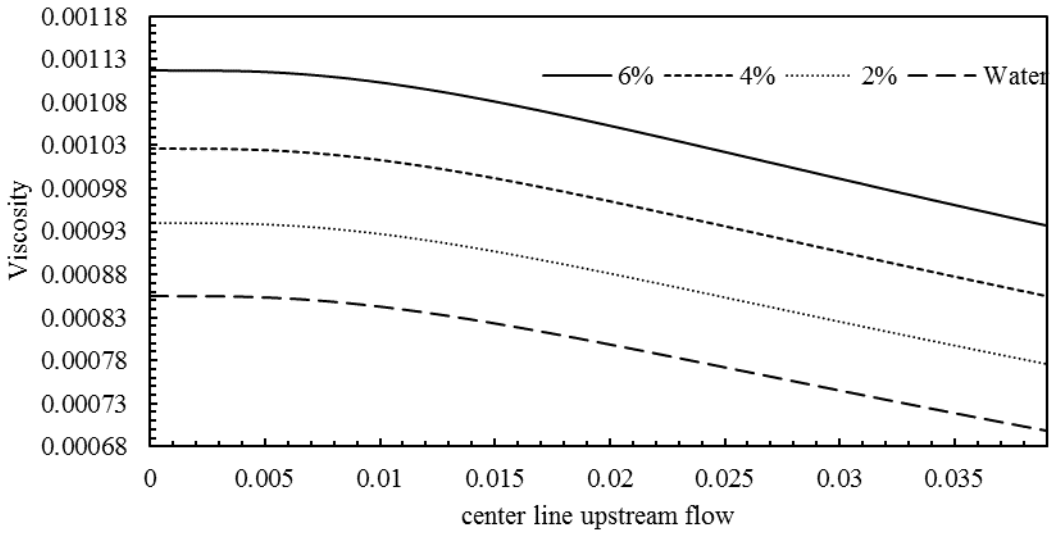

Figure 7-71 Viscosity change at the centre line for upstream pipe

The wall shear stress was investigated at the upstream pipe wall, and the results are portrayed in Figure 7.72. It is evident that the shear stress drops significantly at the microchannel entrance. After that, the shear stress becomes steady without any change. The volume fraction promoted the wall shear stress considerably in the upstream pipe. The rise in shear stress due to the increase in volume fraction was up to 26.71% in the upstream pipe of the microchannel.

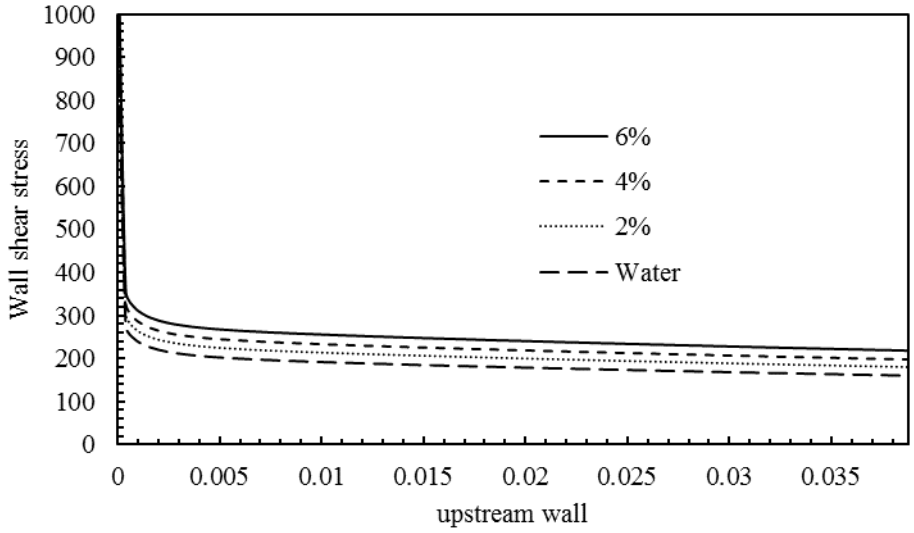

Figure 7-72 Wall shear stress at upstream wall

In order to understand how Pr number changes in the U-bend microchannel, the contours of Pr number for various volume fraction in the cross section is illustrated in Figure 7.73. It can be seen from the variation of Pr number that the higher values are noticed in the core of the cross section of U-bend, these higher values are found when 6% volume fraction was used. It was also detected a minimum Pr number in the left corner of the microchannel.

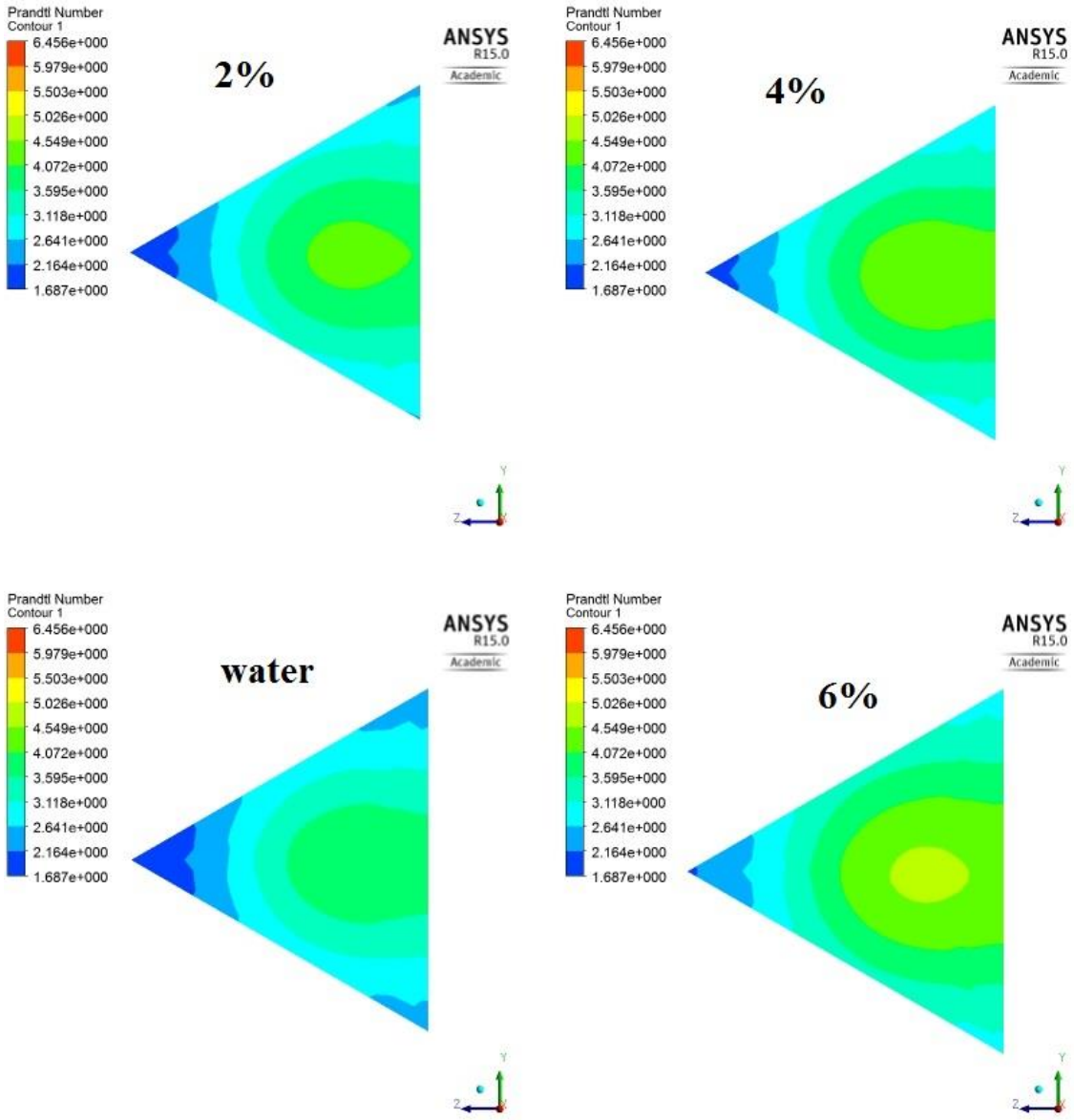

Figure 7-73 Pr number variation with volume fraction at x=0.001

The velocity development inside in the cross section of the U-bend is studied, and the contours at y=0.0008 m and y=0.00035 for Re 500 in all cases tested in this investigations are presented in Figure 7.74. It is obvious that the velocity increases at y=0.00035 m in particular in the left side corner. The lower value of velocities are always in the near wall region where velocity at wall is zero. At y=0.00215 m which represents the location of the end of U-bend, at this point the velocity reduces remarkably at the left corner due to the progress of the flow in the U-bend and approaching the downstream pipe in the microchannel. It is evident from the contours that the velocity varies considerably in the U-bend microchannel as the flow advances in the U-bend.

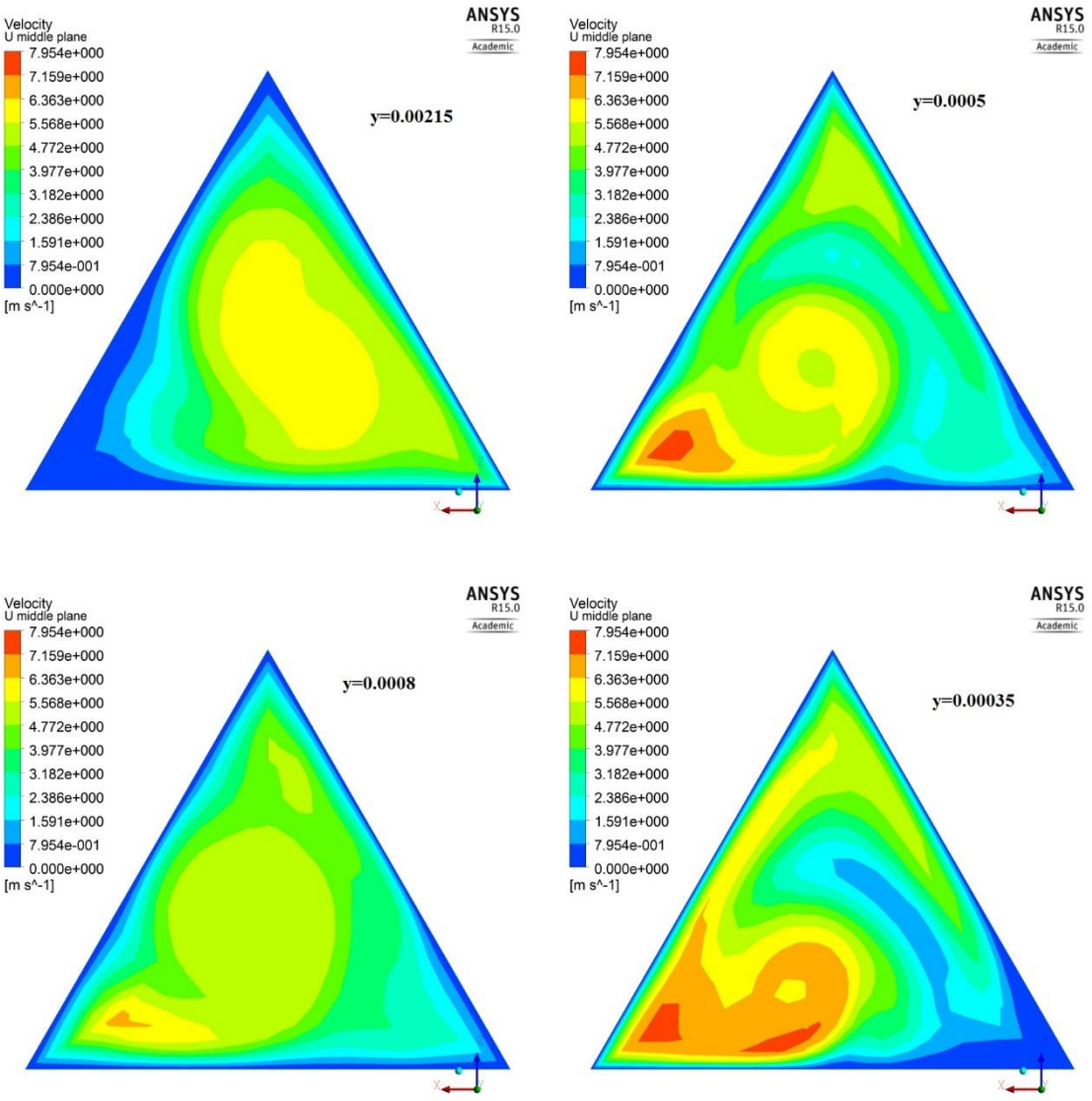

Figure 7-74 Velocity contour in different locations in the U-bend cross section

In order to understand how temperature changes inside the U-bend and the influence of the volume fraction on temperature, the isotherms of the temperature are introduced in Figure 7.75. It can be seen from the figure that the temperature is affected directly with the nanoparticle volume fraction, as the nanoparticle volume fraction rises, the temperature decreases as a results to that. This can be found in all volume fractions tested as well as water. This is in agreement with the previously discussed results in Figure 7.68 and 7.69 where the temperature is deteriorated with the augmentation in volume fraction. It is evident that the minimum temperatures can be found in the left corner and the U-bend core.

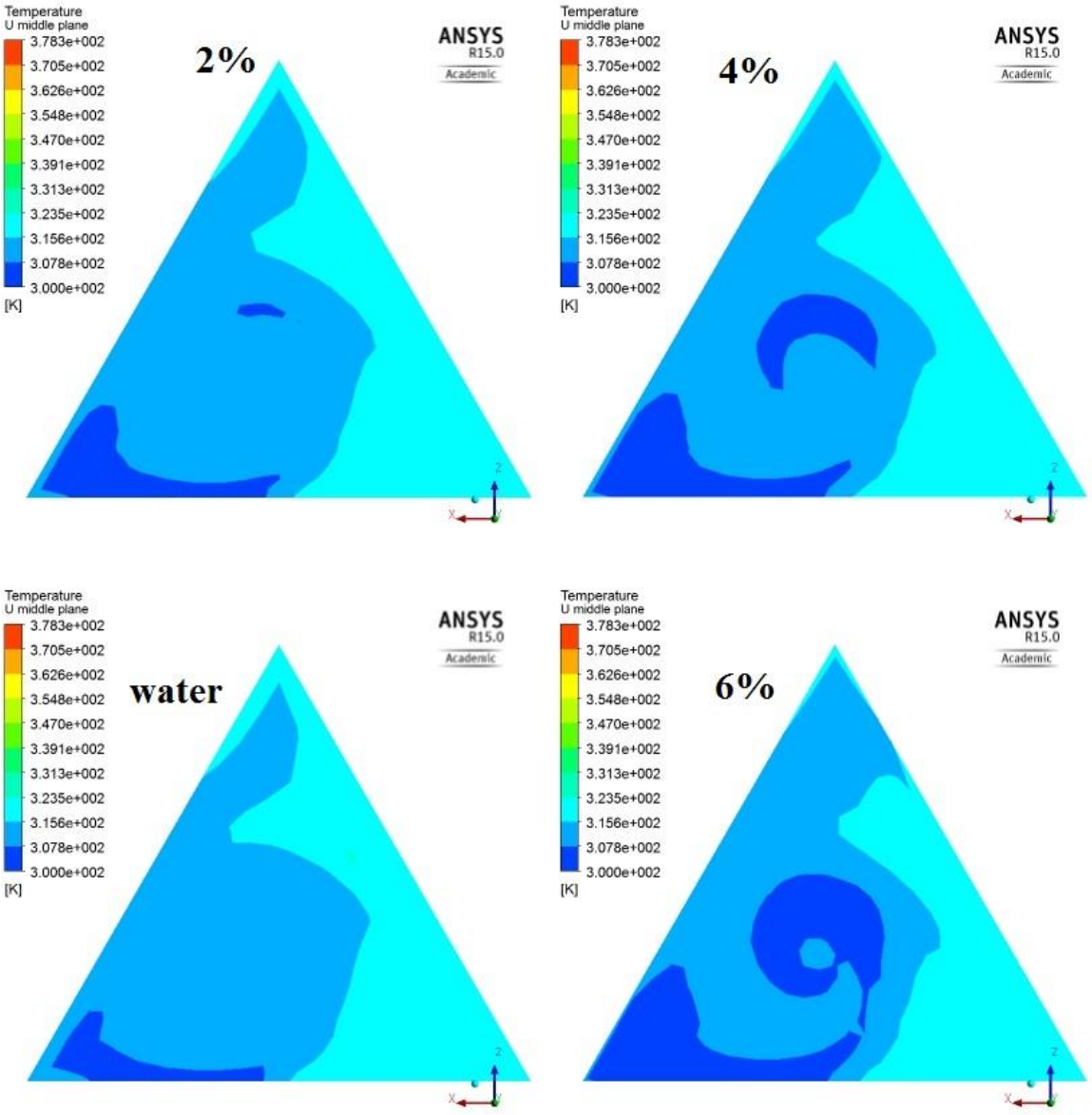

Figure 7-75 Temperature isotherms in cross section in U-bend

The thermal conductivity was also studied inside the cross section of the upstream pipe, and its variation with nanoparticle volume fraction and the results of the contours are depicted in Figure 7.76. It can be seen that the thermal conductivity increases with the increase in volume fraction in all locations of the cross-section. The maximum values of thermal conductivity can be detected in the corners particularly when 6% volume fraction is used. However, the minimum values of thermal conductivity were found in the core of the cross section of the upstream pipe of the microchannel. At the right side, lower values were seen as the right face is assumed adiabatic.

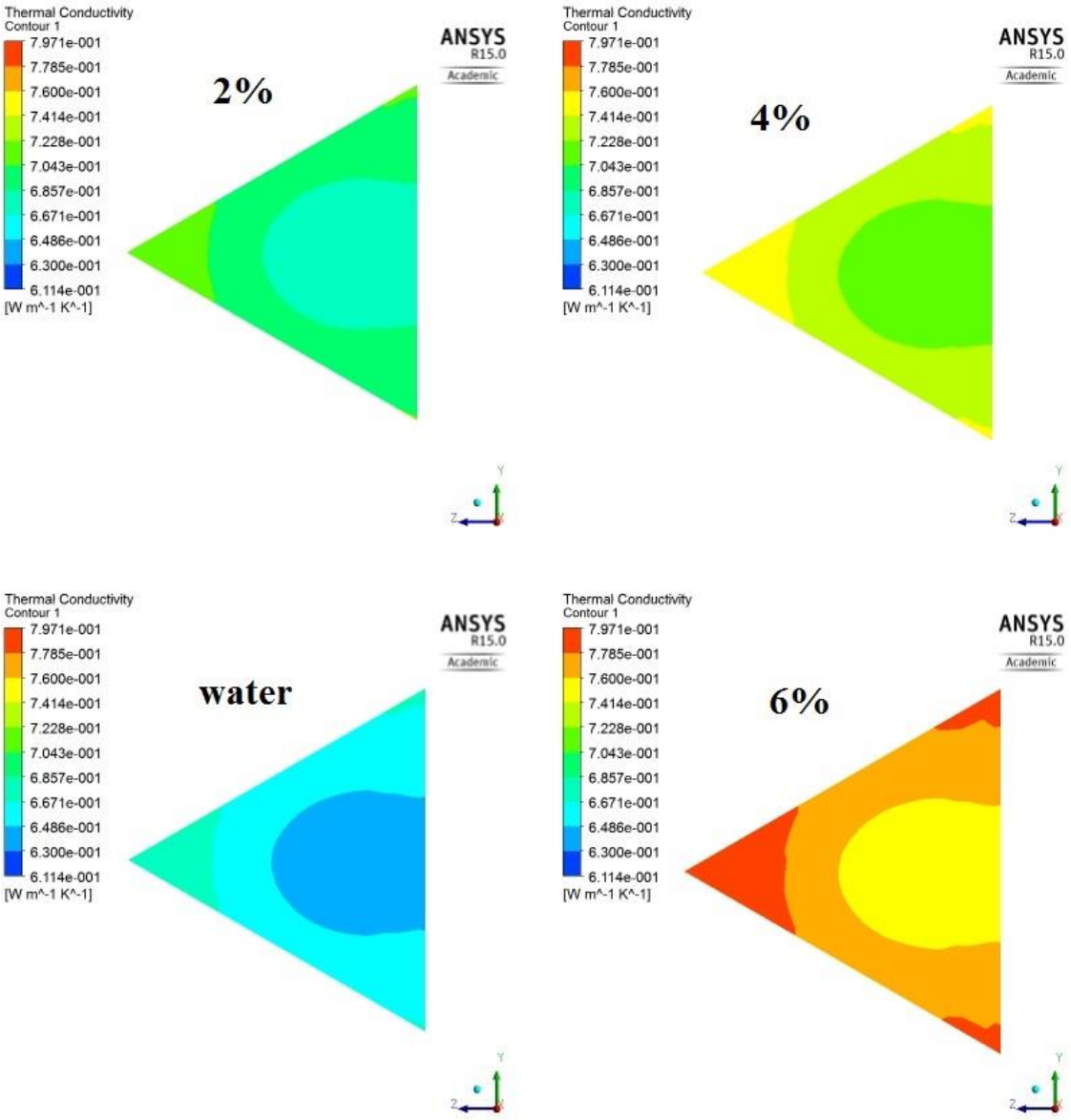

Figure 7-76 Thermal conductivity contour for various volume fraction

The viscosity change with volume fraction was studied in cross section of the U-bend, and the results are portrayed in Figure 7.77. However the higher values of thermal conductivity

were found in the corners of the cross-section, this is in agreement with previously discussed contours of temperature where the lower temperatures were noticed in the corners as the viscosity is temperature dependent thermal property. The higher values of viscosity are noticed in the core of the U-bend cross section

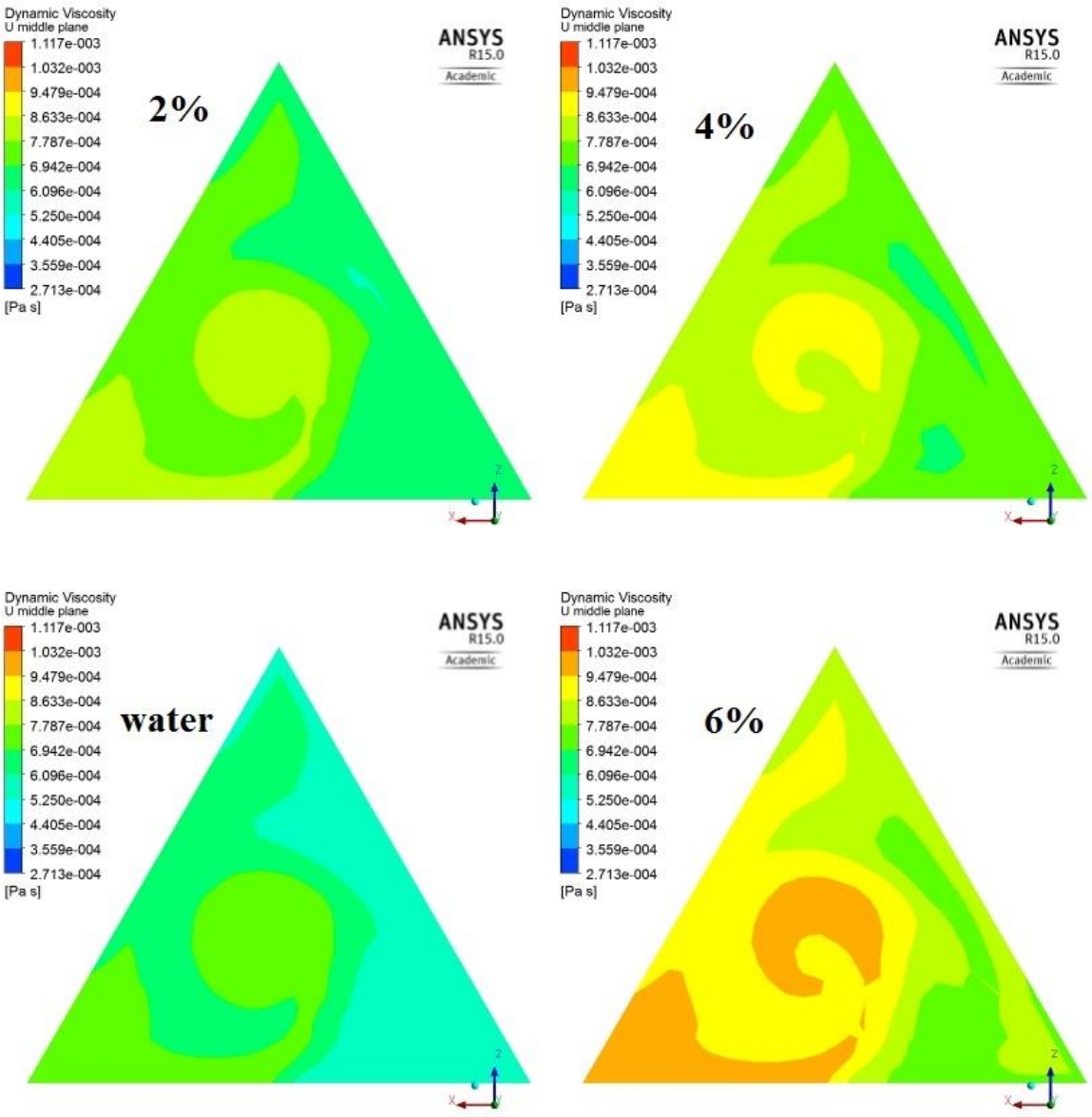

Figure 7-77 Contours of effective viscosity change with volume fraction in cross section of the U-bend

7.6 Summary

In the present Chapter the investigation of the enhancement of the heat transfer and flow characteristics in different configurations of microchannels in particular:

- The enhancement of heat transfer in the circular microchannel.
- The enhancement of the flow in rectangular microchannel with various aspect ratio
- The flow in U-bend circular microchannel was studied, and various parameters were tested in order to give a better understanding of such flows using nanofluids.
- The flows in rectangular U-bend microchannel using nanofluid have been studied thoroughly and the results were introduced and discussed.
- The viscosity augmented by up 25.5% when 6% volume fraction was tested in the centre line in comparison to water. However, this augmentation in viscosity was risen to 27.61% at the upstream wall. This demonstrates that the enhancement of the effective viscosity at the upstream pipe wall is more pronounced than that at the upstream pipe centre line.
- The skin friction increased with the rise in the nanoparticle volume fraction, the rise at the upstream pipe exit was found up to 13.67% when the volume fraction 6% is tested compared to water
- In the upstream pipe of the rectangular microchannel, it was found that the heat transfer enhanced up to 14.73% when 6% volume fraction was tested compared to water.

8 Experimental Work

8.1 Introduction

The heat exchanger is considered as one of the most encountered devices that broadly used in various industrial applications. Over the last several decades, many works have been made to improve the heat transfer of heat exchangers and decrease the time of the heat transfer. Some of the improvement approaches are passive and active techniques such as increasing area and using fluids with suspended nanoparticles.

In the present Chapter, the experimental work and the rig test is presented and described. The rig test was built to measure the heat transfer enhancement and synthesising the nanofluid with various volume fractions and several nanoparticles.

8.2 Design and building and commissioning of rig

The rig test as shown in Figure 8.1 consists of double pipe heat exchanger. The heat exchanger consists of outer stainless steel pipe with diameter 139.7mm thickness 2mm with length 1.8 m. The inner pipe is a copper pipe with diameter 15 mm and length 2 m.

Figure 8-1 Rig test

The schematic diagram is shown in Figure 8.2.Two loops are considered, the cold loop which consists of inner copper pipe, circulating pump purchased from GRUNDFOS with variable speed as shown in Figure 8.7 to deliver the nanofluid in the cold loop. The circulating nanofluid pump works in three different speeds, the maximum head is 5 m, the maximum flow rate is 2.7 m^3/hr and works at temperature up to 110 ^{o} C, the maximum system pressure is 1.0 Mpa.

The hot loop comprises outer stainless steel pipe, hot water pump, and hot water tank.

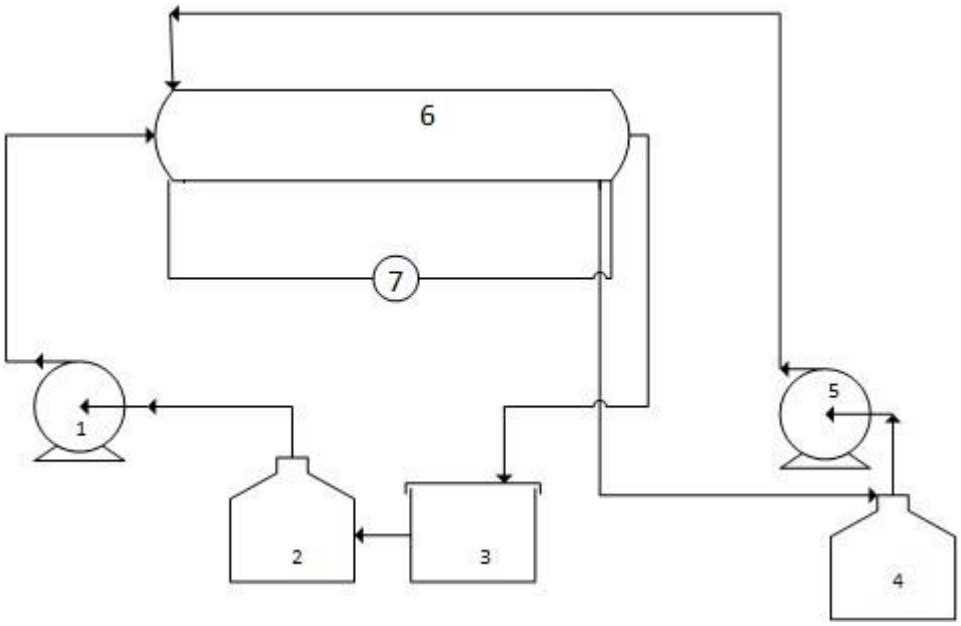

Figure 8-2 Schematic diagram of the experimental setup

1-nanofluid pump, 2-Nanoflui tank 3-Chiller 4-Hot water tank

5-Hot water pump 6-Double pipe heat exchanger 7-Differential manometer

The outer pipe is thermally insulated with two thick layers of glass wool insulation to prevent any heat loss. Four T-type thermocouples 0.5 mm thickness with accuracy ±0.75 % were fitted at the inlet and outlet of the cold and hot loops to measure the temperature at the inlet and outlet of each pipe, Pico data logger was used to record the temperature readings. Two flowmeters purchased from OMEGA Company with accuracy ±3% and repeatability of 0.5% of the full scale and operating pressure up to 13.7 bar and operating temperature range of -20 to 100 ^{o}C as shown in Figure 8.3 were installed at the entry of each loop, each flowmeter is connected to data logger from OMEGA Company with

accuracy of 0.01% as shown in Figure 8.4. The pressure difference along the cold loop was measured by differential manometer purchased from Cole-palmer with ±2% full accuracy as shown in Figure 8.8.

Figure 8-3 Flow meter

Figure 8-4 Digital logger for the flowmeter

In the inner pipe, a chamber was fitted and a viscometer as shown in Figure 8.5, it was purchased from Hydramotion, and inserted in the chamber in order to measure the viscosity of the nanofluid. The viscolite has a range reading of 0 to 5000 cp with accuracy 1% and can give the reading in 1 second. The instrument can work in the temperature range -20 to +120 ^{o}C. The aim of this instrument is to measure the accurate value of the effective viscosity as well as to validate the present proposed model and to compare the readings with available correlations.

Figure 8-5 Viscometer

A chiller as shown in Figure 8.6 is used to cool the nanofluid when leaving the inner pipe and the aim is to circulate the nanofluid in the inner pipe inlet with lower temperature in order to cool the outer pipe medium

Figure 8-6 Chiller for cooling nanofluid

Figure 8-7 Circulating pump

Figure 8-8 Differential Manometer

8.3 Synthesis of various Nanofluids

In the present work, four different nanoparticles powder were purchased from io-ti-tech nanomaterial in Germany as shown in Figure 8.8, the nanoparticles used in the present investigation are Mgo, Tio_2, Cuo and Al_2O_3. The volume fractions were calculated using equation 8.1. The technical data of these nanoparticles are shown in Appendix A1, the quantity used to synthesise the exact amount of volume fraction of each nanoparticle is introduced in Table 8.1, 8.2, 8.3 and 8.4 respectively.

Figure 8-9 Nanoparticle Powder

The plan was to mix the nanoparticle and distilled water in the lab and use the ultrasound bath purchased from Grant instrument as shown in Figure 8.9. However, due to health and safety, high volume fraction with small quantity was mixed in an external supplier (CPI consumer products inventory).

$$\emptyset = \frac{\left[\frac{m_S}{\rho_S}\right]}{\left[\frac{m_S}{\rho_S} + \frac{m_{bf}}{\rho_{bf}}\right]} \tag{8.1}$$

Where m is the mass.

Figure 8-10 Ultrasound bath

After the material mixing by the external supplier, the magnetic stirrer will be used for thirty minutes, and then the suspension will be left in the ultrasound bath for three hours to get a homogenous and stable nanofluid.

Figure 8-11 Magnetic stirrer

Table 8-1 Mgo volume fractions

Volume Fraction	Water Density	Particle Density	Water Volume (ml)	Particle Mass (grams)
0.001	998	3580	10000	35.907
0.004	998	3580	10000	144.063
0.0075	998	3580	10000	271.071
0.015	998	3580	10000	546.270

Table 8-2 TiO2 volume fractions

Volume Fraction	Water Density	Particle Density	Water Volume (ml)	Particle Mass (grams)
0.001	998	4250	9000	38.365
0.004	998	4250	9000	153.922
0.0075	998	4250	8800	283.186
0.015	998	4250	8100	525.289

Table 8-3 CuO volume fractions

Volume Fraction	Water Density	Particle Density	Water Volume (ml)	Particle Mass (grams)
0.001	998	6310	8000	50.631
0.004	998	6310	8000	203.137
0.015	998	6310	7750	746.200

Table 8-4 Al_2O_3 volume fractions

Volume Fraction	Water Density	Particle Density	Water Volume (ml)	Particle mass (grams)
0.001	998	3950	9000	35.656
0.004	998	3950	9000	143.057
0.0075	998	3950	9000	269.178
0.015	998	3950	9000	542.455

8.4 Experimental work with Nanofluids

Due to health and safety regulations in the University, the syntheses of the nanofluid took long time to approve and the commissioning of the nanofluid in the rig test has not been approved till writing of this thesis. Hence, only water has been used to conduct the experiment. The how water was heated to a range of temperatures. The inlet and outlet temperatures of both loops were recorded. All data were taken in this experiment after two hours of operating to ensure steady state and the heat is balanced. The flow rate for both cold and hot loops were taken. The following formulas were used to calculate the desired parameters:

The Nu number of the cold loop is calculated based on the inner diameter of the copper pipe as follows:

$$Nu = \frac{hd_i}{K_{eff}} \tag{8.2}$$

The surface heat transfer coefficient h is calculated as described by Wilson plot [295] and Fernandez et al [296] written as:

$$h = \frac{Q_{average}}{A_i(T_W - T_b)} \tag{8.3}$$

Where $A_i = \pi DL$

$$Q = UA\Delta T_{lm} \tag{8.4}$$

$$Q_{average} = \frac{(Q_C + Q_h)}{2} \tag{8.5}$$

$$Q_C = \dot{m}_c C_{pnf}\left(T_{nf\ out} - T_{nf\ in}\right) \tag{8.6}$$

$$Q_h = \dot{m}_h C_{ph}(T_{h\,in} - T_{h\,out}) \tag{8.7}$$

T_W is the average wall temperature and calculated from the next equation:

$$T_w = \frac{(T_{h,i} - T_{nf,o}) - (T_{H,O} - T_{nf,i})}{\ln\left(\frac{T_{h,i} - T_{nf,o}}{T_{h.o} - T_{nf,i}}\right)} \tag{8.8}$$

$$f = \frac{\Delta p}{\frac{1}{2}\rho u^2 \left(\frac{L}{D_i}\right)} \tag{8.9}$$

The thermophysical properties such as thermal conductivity, specific heat, density and viscosity are calculated as discussed in Chapter seven. The calculations of thermal parameters and non-dimensional numbers such as Nu number, Pr number and Re number are introduced in Table 8.5 and 8.6.

It is worth to mention that conducting the experiment with nanofluid is ready for investigating as all necessary measures were taken while the approval of the start of the work has not been granted till now by the health and safety office in the University.

The temperature readings were taken at the inlet and outlet of each loop; this step was repeated at heating and cooling to ensure a steady temperature reading is reached. The data for temperature for the outer pipe and the inner pipe are shown in Figures 8.12 and 8.13 respectively.

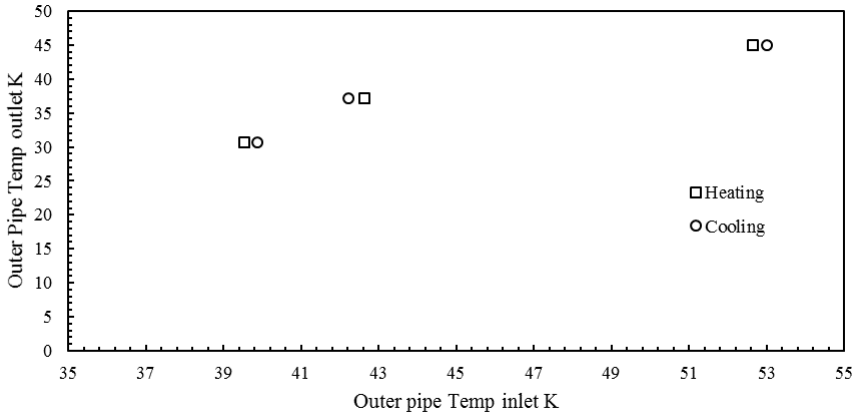

Figure 8-12 Heating and cooling temperature for the inlet and outlet outer pipe

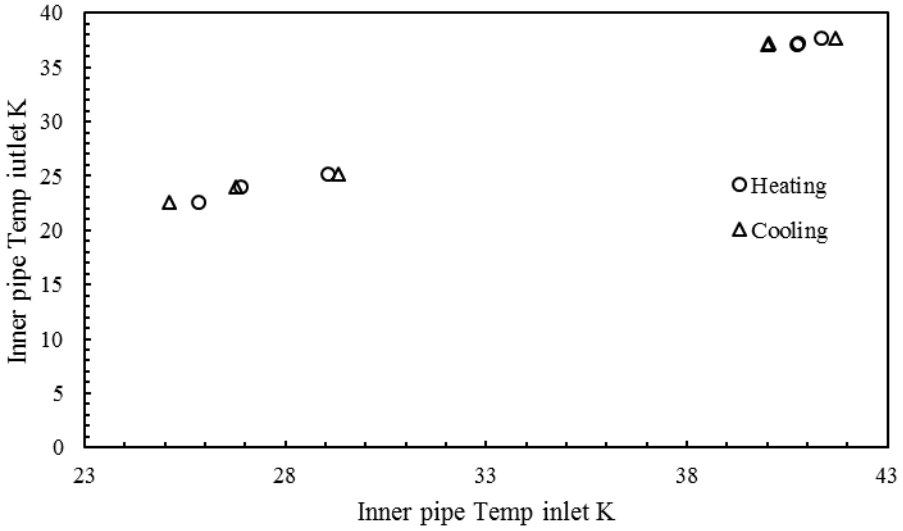

Figure 8-13 Heating and cooling temperatures for the inlet and outlet inner pipe

Table 8-5 Entry parameters for cold and hot

PARAMETERS				
		Hot Fluid	**Cold Fluid**	
Inlet Temperature	T_{in}	35	28	C

Outlet Temperature	T_{out}	33	31	C
Thermal Conductivity	k	0.601	0.601	$W\ m^{-1}K^{-1}$
Specific Heat Capacity	C_p	4200	4200	$J\ kg^{-1}\ K^{-1}$
Viscosity	μ	0.00103	0.009	Pa s
Density	ρ	970	1020	$kg\ m^{-3}$
Mass Flow Rate	$\dot{m}$	0.0038	0.017	$kg\ s^{-1}$
Inside Diameter	d_i	0.1397	0.015	m
Outside Diameter	d_o	0.1417	0.017	m

Table 8-6 Thermal parameters calculations

CALCULATIONS		**Hot Fluid**	**Cold Fluid**	
Heat Transfer	Q	31.92	214.2	W
Prandtl Number	Pr	7.198003	62.89517	
Flow Area	A	0.015101	0.000177	m^2
Hydraulic Diameter	D_h	0.1227	0.015	m
Heat Transfer Surface Area	A_s	0.21471	0.18945	m^2
Fluid Velocity	V	0.000259	0.094314	$m\ s^{-1}$
Reynolds Number	Re	29.97695	160.3339	
Friction Factor	*f*	0.228347	0.04447	
Nusselt Number	Nu	62.38927	40.30971	
Heat Transfer Coefficient	*h*	305.5905	1615.076	$W\ m^{-2}K^{-1}$
Pressure Drop	ΔP	0.001097	233.0159	Pa

9 Conclusions and Future Recommendations

9.1 Conclusions

The main conclusions from this research and the recommendations for future works are introduced in this chapter. The present chapter highlights the major findings of this study answering the research questions raised earlier in chapter one, the heat transfer improvements and the fluid flow characteristics have been investigated thoroughly, and the following conclusions are summarised:

- The literature review revealed that the investigation of heat transfer enhancement utilising nanofluids despite many efforts still need extra works to understand the mechanism of the enhancement due to the nanoparticle suspension. The literature has also demonstrated lack in experimental works that can help to build unified modified of predicting the thermophysical properties and a general correlation to calculate Nu number in forced convection.
- The enhancement of heat transfer in natural convection employing various nanofluids has been studied, and the volume fraction augmentation was found to deteriorate the heat transfer rate. The increase in Ra number in natural convection promoted the heat transfer rate remarkably. The Brownian motion, when incorporated, showed that the Nu number is higher than that the case where no Brownian motion is considered, moreover, it was better when compared to experimental results.
- The inclination angle in backward-facing step influence on the heat transfer rate was investigated, and the results showed that the Nu number decreased by up to 3% when 90^{o} inclination angle is tested compared to 125^{o} inclination angle. Four aspect ratios were tested along with inclination angle effect have been investigated extensively, and the results showed that the increase in aspect ratio improved the

heat transfer rate substantially, this improvement was noticed in all aspect ratios tested.

- A new effective viscosity model has been proposed and tested, and the results were compared to available theoretical and empirical models. The classical model vastly underestimates the effective viscosity of the nanofluid compared to the present model. The new viscosity model was developed and introduced in this study, the model was scrutinised, and a rigours investigation was reported. The proposed model proved a reasonable accuracy level and can be implemented with a good level of reliability. The present model showed a considerable increase in the effective viscosity with the increase in the volume fraction. The introduced model showed a better performance compared to the theoretical models, particularly at higher volume fractions. The present developed model was scrutinised and compared to many experimental data and empirical models and it was found confidently that the present model can be employed at a wider range of volume fractions and varied level of the temperature range.
- The investigation of heat transfer performance and fluid flow have been investigated in various configurations of microchannels. The nanofluid flow inside a circular microchannel under constant temperature was tested and studied in particular the entrance region and the variation of Nu number was introduced. The heat transfer rate in rectangular cross section utilising nanofluid with various aspect ratios has been studied. The Nu number was found to increase with the increase in volume fraction and the increase in Re number. The aspect ratio influence was investigated, and it was found that the Nu number improved considerably with the increase in microchannel aspect ratio. The circular U-bend microchannel with nanofluid was tested under various volume fractions. The increase in volume fraction was found in favour of heat transfer rate in the upstream and downstream pipe of the U-bend microchannel. The enhancement in Nu number in this configuration was studied, and it was found that the heat transfer rate in the upstream pipe is larger than that of the downstream pipe of the U-bend circular microchannel. The velocity gradient, the shear stress and the skin friction

coefficient in the U-bend of the microchannel were studied, and the results of the effect of the volume fraction were presented and discussed. The flow of nanofluid as a coolant in a triangular cross section U-bend microchannel was investigated, and the results were presented and discussed.

- The pressure coefficient and the shear stress increases with the increase in the volume fraction which can be assumed a slight penalty of using nanofluid.
- The contours of thermal conductivity and effective viscosity variation in the triangular upstream and U-bend are introduced. These contours can help in the understanding of the thermal performance particularly in the U-bend. The effect of the volume fraction on the thermal conductivity in the U-bend was investigated, and it increased the thermal conductivity significantly and especially in the corners of the triangle.

9.2 Recommendations for future work

Despite the recent works in terms of enhancement of heat transfer utilising nanofluid, further efforts are needed to validate the available models. In this section, some of the recommendations of future work are listed

- Many works have devoted to investigating the natural convection with low Ra number, however, work in very high Ra number are still very limited.
- Due to the fairly high cost of the nanoparticle, many models were based on a few number of experimental work. Producing a large number of experimental data would help in unifying the thermophysical properties models.
- As mentioned in this research that the microchannel flows utilising nanofluid is preferable compared to conventional fluids, however, there is still a big gap in experimental studies to judge the pressure coefficient correlations used in the microchannel.

- The formulas used in the literature to predict Nu number showed discrepancy results which highlight the need for solid prediction based on additional experimental works.
- Further work in modelling turbulent flows in heat exchangers is essential to present a valid model to simulate the turbulent flow.

References

[1] A. Bejan and A. D. Kraus, *Heat transfer handbook* vol. 1: John Wiley & Sons, 2003.

[2] F. P. Incropera and D. P. De Witt, "Fundamentals of heat and mass transfer," 1985.

[3] S. U. S. Choi and J. A. Eastman, *Enhancing thermal conductivity of fluids with nanoparticles*, 1995.

[4] J. Koo and C. Kleinstreuer, "Viscous dissipation effects in microtubes and microchannels," *International Journal of Heat and Mass Transfer,* vol. 47, pp. 3159-3169, 7// 2004.

[5] J. C. Maxwell, *A treatise on electricity and magnetism* vol. 1: Clarendon press, 1881.

[6] H. F. Oztop, E. Abu-Nada, Y. Varol, and K. Al-Salem, "Computational analysis of non-isothermal temperature distribution on natural convection in nanofluid filled enclosures," *Superlattices and Microstructures,* vol. 49, pp. 453-467, 4// 2011.

[7] B. Ghasemi and S. M. Aminossadati, "Periodic natural convection in a nanofluid-filled enclosure with oscillating heat flux," *International Journal of Thermal Sciences,* vol. 49, pp. 1-9, 1// 2010.

[8] R. S. Vajjha and D. K. Das, "Experimental determination of thermal conductivity of three nanofluids and development of new correlations," *International Journal of Heat and Mass Transfer,* vol. 52, pp. 4675-4682, 10// 2009.

[9] S. Lee, S. U. S. Choi, S. Li, and J. A. Eastman, "Measuring Thermal Conductivity of Fluids Containing Oxide Nanoparticles," *Journal of Heat Transfer,* vol. 121, pp. 280-289, 1999.

[10] K. Khanafer, K. Vafai, and M. Lightstone, "Buoyancy-driven heat transfer enhancement in a two-dimensional enclosure utilizing nanofluids," *International Journal of Heat and Mass Transfer,* vol. 46, pp. 3639-3653, 9// 2003.

[11] C. H. Li and G. P. Peterson, "Experimental investigation of temperature and volume fraction variations on the effective thermal conductivity of nanoparticle suspensions (nanofluids)," *Journal of Applied Physics,* vol. 99, p. 084314, 2006.

[12] A. A. Abbasian Arani and J. Amani, "Experimental investigation of diameter effect on heat transfer performance and pressure drop of TiO2–water nanofluid," *Experimental Thermal and Fluid Science,* vol. 44, pp. 520-533, 2013.

[13] K. C. Lin and A. Violi, "Natural convection heat transfer of nanofluids in a vertical cavity: Effects of non-uniform particle diameter and temperature on thermal conductivity," *International Journal of Heat and Fluid Flow,* vol. 31, pp. 236-245, 2010.

[14] S. Mirmasoumi and A. Behzadmehr, "Effect of nanoparticles mean diameter on mixed convection heat transfer of a nanofluid in a horizontal tube," *International Journal of Heat and Fluid Flow,* vol. 29, pp. 557-566, 4// 2008.

[15] R. Prasher, D. Song, J. Wang, and P. Phelan, "Measurements of nanofluid viscosity and its implications for thermal applications," *Applied Physics Letters,* vol. 89, p. 133108, 2006.

[16] B. C. Pak and Y. I. Cho, "HYDRODYNAMIC AND HEAT TRANSFER STUDY OF DISPERSED FLUIDS WITH SUBMICRON METALLIC OXIDE PARTICLES," *Experimental Heat Transfer,* vol. 11, pp. 151-170, 1998/04/01 1998.

[17] R. M. Moghari, A. S. Mujumdar, M. Shariat, F. Talebi, S. M. Sajjadi, and A. Akbarinia, "Investigation effect of nanoparticle mean diameter on mixed convection Al2O3-water nanofluid flow in an annulus by two phase mixture

model," *International Communications in Heat and Mass Transfer,* vol. 49, pp. 25-35, 2013.

[18] H. Aminfar and R. Motallebzadeh, "Numerical Investigation of the Effects of Nanoparticle Diameter on Velocity Field and Nanoparticle Distribution of Nanofluid Using Lagrangian-Eulerian Approach," *Journal of Dispersion Science and Technology,* vol. 32, pp. 1311-1317, 2011/09/01 2011.

[19] C. H. Chon, K. D. Kihm, S. P. Lee, and S. U. S. Choi, "Empirical correlation finding the role of temperature and particle size for nanofluid (Al2O3) thermal conductivity enhancement," *Applied Physics Letters,* vol. 87, p. 153107, 2005.

[20] P. Keblinski, S. R. Phillpot, S. U. S. Choi, and J. A. Eastman, "Mechanisms of heat flow in suspensions of nano-sized particles (nanofluids)," *International Journal of Heat and Mass Transfer,* vol. 45, pp. 855-863, 2// 2002.

[21] W. Evans, J. Fish, and P. Keblinski, "Role of Brownian motion hydrodynamics on nanofluid thermal conductivity," *Applied Physics Letters,* vol. 88, p. 093116, 2006.

[22] S. P. Jang and S. U. S. Choi, "Role of Brownian motion in the enhanced thermal conductivity of nanofluids," *Applied Physics Letters,* vol. 84, pp. 4316-4318, 2004.

[23] A. Gupta and R. Kumar, "Role of Brownian motion on the thermal conductivity enhancement of nanofluids," *Applied Physics Letters,* vol. 91, p. 223102, 2007.

[24] W. Duangthongsuk and S. Wongwises, "Comparison of the effects of measured and computed thermophysical properties of nanofluids on heat transfer performance," *Experimental Thermal and Fluid Science,* vol. 34, pp. 616-624, 7// 2010.

[25] W. Duangthongsuk and S. Wongwises, "Effect of thermophysical properties models on the predicting of the convective heat transfer coefficient for low concentration nanofluid," *International Communications in Heat and Mass Transfer,* vol. 35, pp. 1320-1326, 2008.

[26] H. Fricke, "A mathematical treatment of the electric conductivity and capacity of disperse systems I. The electric conductivity of a suspension of homogeneous spheroids," *Physical Review,* vol. 24, p. 575, 1924.

[27] D. A. G. Bruggeman, "Berechnung verschiedener physikalischer Konstanten von heterogenen Substanzen. I. Dielektrizitätskonstanten und Leitfähigkeiten der Mischkörper aus isotropen Substanzen," *Annalen der Physik,* vol. 416, pp. 636-664, 1935.

[28] R. Davis, "The effective thermal conductivity of a composite material with spherical inclusions," *International Journal of Thermophysics,* vol. 7, pp. 609-620, 1986.

[29] S. Y. Lu and H. C. Lin, "Effective conductivity of composites containing aligned spheroidal inclusions of finite conductivity," *Journal of Applied Physics,* vol. 79, pp. 6761-6769, 1996.

[30] P. Bhattacharya, S. K. Saha, A. Yadav, P. E. Phelan, and R. S. Prasher, "Brownian dynamics simulation to determine the effective thermal conductivity of nanofluids," *Journal of Applied Physics,* vol. 95, pp. 6492-6494, 2004.

[31] J. Koo and C. Kleinstreuer, "A new thermal conductivity model for nanofluids," *Journal of Nanoparticle Research,* vol. 6, pp. 577-588, 2005.

[32] R. Prasher, P. Bhattacharya, and P. E. Phelan, "Thermal Conductivity of Nanoscale Colloidal Solutions (Nanofluids)," *Physical Review Letters,* vol. 94, p. 025901, 01/18/ 2005.

[33] H. Masuda, A. Ebata, K. Teramae, and N. Hishinuma, "Alteration of Thermal Conductivity and Viscosity of Liquid by Dispersing Ultra-Fine Particles

Dispersion of Al₂O₃, SiO₂ and TiO₂ Ultra-Fine Particles," *Netsu Bussei,* vol. 7, pp. 227-233, 1993.

[34] J. A. Eastman, U. S. Choi, S. Li, L. J. Thompson, and S. Lee, "Enhanced Thermal Conductivity through the Development of Nanofluids," *MRS Online Proceedings Library Archive,* vol. 457, pp. null-null, 1996.

[35] D. C. Venerus, M. S. Kabadi, S. Lee, and V. Perez-Luna, "Study of thermal transport in nanoparticle suspensions using forced Rayleigh scattering," *Journal of Applied Physics,* vol. 100, p. 094310, 2006.

[36] S. A. Putnam, D. G. Cahill, P. V. Braun, Z. Ge, and R. G. Shimmin, "Thermal conductivity of nanoparticle suspensions," *Journal of Applied Physics,* vol. 99, p. 084308, 2006.

[37] X. Zhang, H. Gu, and M. Fujii, "Effective thermal conductivity and thermal diffusivity of nanofluids containing spherical and cylindrical nanoparticles," *Journal of Applied Physics,* vol. 100, p. 044325, 2006.

[38] H. Zhu, C. Zhang, S. Liu, Y. Tang, and Y. Yin, "Effects of nanoparticle clustering and alignment on thermal conductivities of Fe3O4 aqueous nanofluids," *Applied Physics Letters,* vol. 89, p. 023123, 2006.

[39] D.-H. Yoo, K. S. Hong, and H.-S. Yang, "Study of thermal conductivity of nanofluids for the application of heat transfer fluids," *Thermochimica Acta,* vol. 455, pp. 66-69, 4/1/ 2007.

[40] Y. J. Hwang, Y. C. Ahn, H. S. Shin, C. G. Lee, G. T. Kim, H. S. Park*, et al.*, "Investigation on characteristics of thermal conductivity enhancement of nanofluids," *Current Applied Physics,* vol. 6, pp. 1068-1071, 10// 2006.

[41] N. Shalkevich, A. Shalkevich, and T. Bürgi, "Thermal Conductivity of Concentrated Colloids in Different States," *The Journal of Physical Chemistry C,* vol. 114, pp. 9568-9572, 2010/06/03 2010.

[42] W. Duangthongsuk and S. Wongwises, "Measurement of temperature-dependent thermal conductivity and viscosity of TiO2-water nanofluids," *Experimental Thermal and Fluid Science,* vol. 33, pp. 706-714, 4// 2009.

[43] M. Chandrasekar, S. Suresh, and A. Chandra Bose, "Experimental investigations and theoretical determination of thermal conductivity and viscosity of Al2O3/water nanofluid," *Experimental Thermal and Fluid Science,* vol. 34, pp. 210-216, 2// 2010.

[44] M. P. Beck, Y. Yuan, P. Warrier, and A. S. Teja, "The effect of particle size on the thermal conductivity of alumina nanofluids," *Journal of Nanoparticle Research,* vol. 11, pp. 1129-1136, 2009.

[45] S. M. S. Murshed, K. C. Leong, and C. Yang, "Investigations of thermal conductivity and viscosity of nanofluids," *International Journal of Thermal Sciences,* vol. 47, pp. 560-568, 5// 2008.

[46] X. Wang, X. Xu, and S. U. S. Choi, "Thermal Conductivity of Nanoparticle - Fluid Mixture," *Journal of Thermophysics and Heat Transfer,* vol. 13, pp. 474-480, 1999/10/01 1999.

[47] S. M. S. Murshed, K. C. Leong, and C. Yang, "Enhanced thermal conductivity of TiO2—water based nanofluids," *International Journal of Thermal Sciences,* vol. 44, pp. 367-373, 4// 2005.

[48] H. Xie, J. Wang, T. Xi, Y. Liu, F. Ai, and Q. Wu, "Thermal conductivity enhancement of suspensions containing nanosized alumina particles," *Journal of Applied Physics,* vol. 91, pp. 4568-4572, 2002.

[49] M. J. Pastoriza-Gallego, L. Lugo, J. L. Legido, and M. M. Piñeiro, "Thermal conductivity and viscosity measurements of ethylene glycol-based Al2O3 nanofluids," *Nanoscale Research Letters,* vol. 6, p. 221, 2011.

[50] V. D. Bruggeman, "Berechnung verschiedener physikalischer Konstanten von heterogenen Substanzen. I. Dielektrizitätskonstanten und Leitfähigkeiten der Mischkörper aus isotropen Substanzen," *Annalen der physik,* vol. 416, pp. 636-664, 1935.

[51] R. Hamilton and O. Crosser, "Thermal conductivity of heterogeneous two-component systems," *Industrial & Engineering chemistry fundamentals,* vol. 1, pp. 187-191, 1962.

[52] J. Koo and C. Kleinstreuer, "A new thermal conductivity model for nanofluids," *Journal of Nanoparticle Research,* vol. 6, pp. 577-588, 2004/12/01 2004.
[53] Q. Xue, "Model for thermal conductivity of carbon nanotube-based composites," *Physica B: Condensed Matter,* vol. 368, pp. 302-307, 2005.
[54] C. H. Li and G. Peterson, "Experimental investigation of temperature and volume fraction variations on the effective thermal conductivity of nanoparticle suspensions (nanofluids)," *Journal of Applied Physics,* vol. 99, p. 084314, 2006.
[55] J. Buongiorno, "Convective Transport in Nanofluids," *Journal of Heat Transfer,* vol. 128, p. 240, 2006.
[56] E. V. Timofeeva, A. N. Gavrilov, J. M. McCloskey, Y. V. Tolmachev, S. Sprunt, L. M. Lopatina*, et al.*, "Thermal conductivity and particle agglomeration in alumina nanofluids: experiment and theory," *Physical Review E,* vol. 76, p. 061203, 2007.
[57] J. Avsec and M. Oblak, "The calculation of thermal conductivity, viscosity and thermodynamic properties for nanofluids on the basis of statistical nanomechanics," *International Journal of Heat and Mass Transfer,* vol. 50, pp. 4331-4341, 2007.
[58] M. Chandrasekar, S. Suresh, R. Srinivasan, and A. C. Bose, "New analytical models to investigate thermal conductivity of nanofluids," *Journal of nanoscience and nanotechnology,* vol. 9, pp. 533-538, 2009.
[59] R. S. Vajjha, D. K. Das, and P. K. Namburu, "Numerical study of fluid dynamic and heat transfer performance of Al 2 O 3 and CuO nanofluids in the flat tubes of a radiator," *International Journal of Heat and fluid flow,* vol. 31, pp. 613-621, 2010.
[60] L. Godson, B. Raja, D. M. Lal, and S. Wongwises, "Experimental investigation on the thermal conductivity and viscosity of silver-deionized water nanofluid," *Experimental Heat Transfer,* vol. 23, pp. 317-332, 2010.
[61] M. Corcione, "Rayleigh-Bénard convection heat transfer in nanoparticle suspensions," *International Journal of Heat and Fluid Flow,* vol. 32, pp. 65-77, 2// 2011.
[62] A. Einstein, "Eine neue Bestimmung der Moleküldimensionen," *Annalen der Physik,* vol. 324, pp. 289-306, 1906.
[63] G. I. Taylor, "The Viscosity of a Fluid Containing Small Drops of Another Fluid," *Proceedings of the Royal Society of London. Series A,* vol. 138, pp. 41-48, 1932.
[64] H. C. Brinkman, "The Viscosity of Concentrated Suspensions and Solutions," *The Journal of Chemical Physics,* vol. 20, pp. 571-571, 1952.
[65] V. Vand, "Viscosity of Solutions and Suspensions. I. Theory," *The Journal of Physical and Colloid Chemistry,* vol. 52, pp. 277-299, 1948/02/01 1948.
[66] R. Roscoe, "The viscosity of suspensions of rigid spheres," *British Journal of Applied Physics,* vol. 3, p. 267, 1952.
[67] G. Batchelor, "The effect of Brownian motion on the bulk stress in a suspension of spherical particles," *Journal of Fluid Mechanics,* vol. 83, pp. 97-117, 1977.
[68] T. S. Lundgren, "Slow flow through stationary random beds and suspensions of spheres," *Journal of Fluid Mechanics,* vol. 51, pp. 273-299, 1972/01/01 1972.
[69] A. L. Graham, "On the viscosity of suspensions of solid spheres," *Applied Scientific Research,* vol. 37, pp. 275-286, 1981.
[70] N. A. Frankel and A. Acrivos, "On the viscosity of a concentrated suspension of solid spheres," *Chemical Engineering Science,* vol. 22, pp. 847-853, 1967/06/01 1967.
[71] J. Bicerano, J. F. Douglas, and D. A. Brune, "Model for the Viscosity of Particle Dispersions," *Journal of Macromolecular Science, Part C,* vol. 39, pp. 561-642, 1999/09/11 1999.
[72] N.-S. Cheng and A. W.-K. Law, "Exponential formula for computing effective viscosity," *Powder Technology,* vol. 129, pp. 156-160, 1/8/ 2003.
[73] J. Avsec and M. Oblak, "The calculation of thermal conductivity, viscosity and thermodynamic properties for nanofluids on the basis of statistical

nanomechanics," *International Journal of Heat and Mass Transfer,* vol. 50, pp. 4331-4341, 10// 2007.

[74] C. T. Nguyen, F. Desgranges, G. Roy, N. Galanis, T. Maré, S. Boucher*, et al.*, "Temperature and particle-size dependent viscosity data for water-based nanofluids – Hysteresis phenomenon," *International Journal of Heat and Fluid Flow,* vol. 28, pp. 1492-1506, 2007/12/01/ 2007.

[75] C. T. Nguyen, F. Desgranges, N. Galanis, G. Roy, T. Maré, S. Boucher*, et al.*, "Viscosity data for Al2O3–water nanofluid—hysteresis: is heat transfer enhancement using nanofluids reliable?," *International Journal of Thermal Sciences,* vol. 47, pp. 103-111, 2008.

[76] Y. Yang, Z. G. Zhang, E. A. Grulke, W. B. Anderson, and G. Wu, "Heat transfer properties of nanoparticle-in-fluid dispersions (nanofluids) in laminar flow," *International Journal of Heat and Mass Transfer,* vol. 48, pp. 1107-1116, 2005.

[77] K. B. Anoop, S. Kabelac, T. Sundararajan, and S. K. Das, "Rheological and flow characteristics of nanofluids: Influence of electroviscous effects and particle agglomeration," *Journal of Applied Physics,* vol. 106, p. 034909, 2009.

[78] P. K. Namburu, D. P. Kulkarni, A. Dandekar, and D. K. Das, "Experimental investigation of viscosity and specific heat of silicon dioxide nanofluids," *Micro and Nano Letters,* vol. 2, pp. 67-71, 2007.

[79] P. K. Namburu, D. P. Kulkarni, D. Misra, and D. K. Das, "Viscosity of copper oxide nanoparticles dispersed in ethylene glycol and water mixture," *Experimental Thermal and Fluid Science,* vol. 32, pp. 397-402, 11// 2007.

[80] D. P. Kulkarni, D. K. Das, and R. S. Vajjha, "Application of nanofluids in heating buildings and reducing pollution," *Applied Energy,* vol. 86, pp. 2566-2573, 12// 2009.

[81] J. Chevalier, O. Tillement, and F. Ayela, "Rheological properties of nanofluids flowing through microchannels," *Applied Physics Letters,* vol. 91, p. 233103, 2007.

[82] M. J. Pastoriza-Gallego, C. Casanova, J. L. Legido, and M. M. Piñeiro, "CuO in water nanofluid: Influence of particle size and polydispersity on volumetric behaviour and viscosity," *Fluid Phase Equilibria,* vol. 300, pp. 188-196, 1/25/ 2011.

[83] L. Chen, H. Xie, Y. Li, and W. Yu, "Nanofluids containing carbon nanotubes treated by mechanochemical reaction," *Thermochimica Acta,* vol. 477, pp. 21-24, 10/30/ 2008.

[84] A. Turgut, I. Tavman, M. Chirtoc, H. P. Schuchmann, C. Sauter, and S. Tavman, "Thermal Conductivity and Viscosity Measurements of Water-Based TiO2 Nanofluids," *International Journal of Thermophysics,* vol. 30, pp. 1213-1226, 2009.

[85] M. Naik, G. R. Janardhana, K. V. K. Reddy, and B. S. Reddy, "Experimental investigation into rheological property of copper oxide nanoparticles suspended in propylene glycol–water based fluids," *ARPN J Eng Appl Sci,* vol. 5, pp. 29-34, 2010.

[86] H. Zhu, C. Li, D. Wu, C. Zhang, and Y. Yin, "Preparation, characterization, viscosity and thermal conductivity of CaCO3 aqueous nanofluids," *Science China Technological Sciences,* vol. 53, pp. 360-368, 2010.

[87] J.-C. Yang, F.-C. Li, W.-W. Zhou, Y.-R. He, and B.-C. Jiang, "Experimental investigation on the thermal conductivity and shear viscosity of viscoelastic-fluid-based nanofluids," *International Journal of Heat and Mass Transfer,* vol. 55, pp. 3160-3166, 5// 2012.

[88] D. Toghraie, S. M. Alempour, and M. Afrand, "Experimental determination of viscosity of water based magnetite nanofluid for application in heating and cooling systems," *Journal of Magnetism and Magnetic Materials,* vol. 417, pp. 243-248, 11/1/ 2016.

[89] M. Hemmat Esfe, M. Afrand, S. Gharehkhani, H. Rostamian, D. Toghraie, and M. Dahari, "An experimental study on viscosity of alumina-engine oil: Effects of

temperature and nanoparticles concentration," *International Communications in Heat and Mass Transfer,* vol. 76, pp. 202-208, 8// 2016.

[90] M. K. Abdolbaqi, N. A. C. Sidik, A. Aziz, R. Mamat, W. H. Azmi, M. N. A. W. M. Yazid*, et al.*, "An experimental determination of thermal conductivity and viscosity of BioGlycol/water based TiO2 nanofluids," *International Communications in Heat and Mass Transfer,* vol. 77, pp. 22-32, 10// 2016.

[91] M. K. Abdolbaqi, N. A. C. Sidik, M. F. A. Rahim, R. Mamat, W. H. Azmi, M. N. A. W. M. Yazid*, et al.*, "Experimental investigation and development of new correlation for thermal conductivity and viscosity of BioGlycol/water based SiO2 nanofluids," *International Communications in Heat and Mass Transfer,* vol. 77, pp. 54-63, 10// 2016.

[92] O. Soltani and M. Akbari, "Effects of temperature and particles concentration on the dynamic viscosity of MgO-MWCNT/ethylene glycol hybrid nanofluid: Experimental study," *Physica E: Low-dimensional Systems and Nanostructures,* vol. 84, pp. 564-570, 10// 2016.

[93] B. İlhan, M. Kurt, and H. Ertürk, "Experimental investigation of heat transfer enhancement and viscosity change of hBN nanofluids," *Experimental Thermal and Fluid Science,* vol. 77, pp. 272-283, 10// 2016.

[94] G. Żyła and J. Fal, "Experimental studies on viscosity, thermal and electrical conductivity of aluminum nitride–ethylene glycol (AlN–EG) nanofluids," *Thermochimica Acta,* vol. 637, pp. 11-16, 8/10/ 2016.

[95] B. Aladag, S. Halelfadl, N. Doner, T. Maré, S. Duret, and P. Estellé, "Experimental investigations of the viscosity of nanofluids at low temperatures," *Applied Energy,* vol. 97, pp. 876-880, 9// 2012.

[96] L. Syam Sundar, E. Venkata Ramana, M. K. Singh, and A. C. M. Sousa, "Thermal conductivity and viscosity of stabilized ethylene glycol and water mixture Al2O3 nanofluids for heat transfer applications: An experimental study," *International Communications in Heat and Mass Transfer,* vol. 56, pp. 86-95, 8// 2014.

[97] J. Tony and T. Krishnakumar, "Experimental studies of thermal conductivity, viscosity and stability of ethylene glycol nanofluids," *J. IJIRSET,* vol. 2, pp. 611-617, 2013.

[98] M. Jarahnejad, E. B. Haghighi, M. Saleemi, N. Nikkam, R. Khodabandeh, B. Palm*, et al.*, "Experimental investigation on viscosity of water-based Al2O3 and TiO2 nanofluids," *Rheologica Acta,* vol. 54, pp. 411-422, 2015.

[99] N. Nikkam, M. Ghanbarpour, M. Saleemi, E. B. Haghighi, R. Khodabandeh, M. Muhammed*, et al.*, "Experimental investigation on thermo-physical properties of copper/diethylene glycol nanofluids fabricated via microwave-assisted route," *Applied Thermal Engineering,* vol. 65, pp. 158-165, 2014.

[100] W. H. Graf, *Hydraulics of sediment transport*: Water Resources Publication, 1984.

[101] M. Nabeel Rashin and J. Hemalatha, "Viscosity studies on novel copper oxide–coconut oil nanofluid," *Experimental Thermal and Fluid Science,* vol. 48, pp. 67-72, 7// 2013.

[102] M. Abareshi, S. H. Sajjadi, S. M. Zebarjad, and E. K. Goharshadi, "Fabrication, characterization, and measurement of viscosity of α-Fe2O3-glycerol nanofluids," *Journal of Molecular Liquids,* vol. 163, pp. 27-32, 9/1/ 2011.

[103] M. Kole and T. K. Dey, "Effect of aggregation on the viscosity of copper oxide–gear oil nanofluids," *International Journal of Thermal Sciences,* vol. 50, pp. 1741-1747, 9// 2011.

[104] H. Chen, Y. Ding, and C. Tan, "Rheological behaviour of nanofluids," *New journal of physics,* vol. 9, p. 367, 2007.

[105] W. J. Tseng and C.-N. Chen, "Effect of polymeric dispersant on rheological behavior of nickel–terpineol suspensions," *Materials Science and Engineering: A,* vol. 347, pp. 145-153, 4/25/ 2003.

[106] W. J. Tseng and K.-C. Lin, "Rheology and colloidal structure of aqueous TiO2 nanoparticle suspensions," *Materials Science and Engineering: A,* vol. 355, pp. 186-192, 8/25/ 2003.
[107] B. A. Horri, P. Ranganathan, C. Selomulya, and H. Wang, "A new empirical viscosity model for ceramic suspensions," *Chemical Engineering Science,* vol. 66, pp. 2798-2806, 6/15/ 2011.
[108] B. C. Sahoo, R. S. Vajjha, R. Ganguli, G. A. Chukwu, and D. K. Das, "Determination of Rheological Behavior of Aluminum Oxide Nanofluid and Development of New Viscosity Correlations," *Petroleum Science and Technology,* vol. 27, pp. 1757-1770, 2009/10/21 2009.
[109] A. Hernández Battez, J. L. Viesca, R. González, A. García, T. Reddyhoff, and A. Higuera-Garrido, "Effect of Shear Rate, Temperature, and Particle Concentration on the Rheological Properties of ZnO and ZrO2 Nanofluids," *Tribology Transactions,* vol. 57, pp. 489-495, 2014/05/04 2014.
[110] G. Vakili-Nezhaad and A. Dorany, "Effect of Single-Walled Carbon Nanotube on the Viscosity of Lubricants," *Energy Procedia,* vol. 14, pp. 512-517, 2012/01/01 2012.
[111] K. S. Suganthi and K. S. Rajan, "Temperature induced changes in ZnO–water nanofluid: Zeta potential, size distribution and viscosity profiles," *International Journal of Heat and Mass Transfer,* vol. 55, pp. 7969-7980, 12// 2012.
[112] K. S. Suganthi, N. Anusha, and K. S. Rajan, "Low viscous ZnO–propylene glycol nanofluid: a potential coolant candidate," *Journal of Nanoparticle Research,* vol. 15, p. 1986, 2013.
[113] E. V. Timofeeva, J. L. Routbort, and D. Singh, "Particle shape effects on thermophysical properties of alumina nanofluids," *Journal of Applied Physics,* vol. 106, p. 014304, 2009.
[114] G. Żyła, A. Witek, and M. Cholewa, "Viscosity of diethylene glycol-based Y2O3 nanofluids," *Journal of Experimental Nanoscience,* vol. 10, pp. 458-465, 2015/04/13 2015.
[115] R. S. Vajjha, D. K. Das, and B. M. Mahagaonkar, "Density Measurement of Different Nanofluids and Their Comparison With Theory," *Petroleum Science and Technology,* vol. 27, pp. 612-624, 2009/03/23 2009.
[116] R. S. Vajjha and D. K. Das, "Measurements of Specific Heat and Density of Al2O3 Nanofluid," *AIP Conference Proceedings,* vol. 1063, pp. 361-370, 2008.
[117] J. R. Satti, D. K. Das, and D. R. Ray, "Measurements of Densities of Propylene Glycol-Based Nanofluids and Comparison With Theory," *Journal of Thermal Science and Engineering Applications,* vol. 8, pp. 021021-021021, 2016.
[118] Z. Said, M. S. H, A. Kamyar, and R. Saidur, "Experimental investigation on the stability and density of TiO 2 , Al 2 O 3 , SiO 2 and TiSiO 4," *IOP Conference Series: Earth and Environmental Science,* vol. 16, p. 012002, 2013.
[119] J. Ganeshkumar, D. Kathirkaman, K. Raja, V. Kumaresan, and R. Velraj, "Experimental study on density, thermal conductivity, specific heat and viscosity of water-ethylene glycol mixture dispersed with carbon nanotubes," *Thermal Science,* pp. 28-28, 2015.
[120] R. S. Vajjha and D. K. Das, "Specific heat measurement of three nanofluids and development of new correlations," *Journal of heat transfer,* vol. 131, p. 071601, 2009.
[121] D. Shin and D. Banerjee, "Enhanced Specific Heat of Silica Nanofluid," *Journal of Heat Transfer,* vol. 133, pp. 024501-024501, 2010.
[122] A. D. Sommers and K. L. Yerkes, "Experimental investigation into the convective heat transfer and system-level effects of Al2O3-propanol nanofluid," *Journal of Nanoparticle Research,* vol. 12, pp. 1003-1014, 2010.
[123] S.-Q. Zhou and R. Ni, "Measurement of the specific heat capacity of water-based Al2O3 nanofluid," *Applied Physics Letters,* vol. 92, p. 093123, 2008.

[124] B. Barbés, R. Páramo, E. Blanco, M. J. Pastoriza-Gallego, M. M. Piñeiro, J. L. Legido*, et al.*, "Thermal conductivity and specific heat capacity measurements of Al2O3 nanofluids," *Journal of Thermal Analysis and Calorimetry,* vol. 111, pp. 1615-1625, 2013.

[125] J. R. Satti, D. K. Das, and D. Ray, "Specific heat measurements of five different propylene glycol based nanofluids and development of a new correlation," *International Journal of Heat and Mass Transfer,* vol. 94, pp. 343-353, 3// 2016.

[126] H. O'Hanley, J. Buongiorno, T. McKrell, and L.-w. Hu, "Measurement and model validation of nanofluid specific heat capacity with differential scanning calorimetry," *Advances in Mechanical Engineering,* vol. 4, p. 181079, 2012.

[127] S. Sonawane, K. Patankar, A. Fogla, B. Puranik, U. Bhandarkar, and S. Sunil Kumar, "An experimental investigation of thermo-physical properties and heat transfer performance of Al2O3-Aviation Turbine Fuel nanofluids," *Applied Thermal Engineering,* vol. 31, pp. 2841-2849, 10// 2011.

[128] D. Shin and D. Banerjee, "Specific heat of nanofluids synthesized by dispersing alumina nanoparticles in alkali salt eutectic," *International Journal of Heat and Mass Transfer,* vol. 74, pp. 210-214, 7// 2014.

[129] D. Cabaleiro, C. Gracia-Fernández, J. L. Legido, and L. Lugo, "Specific heat of metal oxide nanofluids at high concentrations for heat transfer," *International Journal of Heat and Mass Transfer,* vol. 88, pp. 872-879, 9// 2015.

[130] M. Rebay, S. Kakaç, and R. M. Cotta, *Microscale and Nanoscale Heat Transfer: Analysis, Design, and Application*: CRC Press, 2016.

[131] H. Akoh, Y. Tsukasaki, S. Yatsuya, and A. Tasaki, "Magnetic properties of ferromagnetic ultrafine particles prepared by vacuum evaporation on running oil substrate," *Journal of Crystal Growth,* vol. 45, pp. 495-500, 1978/12/01 1978.

[132] J. A. Eastman, S. U. S. Choi, S. Li, W. Yu, and L. J. Thompson, "Anomalously increased effective thermal conductivities of ethylene glycol-based nanofluids containing copper nanoparticles," *Applied Physics Letters,* vol. 78, pp. 718-720, 2001.

[133] S. Choi, W. Yu, J. R. Hull, Z. Zhang, and F. Lockwood, "Nanofluids for vehicle thermal management," SAE Technical Paper 0148-7191, 2001.

[134] B. Munkhbayar, M. R. Tanshen, J. Jeoun, H. Chung, and H. Jeong, "Surfactant-free dispersion of silver nanoparticles into MWCNT-aqueous nanofluids prepared by one-step technique and their thermal characteristics," *Ceramics International,* vol. 39, pp. 6415-6425, 8// 2013.

[135] H.-t. Zhu, Y.-s. Lin, and Y.-s. Yin, "A novel one-step chemical method for preparation of copper nanofluids," *Journal of Colloid and Interface Science,* vol. 277, pp. 100-103, 9/1/ 2004.

[136] P. Tran and Y. Soong, "Preparation of nanofluids using laser ablation in liquid technique," National Energy Technology Laboratory (NETL), Pittsburgh, PA, and Morgantown, WV2007.

[137] P. Y. Lee, K. Ishizaka, H. Suematsu, W. Jiang, and K. Yatsui, "Magnetic and Gas Sensing Property of Nanosized NiFe2O4 Powders Synthesized by Pulsed Wire Discharge," *Journal of Nanoparticle Research,* vol. 8, p. 29, 2006.

[138] P. K. Jena, E. A. Brocchi, and M. S. Motta, "In-situ formation of Cu–Al2O3 nano-scale composites by chemical routes and studies on their microstructures," *Materials Science and Engineering: A,* vol. 313, pp. 180-186, 8/31/ 2001.

[139] M. P. Beck, T. Sun, and A. S. Teja, "The thermal conductivity of alumina nanoparticles dispersed in ethylene glycol," *Fluid Phase Equilibria,* vol. 260, pp. 275-278, 11/1/ 2007.

[140] S. Suresh, K. P. Venkitaraj, P. Selvakumar, and M. Chandrasekar, "Synthesis of Al2O3–Cu/water hybrid nanofluids using two step method and its thermo physical properties," *Colloids and Surfaces A: Physicochemical and Engineering Aspects,* vol. 388, pp. 41-48, 9/5/ 2011.

[141] G. Paul, J. Philip, B. Raj, P. K. Das, and I. Manna, "Synthesis, characterization, and thermal property measurement of nano-Al95Zn05 dispersed nanofluid prepared by a two-step process," *International Journal of Heat and Mass Transfer,* vol. 54, pp. 3783-3788, 7// 2011.

[142] W. Yu, H. Xie, X. Wang, and X. Wang, "Significant thermal conductivity enhancement for nanofluids containing graphene nanosheets," *Physics Letters A,* vol. 375, pp. 1323-1328, 3/7/ 2011.

[143] T. T. Baby and S. Ramaprabhu, "Synthesis and nanofluid application of silver nanoparticles decorated graphene," *Journal of Materials Chemistry,* vol. 21, pp. 9702-9709, 2011.

[144] Y. Xuan and Q. Li, "Heat transfer enhancement of nanofluids," *International Journal of Heat and Fluid Flow,* vol. 21, pp. 58-64, 2// 2000.

[145] H. E. Patel, S. K. Das, T. Sundararajan, A. Sreekumaran Nair, B. George, and T. Pradeep, "Thermal conductivities of naked and monolayer protected metal nanoparticle based nanofluids: Manifestation of anomalous enhancement and chemical effects," *Applied Physics Letters,* vol. 83, pp. 2931-2933, 2003.

[146] P. Hu, W.-L. Shan, F. Yu, and Z.-S. Chen, "Thermal Conductivity of AlN–Ethanol Nanofluids," *International Journal of Thermophysics,* vol. 29, pp. 1968-1973, 2008.

[147] U. Rea, T. McKrell, L.-w. Hu, and J. Buongiorno, "Laminar convective heat transfer and viscous pressure loss of alumina–water and zirconia–water nanofluids," *International Journal of Heat and Mass Transfer,* vol. 52, pp. 2042-2048, 3// 2009.

[148] P. Razi, M. A. Akhavan-Behabadi, and M. Saeedinia, "Pressure drop and thermal characteristics of CuO–base oil nanofluid laminar flow in flattened tubes under constant heat flux," *International Communications in Heat and Mass Transfer,* vol. 38, pp. 964-971, 8// 2011.

[149] D. Kim, Y. Kwon, Y. Cho, C. Li, S. Cheong, Y. Hwang*, et al.*, "Convective heat transfer characteristics of nanofluids under laminar and turbulent flow conditions," *Current Applied Physics,* vol. 9, pp. e119-e123, 3// 2009.

[150] M. M. Heyhat, F. Kowsary, A. M. Rashidi, M. H. Momenpour, and A. Amrollahi, "Experimental investigation of laminar convective heat transfer and pressure drop of water-based Al2O3 nanofluids in fully developed flow regime," *Experimental Thermal and Fluid Science,* vol. 44, pp. 483-489, 1// 2013.

[151] M. Chandrasekar, S. Suresh, and A. Chandra Bose, "Experimental studies on heat transfer and friction factor characteristics of Al2O3/water nanofluid in a circular pipe under laminar flow with wire coil inserts," *Experimental Thermal and Fluid Science,* vol. 34, pp. 122-130, 2// 2010.

[152] S. Suresh, M. Chandrasekar, P. Selvakumar, and T. Page, "Experimental studies on heat transfer and friction factor characteristics of Al2O3/water nanofluid under laminar flow with spiralled rod inserts," *International Journal of Nanoparticles,* vol. 5, pp. 37-55, 2012.

[153] I. Gherasim, G. Roy, C. T. Nguyen, and D. Vo-Ngoc, "Experimental investigation of nanofluids in confined laminar radial flows," *International Journal of Thermal Sciences,* vol. 48, pp. 1486-1493, 2009/08/01 2009.

[154] H. Chen, W. Yang, Y. He, Y. Ding, L. Zhang, C. Tan*, et al.*, "Heat transfer and flow behaviour of aqueous suspensions of titanate nanotubes (nanofluids)," *Powder Technology,* vol. 183, pp. 63-72, 3/18/ 2008.

[155] S. Suresh, K. P. Venkitaraj, P. Selvakumar, and M. Chandrasekar, "Effect of Al2O3–Cu/water hybrid nanofluid in heat transfer," *Experimental Thermal and Fluid Science,* vol. 38, pp. 54-60, 4// 2012.

[156] Y. Xuan and Q. Li, "Investigation on Convective Heat Transfer and Flow Features of Nanofluids," *Journal of Heat Transfer,* vol. 125, pp. 151-155, 2003.

[157] Q. Li and Y. Xuan, "Convective heat transfer and flow characteristics of Cu-water nanofluid," *Science in China Series E: Technolgical Science,* vol. 45, pp. 408-416, 2002.

[158] W. Duangthongsuk and S. Wongwises, "Heat transfer enhancement and pressure drop characteristics of TiO2–water nanofluid in a double-tube counter flow heat exchanger," *International Journal of Heat and Mass Transfer,* vol. 52, pp. 2059-2067, 3// 2009.

[159] S. M. Fotukian and M. Nasr Esfahany, "Experimental investigation of turbulent convective heat transfer of dilute γ-Al2O3/water nanofluid inside a circular tube," *International Journal of Heat and Fluid Flow,* vol. 31, pp. 606-612, 8// 2010.

[160] L. S. Sundar and K. V. Sharma, "Turbulent heat transfer and friction factor of Al2O3 Nanofluid in circular tube with twisted tape inserts," *International Journal of Heat and Mass Transfer,* vol. 53, pp. 1409-1416, 3// 2010.

[161] A. Zamzamian, S. N. Oskouie, A. Doosthoseini, A. Joneidi, and M. Pazouki, "Experimental investigation of forced convective heat transfer coefficient in nanofluids of Al2O3/EG and CuO/EG in a double pipe and plate heat exchangers under turbulent flow," *Experimental Thermal and Fluid Science,* vol. 35, pp. 495-502, 4// 2011.

[162] S. Suresh, M. Chandrasekar, and S. Chandra Sekhar, "Experimental studies on heat transfer and friction factor characteristics of CuO/water nanofluid under turbulent flow in a helically dimpled tube," *Experimental Thermal and Fluid Science,* vol. 35, pp. 542-549, 4// 2011.

[163] H. Maddah, M. Alizadeh, N. Ghasemi, and S. R. Wan Alwi, "Experimental study of Al2O3/water nanofluid turbulent heat transfer enhancement in the horizontal double pipes fitted with modified twisted tapes," *International Journal of Heat and Mass Transfer,* vol. 78, pp. 1042-1054, 11// 2014.

[164] Y. Xuan and Q. Li, "Investigation on convective heat transfer and flow features of nanofluids," *Journal of Heat Transfer,* vol. 125, pp. 151 - 155, 2003.

[165] J.-Y. Jung, H.-S. Oh, and H.-Y. Kwak, "Forced Convective Heat Transfer of Nanofluids in Microchannels," pp. 327-332, 2006.

[166] "Heat transfer enhancement in turbulent tube flow using Al2O3 nanoparticle suspension," *International Journal of Numerical Methods for Heat & Fluid Flow,* vol. 16, pp. 275-292, 2006.

[167] P. Naphon, M. Nuchjapo, and J. Kurujareon, "Tube side heat transfer coefficient and friction factor characteristics of horizontal tubes with helical rib," *Energy Conversion and Management,* vol. 47, pp. 3031-3044, 2006/11/01/ 2006.

[168] G. Polidori, S. Fohanno, and C. T. Nguyen, "A note on heat transfer modelling of Newtonian nanofluids in laminar free convection," *International Journal of Thermal Sciences,* vol. 46, pp. 739-744, 2007/08/01/ 2007.

[169] U. Rea, T. McKrell, L.-w. Hu, and J. Buongiorno, "Laminar convective heat transfer and viscous pressure loss of alumina–water and zirconia–water nanofluids," *International Journal of Heat and Mass Transfer,* vol. 52, pp. 2042-2048, 2009/03/01/ 2009.

[170] W. Duangthongsuk and S. Wongwises, "An experimental study on the heat transfer performance and pressure drop of TiO2-water nanofluids flowing under a turbulent flow regime," *International Journal of Heat and Mass Transfer,* vol. 53, pp. 334-344, 2010.

[171] R. S. Vajjha, D. K. Das, and D. P. Kulkarni, "Development of new correlations for convective heat transfer and friction factor in turbulent regime for nanofluids," *International Journal of Heat and Mass Transfer,* vol. 53, pp. 4607-4618, 2010/10/01/ 2010.

[172] L. G. Asirvatham, B. Raja, D. Mohan Lal, and S. Wongwises, "Convective heat transfer of nanofluids with correlations," *Particuology,* vol. 9, pp. 626-631, 12// 2011.

[173] A. R. Sajadi and M. H. Kazemi, "Investigation of turbulent convective heat transfer and pressure drop of TiO2/water nanofluid in circular tube," *International*

Communications in Heat and Mass Transfer, vol. 38, pp. 1474-1478, 2011/12/01/ 2011.

[174] R. Ben Mansour, N. Galanis, and C. T. Nguyen, "Experimental study of mixed convection with water–Al2O3 nanofluid in inclined tube with uniform wall heat flux," *International Journal of Thermal Sciences,* vol. 50, pp. 403-410, 2011/03/01/ 2011.

[175] L. Syam Sundar, M. T. Naik, K. V. Sharma, M. K. Singh, and T. C. Siva Reddy, "Experimental investigation of forced convection heat transfer and friction factor in a tube with Fe3O4 magnetic nanofluid," *Experimental Thermal and Fluid Science,* vol. 37, pp. 65-71, 2012/02/01/ 2012.

[176] S. M. Vanaki, P. Ganesan, and H. A. Mohammed, "Numerical study of convective heat transfer of nanofluids: A review," *Renewable and Sustainable Energy Reviews,* vol. 54, pp. 1212-1239, 2// 2016.

[177] M. Akhtari, M. Haghshenasfard, and M. R. Talaie, "Numerical and Experimental Investigation of Heat Transfer of α-Al2O3/Water Nanofluid in Double Pipe and Shell and Tube Heat Exchangers," *Numerical Heat Transfer, Part A: Applications,* vol. 63, pp. 941-958, 2013/06/15 2013.

[178] V. Bianco, F. Chiacchio, O. Manca, and S. Nardini, "Numerical investigation of nanofluids forced convection in circular tubes," *Applied Thermal Engineering,* vol. 29, pp. 3632-3642, 12// 2009.

[179] M. Izadi, A. Behzadmehr, and D. Jalali-Vahida, "Numerical study of developing laminar forced convection of a nanofluid in an annulus," *International Journal of Thermal Sciences,* vol. 48, pp. 2119-2129, 11// 2009.

[180] M. K. Moraveji, M. Darabi, S. M. H. Haddad, and R. Davarnejad, "Modeling of convective heat transfer of a nanofluid in the developing region of tube flow with computational fluid dynamics," *International Communications in Heat and Mass Transfer,* vol. 38, pp. 1291-1295, 11// 2011.

[181] K. B. Anoop, T. Sundararajan, and S. K. Das, "Effect of particle size on the convective heat transfer in nanofluid in the developing region," *International Journal of Heat and Mass Transfer,* vol. 52, pp. 2189-2195, 4// 2009.

[182] A. M. Hussein, R. A. Bakar, and K. Kadirgama, "Study of forced convection nanofluid heat transfer in the automotive cooling system," *Case Studies in Thermal Engineering,* vol. 2, pp. 50-61, 3// 2014.

[183] H. A. Mohammed, P. Gunnasegaran, and N. H. Shuaib, "The impact of various nanofluid types on triangular microchannels heat sink cooling performance," *International Communications in Heat and Mass Transfer,* vol. 38, pp. 767-773, 7// 2011.

[184] Y. Xuan and W. Roetzel, "Conceptions for heat transfer correlation of nanofluids," *International Journal of Heat and Mass Transfer,* vol. 43, pp. 3701-3707, 10/1/ 2000.

[185] S. Z. Heris, M. N. Esfahany, and G. Etemad, "Numerical Investigation of Nanofluid Laminar Convective Heat Transfer through a Circular Tube," *Numerical Heat Transfer, Part A: Applications,* vol. 52, pp. 1043-1058, 2007/09/21 2007.

[186] S. Kumar, S. K. Prasad, and J. Banerjee, "Analysis of flow and thermal field in nanofluid using a single phase thermal dispersion model," *Applied Mathematical Modelling,* vol. 34, pp. 573-592, 3// 2010.

[187] A. Mokmeli and M. Saffar-Avval, "Prediction of nanofluid convective heat transfer using the dispersion model," *International Journal of Thermal Sciences,* vol. 49, pp. 471-478, 3// 2010.

[188] F. Akbaridoust, M. Rakhsha, A. Abbassi, and M. Saffar-Avval, "Experimental and numerical investigation of nanofluid heat transfer in helically coiled tubes at constant wall temperature using dispersion model," *International Journal of Heat and Mass Transfer,* vol. 58, pp. 480-491, 3// 2013.

[189] M. Keshavarz Moraveji and E. Esmaeili, "Comparison between single-phase and two-phases CFD modeling of laminar forced convection flow of nanofluids in a

circular tube under constant heat flux," *International Communications in Heat and Mass Transfer,* vol. 39, pp. 1297-1302, 10// 2012.

[190] M. Mirzaei, M. Saffar-Avval, and H. Naderan, "Heat transfer investigation of laminar developing flow of nanofluids in a microchannel based on Eulerian–Lagrangian approach," *The Canadian journal of chemical engineering,* vol. 92, pp. 1139-1149, 2014.

[191] H. Bahremand, A. Abbassi, and M. Saffar-Avval, "Experimental and numerical investigation of turbulent nanofluid flow in helically coiled tubes under constant wall heat flux using Eulerian–Lagrangian approach," *Powder Technology,* vol. 269, pp. 93-100, 1// 2015.

[192] M. Mahdavi, M. Sharifpur, and J. P. Meyer, "CFD modelling of heat transfer and pressure drops for nanofluids through vertical tubes in laminar flow by Lagrangian and Eulerian approaches," *International Journal of Heat and Mass Transfer,* vol. 88, pp. 803-813, 9// 2015.

[193] A. Behzadmehr, M. Saffar-Avval, and N. Galanis, "Prediction of turbulent forced convection of a nanofluid in a tube with uniform heat flux using a two phase approach," *International Journal of Heat and Fluid Flow,* vol. 28, pp. 211-219, 4// 2007.

[194] S. Mirmasoumi and A. Behzadmehr, "Numerical study of laminar mixed convection of a nanofluid in a horizontal tube using two-phase mixture model," *Applied Thermal Engineering,* vol. 28, pp. 717-727, 5// 2008.

[195] M. Saberi, M. Kalbasi, and A. Alipourzade, "Numerical study of forced convective heat transfer of nanofluids inside a vertical tube," *International Journal of Thermal Technologies,* vol. 3, pp. 10-15, 2013.

[196] M. Akbari, N. Galanis, and A. Behzadmehr, "Comparative analysis of single and two-phase models for CFD studies of nanofluid heat transfer," *International Journal of Thermal Sciences,* vol. 50, pp. 1343-1354, 8// 2011.

[197] M. Akbari, N. Galanis, and A. Behzadmehr, "Comparative assessment of single and two-phase models for numerical studies of nanofluid turbulent forced convection," *International Journal of Heat and Fluid Flow,* vol. 37, pp. 136-146, 10// 2012.

[198] M. K. Moraveji and R. M. Ardehali, "CFD modeling (comparing single and two-phase approaches) on thermal performance of Al2o3/water nanofluid in mini-channel heat sink," *International Communications in Heat and Mass Transfer,* vol. 44, pp. 157-164, 5// 2013.

[199] B. Fani, A. Abbassi, and M. Kalteh, "Effect of nanoparticles size on thermal performance of nanofluid in a trapezoidal microchannel-heat-sink," *International Communications in Heat and Mass Transfer,* vol. 45, pp. 155-161, 7// 2013.

[200] M. Kalteh, A. Abbassi, M. Saffar-Avval, and J. Harting, "Eulerian–Eulerian two-phase numerical simulation of nanofluid laminar forced convection in a microchannel," *International Journal of Heat and Fluid Flow,* vol. 32, pp. 107-116, 2// 2011.

[201] A. Beheshti, M. K. Moraveji, and M. Hejazian, "Comparative Numerical Study of Nanofluid Heat Transfer through an Annular Channel," *Numerical Heat Transfer, Part A: Applications,* vol. 67, pp. 100-117, 2015/01/02 2015.

[202] R. Lotfi, Y. Saboohi, and A. M. Rashidi, "Numerical study of forced convective heat transfer of Nanofluids: Comparison of different approaches," *International Communications in Heat and Mass Transfer,* vol. 37, pp. 74-78, 1// 2010.

[203] M. Sheikholeslami, M. Gorji-Bandpy, S. M. Seyyedi, D. D. Ganji, H. B. Rokni, and S. Soleimani, "Application of LBM in simulation of natural convection in a nanofluid filled square cavity with curve boundaries," *Powder Technology,* vol. 247, pp. 87-94, 10// 2013.

[204] H. Nemati, M. Farhadi, K. Sedighi, E. Fattahi, and A. A. R. Darzi, "Lattice Boltzmann simulation of nanofluid in lid-driven cavity," *International Communications in Heat and Mass Transfer,* vol. 37, pp. 1528-1534, 12// 2010.

[205] M. Nabavitabatabayi, E. Shirani, and M. H. Rahimian, "Investigation of heat transfer enhancement in an enclosure filled with nanofluids using multiple relaxation time lattice Boltzmann modeling," *International Communications in Heat and Mass Transfer,* vol. 38, pp. 128-138, 1// 2011.

[206] G. R. Kefayati, S. F. Hosseinizadeh, M. Gorji, and H. Sajjadi, "Lattice Boltzmann simulation of natural convection in tall enclosures using water/SiO2 nanofluid," *International Communications in Heat and Mass Transfer,* vol. 38, pp. 798-805, 7// 2011.

[207] Y.-T. Yang and F.-H. Lai, "Numerical study of flow and heat transfer characteristics of alumina-water nanofluids in a microchannel using the lattice Boltzmann method," *International Communications in Heat and Mass Transfer,* vol. 38, pp. 607-614, 5// 2011.

[208] J. Buongiorno, "Convective transport in nanofluids," *Journal of Heat Transfer,* vol. 128, pp. 240-250, 2006.

[209] G. A. Sheikhzadeh, M. Dastmalchi, and H. Khorasanizadeh, "Effects of nanoparticles transport mechanisms on Al2O3–water nanofluid natural convection in a square enclosure," *International Journal of Thermal Sciences,* vol. 66, pp. 51-62, 4// 2013.

[210] W. Yu and H. Xie, "A Review on Nanofluids: Preparation, Stability Mechanisms, and Applications," *Journal of Nanomaterials,* vol. 2012, p. 17, 2012.

[211] K. V. Wong and O. De Leon, "Applications of Nanofluids: Current and Future," *Advances in Mechanical Engineering,* vol. 2, January 1, 2010 2010.

[212] D. Wen, G. Lin, S. Vafaei, and K. Zhang, "Review of nanofluids for heat transfer applications," *Particuology,* vol. 7, pp. 141-150, 4// 2009.

[213] R. Saidur, K. Y. Leong, and H. A. Mohammad, "A review on applications and challenges of nanofluids," *Renewable and Sustainable Energy Reviews,* vol. 15, pp. 1646-1668, 4// 2011.

[214] H. A. Mohammed, G. Bhaskaran, N. H. Shuaib, and R. Saidur, "Heat transfer and fluid flow characteristics in microchannels heat exchanger using nanofluids: A review," *Renewable and Sustainable Energy Reviews,* vol. 15, pp. 1502-1512, 4// 2011.

[215] G. Huminic and A. Huminic, "Application of nanofluids in heat exchangers: A review," *Renewable and Sustainable Energy Reviews,* vol. 16, pp. 5625-5638, 10// 2012.

[216] R. Sureshkumar, S. T. Mohideen, and N. Nethaji, "Heat transfer characteristics of nanofluids in heat pipes: A review," *Renewable and Sustainable Energy Reviews,* vol. 20, pp. 397-410, 4// 2013.

[217] O. Mahian, A. Kianifar, S. A. Kalogirou, I. Pop, and S. Wongwises, "A review of the applications of nanofluids in solar energy," *International Journal of Heat and Mass Transfer,* vol. 57, pp. 582-594, 2// 2013.

[218] L. Cheng and L. Liu, "Boiling and two-phase flow phenomena of refrigerant-based nanofluids: Fundamentals, applications and challenges," *International Journal of Refrigeration,* vol. 36, pp. 421-446, 3// 2013.

[219] F. S. Javadi, R. Saidur, and M. Kamalisarvestani, "Investigating performance improvement of solar collectors by using nanofluids," *Renewable and Sustainable Energy Reviews,* vol. 28, pp. 232-245, 12// 2013.

[220] J. Sarkar, "Performance of nanofluid-cooled shell and tube gas cooler in transcritical CO2 refrigeration systems," *Applied Thermal Engineering,* vol. 31, pp. 2541-2548, 10// 2011.

[221] M. N. Pantzali, A. G. Kanaris, K. D. Antoniadis, A. A. Mouza, and S. V. Paras, "Effect of nanofluids on the performance of a miniature plate heat exchanger with

modulated surface," *International Journal of Heat and Fluid Flow,* vol. 30, pp. 691-699, 8// 2009.

[222] B.-H. Chun, H. U. Kang, and S. H. Kim, "Effect of alumina nanoparticles in the fluid on heat transfer in double-pipe heat exchanger system," *Korean Journal of Chemical Engineering,* vol. 25, pp. 966-971, 2008.

[223] G. Huminic and A. Huminic, "Heat transfer characteristics in double tube helical heat exchangers using nanofluids," *International Journal of Heat and Mass Transfer,* vol. 54, pp. 4280-4287, 9// 2011.

[224] S. V. Mousavi, M. Sheikholeslami, M. Gorji bandpy, and M. Barzegar Gerdroodbary, "The Influence of magnetic field on heat transfer of magnetic nanofluid in a sinusoidal double pipe heat exchanger," *Chemical Engineering Research and Design,* vol. 113, pp. 112-124, 9// 2016.

[225] M. Goodarzi, A. S. Kherbeet, M. Afrand, E. Sadeghinezhad, M. Mehrali, P. Zahedi*, et al.*, "Investigation of heat transfer performance and friction factor of a counter-flow double-pipe heat exchanger using nitrogen-doped, graphene-based nanofluids," *International Communications in Heat and Mass Transfer,* vol. 76, pp. 16-23, 8// 2016.

[226] M. M. Sarafraz, F. Hormozi, and V. Nikkhah, "Thermal performance of a counter-current double pipe heat exchanger working with COOH-CNT/water nanofluids," *Experimental Thermal and Fluid Science,* vol. 78, pp. 41-49, 11// 2016.

[227] M. M. Sarafraz and F. Hormozi, "Intensification of forced convection heat transfer using biological nanofluid in a double-pipe heat exchanger," *Experimental Thermal and Fluid Science,* vol. 66, pp. 279-289, 9// 2015.

[228] A. Shakiba and K. Vahedi, "Numerical analysis of magnetic field effects on hydro-thermal behavior of a magnetic nanofluid in a double pipe heat exchanger," *Journal of Magnetism and Magnetic Materials,* vol. 402, pp. 131-142, 3/15/ 2016.

[229] J. Koo and C. Kleinstreuer, "Laminar nanofluid flow in microheat-sinks," *International Journal of Heat and Mass Transfer,* vol. 48, pp. 2652-2661, 6// 2005.

[230] C. T. Nguyen and M. Le Menn, "Two-phase modelling of nanofluid heat transfer in a microchannel heat sink," vol. 1, pp. 451-460, 2009.

[231] J. Li and C. Kleinstreuer, "Entropy Generation Analysis for Nanofluid Flow in Microchannels," *Journal of Heat Transfer,* vol. 132, p. 122401, 2010.

[232] R. Wälchli, T. Brunschwiler, B. Michel, and D. Poulikakos, "Combined local microchannel-scale CFD modeling and global chip scale network modeling for electronics cooling design," *International Journal of Heat and Mass Transfer,* vol. 53, pp. 1004-1014, 2010.

[233] M. Kalteh, A. Abbassi, M. Saffar-Avval, A. Frijns, A. Darhuber, and J. Harting, "Experimental and numerical investigation of nanofluid forced convection inside a wide microchannel heat sink," *Applied Thermal Engineering,* vol. 36, pp. 260-268, 4// 2012.

[234] S. V. B. Vivekanand and V. R. K. Raju, "Simulation of Evaporation Heat Transfer in a Rectangular Microchannel," *Procedia Engineering,* vol. 127, pp. 309-316, 2015.

[235] R. Chein and G. Huang, "Analysis of microchannel heat sink performance using nanofluids," *Applied Thermal Engineering,* vol. 25, pp. 3104-3114, 12// 2005.

[236] S. P. Jang and S. U. S. Choi, "Cooling performance of a microchannel heat sink with nanofluids," *Applied Thermal Engineering,* vol. 26, pp. 2457-2463, 12// 2006.

[237] R. Chein and J. Chuang, "Experimental microchannel heat sink performance studies using nanofluids," *International Journal of Thermal Sciences,* vol. 46, pp. 57-66, 2007/01/01 2007.

[238] E. Manay and B. Sahin, "The effect of microchannel height on performance of nanofluids," *International Journal of Heat and Mass Transfer,* vol. 95, pp. 307-320, 4// 2016.

[239] J. Lee and I. Mudawar, "Assessment of the effectiveness of nanofluids for single-phase and two-phase heat transfer in micro-channels," *International Journal of Heat and Mass Transfer,* vol. 50, pp. 452-463, 2// 2007.
[240] M. D. Byrne, R. A. Hart, and A. K. da Silva, "Experimental thermal–hydraulic evaluation of CuO nanofluids in microchannels at various concentrations with and without suspension enhancers," *International Journal of Heat and Mass Transfer,* vol. 55, pp. 2684-2691, 4// 2012.
[241] T.-C. Hung, W.-M. Yan, X.-D. Wang, and C.-Y. Chang, "Heat transfer enhancement in microchannel heat sinks using nanofluids," *International Journal of Heat and Mass Transfer,* vol. 55, pp. 2559-2570, 4// 2012.
[242] J.-Y. Jung, H.-S. Oh, and H.-Y. Kwak, "Forced convective heat transfer of nanofluids in microchannels," *International Journal of Heat and Mass Transfer,* vol. 52, pp. 466-472, 1/15/ 2009.
[243] K. Anoop, R. Sadr, J. Yu, S. Kang, S. Jeon, and D. Banerjee, "Experimental study of forced convective heat transfer of nanofluids in a microchannel," *International Communications in Heat and Mass Transfer,* vol. 39, pp. 1325-1330, 11// 2012.
[244] E. M. Tokit, H. A. Mohammed, and M. Z. Yusoff, "Thermal performance of optimized interrupted microchannel heat sink (IMCHS) using nanofluids," *International Communications in Heat and Mass Transfer,* vol. 39, pp. 1595-1604, 12// 2012.
[245] T.-C. Hung and W.-M. Yan, "Enhancement of thermal performance in double-layered microchannel heat sink with nanofluids," *International Journal of Heat and Mass Transfer,* vol. 55, pp. 3225-3238, 5// 2012.
[246] A. Malvandi, S. A. Moshizi, and D. D. Ganji, "Two-component heterogeneous mixed convection of alumina/water nanofluid in microchannels with heat source/sink," *Advanced Powder Technology,* vol. 27, pp. 245-254, 1// 2016.
[247] A. Malvandi, S. A. Moshizi, and D. D. Ganji, "Effects of temperature-dependent thermophysical properties on nanoparticle migration at mixed convection of nanofluids in vertical microchannels," *Powder Technology,* vol. 303, pp. 7-19, 12// 2016.
[248] N. R. Kuppusamy, H. A. Mohammed, and C. W. Lim, "Numerical investigation of trapezoidal grooved microchannel heat sink using nanofluids," *Thermochimica Acta,* vol. 573, pp. 39-56, 12/10/ 2013.
[249] N. Alagumurthi and T. Senthilvelan, "Investigation of Heat Transfer in Serpentine Shaped Microchannel Using Al2O3/Water Nanofluid," *Heat Transfer—Asian Research,* 2014.
[250] H. K. Versteeg and W. Malalasekera, *An introduction to computational fluid dynamics: the finite volume method*: Pearson Education, 2007.
[251] D. A. Anderson, J. C. Tannehill, and R. H. Pletcher, "Computational fluid mechanics and heat transfer," 1984.
[252] R. H. Pletcher, J. C. Tannehill, and D. Anderson, *Computational fluid mechanics and heat transfer*: CRC Press, 2012.
[253] J. H. Ferziger and M. Peric, *Computational methods for fluid dynamics*: Springer Science & Business Media, 2012.
[254] W. Minkowycz, E. M. Sparrow, and J. P. Abraham, *Nanoparticle heat transfer and fluid flow*: CRC press, 2012.
[255] A. Workbench, "Release 15, ANSYS," *Inc., Canonsburg, PA, USA*.
[256] Y. Xuan and Q. Li, "Heat transfer enhancement of nanofluids," *Int J Heat Fluid Flow,* vol. 21, pp. 58 - 64, 2000.
[257] K. Khanafer, K. Vafai, and M. Lightstone, "Buoyancy-driven heat transfer enhancement in a two-dimensional enclosure utilizing nanofluids," *Int J Heat Mass Transf,* vol. 46, pp. 3639 - 3653, 2003.
[258] N. Putra, W. Roetzel, and S. Das, "Natural convection of nano-fluids," *Heat and Mass Transfer,* vol. 39, pp. 775-784, 2003/09/01 2003.

[259] H. Saleh, R. Roslan, and I. Hashim, "Natural convection heat transfer in a nanofluid-filled trapezoidal enclosure," *International Journal of Heat and Mass Transfer,* vol. 54, pp. 194-201, 2011.

[260] R. Nasrin, M. A. Alim, and A. J. Chamkha, "Buoyancy-driven heat transfer of water–Al2O3 nanofluid in a closed chamber: Effects of solid volume fraction, Prandtl number and aspect ratio," *International Journal of Heat and Mass Transfer,* vol. 55, pp. 7355-7365, 12// 2012.

[261] B. Ghasemi and S. M. Aminossadati, "Natural Convection Heat Transfer in an Inclined Enclosure Filled with a Water-Cuo Nanofluid," *Numerical Heat Transfer, Part A: Applications,* vol. 55, pp. 807-823, 2009/04/16 2009.

[262] C. J. Ho, W. K. Liu, Y. S. Chang, and C. C. Lin, "Natural convection heat transfer of alumina-water nanofluid in vertical square enclosures: An experimental study," *International Journal of Thermal Sciences,* vol. 49, pp. 1345-1353, 8// 2010.

[263] B. Ghasemi and S. M. Aminossadati, "Brownian motion of nanoparticles in a triangular enclosure with natural convection," *International Journal of Thermal Sciences,* vol. 49, pp. 931-940, 6// 2010.

[264] M. Corcione, E. Habib, and A. Quintino, "A two-phase numerical study of buoyancy-driven convection of alumina–water nanofluids in differentially-heated horizontal annuli," *International Journal of Heat and Mass Transfer,* vol. 65, pp. 327-338, 10// 2013.

[265] E. Abu-Nada, Z. Masoud, H. F. Oztop, and A. Campo, "Effect of nanofluid variable properties on natural convection in enclosures," *International Journal of Thermal Sciences,* vol. 49, pp. 479-491, 2010.

[266] B. F. Armaly, F. Durst, J. C. F. Pereira, and B. Schönung, "Experimental and theoretical investigation of backward-facing step flow," *Journal of Fluid Mechanics,* vol. 127, p. 473, 1983.

[267] G. Biswas, M. Breuer, and F. Durst, "Backward-Facing Step Flows for Various Expansion Ratios at Low and Moderate Reynolds Numbers," *Journal of Fluids Engineering,* vol. 126, p. 362, 2004.

[268] E. Abu-Nada, "Entropy generation due to heat and fluid flow in backward facing step flow with various expansion ratios," *International Journal of Exergy,* vol. 3, p. 419, 2006.

[269] H. A. Mohammed, A. A. Al-aswadi, H. I. Abu-Mulaweh, and N. H. Shuaib, "Influence of nanofluids on mixed convective heat transfer over a horizontal backward-facing step," *Heat Transfer-Asian Research,* vol. 40, pp. 287-307, 2011.

[270] M. S. Pour and S. A. G. Nassab, "Numerical Investigation of Forced Laminar Convection Flow of Nanofluids Over a Backward Facing Step Under Bleeding Condition," *Journal of Mechanics,* vol. 28, pp. N7-N12, 2012.

[271] H. Togun, M. R. Safaei, R. Sadri, S. N. Kazi, A. Badarudin, K. Hooman*, et al.*, "Numerical simulation of laminar to turbulent nanofluid flow and heat transfer over a backward-facing step," *Applied Mathematics and Computation,* vol. 239, pp. 153-170, 2014.

[272] E. Erturk, "Numerical solutions of 2-D steady incompressible flow over a backward-facing step, Part I: High Reynolds number solutions," *Computers & Fluids,* vol. 37, pp. 633-655, 2008.

[273] H. Lan, B. F. Armaly, and J. A. Drallmeier, "Three-dimensional simulation of turbulent forced convection in a duct with backward-facing step," *International Journal of Heat and Mass Transfer,* vol. 52, pp. 1690-1700, 2009.

[274] H. A. Mohammed, O. A. Alawi, and M. A. Wahid, "Mixed convective nanofluid flow in a channel having backward-facing step with a baffle," *Powder Technology,* vol. 275, pp. 329-343, 2015.

[275] A. S. Kherbeet, H. A. Mohammed, K. M. Munisamy, R. Saidur, B. H. Salman, and I. M. Mahbubul, "Experimental and numerical study of nanofluid flow and heat

transfer over microscale forward-facing step," *International Communications in Heat and Mass Transfer,* vol. 57, pp. 319-329, 2014.

[276] A. S. Kherbeet, H. A. Mohammed, K. M. Munisamy, and B. H. Salman, "The effect of step height of microscale backward-facing step on mixed convection nanofluid flow and heat transfer characteristics," *International Journal of Heat and Mass Transfer,* vol. 68, pp. 554-566, 2014.

[277] Y. T. Chen, J. H. Nie, H. T. Hsieh, and L. J. Sun, "Three-dimensional convection flow adjacent to inclined backward-facing step," *International Journal of Heat and Mass Transfer,* vol. 49, pp. 4795-4803, 2006.

[278] J. Kostas, J. Soria, and M. Chong, "Particle image velocimetry measurements of a backward-facing step flow," *Experiments in Fluids,* vol. 33, pp. 838-853, 2002.

[279] O. Mahian, A. Kianifar, C. Kleinstreuer, M. d. A. Al-Nimr, I. Pop, A. Z. Sahin*, et al.*, "A review of entropy generation in nanofluid flow," *International Journal of Heat and Mass Transfer,* vol. 65, pp. 514-532, 10// 2013.

[280] E. Abu-Nada, "Numerical Prediction of Entropy Generation in Separated Flows," *Entropy,* vol. 7, p. 234, 2005.

[281] G. K. Batchelor, "The effect of Brownian motion on the bulk stress in a suspension of spherical particles," *Journal of Fluid Mechanics,* vol. 83, pp. 97-117, 1977.

[282] J. Buongiorno, "Convective Transport in Nanofluids," *Journal of Heat Transfer,* vol. 128, pp. 240-250, 2005.

[283] S. E. B. Maïga, S. J. Palm, C. T. Nguyen, G. Roy, and N. Galanis, "Heat transfer enhancement by using nanofluids in forced convection flows," *International Journal of Heat and Fluid Flow,* vol. 26, pp. 530-546, 2005.

[284] Sait, ocirc, and Nobuhiko, "Concentration Dependence of the Viscosity of High Polymer Solutions. I," *Journal of the Physical Society of Japan,* vol. 5, pp. 4-8, 1950.

[285] C. T. Nguyen, G. Roy, C. Gauthier, and N. Galanis, "Heat transfer enhancement using Al2O3–water nanofluid for an electronic liquid cooling system," *Applied Thermal Engineering,* vol. 27, pp. 1501-1506, 6// 2007.

[286] J. Garg, B. Poudel, M. Chiesa, J. Gordon, J. Ma, J. Wang*, et al.*, "Enhanced thermal conductivity and viscosity of copper nanoparticles in ethylene glycol nanofluid," *Journal of Applied Physics,* vol. 103, p. 074301, 2008.

[287] V. Bianco, O. Manca, and S. Nardini, "Numerical investigation on nanofluids turbulent convection heat transfer inside a circular tube," *International Journal of Thermal Sciences,* vol. 50, pp. 341-349, 2011.

[288] P. C. Mishra, S. Mukherjee, S. K. Nayak, and A. Panda, "A brief review on viscosity of nanofluids," *International Nano Letters,* vol. 4, pp. 109-120, 2014.

[289] S. G. Kandlikar and W. J. Grande, "Evolution of Microchannel Flow Passages--Thermohydraulic Performance and Fabrication Technology," *Heat Transfer Engineering,* vol. 24, pp. 3-17, 2003/01/01 2003.

[290] B. H. Salman, H. A. Mohammed, and A. S. Kherbeet, "Heat transfer enhancement of nanofluids flow in microtube with constant heat flux," *International Communications in Heat and Mass Transfer,* vol. 39, pp. 1195-1204, 10// 2012.

[291] B. H. Salman, H. A. Mohammed, and A. S. Kherbeet, "Numerical and experimental investigation of heat transfer enhancement in a microtube using nanofluids," *International Communications in Heat and Mass Transfer,* vol. 59, pp. 88-100, 2014.

[292] L. Chai, G. D. Xia, and H. S. Wang, "Laminar flow and heat transfer characteristics of interrupted microchannel heat sink with ribs in the transverse microchambers," *International Journal of Thermal Sciences,* vol. 110, pp. 1-11, 2016.

[293] S. K. Mohammadian, H. Reza Seyf, and Y. Zhang, "Performance Augmentation and Optimization of Aluminum Oxide-Water Nanofluid Flow in a Two-Fluid Microchannel Heat Exchanger," *Journal of Heat Transfer,* vol. 136, p. 021701, 2013.

[294] P.-S. Lee, S. V. Garimella, and D. Liu, "Investigation of heat transfer in rectangular microchannels," *International Journal of Heat and Mass Transfer,* vol. 48, pp. 1688-1704, 2005.

[295] E. E. Wilson, *A Basis of Rational Design of Heat Transfer Apparatus,* pp. 47-70, 1915.

[296] J. Fernández-Seara, F. J. Uhía, J. Sieres, and A. Campo, "A general review of the Wilson plot method and its modifications to determine convection coefficients in heat exchange devices," *Applied Thermal Engineering,* vol. 27, pp. 2745-2757, 2007/12/01/ 2007.

Appendix A Nanomaterial technical propoerties

io·li·tec nanomaterials

Technical Data Sheet

Titanium(IV)oxide, anatase

Revision Date: 02/02/2009
Date Issued: 03/01/2007

1 IDENTIFICATION OF THE SUBSTANCE/PREPARATION AND THE COMPANY / UNDERTAKING

Product name	Titanium(IV)oxide, anatase, Nanopowder
Product code	NO-0038-HP
Supplier	IoLiTec Ionic Liquids Technologies GmbH Salzstrasse 184 D-74076 Heilbronn Germany
Telephone	+49 (0)7131 - 898390
Emergency telephone	+49 (0)179 - 5322578

2 COMPOSITION / INFORMATION ON INGREDIENTS

Ingredient name	Titanium(IV)oxide, anatase
CAS No.	1317-70-0
Empirical Formula	TiO_2
Molecular weight	79.87 amu
Purity	99.5+%
Average Particle Size	20 nm
Specific Surface Area	>120 m^2/g
Colour	White
Morphology	Spherical
Bulk Density	-
True Density	0.3 g/cm^3
Melting point	1825°C
Boiling point	-

io·li·tec nanomaterials

Technical Data Sheet

Titanium(IV)oxide, anatase

Revision Date: 02/02/2009
Date Issued: 03/01/2007

3 TRANSMISSION ELECTRON MICROSCOPY

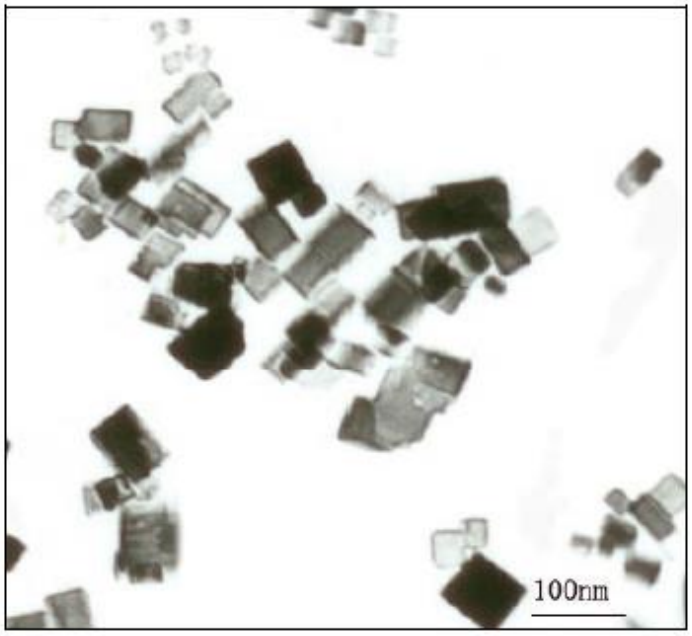

4 ORDER INFORMATION

NO-0038P can be obtained in the following standard quantities:

Quantity	Price
25	Please enquire
100 g	Please enquire
500 g	Please enquire
1 kg	Please enquire
Bulk	Please enquire

Please send your order via email to order@nanomaterials.iolitec.de
or fax +49 (0)7131 – 89839109.

Technical Data Sheet

Magnesium Oxide Powder

Revision Date: 03-02/2007
Date Issued: 03-02/2007

1 IDENTIFICATION OF THE SUBSTANCE/PREPARATION AND THE COMPANY / UNDERTAKING

Product name	Magnesium oxide powder
Product code	NO-0012-HP
Supplier	IoLiTec Ionic Liquids Technologies GmbH & Co KG Ferdinand-Porsche-Straße 5/1 D-79211 Denzlingen Germany
Fax	+49 (0)7666 - 9129345
Emergency telephone	+49 (0)179-5322578

2 COMPOSITION / INFORMATION ON INGREDIENTS

Ingredient name	Magnesium oxide
CAS No.	1309-48-4
Empirical Formula	MgO
Molecular weight	40.31 amu
Purity	~99.9 %
Average Particle Size	~ 35 nm
Specific Surface Area	> 50 m^2/g
Bulk Density	-
True Density	3.60 g/cm^3
Melting point	2850 °C
Boiling point	3600 °C

Technical Data Sheet

Magnesium Oxide Powder

Revision Date: 03-02/2007
Date Issued: 03-02/2007

3 SPECIFICATIONS

MgO: ~99.9%

4 TRANSMISSION ELECTRON MICROSCOPY

Not available

5 X-RAY DIFFRACTION PATTERN

Not available

6 ORDER INFORMATION

7 OTHER INFORMATION

Technical Data Sheet

Copper(II)Oxide Powder

Revision Date: 02/02/2009
Date Issued: 03/02/2007

1 IDENTIFICATION OF THE SUBSTANCE/PREPARATION AND THE COMPANY / UNDERTAKING

Product name	Copper(II)oxide powder, 99.9%, 40-80 nm
Product code	NO-0031-HP
Supplier	IoLiTec Ionic Liquids Technologies GmbH Salzstrasse 184 D-74076 Heilbronn Germany
Telephone	+49 (0)7131 - 898390
Fax	+49 (0)7131 - 89839109
Emergency telephone	+49 (0)179 - 5322578

2 COMPOSITION / INFORMATION ON INGREDIENTS

Ingredient name	Copper(II)oxide
CAS No.	1317-38-0
Empirical Formula	CuO
Molecular weight	79.55 amu
Purity	99.9%
Average Particle Size	40-80 nm (BET, TEM)
Specific Surface Area	11-17 m^2/g
Colour	Black
Morphology	See SEM picture
Bulk Density	-
True Density	-

io·li·tec nanomaterials

Technical Data Sheet

Copper(II)Oxide Powder

Revision Date: 02/02/2009
Date Issued: 03/02/2007

3 SPECIFICATIONS: ICP-OES

Element	content
Al	< 0.01 %
Ba	< 0.01 %
Cd	< 0.01 %
Co	< 0.01 %
Cr	< 0.01 %
Fe	< 0.01 %
Mn	< 0.01 %
Pb	< 0.01 %
Zn	< 0.02 %
Ca	< 0.05 %

4 SCANNING ELECTRON MICROSCOPY

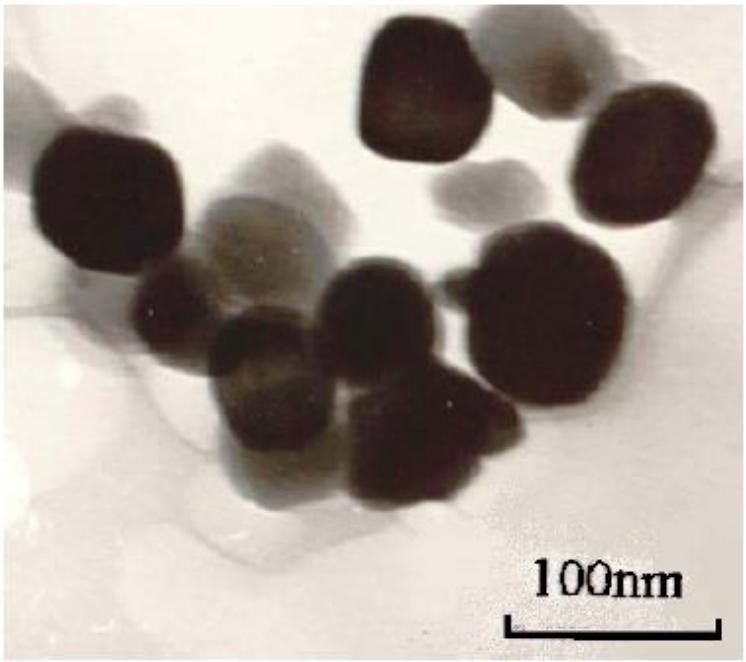

io·li·tec nanomaterials

Technical Data Sheet

Copper(II)Oxide Powder

Revision Date: 02/02/2009
Date Issued: 03/02/2007

6 ORDER INFORMATION

NO-0031-HP can be obtained in the following standard quantities:

Quantity	Price
25 g	Please enquire
50 g	Please enquire
100 g	Please enquire
500 g	Please enquire
1 kg	Please enquire
Bulk	Please enquire

Please send your order via email to order@nanomaterials.iolitec.de
or fax +49 (0)7131 – 89839109.

7 OTHER INFORMATION

DISCLAIMER

THE ABOVE INFORMATION IS BELIEVED TO BE CORRECT BUT DOES NOT PURPOPOSED TO BE ALL INCLUSIVE AND SHALL BE USED ONLY AS A GUIDE. IOLITEC SHALL NOT BE HELD LIABLE FOR ANY DAMAGE RESULTING FROM HANDLING OR FROM CONTACT WITH THE ABOVE PRODUCT. THIS INFORMATION RELATES ONLY TO THE SPECIFIC MATERIAL DESIGNATED AND MAY NOT BE VALID FOR SUCH MATERIAL USED IN COMBINATION WITH ANY OTHER MATERIALS OR ANY PROCESS. IT IS THE USERE'S RESPONISIBILTY TO SATISFY HIMSELF AS TO THE SUITABILITY OF SUCH INFORMATION FOR HIS OWN PARTICULAR USE.

IT IS THE USERE'S RESPONISIBILTY TO SATISFY HIMSELF AS TO THE SUITABILITY OF SUCH INFORMATION FOR HIS OWN PARTICULAR USE.

IN NO WAY SHALL IOLITEC BE LIABLE FOR ANY CLAIMS, LOSSES OR DAMAGES OF ANY THIRD PARTY OR FOR THE LOST PROFITS OR ANY SPECIAL, INDIRECT, INCIDENTAL, CONSEQUENTIAL OR EXEMPLARY DAMAGES, HOWSOEVER ARISING, EVEN IF THE COMPANY HAS BEEN ADVISED OF THE POSSIBILITY OF SUCH DAMAGES.

Technical Data Sheet

Aluminium oxide, gamma

Revision Date: 01/02/2009
Date Issued: 03/01/2008

1 IDENTIFICATION OF THE SUBSTANCE/PREPARATION AND THE COMPANY / UNDERTAKING

Product name	Aluminium oxide, alpha, Nanopowder
Product code	NO-0036-HP
Supplier	IoLiTec Ionic Liquids Technologies GmbH Salzstrasse 184 D-74076 Heilbronn Germany
Telephone	+49 (0)7131 - 898390
Fax	+49 (0)7131 - 89839109
Emergency telephone	+49 (0)179 - 5322578

2 COMPOSITION / INFORMATION ON INGREDIENTS

Ingredient name	Aluminium oxide, gamma
CAS No.	1344-28-1
Empirical Formula	γ-Al_2O_3
Molecular weight	101.96 amu
Purity	99+ %
Average Particle Size	20 nm
Specific Surface Area	<200 m^2/g
Colour	white
Morphology	spherical
Bulk Density	-
True Density	0.9 g/cm^3
Melting point	2045°C

io·li·tec nanomaterials

Technical Data Sheet

Aluminium oxide, gamma

Revision Date: 01/02/2009
Date Issued: 03/01/2008

Boiling point	2980°C

3 TRANSMISSION ELECTRON MICROSCOPY

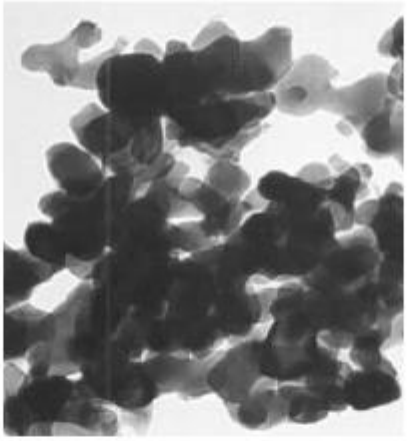

4 OTHER INFORMATION

DISCLAIMER

THE ABOVE INFORMATION IS BELIEVED TO BE CORRECT BUT DOES NOT PURPOPOSED TO BE ALL INCLUSIVE AND SHALL BE USED ONLY AS A GUIDE. IOLITEC SHALL NOT BE HELD LIABLE FOR ANY DAMAGE RESULTING FROM HANDLING OR FROM CONTACT WITH THE ABOVE PRODUCT. THIS INFORMATION RELATES ONLY TO THE SPECIFIC MATERIAL DESIGNATED AND MAY NOT BE VALID FOR SUCH MATERIAL USED IN COMBINATION WITH ANY OTHER MATERIALS OR ANY PROCESS. IT IS THE USERE'S RESPONISIBILTY TO SATISFY HIMSELF AS TO THE SUITABILITY OF SUCH INFORMATION FOR HIS OWN PARTICULAR USE.

Appendix B UDF Models

Batchelor Model

```
#include "udf.h"
#define fi 0.02
#define ro_s 3950
/*#define cp_f 1845*/

DEFINE_PROPERTY(cell_density, cell, thread)
{
real ro_nf;
real ro_f;
real tt= C_T(cell, thread);
ro_f=1000*(1-((tt+15.7917)*((tt-277.1363)*(tt-277.1363)/(508929.2*(tt-205.0204)))));
ro_nf=(((1-fi)*(ro_f))+(fi*(ro_s)));
return ro_nf;
}
DEFINE_SPECIFIC_HEAT(cell_specific_heat, T, Tref, h, yi)
{
real cp;
real cp_f;
real cp_s;
real ro_f;
cp_s= 765;
cp_f=9616.873445-48.73648329*T+0.1444662*((pow((T) ,2)))-0.000141414*((pow((T) ,3)));
ro_f=1000*(1-((T+15.7917)*((T-277.1363)*(T-277.1363)/(508929.2*(T-205.0204)))));
cp=((1-fi)*(ro_f*(cp_f))+(fi*(ro_s*(cp_s))))/(((1-fi)*ro_f)+fi*ro_s);
*h = cp*(T-Tref);
return cp;
}
DEFINE_PROPERTY(thermal_conductivity, cell, thread)
{
real tt= C_T(cell, thread);
real mu_f;
real ro_f;
real k_eff;
real ks;
real kf;
real Re;
real Pr;
real cp_f;
cp_f =9616.873445-48.73648329*tt+0.1444662*((pow((tt) ,2)))-0.000141414*((pow((tt)
,3)));
kf=-1.1245+0.009734*tt-0.000013158*tt*tt;
ks=35;
mu_f=0.02165-0.0001208*tt+(1.7184e-7)*tt*tt;
ro_f=1000*(1-((tt+15.7917)*((tt-277.1363)*(tt-277.1363)/(508929.2*(tt-205.0204)))));
Re= (2*ro_f*tt*1.3806488e-23)/((22/7)*25e-9*(mu_f*mu_f));
Pr= (mu_f*cp_f)/(kf);
k_eff=kf*(1+(4.4*(pow((Re) ,0.4)))*(pow((Pr) ,0.66))*(pow((tt/273.15)
,10))*(pow((ks/kf) ,0.03))*(pow((fi) ,0.66)));
return k_eff;
}
DEFINE_PROPERTY(viscosity, cell, thread)
{
real mu_f;
real mu_eff;
real tt= C_T(cell, thread);
mu_f=0.02165-0.0001208*tt+(1.7184e-7)*tt*tt;
mu_eff =mu_f*(1+2.5*fi+6.2*fi*fi);
```

```
return mu_eff;
}
```

Brinkman model

```
#include "udf.h"
#define fi 0.02
#define ro_s 3950
/*#define cp_f 1845*/

DEFINE_PROPERTY(cell_density, cell, thread)
{
real ro_nf;
real ro_f;
real tt= C_T(cell, thread);
ro_f=1000*(1-((tt+15.7917)*((tt-277.1363)*(tt-277.1363)/(508929.2*(tt-205.0204)))));
ro_nf=(((1-fi)*(ro_f))+(fi*(ro_s)));
return ro_nf;
}
DEFINE_SPECIFIC_HEAT(cell_specific_heat, T, Tref, h, yi)
{
real cp;
real cp_f;
real cp_s;
real ro_f;
cp_s= 765;
cp_f=9616.873445-48.73648329*T+0.1444662*((pow((T) ,2)))-0.000141414*((pow((T) ,3)));
ro_f=1000*(1-((T+15.7917)*((T-277.1363)*(T-277.1363)/(508929.2*(T-205.0204)))));
cp=((1-fi)*(ro_f*(cp_f))+(fi*(ro_s*(cp_s))))/(((1-fi)*ro_f)+fi*ro_s);
*h = cp*(T-Tref);
return cp;
}
DEFINE_PROPERTY(thermal_conductivity, cell, thread)
{
real tt= C_T(cell, thread);
real mu_f;
real ro_f;
real k_eff;
real ks;
real kf;
real Re;
real Pr;
real cp_f;
cp_f =9616.873445-48.73648329*tt+0.1444662*((pow((tt) ,2)))-0.000141414*((pow((tt)
,3)));
kf=-1.1245+0.009734*tt-0.000013158*tt*tt;
ks=35;
mu_f=0.02165-0.0001208*tt+(1.7184e-7)*tt*tt;
ro_f=1000*(1-((tt+15.7917)*((tt-277.1363)*(tt-277.1363)/(508929.2*(tt-205.0204)))));
Re= (2*ro_f*tt*1.3806488e-23)/((22/7)*25e-9*(mu_f*mu_f));
Pr= (mu_f*cp_f)/(kf);
k_eff=kf*(1+(4.4*(pow((Re) ,0.4)))*(pow((Pr) ,0.66))*(pow((tt/273.15)
,10))*(pow((ks/kf) ,0.03))*(pow((fi) ,0.66)));
return k_eff;
}
DEFINE_PROPERTY(viscosity, cell, thread)
{
real mu_f;
```

```
real mu_eff;
real tt= C_T(cell, thread);
mu_f=0.02165-0.0001208*tt+(1.7184e-7)*tt*tt;
mu_eff =mu_f/(pow((1-fi) ,2.5));
return mu_eff;
}
```

Einstein model

```
#include "udf.h"
#define fi 0.02
#define ro_s 3950
/*#define cp_f 1845*/

DEFINE_PROPERTY(cell_density, cell, thread)
{
real ro_nf;
real ro_f;
real tt= C_T(cell, thread);
ro_f=1000*(1-((tt+15.7917)*((tt-277.1363)*(tt-277.1363)/(508929.2*(tt-205.0204)))));
ro_nf=(((1-fi)*(ro_f))+(fi*(ro_s)));
return ro_nf;
}
DEFINE_SPECIFIC_HEAT(cell_specific_heat, T, Tref, h, yi)
{
real cp;
real cp_f;
real cp_s;
real ro_f;
cp_s= 765;
cp_f=9616.873445-48.73648329*T+0.1444662*((pow((T) ,2)))-0.000141414*((pow((T) ,3)));
ro_f=1000*(1-((T+15.7917)*((T-277.1363)*(T-277.1363)/(508929.2*(T-205.0204)))));
cp=((1-fi)*(ro_f*(cp_f))+(fi*(ro_s*(cp_s))))/(((1-fi)*ro_f)+fi*ro_s);
*h = cp*(T-Tref);
return cp;
}
DEFINE_PROPERTY(thermal_conductivity, cell, thread)
{
real tt= C_T(cell, thread);
real mu_f;
real ro_f;
real k_eff;
real ks;
real kf;
real Re;
real Pr;
real cp_f;
cp_f =9616.873445-48.73648329*tt+0.1444662*((pow((tt) ,2)))-0.000141414*((pow((tt)
,3)));
kf=-1.1245+0.009734*tt-0.000013158*tt*tt;
ks=35;
mu_f=0.02165-0.0001208*tt+(1.7184e-7)*tt*tt;
ro_f=1000*(1-((tt+15.7917)*((tt-277.1363)*(tt-277.1363)/(508929.2*(tt-205.0204)))));
Re= (2*ro_f*tt*1.3806488e-23)/((22/7)*25e-9*(mu_f*mu_f));
Pr= (mu_f*cp_f)/(kf);
k_eff=kf*(1+(4.4*(pow((Re) ,0.4)))*(pow((Pr) ,0.66))*(pow((tt/273.15)
,10))*(pow((ks/kf) ,0.03))*(pow((fi) ,0.66)));
return k_eff;
}
DEFINE_PROPERTY(viscosity, cell, thread)
```

```
{
real mu_f;
real mu_eff;
real tt= C_T(cell, thread);
mu_f=0.02165-0.0001208*tt+(1.7184e-7)*tt*tt;
mu_eff =mu_f*(1+2.5*fi);
return mu_eff;
}
```

Maiga model

```
#include "udf.h"
#define fi 0.02
#define ro_s 3950
/*#define cp_f 1845*/

DEFINE_PROPERTY(cell_density, cell, thread)
{
real ro_nf;
real ro_f;
real tt= C_T(cell, thread);
ro_f=1000*(1-((tt+15.7917)*((tt-277.1363)*(tt-277.1363)/(508929.2*(tt-205.0204)))));
ro_nf=(((1-fi)*(ro_f))+(fi*(ro_s)));
return ro_nf;
}
DEFINE_SPECIFIC_HEAT(cell_specific_heat, T, Tref, h, yi)
{
real cp;
real cp_f;
real cp_s;
real ro_f;
cp_s= 765;
cp_f=9616.873445-48.73648329*T+0.1444662*((pow((T) ,2)))-0.000141414*((pow((T) ,3)));
ro_f=1000*(1-((T+15.7917)*((T-277.1363)*(T-277.1363)/(508929.2*(T-205.0204)))));
cp=((1-fi)*(ro_f*(cp_f))+(fi*(ro_s*(cp_s))))/(((1-fi)*ro_f)+fi*ro_s);
*h = cp*(T-Tref);
return cp;
}
DEFINE_PROPERTY(thermal_conductivity, cell, thread)
{
real tt= C_T(cell, thread);
real mu_f;
real ro_f;
real k_eff;
real ks;
real kf;
real Re;
real Pr;
real cp_f;
cp_f =9616.873445-48.73648329*tt+0.1444662*((pow((tt) ,2)))-0.000141414*((pow((tt)
,3)));
kf=-1.1245+0.009734*tt-0.000013158*tt*tt;
ks=35;
mu_f=0.02165-0.0001208*tt+(1.7184e-7)*tt*tt;
ro_f=1000*(1-((tt+15.7917)*((tt-277.1363)*(tt-277.1363)/(508929.2*(tt-205.0204)))));
Re= (2*ro_f*tt*1.3806488e-23)/((22/7)*25e-9*(mu_f*mu_f));
Pr= (mu_f*cp_f)/(kf);
k_eff=kf*(1+(4.4*(pow((Re) ,0.4)))*(pow((Pr) ,0.66))*(pow((tt/273.15)
,10))*(pow((ks/kf) ,0.03))*(pow((fi) ,0.66)));
```

```
return k_eff;
}
DEFINE_PROPERTY(viscosity, cell, thread)
{
real mu_f;
real mu_eff;
real tt= C_T(cell, thread);
mu_f=0.02165-0.0001208*tt+(1.7184e-7)*tt*tt;
mu_eff =mu_f*(1+7.3*fi+123*fi*fi);
return mu_eff;
}
```

Nguyen model

```
#include "udf.h"
#define fi 0.02
#define ro_s 3950
/*#define cp_f 1845*/

DEFINE_PROPERTY(cell_density, cell, thread)
{
real ro_nf;
real ro_f;
real tt= C_T(cell, thread);
ro_f=1000*(1-((tt+15.7917)*((tt-277.1363)*(tt-277.1363)/(508929.2*(tt-205.0204)))));
ro_nf=(((1-fi)*(ro_f))+(fi*(ro_s)));
return ro_nf;
}
DEFINE_SPECIFIC_HEAT(cell_specific_heat, T, Tref, h, yi)
{
real cp;
real cp_f;
real cp_s;
real ro_f;
cp_s= 765;
cp_f=9616.873445-48.73648329*T+0.1444662*((pow((T) ,2)))-0.000141414*((pow((T) ,3)));
ro_f=1000*(1-((T+15.7917)*((T-277.1363)*(T-277.1363)/(508929.2*(T-205.0204)))));
cp=((1-fi)*(ro_f*(cp_f))+(fi*(ro_s*(cp_s))))/(((1-fi)*ro_f)+fi*ro_s);
*h = cp*(T-Tref);
return cp;
}
DEFINE_PROPERTY(thermal_conductivity, cell, thread)
{
real tt= C_T(cell, thread);
real mu_f;
real ro_f;
real k_eff;
real ks;
real kf;
real Re;
real Pr;
real cp_f;
cp_f =9616.873445-48.73648329*tt+0.1444662*((pow((tt) ,2)))-0.000141414*((pow((tt)
,3)));
kf=-1.1245+0.009734*tt-0.000013158*tt*tt;
ks=35;
mu_f=0.02165-0.0001208*tt+(1.7184e-7)*tt*tt;
ro_f=1000*(1-((tt+15.7917)*((tt-277.1363)*(tt-277.1363)/(508929.2*(tt-205.0204)))));
Re= (2*ro_f*tt*1.3806488e-23)/((22/7)*25e-9*(mu_f*mu_f));
```

```
Pr= (mu_f*cp_f)/(kf);
k_eff=kf*(1+(4.4*(pow((Re) ,0.4)))*(pow((Pr) ,0.66))*(pow((tt/273.15)
,10))*(pow((ks/kf) ,0.03))*(pow((fi) ,0.66)));
return k_eff;
}
DEFINE_PROPERTY(viscosity, cell, thread)
{
real mu_f;
real mu_eff;
real tt= C_T(cell, thread);
mu_f=0.02165-0.0001208*tt+(1.7184e-7)*tt*tt;
mu_eff =mu_f*(1+0.025*fi+0.015*fi*fi);
return mu_eff;
}
```